UC Berkeley
UC Berkeley Electronic Theses and Dissertations

Title

Estimation and Utilization of Reconstruction Uncertainty for Atom Probe Feature Extraction

Permalink

https://escholarship.org/uc/item/7vg2f8rb

Author

Still, Evan

Publication Date

2023

Peer reviewed|Thesis/dissertation

Estimation and Utilization of Reconstruction Uncertainty for Atom Probe Feature
Extraction

By

Evan Still

A dissertation submitted in partial satisfaction of the

requirements for the degree of

Doctor of Philosophy

in

Engineering-Nuclear Engineering

in the

Graduate Division

of the

University of California, Berkeley

Committee in charge:

Professor Peter Hosemann, Chair
Associate Professor Lee Bernstein
Assistant Professor Mary Scott
Dr. Dan Schreiber

Spring 2023

Estimation and Utilization of Reconstruction Uncertainty for Atom Probe Feature
Extraction

Abstract

Estimation and Utilization of Reconstruction Uncertainty for Atom Probe Feature
Extraction

by

Evan Still

Doctor of Philosophy in Engineering-Nuclear Engineering

University of California, Berkeley

Professor Peter Hosemann, Chair

Atom Probe Tomography (APT) is a powerful analytical technique for 3D characterization
of materials at the atomic scale which has been widely used to study irradiation induced
features. However, the accuracy and reliability of the atom probe reconstruction and post-
processing methods such as cluster analysis is often neglected. In an effort to account for
both of these limitations we introduce a two-step method for quantifying the quality of an
atom probe reconstruction and the resulting secondary analysis.

First, we developed a pointwise measure of uncertainty for APT data based on linear er-
ror propagation. This approach provide a systematic way of estimating the uncertainty
in the atom positions and the most influential reconstruction parameters. The pointwise
uncertainty measure can be used to assess the local quality of APT data and govern alter-
nate reconstruction directions which minimize uncertainty. Furthermore, focusing the error
analysis not on resolution but on parameter and coordinate uncertainty enables error to be
propagated through complex processes such as the measurement of isotopically enriched thin
films.

Second, we developed a method which extends monte-carlo consensus clustering from K-
based clustering algorithms to density-based clustering algorithms. In doing so a measure of
relative stability is introduced to describe the ambiguity of clustering observed in an APT
sample and automate the selection of the distance parameter for DBSCAN (Density-based
spatial clustering of applications with noise). Our approach uses Monte-Carlo perturbation
statistics, and thus could be linked to use the pointwise uncertainty established in the first
part of this work, to generate alternate atom probe datasets and then apply DBSCAN to
each of these datasets. In doing so the sample size for which to calculate grows in magnitude
enabling more thorough post-clustering filtration methods with which to extract clusters
from high-noise scenarios. We use statistical methods to analyze the results and determine

the optimal DBSCAN parameters that maximize the clustering performance and minimize the uncertainty.

The efficacy and utility of pointwise error propagation is demonstrated through a case study on the measurement of an isotopically enriched iron thin film while our novel clustering algorithm, Density-based Monte-Carlo Consensus Clustering (DMC3), is benchmarked against a round robin study on binary Fe-Cu systems with an emphasis on irradiation induced hardening. Our approaches provides a quantitative and objective way of assessing the quality of APT data and improving the reliability of APT data analysis.

To all of the cats I met along the way.

Contents

List of Figures

List of Tables

Acknowledgments

I would like to thank my advisors Peter Hosemann and Dan Schreiber for believing in me even when I did not believe in myself and providing the guidance and encouragement that enabled me to find a research niche that I could passionately explore. Without both of them I would not have found the willpower to continue on with my doctorate. At this point I would also like to thank Dan and by extension Pacific Northwest National Lab for the provision of atom probe data for testing and development.

My gratitude for my Dissertation Committee cannot be understated, especially due to their willingness to provide feedback on topics that both fall within and outside of their immediate expertise: Dr. Peter Hosemann, Dr. Dan Schreiber, Dr. Mary Scott, and Dr. Lee Bernstein.

It would be impossible to name all of the colleagues I have made over my ten years (I stopped counting) at Berkeley pursuing both my Bachelors and Doctorate, but each one knows which group they belong to. First and foremost I would like to thank the extended Nuclear Materials group for the ritualistic research meetings and their contribution to my coffee addiction. I would like to thank the Thermal Hydraulics group (and Dr. Alan Bolind the enabler) for giving me access to their office and another home in Etcheverry beyond the Materials office.

Above all, I am gracious for the friendships I have made outside of academia over the past three years for providing an escape and reminding me that a world exists outside of academia. The Watergate will always hold a special place in my heart for teaching me the necessary skills to negotiate with and manipulate landlords. Without Tanner, Alyssa, Pod, and Isabelle I would not have made it through statistics and subsequently been unable to complete the first half of this work. I would like to thank the incorporeal forms of soup and InsomniacCat for their assistance in maintaining my physical wellbeing (through the provision of food) and my mental wellbeing, even if it resulted in the emotional damage from but not limited to Cyberpunk Edgerunners. To my other terminally online friends; Amayamar, Razgiz, dragonknight, and Baba Yaga, thank you for all of the late nights playing games when I could not sleep and most importantly introducing me to Monster Hunter. Finally, I would like to thank Hideaki Anno for their work on the Evangelion series and inspiring the use of NERV as an acronym.

Chapter 1

Introduction

1.1 Motivation

In recent years, the world has been facing a serious issue of climate change, and it has become imperative for the global community to shift towards sustainable and renewable sources of energy. Nuclear fission energy has been used commercially to produce electricity for the last 60 years, and the arguments for its continued use as a solution to the climate crisis primarily focused on the socioeconomic implications and the environmental impact compared to alternative fuel sources. On the socioeconomic front, nuclear energy provides a reliable baseload energy and it is believed that it will aid emerging economies on their path to energy independence without disproportionately impacting underserved communities [52, 103, 70, 53]. Thus far use of nuclear energy has prevented over 1.84 million deaths related to air pollution and 60 gigatonnes (Gt) of CO2 greenhouse gas emissions that would have resulted from burning fossil fuels [69, 93]. Furthermore, current predictions indicate that nuclear energy could prevent an additional 420k-7.04 million deaths and 80-240 Gt of CO2 emissions by 2050 [69]. However, similar to other extractive industries it is often underserved communities which are impacted most by the exploitative tactics of mining conglomerates and the residual health impacts from mismanaged waste leading to resistance from the local populous [90, 76, 101, 53]. Without confronting the historic impacts of nuclear energy on underprivileged communities and working to address the concerns of the modern-day stakeholders in the use and growth of nuclear power will be stifled on the social stage, regardless of legislative or technical solutions to the economic, security, and safety challenges that so far have limited the expansion of nuclear.

Nuclear fission energy has been used commercially to produce electricity for more than 60 years for commercial power generation. The United States, being world's largest producer of nuclear power, has accounted for more than 30% of electricity generated by nuclear power in the world. The 93 currently operating nuclear reactors account for 20% of the USA's electricity production [93]. In the United States, nuclear power plants are either pressurized water reactors (PWRs) or boiling water reactors (BWRs), with other reactor types including

heavy water reactors, gas-cooled reactors, graphite-moderated reactors, and liquid-metal-cooled reactors primarily serving as research reactors. Despite the low rate of mortality compared to other fuel sources such as goal, there have been several accidents in the past that have resulted in nuclear radiation leaks, including the Three Mile Island accident in the United States and the Chernobyl and Fukushima disasters [100]. These incidents have caused public concern regarding the safety of nuclear power plants and have motivated the development of improved reactor designs that incorporate accident tolerant fuels and passive safety mechanisms as core requirements of fourth generation reactors [118, 11, 15, 99, 118, 68, 51, 1].

Challenges for generation IV reactors

Generation IV reactors are still in the conceptual design stage, but they hold great promise in terms of addressing some of the current limitations of nuclear energy. These reactors aim to achieve higher fuel efficiency, reduce the volume and longevity of nuclear waste, and enhance safety features. One of the key features of these reactors is the use of new types of fuel, such as liquid metal, gas, or molten salt, which could potentially provide higher energy yields and longer fuel cycles. Additionally, development the aforementioned passive are a primary avenue of research, funding via multiple US Department of Energy (DOE) programs [21, 49].

The implementation of Generation IV reactors faces significant technical and regulatory challenges. The use of new fuel types and coolants requires the development of new materials that can withstand the extreme environments within the reactor, such as high temperatures, corrosive salts, and fast neutron fluxes. One of the main challenges for materials in current and next-generation reactors is the effect of radiation damage on the mechanical properties of these materials. Radiation damage can cause changes in the microstructure of the materials, such as the formation of voids, dislocations, and precipitates, which can lead to material embrittlement and degradation of mechanical properties. Additionally, radiation can cause changes in the chemical properties of materials, resulting in changes to local chemistry.

Another challenge for materials in reactors is the need for materials that can withstand high temperatures and corrosive environments in spite of chemical changes depletion brought on by irradiation, implantation, and transmutation. Many of the structural materials used in reactors, such as stainless steels and nickel-based alloys, have excellent corrosion resistance but are limited by their temperature capabilities. The development of new materials, such as advanced ceramics and high-temperature alloys, that can withstand higher temperatures and harsher environments could lead to more efficient and safer reactor designs [110].

In summary, nuclear energy has the potential to play a critical role in combating climate change and providing sustainable and reliable energy sources. Current and next-generation reactor designs offer significant improvements in terms of fuel efficiency, waste reduction, and safety features. However, the development of new materials that can withstand the extreme environments within reactors is critical for realizing the full potential of nuclear energy. Addressing the challenges associated with materials science in nuclear energy will

require sustained investment in research and development to improve our understanding of material behavior in extreme environments and to develop new materials with enhanced properties. It is important for policymakers, the nuclear industry, and the scientific community to collaborate and prioritize the development of advanced materials for nuclear energy applications. By addressing the materials science challenges, we can unlock the full potential of nuclear energy and realize a clean, sustainable, and reliable energy future.

1.2   Irradiation effects

Radiation damage is a critical issue for the longevity of materials in a reactor environment not only due to the intrinsic damage to the crystal structure but the synergistic effects with other degradation phenomena. The degree of radiation damage is quantified by the average number of times, each atom has been displaced from its lattice site, which is the definition of displacement per atom (dpa). These displacements originate from the transfer of energy from incoming energetic particles (neutron and ion) to lattice atoms, such that energy transfer is sufficient to break the bonds of that atom and its neighbors, denoted as the displacement energy. The displaced atom goes on to cause further displacements producing interstitials, vacancies, and anti-site defects in a chain reaction referred to as a displacement cascade. While the majority of the defects annihilate during the subsequent recombination process, the remaining defects form defect clusters, migrate to defect sinks, or remain as anti-site defects. The increase in point defect concentration contributes to radiation-enhanced diffusion, and thus phase instability, dissolution, and segregation of elements. These indirect phenomena then enhance other degradation phenomena such as corrosion, creep, and embrittlement, etc. The accumulation of radiation-induced defects (interstitial/vacancy loops, voids, precipitates) lead to significant hardening and embrittlement of the structural materials, which significantly influences the safety consideration of the structural components in service.

The Kinchin-Pease model is a widely used approach for describing and correlating the behavior of point defects in crystalline materials with the measure of dpa under radiation exposure. The fundamental assumption of the Kinchin-Pease model is that the number of point defects generated in a material is proportional to the dpa. It also assumes that the migration of point defects is driven by random thermal motion, and that the rate of defect migration depends on the concentration of defects and the concentration of mobile point defects such as vacancies [92, 71]. Despite these limiting assumptions the Kinchin-Pease model remains widely used in part due to the experimental difficulty in measuring the true number of displacements given recombination and its efficacy at providing a relative measure to compare the presence of phenomena for the same class of materials.

There have been efforts to overcome these limitations, namely sophisticated models such as the Norgett-Robinson-Torrens (NRT) model and the Modified Kinchin-Pease (MKP) model [91, 18]. These models take into account the effects of displacement cascades, as well as the migration and interaction of point defects, in predicting the behavior of materials

exposed to high-energy particles [18]. While the NRT model and the MKP model are more complex than the Kinchin-Pease model, but they provide more accurate predictions of the behavior of materials exposed to radiation.

Thus far only displacement damage has been considered however there is a second dominant mechanism for radiation damage. That being transmutation damage where a nuclear reaction transmutes a lattice atom into another element or isotope. Under a fast spectrum neutron flux, transmutation of alloying elements does not typically happen in high enough quantities to have an effect on the thermodynamic stability of the alloy. However, the production of alpha particles from (n, α) reactions have a significant effect on the mechanical properties of the alloy. The production of alpha particles and the subsequent capture of electrons can lead to formation of helium bubbles which in steel can lead to significant embrittlement, reducing the material's ability to deform and absorb energy [16, 30].

Radiation enhanced phenomena

Irradiation-assisted creep and swelling are two volumetric phenomena that affect the behavior and properties of materials exposed to radiation. Creep is a type of plastic deformation that occurs over an extended period of time to a material that is exposed to elevated temperature and stress [131, 10, 86, 79]. There are three modes of creep with two modes governed by diffusion, which enable mass transfer within the material by mobile point defects [134, 98]. The first and diffusionless mode of creep is called dislocation climb and takes place at relatively high stresses and low temperatures. In this mode, plastic deformation of a crystal can be achieved by shifting an extra plane of atoms one lattice spacing across the crystal plane and is not governed by diffusion but can be enhanced via solute drag [133, 130, 77, 19, 124, 12].

The second mode of creep is Coble creep, which occurs at relatively moderate temperatures and stresses. In Coble creep, the deformation mechanism involves atoms diffusing along grain boundaries where there are increased vacancy concentrations allowing conservation of volume but eliciting shape change [134, 98]. For both dislocation and Coble creep grain boundary sliding is generally observed and preventing the formation of cracks and voids at the grain boundaries [31, 132, 125, 115]. In some cases, though the presence of structural features such as coherent precipitates can inhibit the movement of adjacent grains preventing grain boundary sliding and thus enabling crack formation [125, 115]. The third mode of creep is Nabarro-Herring creep, which occurs at high temperatures and low stresses. While both Nabarro-Herring and Coble creep rely on atomic diffusion Nabarro-Herring describes atoms diffusion across the grains and is not limited to the grain boundaries requiring a higher activation energy [134, 98, 10, 86, 79]. Another important distinction for these two modes is that Coble creep possesses a directional dependence. This dependence is based on the alignment of the grains major-axis with the application of stress. If the grains are mainly aligned orthogonal to the stress direction for instance the diffusing atoms will have to travel orthogonal to the loading direction along grain boundaries until a new parallel boundary is reached before they can travel in the same direction as the stress and vacancy gradient [119].

Swelling is the volumetric increase of a material and the coupled reduction of density, and it occurs as a result of the interactions between interstitials and dislocations during the initial displacement cascade. In the initial displacement cascade, interstitials and vacancies are created in equal numbers, and subsequent recombination reduces their concentrations equivalently. However, interstitials are able to travel through the crystal lattice more rapidly than vacancies and dislocations have a larger capture radius for interstitials than vacancies [127, 89, 129]. interstitials The combination of enhanced mobility and capture radius, which is due to the larger stress field that an interstitial imposes on the surrounding crystal, the excess interstitials are quickly absorbed by dislocations, leaving behind an excess of vacancies. Swelling exhibits temperature dependence, and its degree is governed by the point defect concentrations, which were developed through point defect balance equations, evaluating the strength of each source and sink for each type of defect at a given temperature and in the case of 316 stainless steel maximum swelling was found to occur at 500°C when irradiated to 30 dpa. This experiment found that the bubbles were the primary contributor to the swelling and not voids [56].

The temperature dependence of irradiation-assisted creep and swelling cannot be understated and is critical in understanding the underlying mechanisms and predicting their effects. Irradiation-induced point defects can contribute to the onset of dislocation climb and Coble creep at lower temperatures than what would be observed otherwise. On the other hand the onset of Nabarro-Herring creep typically takes place at high temperatures such that that the equilibrium vacancy concentration exceeds that which are produced under irradiation [6, 56, 89]. In this case the kinetics are predominately governed temperature rather and not radiation. The degree of swelling is also governed by the point defect concentrations, which are temperature-dependent. When the temperature is too low, swelling is inhibited, as the point defects do not have sufficient mobility to coalesce into voids. If the temperature is too high, then the high mobility of point defects allows them to be consumed by point defect sinks at a rate exceeding that of void production. In the moderate temperature range, void swelling is able to occur, as the point defects have sufficient mobility to cluster, but insufficient mobility to reach absorption sites [64].

Radiation induced precipitation

Stainless steel pressure vessels are an essential component of a nuclear power plant, which houses the nuclear reactor core and its coolant under high pressure and temperature. However, the radiation environment in a nuclear reactor can lead to changes in the microstructure and mechanical properties of stainless steel, impacting its safety and reliability. One of the primary concerns is radiation-induced precipitation and embrittlement, which can be exacerbated by the presence of impurities such as copper [96, 97, 82, 67].

Radiation-induced precipitation occurs when solute atoms in the steel aggregate to form precipitates due to the increase in defect concentrations resulting from as irradiation. In reactors this process is caused by the displacement of atoms due to energetic neutrons, but can also be emulated to some degree by the use of heavy ions in lab environments. Under the

enhanced diffusion conditions of irradiation, the solute species may undergo rapid diffusion that enables the solutes to aggregate near nucleation sites such as grain boundaries [65, 67, 82]. In the case of stainless steel, this radiation induced segregation can alter the corrosion resistance due to the nucleation of chromium carbides at the grain boundary which depletes the surface chromium concentration and/or embrittle the material altering its toughness depending on the specific precipitate structure [62].

One of the most significant solute species for embrittlement is copper. Historically, the copper concentration in steel was minimized such that copper precipitates could not form under normal use cases. However, the point defect generation resulting from irradiation enables precipitation even with sub 0.1 wt% Cu content leading to significant changes in the mechanical properties of the steel [87, 97, 96]. Segregation and subsequent precipitation for solutes such as Cu and Mn,at the grain boundaries results in local loss of ductility referred to as grain boundary embrittlement. Underlying this phenomena is the decrease in the cohesion energy of the grain boundary, which reduces the resistance to deformation, leading to cracking or fracture [] gb embrittlement irradiation induced cu precipitation.

The exact hardening mechanisms; coherency, modulus mismatch, and order strengthening, given Cu precipitates in steel alloys varies depending on the specific alloys and size of the precipitates. The impact of fine Cu precipitates in BCC steel has been predominantly estimated using the dispersed barrier hardening model [97, 96, 116]. In this model the individual precipitates are assumed to act as barriers to dislocation motion according to the Orowan mechanism where the precipitates act as pinning points about which the dislocations bow and produce dislocation loops until the stress is sufficient to shear the features [97, 96, 116, 126]. Superposition is then used to expand the model to consider the impact of many precipitates.

In the above scenario the fine scale precipitates are generally BCC and coherent with the surrounding matrix and thus an example of coherency strengthening. Due to the coherency there is no strict "barrier" preventing dislocation movement through the precipitates, but instead the relative mismatch in lattice spacing of the features produces a strain field which interacts with the dislocation causing the hardening. On the other hand as Cu precipitates grow in size they transition to an FCC lattice and modulus hardening is a better descriptor of the strengthening mechanism. Modulus strengthening occurs due to the mismatch in the elastic modulus between the precipitates and the matrix. The relative mismatch in modulus results in lattice strains which increase the resistance to dislocation motion [104, 63]. In this scenario the Cu precipitates possess a lower modulus than the matrix, contributing to an increase in strength of the material without leaving behind Orowan loops [104].

1.3 Reproducible data analysis for APT

Technique summary

As a characterization technique atom probe tomography (APT) fills a unique niche by combining isotopic information with a three-dimensional reconstruction to investigate the atomic arrangement of materials. Improvements to the atom probe, such as the inclusion of UV lasers, have enabled to study a wide range of materials, including metals, semiconductors, ceramics, and polymers. APT is particularly useful for studying radiation-induced microstructures because it can provide a detailed 3D view of the material at the atomic scale.

For example, APT has been used to study the formation of voids in metals exposed to high-energy radiation. Voids are empty spaces that form in the material as a result of radiation damage, and they can have a significant impact on the mechanical properties of the material. APT can identify the position and size of individual voids in the material, allowing researchers to study their formation and evolution over time. Similarly, APT has been used to study the formation of dislocation loops in metals exposed to radiation. Detection of dislocation loops however remains difficult with atom probe and requires the loops to become decorated by solute species in high concentrations [113, 47, 48].

In practice, APT works as follows: a small needle-shaped sample is prepared and mounted on a conductive tip, which is then placed inside a high-vacuum chamber. A high electric field is applied to the tip, which ionizes atoms from the surface of the sample that are then accelerated according to a potential gradient and towards a detector. As the ions impact the detector, a mass-to-charge ratio is assigned based upon the time past between the pulse application and collision. The location on the position-sensitive is then combined with assumptions about the flight path and material properties to back project the ions resulting in a 3d reconstruction of their initial location [5, 36, 40, 74].

One of the key advantages attributed to APT is an extremely high spatial resolution. It can identify individual atoms with a resolution of about 0.1 nm in depth and 0.3 nm laterally, which is comparable to the resolution of conventional transmission electron microscopy (TEM), although high resolution and atomic scale TEM can achieve much higher resolution with less ambiguity [44, 43, 24]. While a 0.1 nm depth and 0.3 nm lateral resolution was attributed to APT, in truth achieving this requires samples with well understood evaporation properties such as silicon and calibration of the reconstruction by tweaking many input parameters to resolve features with known properties apriori [85, 38, 42]. This is most commonly done by indexing crystallographic poles in the detector hit map and measuring the interplanar spacing, hence the sub nm resolution, or as is the case for this work by minimizing the curvature of an isotopically enriched thin film [85, 38, 42, 23, 22]. These features are absent in many specimens and in those cases reconstructions are tuned by the eye of subject matter experts with local measurements of the interatomic spacing providing a vague definition of resolution.

Uncertainty quantification of APT reconstructions and analysis

In light of these limitations on the resolution of atom probe this work aims to quantify the uncertainty of the reconstruction on a point by point basis using linear error propagation. Doing so with linear error propagation enables closed form solutions describing each input variable's impact on the depth and lateral uncertainties determining the importance of accurately selecting each variable. The aim of this approach is two fold, 1. is to confirm community beliefs on the most important variables, and 2. to assess if observations on lateral vs depth resolution also apply to pointwise error. Conventional wisdom dictates that the evaporation field/field factor and image compression factor are the most important parameters as varying these provide the largest visual changes for a reconstruction. The discussion of resolution vs error is focused on the a summative step in the reconstruction algorithm where the depth coordinate of the second, third, etc. ions depend on the prior points. It then follows that the depth uncertainty should increase as a function of evaporation order while the lateral uncertainty remains relatively constant. The hypothesis can be summarized as follows:

Sole use of resolution is an insufficient measure of variability for atom probe reconstructions because:.

- The X, Y dimensions possess heteroscedastic variance.

- The Nth ion's position in Z is dependent on the prior N-1 ions resulting in a variance that scales with ion order and thus sample depth.

  - Thus, features identified near the specimen base are inherently less accurate than those at the specimen apex.

To evaluate this hypothesis chapters 2 and 3 establish the principles behind the employed error propagation methods and demonstrate the application of linear error propagation to the reconstruction algorithm. With these observation chapter 4 reflects on how the pointwise error estimates can be used for complex calculations given the covariance between points. Chapter 5 then demonstrates how a thin film can be used to calibrate the image compression factor and field factor. Additionally, this chapter provides a numerical sensitivity analysis of the different input parameters as a function of spatial position within the atom probe tip. Finally, chapter 6 demonstrates how these methods can be applied when estimating the aforementioned thin film's thickness and how the the thickness varies as a function of lateral position.

Automation of APT Analysis

The remainder of this thesis focuses on the extraction of features from atom probe data, specifically the use of clustering algorithms to identify solute-enriched precipitates. Such algorithms can be loosely grouped into K-based methods, where the user supplies the number of clusters (K) to find, and density-based methods where the user provides an effective density

threshold with which to define clusters. For the analysis of atom probe data density-based methods make up the majority of used algorithms, with density-based spatial clustering of applications with noise (DBSCAN) being of special importance [122, 27, 78, 46].

DBSCAN is one of the original density-based clustering algorithms and has been applied to a wide variety of machine learning and data analysis problems over nearly every scientific field which employs clustering algorithms. As a density-based clustering algorithm DBSCAN establishes a density threshold through the use of two parameters: epsilon (ϵ) and order (O), otherwise referred to as minimum points (MinPts) [29]. Epsilon is a distance threshold that defines the maximum distance between two points in a cluster. If two points are within epsilon distance of one another, they are considered part of the same cluster. The order parameter (O) specifies the minimum number of points required for a cluster to be formed and expanded. Points that are not part of any cluster are considered noise and in the case of atom probe would represent the matrix distribution of a solute species.

When analyzing APT data using DBSCAN, selecting the appropriate values for epsilon and order is critical to obtaining accurate and meaningful results. There are several methods for selecting appropriate values for epsilon and order. One common method is to use the k-distance graph, which plots the distance to the k-th nearest neighbor for each point in the dataset. The k-distance graph can be used to visually identify appropriate values for epsilon given an order of k. The knee point of the graph is a good starting point for selecting epsilon although this method is known to breakdown for data with a high background concentration and still leaves the order parameter to be set.

Parameter selection for DBSCAN and other density-based methods have been relatively stagnant over the past decade despite significant strides being made for the selection of the cluster number in K-based methods. In particular, recent developments of the monte-carlo consensus methods have leveraged computational power to automatically select K for K-means, K-centroids, etc. and even provides a hypothesis test to ensure that the data is better represented by multiple clusters as opposed to one cluster. This is a fundamental limitation of all K-based clustering algorithms. In chapter 7 the consensus clustering process is modified for use with density-based algorithms resulting in density-based monte-carlo consensus clustering or DMC3. The ability for DMC3 to optimize both the order and epsilon parameter in variable noise levels is also assessed here. Then in chapter 8 DMC3 is applied to a set of simulated Fe-Cu systems that were a part of prior round robin study to provide a basis of comparison with the analysis of leading subject matter experts [27, 78].

Chapter 2

Summary of error propagation methods

2.1   Approaches to uncertainty propagation

Prior attempts to understand the inherent inaccuracies in the atom probe reconstruction process have focused on determining an experimental interplanar spacing to compare with known lattice parameters to both calibrate the dataset and estimate the resolution of APT [44, 42]. In this context, differences from the known lattice parameters are representative of the bias in our estimate while the resolution is indicative of experimental uncertainty. Note that the accuracy of such measurements has an inverse relationship with the distance from the reference feature often a pole figure.

The emphasis on resolution is carried over from microscopy and provides context on the smallest identifiable features given the system hardware, but does not provide information such as variance, mean, and median for individual measurements. To instead quantify the uncertainty on a pointwise basis statistical methods for error propagation are employed. This work focuses predominantly on linear propagation of error from an experimental standpoint however additionally details monte-carlo methods for instances where application of linear propagation is inapplicable due to either theoretical or practical constraints.

2.2   Linear propagation of uncertainty

Consider a quantity x which is a function, f, of two measurements, u and v, for which the variance, var(x) is unknown. Assume that (x, u, v) are representative of approximately normal random variables denoted (X, U, V) where (U, V) posses known variances and a covariance, cov(U, V). Additionally assume that f is continuous, differentiable, and can be locally approximated as a linear function. Then var(X) is given according to equation 2.1

which can alternatively be written in terms of the standard deviations, σ [117, 72, 7].

$$var(X) = \left(\frac{\partial f}{\partial U}\right)^2 var(U) + \left(\frac{\partial f}{\partial V}\right)^2 var(V) + 2\frac{\partial f}{\partial U}\frac{\partial f}{\partial V}cov(U,V) \tag{2.1a}$$

$$\sigma_X^2 = \left(\frac{\partial f}{\partial U}\right)^2 \sigma_U^2 + \left(\frac{\partial f}{\partial V}\right)^2 \sigma_V^2 + 2\frac{\partial f}{\partial U}\frac{\partial f}{\partial V}\sigma_{U,V} \tag{2.1b}$$

When propagating uncertainty through a series of operations it is common to utilize a step by step approach to determine the error of individual operations and treat those as the deviations for a subsequent operation. One consideration when employing this approach is that a series of independent measurements may result in non-zero covariance in subsequent steps if multiple intermediate variables share dependencies. To demonstrate this aspect consider the scenario where U, V are no longer representative of measurements but calculated quantities similar to X with an unknown cov(U, V). Furthermore, in this example let U, V be function of a series of independent measurements, M_1 and M_2. Directly using equation 2.1 in this scenario will result in an error estimate that cannot incorporate the cov(U, V). There are three approaches to then include the covariance term in this estimate, the first of which employs the conventional covariance formula, equation 2.2, the second employing the Cauchy-Schwarz inequality, equation 2.3, and the third of which involves rewriting the final function for X in terms of M_1 and M_2.

$$cov(U,V) = \frac{1}{N}\sum_{i=1}^{N}(u_i - \overline{u})(v_i - \overline{v}) \tag{2.2}$$

Firstly, utilization of equation 2.3 gives an exact magnitude and sign of the covariance however requires multiple sample pairs for each measurement, m_i, and thus (u_i, v_i). A positive covariance indicates the scenario where an overestimate of U is always accompanied by an overestimate in V with respect to the mean values resulting in $(u_i - \overline{u})$ and $(v_i - \overline{v})$ possessing the same sign. An alternative scenario is where an overestimate in U is accompanied by an underestimate in V which results in a negative covariance, and thus a smaller total variance than expected without the covariance correction. The final scenario is where an overestimate in U is accompanied by an underestimate of equal magnitude in V resulting in a covariance of 0 but does not mean the variables are independent.

$$|cov(U,V)| \leq \sqrt{var(U)var(V)} \tag{2.3}$$

Secondly, in the absence of multiple sample pairs but known variances the Cauchy-Schwarz inequality, equation 2.3, provides an upper bound on the magnitude of the covariance but does not indicate the relationship between the two variables and thus the sign. From this an upper and lower bound can be provided on the variance of X, as shown in equations 2.4 and 2.5, but the distribution of var(X) will remain unknown.

$$C = \left(\frac{\partial f}{\partial U}\right)^2 var(U) + \left(\frac{\partial f}{\partial V}\right)^2 var(V) \tag{2.4}$$

$$C - |2\frac{\partial f}{\partial U}\frac{\partial f}{\partial V}\sqrt{var(U)var(V)}| \leq var(X) \leq C + |2\frac{\partial f}{\partial U}\frac{\partial f}{\partial V}\sqrt{var(U)var(V)}| \qquad (2.5)$$

The final approach is to substitute the functions for U, V into X such that X incorporates the input variables for U, V. If $U = f(M_1)$ and $V = f(M_1, M_2)$ then $X = f(M_1, M_2)$. Equation 2.1 can then be rewritten in terms of M_1 and M_2 which if independent removes the need for the covariance term and alternatively have a known covariance. For a more complex series of equations with an arbitrary number of variables equations 2.1 can be generalized as a summation over the partial derivatives and variances with respect to each variable. In equations 2.6 X is written as a function of M which represents a list of variables, $M_1, M_2, ...M_N$ to iterate over.

$$var(X) = \sum_{i=1}^{|M|} \left(\frac{\partial f}{\partial M_i}\right)^2 var(M_i) + \sum_{i=1}^{|M|} \sum_{j=1}^{|M|-i} 2\frac{\partial f}{\partial M_i}\frac{\partial f}{\partial M_{i+j}}cov(M_{i+j}, M_j) \qquad (2.6a)$$

$$\sigma_X^2 = \sum_{i=1}^{|M|} \left(\frac{\partial f}{\partial M_i}\right)^2 \sigma_{M_i}^2 + \sum_{i=1}^{|M|} \sum_{j=1}^{|M|-i} 2\frac{\partial f}{\partial M_i}\frac{\partial f}{\partial M_{i+j}}\sigma_{M_{i+j}, M_j} \qquad (2.6b)$$

2.3   Monte-Carlo uncertainty propagation

As an alternative to linear propagation of uncertainty monte-carlo methods can instead be employed to overcome some of the limitations described in section 2.2 in exchange for increased computational costs. Consider the same initial scenario with random variables (X, U, V) where x is f(u, v). Furthermore, maintain the assumption that the variables U, V have known variances and covariance.

The var(X) and E(X) are estimated using a series of N monte-carlo trials where each trial consists of a sampling and evaluation step. In the sampling step random samples u, v are drawn from U, V. In this scenario it is important to note however that if U, V are dependent variables that one of the samples must be drawn from the conditional distribution. For instance if u is sampled from U than v must be drawn from the conditional distribution of V given u. Next, the evaluation step consists of evaluating f(u, v) and storing the estimate, x. After N trials E(X) and var(X) are found by taking the mean and variance of x from each monte-carlo trial. For an algorithmic description of this process reference algorithm 1.

In the prior approach to find the variance of X two additional constraints were required; 1. that X, U, V follow a normal distribution, and 2. that f was continuous, differentiable, and approximately linear. Constraint 1 is relaxed such that any distribution is valid for U and V if a random sample can be generated. Constraint 2 is eliminated by treating f as a black-box. Treatment of f as a black-box further generalizes this application to complex processes where linear propagation is unsuitable such as tomographic reconstructions [75, 3, 33].

Algorithm 1 Monte-carlo error propagation

---

for i = 1 to N **do**
    Create sample u_i from U
    Create sample v_i from U|V
    Compute $x_i = f(u_i, v_i)$
end for
Compute $\hat{x} = \dfrac{\sum_{i=1}^{N} x_i}{N}$
Compute $\widehat{var}(x) = \dfrac{\sum_{i=1}^{N}(x_i - \hat{x})^2}{N - 1}$

The main detriment to this method is the computational cost required when sampling and evaluating the function for hundreds if not thousands of times. There are situations however where monte-carlo has the computational advantage over linear propagation. Generally, this is restricted to scenarios where the partial derivatives of the function serve as a computational bottleneck for the linear method. In the case of atom probe tomography this limit is intrinsic to shank angle reconstructions as the depth increment for each ion is dependent on the prior ions' increment. The required derivatives are then a recursive function which is evaluated for millions of ions.

Chapter 3

Reconstruction error propagation

Reconstruction of atom probe tomographs continue to be a complex problem due to a multitude of factors, some of which are specimen specific and others artificial. On the specimen specific front, heterogeneity within the material can lead to distortions in the required evaporation field. This impact is most evident in the presence of precipitates where precipitates with a higher required field relative the matrix resist the evaporation process and eventually produce protrusions on the specimen surface. Once evaporation is possible these protrusions act as a secondary tip and lead to a disproportionately large projection of the precipitate onto the detector surface, referred to as under-focusing [40, 74].

At the other extreme exists over-focusing which occurs when the precipitate preferentially evaporates leaving a cavity within the specimen. This cavity then projects ions from the cavity edge inwards shrinking the relative size of the feature and distorting the density. Proprietary reconstructions algorithms held both by commercial companies and research institutions serve as the artificial barrier to accurate reconstruction processes. In spite of this the basic principles of common reconstruction processes are well known and documented in the literature [40, 5, 74].

All reconstructions are founded upon two principles, 1. the specimen radius of curvature and the electric field are related and 2. an evaporation event can be converted into a depth increment and thus the final depth coordinates of the ions can be deduced from the order of evaporation. The primary difference in reconstruction algorithms is the treatment of the depth increment, where voltage-based algorithms rely purely on the applied voltage at any given moment and shank-angle reconstructions require that the changing specimen radius and depth increment maintain a constant angular relationship. In the analysis presented in this work the emphasis is placed upon voltage-based methods as shank-angle approaches are not conducive to linear propagation of uncertainty.

3.1   Basis for tomographic reconstruction

The base tenant that enables the reconstruction process is that the electric field, F, experi-
enced at the sample apex is inversely proportional the surface curvature and thus the radius,
R, given that the specimen apex is modeled as a hemispherical cap as shown in figure 3.1
alongside the point-projection schematic [50]. To account for the fact that the specimen
shank will result in a decrease in the produced field relative to a perfect sphere a correction
term is included in equation 3.1 and is referred to as the field factor, k_f. It should be noted
that while trends have been observed relating the shank angle and radius to k_f in the works
of Larson et al, [73], no general trend has been identified. Despite this it has been shown
that trends can be derived for a given material [41].

$$F = F(V, k_f, R) = \frac{V}{k_f R} \tag{3.1}$$
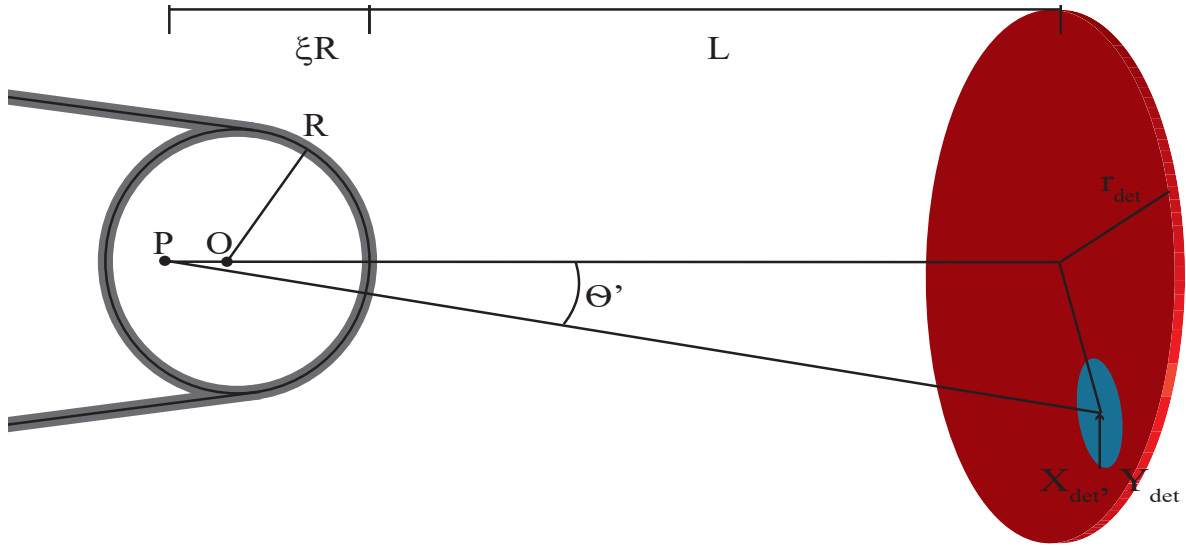
Figure 3.1: Schematic view of the ion point-projection from specimen apex. Here O and P
define the apex origin and projection origin and θ' indicates the compressed launch angle.

As the evaporation process occurs the specimen will inherently blunt given a non-zero
shank angle and result in a decrease in the experienced field. It follows then that an ever
increasing voltage must be applied to induce field evaporation. Given that the voltage,
V, is known and not the specimen curvature equation 3.1 is refactored as equation 3.2 to
determine the radius of curvature during the ith evaporation event at the voltage, V_i. For
both of these equations it should be noted that while V is a measured quantity a global
estimate of F is often used alongside a user defined k_f. A common method for estimating F
is to set it equal to the field of the most dominant element or can be determined according to

field evaporation model [120, 83]. Furthermore, dynamic reconstruction processes attempt to overcome the limitations on k_f and F by providing local estimates of both parameters such that the lattice spacing is preserved to produce a local estimate of F [38, 41, 57, 22].

$$R_i = R(V_i, k_f, F) = \frac{V_i}{k_f F} \tag{3.2}$$

The partial derivatives for R_i are then:

$$\frac{\partial R_i}{\partial V_i} = \frac{1}{F k_f} = \frac{R_i}{V_i} \tag{3.3}$$

$$\frac{\partial R_i}{\partial V_i} = -\frac{V_i}{F^2 k_f} = -\frac{R_i}{F} \tag{3.4}$$

$$\frac{\partial R_i}{\partial k_f} = -\frac{V_i}{F k_f^2} = -\frac{R_i}{k_f} \tag{3.5}$$

Applying the general form of equation 2.1 to equation 3.2 establishes the following relationships for the uncertainty in R_i given estimates of the variances and or standard deviations of V_i, k_f, and F.

$$var(R_i) = \left(\frac{\partial R_i}{\partial V_i}\right)^2 var(V_i) + \left(\frac{\partial R_i}{\partial k_f}\right)^2 var(k_f) + \left(\frac{\partial R_i}{\partial F}\right)^2 var(F) \tag{3.6a}$$

$$+ 2\frac{\partial R_i}{\partial V_i}\frac{\partial R_i}{\partial k_f}cov(V_i, k_f) + 2\frac{\partial R_i}{\partial V_i}\frac{\partial R_i}{\partial F}cov(V_i, F) + 2\frac{\partial R}{\partial k_f}\frac{\partial R_i}{\partial F}cov(k_f, F) \tag{3.6b}$$

$$\sigma_{R_i}^2 = \left(\frac{R_i}{V_i}\right)^2 \sigma_{V_i}^2 + \left(\frac{R_i}{k_f}\right)^2 \sigma_{k_f}^2 + \left(\frac{R_i}{F}\right)^2 \sigma_F^2 \tag{3.6c}$$

In equation 3.6c it is assumed that there are no covariance with respect to the initial variables. This generally holds with respect to V_i however F and k_f often influence the selection of one another. So much so that it is common to treat them as one variable. For all further derivations covariances between the initial variables will be neglected but covariances between dependent variables are accounted for.

Once R_i is found, the spatial coordinates perpendicular to the specimen tip axis (X_i, Y_i), are identified using the detector coordinates and magnification effects of the instrument. This transformation is dependent on the exact reconstruction protocol and is detailed in section 3.2 and 3.3 for small-angle and wide-angle reconstructions. Note however, that X_i and Y_i can be calculated independently for each ion.

General spatial uncertainty in Z

From the original approximation of the specimen as a conical segment with a hemispherical cap the depth coordinate of an ion can be split into two components. The first of which dz'

indicates the relative position of the ion on the spherical cap and the second dz which will indicate the incremental change of the apex as the specimen undergoes field evaporation. The depth coordinate for ion, i, is then given as:

$$Z_i = \left(\sum_{j=1}^{i} dz_j \right) + dz_i' \tag{3.7}$$

Unlike X_i and Y_i where each point can be calculated independently from one another the position of Z_i requires knowledge of the prior i-1 ions. Ignoring dz_i', as it is independent of dz_j' for all (i, j), naive propagation of error for Z_i results in a summation of i error terms corresponding to the current ion and all prior ions depth increments as shown in equation 3.8.

$$\sigma_{Z_i}^2 = \sum_{j=1}^{i} \sigma_{dz_j}^2 \tag{3.8}$$

It then follows that the uncertainty of points $i + 1$ is greater than point i and so on such that the pointwise error compounds as further points are added to the reconstruction giving rise to the first hypothesis: the error associated with feature properties scales with respect to the evaporation order and thus features composed of ions far from the the reconstruction origin are inherently less accurate. Furthermore, dz_{i+1}, dz_i, dz_{i-1}, etc. are not independent and require the incorporation of at least $(i - 1)i/2$ covariance terms. If the points have a positive covariance the resulting variances are expected to be higher than the naive estimate and is likely the case as each depth increment will be influenced by predominantly shared variables. The need to consider the covariance terms is avoided by propagation of error for the final equations written in terms of the initial independent variables, S.

Contributions to dz

Calculation of the depth increment is tied to that of the analyzed volume where this volume is the summation over the volume of the evaporated ions, Φ_i, as seen in equation 3.9:

$$V_{evap} = \sum^{n} \Omega_i \tag{3.9a}$$

$$= n_{evap}\Omega \tag{3.9b}$$

where there have been n evaporation events and an average atomic volume, Φ, can serve as a simplifying assumption. One additional consideration is that of the instrument detection efficiency, η, resulting in a lesser number of detected events such that $n_d = \eta n_{evap}$.

Furthermore, the analyzed volume, V_{evap} (not to be confused with the applied voltage, V_i) must still be related to the specimen geometry and the corresponding evolution as a function of depth as in equation 3.10.

$$V_{evap} = \int_0^{Z_{max}} w_v(z) dz \tag{3.10}$$
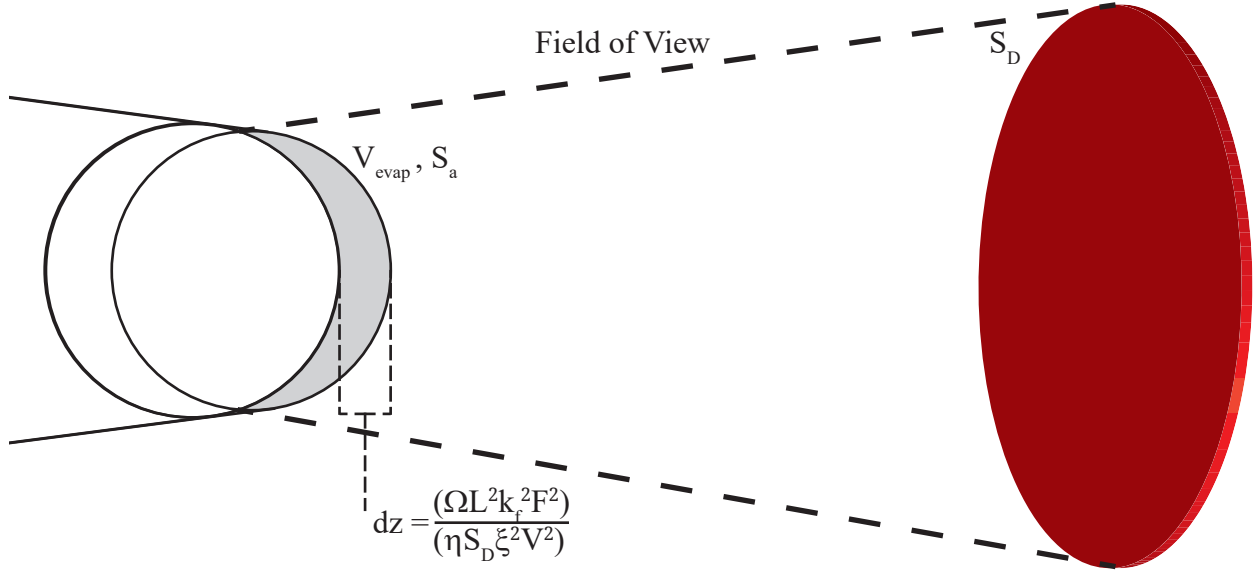
Figure 3.2: Schematic representation of the depth increment given known evaporated volume and the surface area for both the specimen and detector.

Here, $w_v(z)$, describes the relative volume change as a function of the current depth and serves as the main difference in existing reconstruction protocols [9, 45, 61, 5]. Combining equations 3.9 and 3.10 establishes the ion-specific, equation 3.11a, and general form, equation 3.11b, of dz.

$$dz_i = \frac{\Omega_i}{\eta w_V(z_i)} \tag{3.11a}$$

$$dz = \frac{\Omega}{\eta w_V(z)} \tag{3.11b}$$

In the case of both voltage-based reconstructions presented in this work V_{evap} is estimated as the product of the depth and specimen surface area within the detector field-of-view, S_a. A reverse projection of the detector surface area, S_D, onto the specimen apex tangent plane, as in figure 3.2, relates the two areas according to equation 3.12 under a small angle approximation.

$$S_a = \frac{S_D}{M_{proj}^2} \tag{3.12}$$

If the ion volume is assumed to be distributed homogeneously across S_a such that $w_V(z) = S_a$ then combining equations 3.11a and 3.12 while substituting for M_{proj} establishes the following relationship which can be written as a constant term, C_{dz} and non-constant

component.

$$dz_i = \frac{\Omega_i L^2 F^2 k_f^2}{\eta S_D \xi^2 V_i^2} \tag{3.13a}$$

$$= C_{dz} \frac{\Omega_i}{V_i^2} \tag{3.13b}$$

Performing error propagation on equation 3.13a requires eight partial derivatives resulting in the following equations:

$$\frac{\partial dz_i}{\partial F} = 2 \left(\frac{L^2 F^2 k_f^2 \Omega_i}{\eta S_D \xi^2 V_i^2} \right) \left(\frac{1}{F} \right) \tag{3.14}$$

$$\frac{\partial dz_i}{\partial V_i} = -2 \left(\frac{L^2 F^2 k_f^2 \Omega_i}{\eta S_D \xi^2 V_i^2} \right) \left(\frac{1}{V_i} \right) \tag{3.18}$$

$$\frac{\partial dz_i}{\partial k_f} = 2 \left(\frac{L^2 F^2 k_f^2 \Omega_i}{\eta S_D \xi^2 V_i^2} \right) \left(\frac{1}{k_f} \right) \tag{3.15}$$

$$\frac{\partial dz_i}{\partial \xi} = -2 \left(\frac{L^2 F^2 k_f^2 \Omega_i}{\eta S_D \xi^2 V_i^2} \right) \left(\frac{1}{\xi} \right) \tag{3.19}$$

$$\frac{\partial dz_i}{\partial L} = 2 \left(\frac{L^2 F^2 k_f^2 \Omega_i}{\eta S_D \xi^2 V_i^2} \right) \left(\frac{1}{L} \right) \tag{3.16}$$

$$\frac{\partial dz_i}{\partial S_D} = - \left(\frac{L^2 F^2 k_f^2 \Omega_i}{\eta S_D \xi^2 V_i^2} \right) \left(\frac{1}{S_D} \right) \tag{3.20}$$

$$\frac{\partial dz_i}{\partial \Omega_i} = \left(\frac{L^2 F^2 k_f^2 \Omega_i}{\eta S_D \xi^2 V_i^2} \right) \left(\frac{1}{\Omega_i} \right) \tag{3.17}$$

$$\frac{\partial dz_i}{\partial \eta} = - \left(\frac{L^2 F^2 k_f^2 \Omega_i}{\eta S_D \xi^2 V_i^2} \right) \left(\frac{1}{\eta} \right) \tag{3.21}$$

As written above it is evident that the eight partials can be expressed as a product of dz_i and $1/T$ where T indicates which variable the derivative is with respect to. The eight equations can be then condensed into one equation 3.22a with the inclusion of $F(T)$ to account for the constant term.

$$\frac{\partial dz_i}{\partial T} = (dz_i) \left(\frac{F(T)}{T} \right) = C_{dz} \frac{\Omega_i}{V_i^2} \frac{F(T)}{T} \tag{3.22a}$$

$$\text{where } F(T) = \begin{cases} 2, & \text{if } T \text{ is in } \{F, k_f, L\} \\ 1, & \text{if } T = \Omega_i \\ -2, & \text{if } T \text{ is in } \{V_i, \xi\} \\ -1, & \text{if } T \text{ is in } \{S_D, \eta\} \end{cases} \tag{3.22b}$$

Cumulative effect of dz_i

So far the interdependence of evaporation events has been neglected however, as noted in equation 3.7 each ion is associated with a unique depth increment, dz_i, but the total depth of an ion is dependent on the preceding ions. It is thus important to distinguish between measurement dependent variables, such as voltage and ionic identity, and universal variables, such as the previously established L, F, k_f, ξ, η, and S_{det}.

To demonstrate how error propagation can be utilized without introducing covariance terms for the non-ion specific variables consider the error contribution of F. The partial

derivative for Z_i with respect to F can be written and simplified as follows:

$$\frac{\partial Z_i}{\partial F} = \frac{\partial}{\partial F}\left(\left(\sum_{j=1}^{i} dz_j\right) + dz_i'\right) \tag{3.23a}$$

$$= \frac{\partial}{\partial F}\left(\sum_{j=1}^{i} dz_j\right) + \frac{\partial}{\partial F}dz_i' \tag{3.23b}$$

$$= \left(\sum_{j=1}^{i} \frac{\partial}{\partial F}dz_j\right) + \frac{\partial}{\partial F}dz_i' \tag{3.23c}$$

For now focus on the summation as dz_i' is reconstruction specific. Substituting equation 3.22a for $\partial dz_j/\partial F$ replaces the summation of derivatives with a summation of the original dz_j for $j \leq i$.

$$\frac{\partial Z_i}{\partial F} = \left(\sum_{j=1}^{i} 2dz_j\frac{1}{F}\right) + \frac{\partial}{\partial F}dz_i' \tag{3.24a}$$

$$= \frac{2}{F}\left(\sum_{j=1}^{i} dz_j\right) + \frac{\partial}{\partial F}dz_i' \tag{3.24b}$$

$$= C_{dz}\frac{2}{F}\left(\sum_{j=1}^{i} \frac{\Omega_j}{V_j^2}\right) + \frac{\partial}{\partial F}dz_i' \tag{3.24c}$$

Note that this substitution is applicable for all but two of the variables, Ω_i and V_i, as those properties are event specific. The general form of the derivatives of Z_i are thus:

$$\frac{\partial Z_i}{\partial T} = \frac{F(T)}{T}\left(\sum_{j=1}^{i} dz_j\right) + \frac{\partial}{\partial T}dz_i' \text{ for T in } \{F, k_f, L, \xi, S_D, \eta\} \tag{3.25a}$$

$$= C_{dz}\frac{F(T)}{T}\left(\sum_{j=1}^{i} \frac{\Omega_j}{V_j^2}\right) + \frac{\partial}{\partial T}dz_i' \tag{3.25b}$$

Focusing on the summative component of Z_i the following ratios expose the relative importance of each variable described by equation 3.25a. Voltage and ionic volumes are neglected in this comparison as each point may have a distinct measurement which affects the summation in an inconsistent way compared to $\{F, k_f, L, \xi, S_D, \eta\}$ and will instead be covered in the following sections.

$$\left(\frac{\partial \sum dz_j}{\partial F}\right)^2 \bigg/ \left(\frac{\partial \sum dz_j}{\partial k_f}\right)^2 = \left(\frac{k_f}{F}\right)^2 < 1 \qquad (3.26)$$

$$\left(\frac{\partial \sum dz_j}{\partial S_D}\right)^2 \bigg/ \left(\frac{\partial \sum dz_j}{\partial \eta}\right)^2 = \left(\frac{\eta}{S_D}\right)^2 < 1 \qquad (3.30)$$

$$\left(\frac{\partial \sum dz_j}{\partial F}\right)^2 \bigg/ \left(\frac{\partial \sum dz_j}{\partial L}\right)^2 = \left(\frac{L}{F}\right)^2 > 1 \qquad (3.27)$$

$$\left(\frac{\partial \sum dz_j}{\partial \xi}\right)^2 \bigg/ \left(\frac{\partial \sum dz_j}{\partial S_D}\right)^2 = \left(\frac{2S_D}{\xi}\right)^2 > 1 \qquad (3.31)$$

$$\left(\frac{\partial \sum dz_j}{\partial F}\right)^2 \bigg/ \left(\frac{\partial \sum dz_j}{\partial \eta}\right)^2 = \left(\frac{2\eta}{F}\right)^2 < 1 \qquad (3.28)$$

$$\left(\frac{\partial \sum dz_j}{\partial \xi}\right)^2 \bigg/ \left(\frac{\partial \sum dz_j}{\partial \eta}\right)^2 = \left(\frac{2\eta}{\xi}\right)^2 \approx 1 \qquad (3.32)$$

$$\left(\frac{\partial \sum dz_j}{\partial k_f}\right)^2 \bigg/ \left(\frac{\partial \sum dz_j}{\partial \xi}\right)^2 = \left(\frac{\xi}{k_f}\right)^2 \lesssim 1 \qquad (3.29)$$

$$\left(\frac{\partial \sum dz_j}{\partial L}\right)^2 \bigg/ \left(\frac{\partial \sum dz_j}{\partial S_D}\right)^2 = \left(\frac{2S_D}{L}\right)^2 > 1 \qquad (3.33)$$

The ratios are evaluated using some typical magnitudes of $\{F, k_f, L, \xi, S_D, \eta\}$ which are $\{33, 3.3, 380, 1.65, \pi 15^2, .80\}$ for 304SS as the basis for a numerical comparison. Organizing the partials according to the ratios reveals the following ranking of uncertainty sensitivity.

$$\left(\frac{\partial \sum dz_j}{\partial S_D}\right)^2 < \left(\frac{\partial \sum dz_j}{\partial L}\right)^2 < \left(\frac{\partial \sum dz_j}{\partial F}\right)^2 < \left(\frac{\partial \sum dz_j}{\partial k_f}\right)^2 \lesssim \left(\frac{\partial \sum dz_j}{\partial \xi}\right)^2 \approx \left(\frac{\partial \sum dz_j}{\partial \eta}\right)^2 \qquad (3.34)$$

Generally the differences between variables are stark and often an order of magnitude in difference however three variables; k_f, η, ξ are of comparable magnitude and thus the ranking is not guarantied.

In the case of η and ξ the two parameters respectively range from 0.5 to a theoretical limit of 1 and 1 to 2. Given that η is multiplied by a factor of 2 in equation 3.32 the numerator and denominator would both occupy $[1, 2]$ and the actual comparison will depend on the user specified ξ and instrument specific η. For the analysis of k_f in this work a value of 3.3 is used resulting in a smaller squared partial when compared to ξ or η. The field factor however is often used as a calibration factor and can occupy a great range of possible values depending on the exact calibration method and calibration feature. The impact of calibration factor is left out of this analysis and thus we conclude that $(\partial \sum dz_j / \partial k_f)^2$ is approximately less than $(\partial \sum dz_j / \partial \xi)^2$. Finally, it should be noted that the ranking in equation 3.34 does not necessarily hold true for the partials of Z_i as the behavior of dz_i' and covariance terms must be accounted for.

Voltage contribution

The evaporation process is dependent upon the maintenance of a standing voltage in addition to a voltage pulse and it is possible that both have an intrinsic error. As a simplifying

assumption treat these as a singular voltage such that there is only one associated measurement error associated. This assumption is supported by the availability of the raw data as the LEAP and associated software only provide two data formats that include the voltage information, and even then do not always record the voltages separately but only provide a total voltage. From this assumption there are two possible approaches to account for the voltage component dependent upon the nature of the voltage pulse and the instrument accuracy.

Approach one treats each voltage pulse as an independent measurement with an associated error. Under this approach Z_i is a function of i voltages and thus i different error contribution terms. Equation 3.35 describes the partial derivatives of Z_i with respect to an applied voltage, V_j.

$$\frac{\partial Z_i}{\partial V_j} = \left(\sum_{k=1}^{i} \frac{\partial}{\partial V_j} dz_k \right) + \frac{\partial}{\partial V_j} dz_i' \text{ for } j < i \tag{3.35}$$

Note, that for both reconstruction methods in this work dz_i' is dependent solely on V_i and that the ion specific depth increments, denoted here as dz_k, are independent of V_j when $j \neq k$. Therefor $\frac{\partial}{\partial v_j} dz_k = 0$ for $j \neq k$ and $\frac{\partial}{\partial V_j} dz_i = 0$ for $j \neq i$. The first i-1 terms then share a common form while the ith term must also account for the depth adjustment, equation 3.36.

$$\frac{\partial Z_i}{\partial V_j} = \begin{cases} \frac{\partial}{\partial V_j} dz_j & = -\frac{2}{V_j} dz_j, \text{if } j < i \\ \frac{\partial}{\partial V_j} dz_j + \frac{\partial}{\partial V_j} dz_i' & = -\frac{2}{V_j} dz_j + \frac{\partial}{\partial V_j} dz_i', \text{if } j = i \end{cases} \tag{3.36}$$

By neglecting the covariance terms the overall voltage can then be written as the following summation:

$$var(Z_i|V_0, V_1, ...V_i) = \left[\sum_{j}^{i-1} \left(\frac{2}{V_j} dz_j \right)^2 \sigma_{V_j}^2 \right] + \left[-\frac{2}{V_i} dz_i + \frac{\partial}{\partial V_i} dz_i' \right]^2 \sigma_{V_i}^2 \tag{3.37}$$

The above approach is especially useful when the system is modeled using percent error for voltage as the percent error, $p_j V_j$, as the V_j^1 term from $\partial dz_j / \partial V_j$ cancels with the the one contained within Σ_{V_j}. An alternative scenario is that of a fixed error, σ_V, regardless of the applied voltage. Substituting σ_V in for all σ_{V_i} results in the following simplification of equation 3.37.

$$var(Z_i|V_0, V_1, ...V_i) = \sigma_V^2 \left(\left[\sum_{j}^{i-1} \left(\frac{2}{V_j} dz_j \right)^2 \right] + \left[-\frac{2}{V_i} dz_i + \frac{\partial}{\partial V_i} dz_i' \right]^2 \right) \tag{3.38}$$

Thus far, the voltage pulses have been assumed to be independent and to assess the validity of this assumption both the physics underlying field evaporation and the control systems of the atom probe should be considered. From the perspective of evaporation physics recall that the required voltage to induce an evaporation event is dependent on the material specific field, F, and the specimen apex's curvature, R. If the specimen is homogeneous then F remains constant and only the curvature determines the required voltage.

Assuming the conventional conical shape for the specimen shaft then it follows that the specimen apex is blunted with each evaporation and thus both the radius and evaporation voltage increase. It follows that the expectation of V_i, $E(V_i)$, should be greater than $E(V_{i-1})$ and that if $E(V_{i-1}) + \sigma_{V_{i-1}}$ is applied prior than $E(V_i) \geq E(V_{i-1}) + \sigma_{V_{i-1}}$. This relationship shows that the expectations are positively correlated. It should be noted that the samples are often heterogeneous and have other features that can alter the required field. One such feature are crystallographic poles which generally require a lower field such that if event i and i-1 are from different poles then V_i is not guarantied to be greater than V_{i-1} [25, 39, 37, 40].

Now consider the voltages from an instrumentation perspective. The LEAP does not require the voltage curves to be monotonic and can lower the applied voltage to account for changes in the experimental conditions and is controlled via a threshold on the detection rate. The detection rate is often set to 0.01 ions per pulse with the main goal of reducing simultaneous evaporation events but also reduces the correlation between subsequent events [74]. This controls the rate at which the voltage changes such that if the rate is below the threshold the instrument voltage is increased more rapidly but if the rate is exceeded the voltage ramp rate is decreased and can even be negative resulting in a lower pulse voltage than the prior. This behavior is most often seen when precipitates or other material phases are encountered with a lower required field or when microfractures occur which effectively sharpen the specimen [74, 40].

Furthermore, inverting the rate suggests that there are approximately 100 pulses per evaporation and thus 100 pulses in between events. In the homogeneous case established prior a pulse voltage would be most strongly correlated with the preceding pulse. It follows that the correlation between two pulses decreases as the number of intermediate pulses increase. Applying this to the evaporation event suggests that a discrepancy in event i-1, σ_{i-1}, affect on event i is likely to be overwhelmed by errors in the intermediary 100 pulses which are not provided in the user accessible data format.

Under the above considerations the authors believe that the covariances can neither be robustly estimated from an experimental standpoint nor will have a significant impact on the reconstruction. Despite this, the full variance is provided as equation 3.39 and the Cayley-Schwarz inequality, equation 2.3, would be required to estimate the impact given that no concrete associations between pulses can be derived. Note that dz_j is further simplified as in equation 3.13b.

$$var(Z_i|V_0, V_1, ...V_i) = \left[4C_{dz}^2 \sum_j^{i-1} \left(\frac{\Omega_j}{V_j^2} \right)^2 \frac{\sigma_{V_j}^2}{V_j^2} \right] + \left[4C_{dz}^2 \sum_j^{i-1} \sum_k^{1-2} \left(\frac{\Omega_j}{V_j^2} \right) \left(\frac{\Omega_k}{V_k^2} \right) \frac{Cov(V_j, V_k)}{V_j V_k} \right]$$

$$+ \left[2C_{dz} \frac{\Omega_i}{V_i^2} - V_i \frac{\partial dz_i'}{\partial V_i} \right]^2 \frac{\sigma_{V_i}^2}{V_i^2} + \left[2 \sum_j^{i-1} \left(C_{dz} \frac{\Omega_j}{V_j^2} \right) \left(C_{dz} \frac{\Omega_i}{V_i^2} - V_i \frac{\partial dz_i'}{\partial V_i} \right) \frac{Cov(V_j, V_i)}{V_j V_i} \right]$$

$$(3.39)$$

Volume Contribution

Ionic volumes remain the only variables that have yet to be accounted. For each event the TOF generates a M-Z spectrum which is used to assign an ionic identity and thus volume for each ion. For the following derivations neglect the uncertainties in the spectrum and those in the subsequent identity assignment. Consider instead the errors in m ionic volumes where $\omega = \{\omega_1, \omega_2, ...\omega_m\}$, not to be confused with Ω_i which is the volume assigned to the ith evaporation event and must be equivalent to a value contained within ω. Note that the most commonly used volumes are those assigned by the IVAS software which does not provide a clear definition for its volumes.

It is reasonable to assume however that if each element has a prescribed ionic volume than complex ions such as FeO_2 would be the sum of the individual volumes. Under this operating assumption complex ions which share a constituent are correlated. For example consider the ionic volumes for FeO_2 and NiO_3 which share oxygen as a common constituent. The covariance of the two complex ions can be separated as in equation 3.40 given the bilinearity of covariance.

$$
\begin{aligned}
Cov(FeO_2, NiO_3) =& Cov(Fe + 2O, Ni + 3O) \\
=& Cov(Fe, Ni) + 3Cov(Fe, O) + Cov(Ni, O) + (2 \cdot 3)Cov(O, O) \quad (3.40) \\
=& 6var(O) = 6\sigma_O^2
\end{aligned}
$$

Here Fe, O, and Ni are standing in for the respective ionic volumes. Thus, the covariance between any two complex ions is a weighted summation over the variances of the common elements where the weights are the products of the subscripts.

Given that dz' is independent of Ω the variance with respect to the volumes is dependent solely on the depth increments, dz_i. The variance of one such increment is defined in equation 3.44.

$$
var(dz_i|\omega_0, \omega_1, ...\omega_m) = \left[\sum_j^m \left(\frac{\partial}{\partial \omega_j} dz_i\right)^2 \sigma_{\omega_j}^2\right] + \left[2\sum_j^m \sum_k^{m-1} \frac{\partial dz_i}{\partial \omega_j} \frac{\partial dz_i}{\partial \omega_k} Cov(\omega_j, \omega_k)\right] \quad (3.41)
$$

Recall that:

$$
\frac{\partial}{\partial \Omega_i} dz_i = \frac{dz_i}{\Omega_i} = C_{dz} \frac{\Omega_i}{v_i^2} \frac{1}{\Omega_i}
$$

which can be generalized as equation 3.42a for any possible ionic volume through the use of an indicator variable, 3.42b, that establishes if the ith ions identity is equivalent to the jth possible ionic identity.

$$
\frac{\partial}{\partial \omega_j} dz_i = \frac{C_{dz}}{V_i^2} I(\omega_j, \Omega_i) \quad (3.42a)
$$

$$
I(\omega_j, \Omega_i) = \begin{cases} 1, \text{if } \omega_j = \Omega_i \\ 0, \text{else} \end{cases} \quad (3.42b)
$$

Substituting equation 3.42a into equation 3.41 results in the following simplification.

$$
\begin{aligned}
var(dz_i|\omega_0, \omega_1, ...\omega_m) = {} & \left[\sum_j^m \left(\frac{C_{dz}}{v_j^2} I(\omega_j, \Omega_i) \right)^2 \sigma_{\omega_j}^2 \right] \\
& + \left[2 \sum_j^m \sum_k^{m-1} \left(\frac{C_{dz}}{v_i v_j} \right)^2 I(\omega_j, \Omega_i) I(\omega_k, \Omega_i) Cov(\omega_j, \omega_k) \right]
\end{aligned}
\tag{3.43}
$$

Now consider the variance of Z_i given ω provided in 3.44 and the corresponding simplifications using equation 3.42.

$$
var(Z_i|\omega_0, \omega_1, ...\omega_m) = \sum_j^i var(dz_j|\omega_0, \omega_1, ...\omega_m)
\tag{3.44a}
$$

$$
var(Z_i|\omega_0, \omega_1, ...\omega_m) = \sum_j^m \left(\frac{\partial}{\partial \omega_j} z_i \right)^2 \sigma_{\omega_j}^2 + \left[2 \sum_j^m \sum_k^{m-1} \frac{\partial z_i}{\partial \omega_j} \frac{\partial z_i}{\partial \omega_k} Cov(\omega_j, \omega_k) \right]
\tag{3.44b}
$$

$$
\begin{aligned}
var(Z_i|\omega_0, \omega_1, ...\omega_m) = {} & C_{dz}^2 \sum_j^m \left(\sum_k^i \frac{1}{V_k^2} I(\omega_j, \Omega_k) \right)^2 \sigma_{\omega_j}^2 \\
& + 2 C_{dz}^2 \left[\sum_j^m \sum_k^{m-1} \left(\sum_a^i \sum_b^i \frac{1}{V_a^2 V_b^2} I(\omega_j, \Omega_a) I(\omega_k, \Omega_b) \right) Cov(\omega_j, \omega_k) \right]
\end{aligned}
\tag{3.44c}
$$

In these equations the indicator variables are responsible for setting the covariance terms to zero when the compared depth increments, dz_a and dz_b, are not dependent on the respective ionic volumes, ω_j and ω_k. The indicator variable also ensures that the variance of an individual increment is only contributed alongside dz_i which are dependent on the same ionic volume.

For the remainder of this work the covariance terms are neglected due to the use of the IVAS provided ionic volumes for which the constituent volumes are ill-defined. Furthermore, the impact of mass-spectra ranging and the notion of probabilistic assignment of identity are left as future work once current advancements in the ranging process have been adopted within the IVAS (or its successors) software [14, 13, 54, 81, 80, 28].

3.2 The Bas protocol

The Bas reconstruction protocol employs a small angle approximation such that a simple point projection transforms the detector coordinates. A fundamental flaw with this method when applied to modern instruments is that the field-of-view has greatly increased since the original work by Bas et al and the small angle approximation is no longer valid with

respect to the flight path [5]. Performing reconstructions with this procedure will result in an artificially narrowed field-of-view and an elongated tip as the volume associated with the wide field-of-view now contributes to an enlarged depth increment.

Continuing from section 3.1 equation 3.2 the Bas protocol treats the detector image as a point projection of the sample such that equation 3.45 describes the magnification of the detector image when given a known flight length, L, and another user-defined parameter the image compression factor, ξ. Equations 3.46 through further 3.48 further define the partials of M_i^{proj}.

$$M_i^{proj} = M^{proj}(L, \xi, R_i) \approx \frac{L}{\xi R_i} + 1 \tag{3.45}$$

$$\frac{\partial M_i^{proj}}{\partial L} = \frac{1}{\xi R_i} = \frac{M_i^{proj} - 1}{L} \tag{3.46}$$

$$\frac{\partial M_i^{proj}}{\partial \xi} = -\frac{L}{\xi^2 R_i} = -\frac{M_i^{proj} - 1}{\xi} \tag{3.47}$$

$$\frac{\partial M_i^{proj}}{\partial R_i} = -\frac{L}{\xi R_i^2} = -\frac{M_i^{proj} - 1}{R_i} \tag{3.48}$$

$$\sigma_{M_{proj}}^2 = \left(\frac{\partial M_i^{proj}}{\partial L}\right)^2 \sigma_L^2 + \left(\frac{\partial M_i^{proj}}{\partial \xi}\right)^2 \sigma_\xi^2 + \left(\frac{\partial M_i^{proj}}{\partial R_i}\right)^2 \sigma_{R_i}^2 \tag{3.49}$$

Taking the ratios of the above derivatives shows that the relative importance of L, ξ, and V_i to $Var(M_i^{proj})$ is proportional to their ratios shown below.

$$\left(\frac{\partial M_i^{proj}}{\partial L}\right)^2 \Big/ \left(\frac{\partial M_i^{proj}}{\partial \xi}\right)^2 = \left(\frac{\xi}{L}\right)^2 \tag{3.50}$$

$$\left(\frac{\partial M_i^{proj}}{\partial L}\right)^2 \Big/ \left(\frac{\partial M_i^{proj}}{\partial R_i}\right)^2 = \left(\frac{R_i}{L}\right)^2 \tag{3.51}$$

$$\left(\frac{\partial M_i^{proj}}{\partial \xi}\right)^2 \Big/ \left(\frac{\partial M_i^{proj}}{\partial R_i}\right)^2 = \left(\frac{R_i}{\xi}\right)^2 \tag{3.52}$$

Given that the magnitude of L is approximately 180 and that ξ generally between 1 and 2 it follows from equation 3.50 that:

$$\left(\frac{\partial M_i^{proj}}{\partial L}\right)^2 \lesssim \left(\frac{\partial M_i^{proj}}{\partial \xi}\right)^2 \tag{3.53}$$

Indicating that accurate estimation of ξ is more important the L for reducing the error in M_i^{proj}. A similar comparison is omitted for R_i as it varies throughout the experiment

and because it is a function of V_i, F, k_f. Full error propagation must also consider these derivatives which are accounted for via the chain rule.

$$\frac{\partial M_i^{proj}}{\partial V_i} = \frac{\partial M_i^{proj}}{\partial R_i} \frac{\partial R_i}{\partial V_i} \tag{3.54}$$

$$\frac{\partial M_i^{proj}}{\partial F} = \frac{\partial M_i^{proj}}{\partial F} \frac{\partial R_i}{\partial F} \tag{3.55}$$

$$\frac{\partial M_i^{proj}}{\partial k_f} = \frac{\partial M_i^{proj}}{\partial k_f} \frac{\partial R_i}{\partial k_f} \tag{3.56}$$

The first term in the above is constant among all three equations such that the ratios are the ratios of the derivatives of R_i instead as shown below.

$$\left(\frac{\partial M_i^{proj}}{\partial V_i}\right)^2 / \left(\frac{\partial M_i^{proj}}{\partial F}\right)^2 = \left(\frac{\partial R_i}{\partial V_i}\right)^2 / \left(\frac{\partial R_i}{\partial F}\right)^2 = \left(\frac{F}{V_i}\right)^2 \tag{3.57}$$

$$\left(\frac{\partial M_i^{proj}}{\partial F}\right)^2 / \left(\frac{\partial M_i^{proj}}{\partial k_f}\right)^2 = \left(\frac{\partial R_i}{\partial F}\right)^2 / \left(\frac{\partial R_i}{\partial k_f}\right)^2 = \left(\frac{k_f}{F}\right)^2 \tag{3.58}$$

Taking some conventional values for F and k_f of 33 and 3.3 in the case of steel specimens the ratio in equation 3.58 is less than one and indicates that $\left(\partial M_i^{proj}/\partial F\right)^2 < \left(\partial M_i^{proj}/\partial k_f\right)^2$. This behavior should generally remain even with different sets of F and k_f as values for the evaporation field are roughly an order of magnitude larger than the field factor. Additionally, as voltage ranges from 1,000V to 8,000V in a typical experiment equation 3.57 should also evaluate to less than one in all circumstances.

A full analysis of $Var(M_i^{proj})$ would require comparisons between L and ξ to V_i, F, k_f as well, however now that the general method has been described such analyses will be reserved for the final reconstructed coordinates.

Spatial uncertainty in X, Y

The original position of an ion is found by projecting the event position with respect to the detector onto the current specimen apex. For a small field of view and a straight flight path instrument a single point projection as demonstrated in 3.3 is sufficient whereas either a large field of view or a reflectron instrument would require corrections for the curvature of the flight path. An overview of the process for calculating the X, Y coordinates can be found in figure 3.3.

The reconstructed X coordinate and the immediate partials are given by equations 3.59

through 3.61.

$$X_i = X(X_i^{det}, M_i^{proj}) = \frac{X_i^{det}}{M_i^{proj}} = \frac{X_i^{det}}{\frac{LFk_f}{V_i\xi} + 1} \tag{3.59}$$

$$\frac{\partial X_i}{\partial X_i^{det}} = \frac{1}{M_i^{proj}} = \frac{X_i}{X_i^{det}} \tag{3.60}$$

$$\frac{\partial X_i}{\partial M_i^{proj}} = -\frac{X_i^{det}}{\left(M_i^{proj}\right)^2} = -\frac{X_i}{M_i^{proj}} \tag{3.61}$$

Continuing with Y_i and it's derivatives below:

$$Y_i = Y(Y_i^{det}, M_i^{proj}) = \frac{Y_i^{det}}{M_i^{proj}} = \frac{Y_i^{det}}{\frac{LFk_f}{V_i\xi} + 1} \tag{3.62}$$

$$\frac{\partial Y_i}{\partial Y_i^{det}} = \frac{1}{M_i^{proj}} = \frac{Y_i}{Y_i^{det}} \tag{3.63}$$

$$\frac{\partial Y_i}{\partial M_i^{proj}} = -\frac{Y_i^{det}}{\left(M_i^{proj}\right)^2} = -\frac{Y_i}{M_i^{proj}} \tag{3.64}$$

Error propagation and sensitivity analyses is demonstrated first using X_i as the same equations and relationships will hold for Y_i with the exception that all instance of X_i and X_i^{det} would be substituted with Y_i and Y_i^{det}. Noting that X_i has dependencies on L, ξ, and
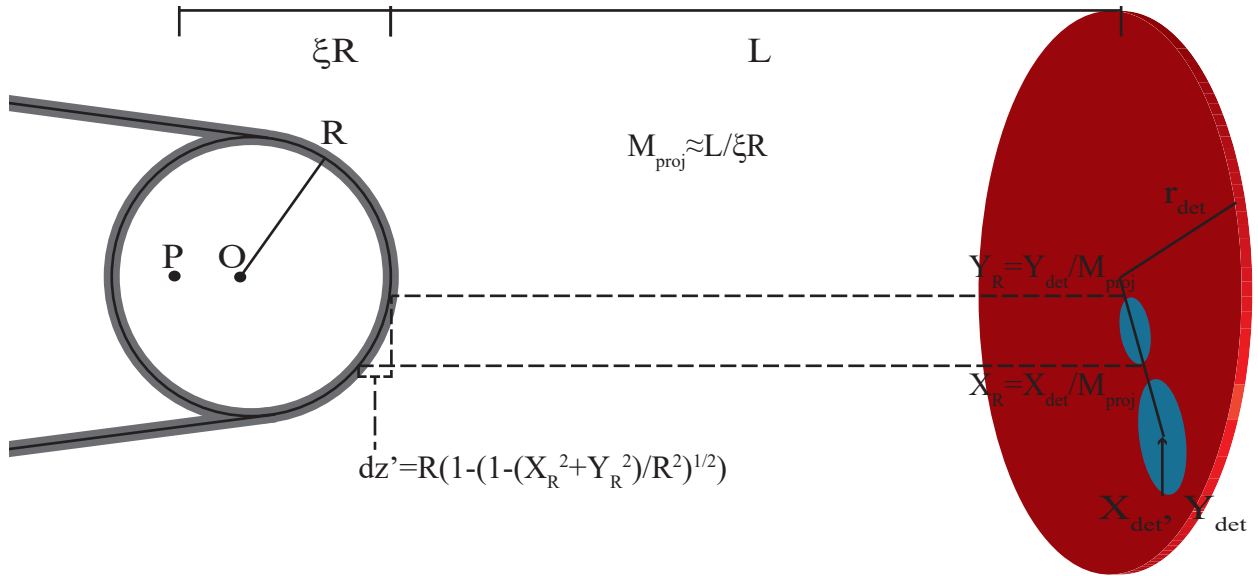
Figure 3.3: Placement of an ion on the hemispherical cap in X, Y alongside the depth correction under the Bas reconstruction protocol.

R_i through M_i^{proj} with R_i introducing dependencies on V_i, F, and k_f the complete list of partials for X_i are described in equations 3.60 through 3.70

$$\frac{\partial X_i}{\partial X_i^{det}} = \frac{X_i}{X_i^{det}} \qquad (3.60)$$

$$\frac{\partial X_i}{\partial R_i} = -\frac{\partial X_i}{\partial M_i^{proj}} \frac{M_i^{proj} - 1}{R_i} \qquad (3.67)$$

$$\frac{\partial X_i}{\partial M_i^{proj}} = -\frac{X_i}{M_i^{proj}} \qquad (3.61)$$

$$\frac{\partial X_i}{\partial F} = -\frac{\partial X_i}{\partial M_i^{proj}} \frac{\partial M_i^{proj}}{\partial R_i} \frac{R_i}{F} \qquad (3.68)$$

$$\frac{\partial X_i}{\partial L} = \frac{\partial X_i}{\partial M_i^{proj}} \frac{M_i^{proj} - 1}{L} \qquad (3.65)$$

$$\frac{\partial X_i}{\partial k_f} = -\frac{\partial X_i}{\partial M_i^{proj}} \frac{\partial M_i^{proj}}{\partial R_i} \frac{R_i}{k_f} \qquad (3.69)$$

$$\frac{\partial X_i}{\partial \xi} = -\frac{\partial X_i}{\partial M_i^{proj}} \frac{M_i^{proj} - 1}{\xi} \qquad (3.66)$$

$$\frac{\partial X_i}{\partial V_i} = \frac{\partial X_i}{\partial M_i^{proj}} \frac{\partial M_i^{proj}}{\partial R_i} \frac{R_i}{V_i} \qquad (3.70)$$

Using the process demonstrated in equations 3.57 and 3.58 for X_i the partials are first grouped into two sets of like terms, $\{L, \xi\}$ and $\{F, k_f, V_i\}$ with X_i^{det} as an outlier. Focusing first on $\{L, \xi\}$ the squared ratio of the partial is identical to that of 3.50 such that equation 3.53 still holds and is expanded to include σ_L and σ_ξ below where p_i indicates the percent error of L and ξ.

$$\left(\frac{\partial X_i}{\partial L}\right)^2 \sigma_L^2 \lesssim \left(\frac{\partial X_i}{\partial \xi}\right)^2 \sigma_\xi^2 \text{ for } \sigma_L^2 \lesssim \frac{L^2}{\xi^2}\sigma_\xi^2 \qquad (3.71)$$

$$\left(\frac{\partial X_i}{\partial L}\right)^2 \sigma_L^2 \approx \left(\frac{\partial X_i}{\partial \xi}\right)^2 \sigma_\xi^2 \text{ if } \sigma_L^2 = p_i^2 L^2, \ \sigma_\xi^2 = p_i^2 \xi^2 \qquad (3.72)$$

Recalling that $L \approx 380$ and that ξ is in $[1, 2]$, equation 3.71 shows that errors in ξ will generally dominate the final error estimate in comparison to L. A comparable impact by σ_L^2 would require it to be approximately 190 times that of σ_ξ^2. Such a measurement error is orders of magnitude greater than any true measurement uncertainty for the flight path length in conventional instruments and so the influence of L can generally be treated as negligible in the case of the small-angle reconstruction.

Continuing with the impact of $\{F, k_f, V_i\}$ the first two terms in the partials cancel resulting in ratios identical to those derived in equations 3.57 and 3.58. Including the error terms as in 3.71 then results in:

$$\left(\frac{\partial X_i}{\partial V_i}\right)^2 \sigma_{V_i}^2 < \left(\frac{\partial X_i}{\partial F}\right)^2 \sigma_F^2 < \left(\frac{\partial X_i}{\partial k_f}\right)^2 \sigma_{k_f}^2 \text{ for } \sigma_{V_i}^2 \leq \frac{V_i^2}{F^2}\sigma_F^2 \text{ and } \sigma_F^2 \leq \frac{F^2}{k_F^2}\sigma_{k_f}^2 \qquad (3.73)$$

$$\left(\frac{\partial X_i}{\partial V_i}\right)^2 \sigma_{V_i}^2 = \left(\frac{\partial X_i}{\partial F}\right)^2 \sigma_F^2 = \left(\frac{\partial X_i}{\partial k_f}\right)^2 \sigma_{k_f}^2 \text{ if } \sigma_{V_i}^2 = p_i^2 V_i^2, \ \sigma_F^2 = p_i^2 F^2, \ \sigma_{k_f}^2 = p_i^2 k_f^2 \qquad (3.74)$$

From the above, it would generally require the error in F to be an order of magnitude larger than that of k_f to overcome this trend recalling that F is generally an order of

magnitude larger than k_f. Furthermore, for the applied voltage to be the dominant error term then σ_{V_i} would have to be approximately 100 times larger than σ_F or 1,000 times that of σ_{k_f}. If instead the uncertainty is expressed as a percent error as in equation 3.74 with a constant percent amongst all variables the three variables have equal contributions to the final uncertainty.

Determination of the sensitivity between the groups $\{L, \xi\}$, $\{F, k_f, V_i\}$ and X_i^{det} remains and comparing $\{L, \xi\}$ with $\{F, k_f, V_i\}$ provides direct relationships with the exception of ξ and k_f. The results can be summarized with only two equations.

$$\left(\frac{\partial X_i}{\partial L}\right)^2 \Big/ \left(\frac{\partial X_i}{\partial V_i}\right)^2 = \left(\frac{V_i}{L}\right)^2 \tag{3.75}$$

$$\left(\frac{\partial X_i}{\partial \xi}\right)^2 \Big/ \left(\frac{\partial X_i}{\partial k_f}\right)^2 = \left(\frac{k_f}{\xi}\right)^2 \tag{3.76}$$

As $V_i > L$ for all V_i equation 3.75 allows the impact of L to be directly compared with k_f and F in addition to the voltage. However, because ξ and k_f are of similar order and magnitude there is no guarantee that $\xi > k_f$ or vice-versa in equation 3.76 and heavily depend on the user selected parameters. Thus, for the Bas reconstruction we consider k_f to have a lesser or comparable impact to ξ on the uncertainty in X_i denoted by $\lesssim$. In the absence of computational work validating the ratios with respect to X_i^{det} we expect that:

$$\left(\frac{\partial X_i}{\partial L}\right)^2 < \left(\frac{\partial X_i}{\partial V_i}\right)^2 < \left(\frac{\partial X_i}{\partial F}\right)^2 < \left(\frac{\partial X_i}{\partial k_f}\right)^2 \lesssim \left(\frac{\partial X_i}{\partial \xi}\right)^2 \tag{3.77}$$

Recalling that the only difference between X_i and Y_i is the usage of Y_i^{det} instead of X_i^{det} all of the derivations above from equations 3.60 through 3.77 apply with the aforementioned substitution. In the interest of brevity only the observations regarding the relative importance of different variables with respect to the propagation of error are included below.

$$\left(\frac{\partial Y_i}{\partial L}\right)^2 \sigma_L^2 \lesssim \left(\frac{\partial Y_i}{\partial \xi}\right)^2 \sigma_\xi^2 \text{ for } \sigma_L^2 \lesssim \frac{L^2}{\xi^2}\sigma_\xi^2 \tag{3.78}$$

$$\left(\frac{\partial Y_i}{\partial L}\right)^2 \sigma_L^2 \approx \left(\frac{\partial Y_i}{\partial \xi}\right)^2 \sigma_\xi^2 \text{ if } \sigma_L^2 = p_i^2 L^2, \ \sigma_\xi^2 = p_i^2 \xi^2 \tag{3.79}$$

$$\left(\frac{\partial Y_i}{\partial V_i}\right)^2 \sigma_{V_i}^2 < \left(\frac{\partial Y_i}{\partial F}\right)^2 \sigma_F^2 < \left(\frac{\partial Y_i}{\partial k_f}\right)^2 \sigma_{k_f}^2 \text{ for } \sigma_{V_i}^2 \le \frac{V_i^2}{F^2}\sigma_F^2 \text{ and } \sigma_F^2 \le \frac{F^2}{k_F^2}\sigma_{k_f}^2 \tag{3.80}$$

$$\left(\frac{\partial Y_i}{\partial V_i}\right)^2 \sigma_{V_i}^2 = \left(\frac{\partial Y_i}{\partial F}\right)^2 \sigma_F^2 = \left(\frac{\partial Y_i}{\partial k_f}\right)^2 \sigma_{k_f}^2 \text{ if } \sigma_{V_i}^2 = p_i^2 V_i^2, \ \sigma_F^2 = p_i^2 F^2, \ \sigma_{k_f}^2 = p_i^2 k_f^2 \tag{3.81}$$

$$\left(\frac{\partial Y_i}{\partial L}\right)^2 < \left(\frac{\partial Y_i}{\partial V_i}\right)^2 < \left(\frac{\partial Y_i}{\partial F}\right)^2 < \left(\frac{\partial Y_i}{\partial k_f}\right)^2 \lesssim \left(\frac{\partial Y_i}{\partial \xi}\right)^2 \tag{3.82}$$

Spatial uncertainty in Z due to dz$'_i$

Section 3.1 provided the basis for understanding the depth uncertainty within atom probe reconstructions as a function of the cumulative depth increment but thus far neglected to account for the reconstruction specific depth correction, dz'_i. The depth correction corresponds to placement of the ion atop the specimen apex and thus is bound by $[0, R/2]$. In this case 0 indicates placement of the ion directly atop the specimen apex. Under the conical model with a hemispherical cap the maximum correction indicates evaporation from the point at which the cap and cone intersect. As shown in equation 3.83b this correction factor is dependent on the lateral position of the evaporation event.

$$dz'_i = dz'(R_i, X_i^2, Y_i^2) = R_i \left(1 - \sqrt{1 - \frac{X_i^2 + Y_i^2}{R_i^2}} \right) \tag{3.83a}$$

$$= R_i \left(1 - \sqrt{1 - \frac{\left(X_i^{det}\right)^2 + \left(Y_i^{det}\right)^2}{\left(M_i^{proj}\right)^2 R_i^2}} \right) \tag{3.83b}$$

While initially dependent on R_i, X_i, and Y_i as in equation 3.83a substitution for X_i, and Y_i reveals a dependence on the detector coordinates and the magnification. Repeating this process for the magnification factor, etc. shows that dz'_i is a function of X_i^{det}, Y_i^{det}, L, ξ, F, k_f, and V_i. The derivatives required under application of linear error propagation are then:

$$\frac{\partial dz'_i}{\partial X_i} = \frac{X_i}{\sqrt{1 - \frac{X_i^2 + Y_i^2}{R_i}}} \tag{3.84}$$

$$\frac{\partial dz'_i}{\partial Y_i} = \frac{Y_i}{\sqrt{1 - \frac{X_i^2 + Y_i^2}{R_i}}} \tag{3.85}$$

$$\frac{\partial dz'_i}{\partial X_i^{det}} = \frac{\partial dz'_i}{\partial X_i} \frac{\partial X_i}{\partial X_i^{det}} \tag{3.86}$$

$$\frac{\partial dz'_i}{\partial Y_i^{det}} = \frac{\partial dz'_i}{\partial Y_i} \frac{\partial Y_i}{\partial Y_i^{det}} \tag{3.87}$$

$$\frac{\partial dz'_i}{\partial L} = \frac{\partial dz'_i}{\partial M_i^{proj}} \frac{\partial M_i^{proj}}{\partial L} \tag{3.88}$$

$$\frac{\partial dz'_i}{\partial \xi} = \frac{\partial dz'_i}{\partial M_i^{proj}} \frac{\partial M_i^{proj}}{\partial \xi} \tag{3.89}$$

$$\frac{\partial dz'_i}{\partial F} = \frac{\partial dz'_i}{\partial R_i} \frac{\partial R_i}{\partial F} \tag{3.90}$$

$$\frac{\partial dz'_i}{\partial k_f} = \frac{\partial dz'_i}{\partial R_i} \frac{\partial R_i}{\partial k_f} \tag{3.91}$$

$$\frac{\partial dz'_i}{\partial V_i} = \frac{\partial dz'_i}{\partial R_i} \frac{\partial R_i}{\partial V_i} \tag{3.92}$$

Once more observation of the partials reveals that the variables can be grouped into three sets such that the error contributions can be trivially compared. These sets are the same as those for the spatial uncertainty in (X, Y) namely; $\{X_i^{det}, Y_i^{det}\}$, $\{L, \xi\}$, and $\{F, k_f, V_i\}$. However, two of the required partials ($\partial dz'_i / \partial M_i^{proj}$, $\partial dz'_i / \partial R_i$) have yet to be defined as X_i and Y_i both introduce dependencies on M_i^{proj} while the original equation for dz'_i as well as X_i and Y_i share dependencies on R_i. These two derivatives given in equations 3.93 and 3.94

serve to complicate non-numeric comparisons between the three variable sets.

$$\frac{\partial dz_i'}{\partial M_i^{proj}} = \frac{\partial dz_i'}{\partial X_i}\frac{\partial X_i}{\partial M_i^{proj}} + \frac{\partial dz_i'}{\partial Y_i}\frac{\partial Y_i}{\partial M_i^{proj}} \tag{3.93}$$

$$\frac{\partial dz_i'}{\partial R_i} = \frac{\left(X_i\frac{\partial X_i}{\partial M_i^{proj}}\frac{\partial M_i^{proj}}{\partial R_i} + Y_i\frac{\partial Y_i}{\partial M_i^{proj}}\frac{\partial M_i^{proj}}{\partial R_i} - \frac{(X_i^2 + Y_i^2)}{2R_i}\right)}{\left(1 - \frac{X^2 + Y_i^2}{R_i}\right)^{0.5}} + \frac{dz_i'}{R_i} \tag{3.94}$$

Comparing the constituents within the three sets as in equations 3.95 through 3.98 reveals the expected relationships reaffirming those described for the uncertainty in the $\sum dz_j$ and those for the spatial error in $(X_i,\ Y_i)$ with the exception that three sets cannot be compared with one another. An additional observation comes from X_i^{det} and Y_i^{det} as there comparison is the only one which depends on the spatial position of the event. Under the conditions that the event is near the $|X_i^{det}| = |Y^{det}|$ lines or near the detector center the influence of the two parameters are approximately equal. X_i^{det} dominates Y_i^{det} and vice versa when the events are near the detectors X and Y axis respectively. As a simplification the sensitivity of $Var(dz_i')$ to $(X_i^{det},\ Y_i^{det})$ is treated as approximately equal.

$$\left(\frac{\partial dz_i'}{\partial X_i^{det}}\right)^2 / \left(\frac{\partial dz_i'}{\partial Y_i^{det}}\right)^2 = \left(\frac{X_i^{det}}{Y_i^{det}}\right)^2 \quad (3.95) \qquad \left(\frac{\partial dz_i'}{\partial F}\right)^2 / \left(\frac{\partial dz_i'}{\partial k_f}\right)^2 = \left(\frac{k_f}{F}\right)^2 < 1 \quad (3.97)$$

$$\left(\frac{\partial dz_i'}{\partial L}\right)^2 / \left(\frac{\partial dz_i'}{\partial \xi}\right)^2 = \left(\frac{\xi}{L}\right)^2 < 1 \quad (3.96) \qquad \left(\frac{\partial dz_i'}{\partial F}\right)^2 / \left(\frac{\partial dz_i'}{\partial V_i}\right)^2 = \left(\frac{V_i}{F}\right)^2 > 1 \quad (3.98)$$

Similar to the sensitivity of $\sum dz_j$ equation 3.99 cannot be generalized to the final depth coordinate, Z_i. Based upon both sets of sensitivities one would expect equation 3.99 to hold for Z_i however this would require the covariance terms to be neglected. A sensitivity analysis for Z_i then requires a numeric evaluation which is omitted from this segment as a numeric evaluation on one specimen cannot be generalized to all samples given the large range of input variability even if the associated uncertainties were of similar magnitude.

$$\left(\frac{\partial dz_i'}{\partial X_i^{det}}\right)^2 \approx \left(\frac{\partial dz_i'}{\partial Y_i^{det}}\right)^2 \quad \left(\frac{\partial dz_i'}{\partial L}\right)^2 < \left(\frac{\partial dz_i'}{\partial \xi}\right)^2 \quad \left(\frac{\partial dz_i'}{\partial V_i}\right)^2 < \left(\frac{\partial dz_i'}{\partial F}\right)^2 < \left(\frac{\partial dz_i'}{\partial k_f}\right)^2 \tag{3.99}$$

3.3   The Gault protocol

Recall that the aforementioned Bas reconstruction protocol requires the use of a small angle approximation and thus is most valid for small field-of-view instruments. Modern atom

probes such as the LEAP series possess wide field-of-view made possible in part due to the local electrode configuration. To account for the wide field-of-view the coordinates are calculated following the protocols outlined by Gault [36]. The Gault protocols themselves are improvements upon the original wide-angle reconstructions outlined by Geiser and included in the works of Larson et al that sought to diminish the reliance on specimen geometry assumptions [74].

The two key differences between the Bas and Gault protocols are that the volume increment in Gault accounts for specimen apex post evaporation and subtracts the volume of a second hemispherical cap from the truncated cone when performing a shank-angle reconstruction and that Gault protocol is performed in a cylindrical coordinate space as described in equations 3.100 and 3.101 prior to being converted to the final euclidean coordinates. Note however, that the reconstruction presented here uses a strictly voltage-based evolution comparable to the wide-angle reconstruction provided by the open source Atom Probe Toolbox [32]

$$r_i = r\left(X_i^{det}, Y_i^{det}\right) = \sqrt{\left(X_i^{det}\right)^2 + \left(Y_i^{det}\right)^2} \tag{3.100}$$

$$\phi_i = \phi\left(Y_i^{det}, X_i^{det}\right) = \text{atan}_2\left(Y_i^{det}, X_i^{det}\right) \tag{3.101}$$

Note that atan2 denotes the signed arctangent. The partial derivatives of r and ϕ are then given below:

$$\frac{\partial}{\partial X_i^{det}} r_i = \frac{X_i^{det}}{r_i} = \frac{X_i^{det}}{\sqrt{\left(X_i^{det}\right)^2 + \left(Y_i^{det}\right)^2}} \tag{3.102}$$

$$\frac{\partial}{\partial Y_i^{det}} r_i = \frac{Y_i^{det}}{r_i} = \frac{Y_i^{det}}{\sqrt{\left(X_i^{det}\right)^2 + \left(Y_i^{det}\right)^2}} \tag{3.103}$$

$$\frac{\partial}{\partial X_i^{det}} \phi_i = -\frac{Y_i^{det}}{r_i^2} = -\frac{Y_i^{det}}{\left(X_i^{det}\right)^2 + \left(Y_i^{det}\right)^2} \tag{3.104}$$

$$\frac{\partial}{\partial Y_i^{det}} \phi_i = \frac{X_i^{det}}{r_i^2} = \frac{X_i^{det}}{\left(X_i^{det}\right)^2 + \left(Y_i^{det}\right)^2} \tag{3.105}$$

From equations 3.102 to 3.105 it is clear that the partials are proportional to one another such that the following two relationships stand.

$$(X_i^{det})^{-1}\frac{\partial}{\partial X_i^{det}} r_i = (Y_i^{det})^{-1}\frac{\partial}{\partial Y_i^{det}} r_i = \frac{1}{r_i} \tag{3.106}$$

$$(Y_i^{det})^{-1}\frac{\partial}{\partial X_i^{det}} \phi_i = (X_i^{det})^{-1}\frac{\partial}{\partial Y_i^{det}} \phi_i = -\frac{1}{r_i^2} \tag{3.107}$$

Now that the cylindrical coordinates have been established the projected launch angle and the derivatives with respect to its direct dependencies L, the flight length, and r_i and

are defined in equations 3.108 through 3.110.

$$\theta_i^P = \theta^P(L, r_i) = \operatorname{atan}\left(\frac{r_i}{L}\right) = \operatorname{atan}\left(\frac{\sqrt{\left(X_i^{det}\right)^2 + \left(Y_i^{det}\right)^2}}{L}\right) \tag{3.108}$$

$$\frac{\partial}{\partial L}\theta^P(L, r_i) = -\frac{r_i}{L^2\left(1 + \frac{r_i^2}{L^2}\right)} = -\frac{\sqrt{\left(X_i^{det}\right)^2 + \left(Y_i^{det}\right)^2}}{L^2\left(1 + \frac{\left(X_i^{det}\right)^2 + \left(Y_i^{det}\right)^2}{L^2}\right)} \tag{3.109}$$

$$\frac{\partial}{\partial r_i}\theta^P(L, r_i) = \frac{1}{L\left(1 + \frac{r_i^2}{L^2}\right)} = \frac{1}{L\left(1 + \frac{\left(X_i^{det}\right)^2 + \left(Y_i^{det}\right)^2}{L^2}\right)} \tag{3.110}$$

However, because r_i is itself dependent on the detector coordinates full error propagation of θ_i^P must consider the derivatives with respect to X_i^{det} and Y_i^{det} which can be accounted for via the chain rule.

$$\frac{\partial}{\partial X_i^{det}}\theta^P(L, r_i) = \frac{d}{dX_i^{det}}r_i\frac{d}{dr_i}\theta_i^P = \frac{\frac{d}{dX_i^{det}}r_i}{L\left(1 + \frac{r_i^2}{L^2}\right)} = \frac{X_i^{det}}{Lr_i\left(1 + \frac{\left(X_i^{det}\right)^2 + \left(Y_i^{det}\right)^2}{L^2}\right)} \tag{3.111}$$

$$\frac{\partial}{\partial Y_i^{det}}\theta^P(L, r_i) = \frac{d}{dY_i^{det}}r_i\frac{d}{dr_i}\theta_i^P = \frac{\frac{d}{dY_i^{det}}r_i}{L\left(1 + \frac{r_i^2}{L^2}\right)} = \frac{Y_i^{det}}{Lr_i\left(1 + \frac{\left(X_i^{det}\right)^2 + \left(Y_i^{det}\right)^2}{L^2}\right)} \tag{3.112}$$

From equations 3.111 and 3.112 it is clear that the relationship described in equation 3.107 holds true. The simplification of future derivatives will be left as an exercise for the reader given that the methodology has been defined, although it will be noted when partials can be related to one another.

Given that the projected flight angle, θ^P, is due to the compression of the original flight angle, θ, the image compression factor is utilized as a correction factor. The correction method differs from the Bas protocol however in that a simple magnification correction is not applied but instead θ^P is uncompressed to return the true angle, θ, using the user estimate of the image compression factor, ξ as shown in equation 3.113.

$$\theta_i = \theta\left(\xi, \theta_i^P\right) = \theta_i^P + \operatorname{asin}\left((\xi - 1)\sin\left(\theta_i^P\right)\right) \tag{3.113}$$

θ is then directly dependent on ξ and θ_i^P which introduces dependencies on L, X_i^{det}, and Y_i^{det}. The partials with respect to the direct dependencies can then be defined below.

$$\frac{\partial}{\partial \xi}\theta\left(\xi, \theta_i^P\right) = \frac{\sin\left(\theta_i^P\right)}{\sqrt{-(\xi - 1)^2\sin^2\left(\theta_i^P\right) + 1}} \tag{3.114}$$

$$\frac{\partial}{\partial \theta_i^P}\theta\left(\xi, \theta_i^P\right) = \frac{(\xi - 1)\cos\left(\theta_i^P\right)}{\sqrt{-(\xi - 1)^2\sin^2\left(\theta_i^P\right) + 1}} + 1 \tag{3.115}$$

Now that the true flight angle has been found only the radius is left to determine the radial placement of the ion relative to the specimen's major axis. In the absence of a predefined shank angle this protocol will once again relate the radius of curvature to the voltage. Recall equation 3.2 and the partial derivatives originally detailed in equations 3.3, 3.4, 3.5.

$$R_i = \frac{V_i}{k_f F} \tag{3.2}$$

$$\frac{\partial}{\partial V_i} R(V_i, k_f, F) = \frac{1}{F k_f} = \frac{1}{F k_f} \tag{3.3}$$

$$\frac{\partial}{\partial F} R(V_i, k_f, F) = -\frac{R_i}{F} = -\frac{V_i}{F^2 k_f} \tag{3.4}$$

$$\frac{\partial}{\partial k_f} R(V_i, k_f, F) = -\frac{R_i}{k_f} = -\frac{V_i}{F k_f^2} \tag{3.5}$$

Furthermore note the following relationship between the three derivatives which will be later used to simplify more complex expressions.

$$V_i \frac{\partial}{\partial V_i} R(V_i, k_f, F) = -F \frac{\partial}{\partial F} R(V_i, k_f, F) = -k_f \frac{\partial}{\partial k_f} R(V_i, k_f, F) = \frac{V_i}{k_f F} = R_i \tag{3.116}$$

The radial distance and the partial derivatives are defined in equations 3.117 through 3.119.

$$d_i = d(R_i, \theta_i) = R_i \sin(\theta_i) \tag{3.117}$$

$$\frac{\partial}{\partial R_i} d(R_i, \theta_i) = \sin(\theta_i) \tag{3.118}$$

$$\frac{\partial}{\partial \theta_i} d(R_i, \theta_i) = R_i \cos(\theta_i) \tag{3.119}$$

At this point, the shared dependencies of X_i, Y_i, and Z_i have been established and only defining their functions and derivatives in the subsequent two sections remain.

Spatial uncertainty in X, Y

Finally, the reconstructed X, Y coordinates are found by converting the polar coordinates ϕ_i and d_i to cartesian coordinates. Here ϕ_i represents the angle of the event on the detector and d_i the radial distance from the apex. Starting with X and it's partial derivatives in equations 3.120 through 3.122.

$$X_i = X(d_i, \phi_i) = d_i \cos(\phi_i) = \frac{R_i X_i^{det} \sin(\theta_i)}{\sqrt{\left(X_i^{det}\right)^2 + \left(Y_i^{det}\right)^2}} \tag{3.120}$$

$$\frac{\partial}{\partial d_i} X(d_i, \phi_i) = \cos(\phi_i) \tag{3.121}$$

$$\frac{\partial}{\partial \phi_i} X(d_i, \phi_i) = -d_i \sin(\phi_i) \tag{3.122}$$

Now continuing with Y_i and it's derivatives below:

$$Y_i = Y(d_i, \phi_i) = d_i \sin(\phi_i) = \frac{R_i Y_i^{det} \sin(\theta_i)}{\sqrt{\left(X_i^{det}\right)^2 + \left(Y_i^{det}\right)^2}} \tag{3.123}$$

$$\frac{\partial}{\partial d_i} Y(d_i, \phi_i) = \sin(\phi_i) \tag{3.124}$$

$$\frac{\partial}{\partial \phi_i} Y(d_i, \phi_i) = d_i \cos(\phi_i) \tag{3.125}$$

At this point it should be noted that will focus primarily on algebraic approximations as exact solutions as in section 3.2 is infeasible for the wide angle reconstructions. This is due to the nested trigonometric functions which prevent even algorithmic methods, such as trigsimp, from arriving at a solution within a reasonable time frame [34]. However, the relative importance of some terms can be shown algebraically and the overall behavior validated computationally.

Starting with X_i consider first the influence of V_i, F, and k_f on whose partials are denoted below according to the chain rule.

$$\frac{\partial X_i}{\partial V_i} = \frac{\partial X_i}{\partial d_i} \frac{\partial d_i}{\partial R_i} \frac{\partial R_i}{\partial V_i} \tag{3.126}$$

$$\frac{\partial X_i}{\partial F} = \frac{\partial X_i}{\partial d_i} \frac{\partial d_i}{\partial R_i} \frac{\partial R_i}{\partial F} \tag{3.127}$$

$$\frac{\partial X_i}{\partial k_f} = \frac{\partial X_i}{\partial d_i} \frac{\partial d_i}{\partial R_i} \frac{\partial R_i}{\partial k_f} \tag{3.128}$$

All three derivatives share the first two terms and thus taking the ratios will result in only the partials with respect to R_i remaining for comparison. Note that due to the partials cancelling the following two ratios are also true with respect to Y_i.

$$\left(\frac{\partial X_i}{\partial V_i}\right)^2 \bigg/ \left(\frac{\partial X_i}{\partial F}\right)^2 = \left(\frac{F}{V_i}\right)^2 \tag{3.129}$$

$$\left(\frac{\partial X_i}{\partial F}\right)^2 \bigg/ \left(\frac{\partial X_i}{\partial k_f}\right)^2 = \left(\frac{k_f}{F}\right)^2 \tag{3.130}$$

Taking some conventional values for F and k_f of 33 and 3.3 the ratio in equation 3.130 is less than one and this behavior should remain for different sets of values as F is roughly an order of magnitude larger than the field factor, k_f. Furthermore, as the voltage ranges from 1,000V to 8,000V in a typical experiment than 3.129 should also evaluate to less than

one in all circumstances. Subsequently, the following relationships hold.

$$\left(\frac{\partial X_i}{\partial V_i}\right)^2 < \left(\frac{\partial X_i}{\partial F}\right)^2 < \left(\frac{\partial X_i}{\partial k_f}\right)^2 \tag{3.131}$$

$$\left(\frac{\partial X_i}{\partial V_i}\right)^2 \sigma_{V_i}^2 < \left(\frac{\partial X_i}{\partial F}\right)^2 \sigma_F^2 < \left(\frac{\partial X_i}{\partial k_f}\right)^2 \sigma_{k_f}^2 \text{ for } \sigma_{V_i}^2 \leq \frac{V_i^2}{F^2}\sigma_F^2 \text{ and } \sigma_F^2 \leq \frac{F^2}{k_F^2}\sigma_{k_f}^2 \tag{3.132}$$

$$\left(\frac{\partial X_i}{\partial V_i}\right)^2 \sigma_{V_i}^2 = \left(\frac{\partial X_i}{\partial F}\right)^2 \sigma_F^2 = \left(\frac{\partial X_i}{\partial k_f}\right)^2 \sigma_{k_f}^2 \text{ if } \sigma_{V_i}^2 = p_i^2 V_i^2, \ \sigma_F^2 = p_i^2 F^2, \ \sigma_{k_f}^2 = p_i^2 k_f^2 \tag{3.133}$$

From these relationships we note that error in k_f has a larger impact than F or V_i as shown in 3.132 where given an equal magnitude of error k_f produces the largest contribution. Generally, it would require the error in F to be an order of magnitude larger than that of k_f to overcome this trend given typical values of the two. Furthermore, for the applied voltage to be the dominant error term then σ_{V_i} would have to be approximately 100 times larger than σ_F or 1,000 times that of σ_{k_F}. If instead the uncertainty is expressed as a percent error with a constant percent amongst all variables the three variables have equal contributions to the final uncertainty. Note that the same relationships holds true for Y_i, which are included below, but the derivation is left out in the interest of both brevity and completeness.

$$\left(\frac{\partial Y_i}{\partial V_i}\right)^2 < \left(\frac{\partial Y_i}{\partial F}\right)^2 < \left(\frac{\partial Y_i}{\partial k_f}\right)^2 \tag{3.134}$$

$$\left(\frac{\partial Y_i}{\partial V_i}\right)^2 \sigma_{V_i}^2 < \left(\frac{\partial Y_i}{\partial F}\right)^2 \sigma_F^2 < \left(\frac{\partial Y_i}{\partial k_f}\right)^2 \sigma_{k_f}^2 \text{ for } \sigma_{V_i}^2 \leq \frac{V_i^2}{F^2}\sigma_F^2 \text{ and } \sigma_F^2 \leq \frac{F^2}{k_F^2}\sigma_{k_f}^2 \tag{3.135}$$

$$\left(\frac{\partial Y_i}{\partial V_i}\right)^2 \sigma_{V_i}^2 = \left(\frac{\partial Y_i}{\partial F}\right)^2 \sigma_F^2 = \left(\frac{\partial Y_i}{\partial k_f}\right)^2 \sigma_{k_f}^2 \text{ if } \sigma_{V_i}^2 = p_i^2 V_i^2, \ \sigma_F^2 = p_i^2 F^2, \ \sigma_{k_f}^2 = p_i^2 k_f^2 \tag{3.136}$$

The influence of L, ξ, X_i^{det}, and Y_i^{det} remain and can be grouped into two subgroups of similar behavior, $\{L, \xi\}$ and $\{X_i^{det}, Y_i^{det}\}$. Starting with L and ξ the two partial derivatives share two terms in common although the flight length L requires one additional term.

$$\frac{\partial X_i}{\partial \xi} = \frac{\partial X_i}{\partial d_i}\frac{\partial d_i}{\partial \theta_i}\frac{\partial \theta_i}{\partial \xi} \tag{3.137}$$

$$\frac{\partial X_i}{\partial L} = \frac{\partial X_i}{\partial d_i}\frac{\partial d_i}{\partial \theta_i}\frac{\partial \theta_i}{\partial \theta_i^P}\frac{\partial \theta_i^P}{\partial L} \tag{3.138}$$

Once again the ratio of the squared partials is taken in order to show that the estimation of the image compression factor generally has a larger impact than any measurement uncertainty in the flight length. Note that $\theta_i^P \approx r_i/L$ according to the small angle approximation as the detector radius, r_i is roughly 15mm at most while the flight length is on the order of 380mm for a LEAP 4000 XHR.

$$
\left(\frac{\partial X_i}{\partial L}\right)^2 \Big/ \left(\frac{\partial X_i}{\partial \xi}\right)^2 = \left(\frac{\partial \theta_i}{\partial \theta_i^P}\frac{\partial \theta_i^P}{\partial L}\right)^2 \Big/ \left(\frac{\partial \theta_i}{\partial \xi}\right)^2
$$

$$
= \frac{\left[\dfrac{(\xi-1)\cos\left(\theta_i^P\right)}{\sqrt{-(\xi-1)^2\sin^2\left(\theta_i^P\right)+1}}+1\right]^2 \left[-\dfrac{r_i}{L^2\left(1+\frac{r_i^2}{L^2}\right)}\right]^2}{\left[\dfrac{\sin\left(\theta_i^P\right)}{\sqrt{-(\xi-1)^2\sin^2\left(\theta_i^P\right)+1}}\right]^2}
$$

$$
\approx \frac{\left[\dfrac{(\xi-1)\left(1-\left(\theta_i^P\right)^2/2\right)}{\sqrt{-(\xi-1)^2\left(\theta_i^P\right)^2+1}}+1\right]^2 \left[-\dfrac{r_i}{L^2\left(1+\frac{r_i^2}{L^2}\right)}\right]^2}{\left[\dfrac{\left(\theta_i^P\right)}{\sqrt{-(\xi-1)^2\left(\theta_i^P\right)^2+1}}\right]^2} \tag{3.139}
$$

via small angle approximations*

$$
\approx \frac{\left[\dfrac{(\xi-1)\left(1-\left(\frac{r_i}{L}\right)^2/2\right)}{\sqrt{-(\xi-1)^2\left(\frac{r_i}{L}\right)^2+1}}+1\right]^2 \left[-(\xi-1)^2\left(\frac{r_i}{L}\right)^2+1\right]}{\left[L^2\left(1+\frac{r_i^2}{L^2}\right)^2\right]}
$$

Given that $L \gg r_i$ taking the limit as r_i/L approaches 0 provides a further approximation of 3.139. Additionally, this limit also indicates the exact behavior along the reconstruction's major axis.

$$\lim_{r_i/L \to 0} \left(\frac{\partial X_i}{\partial L}\right)^2 / \left(\frac{\partial X_i}{\partial \xi}\right)^2 \approx \frac{\lim\limits_{r_i/L \to 0} \left[\frac{(\xi - 1)\left(1 - \left(\frac{r_i}{L}\right)^2/2\right)}{\sqrt{-(\xi - 1)^2 \left(\frac{r_i}{L}\right)^2 + 1}} + 1\right]^2 \lim\limits_{r_i/L \to 0}\left[-(\xi - 1)^2\left(\frac{r_i}{L}\right)^2 + 1\right]}{\lim\limits_{r_i/L \to 0}\left[L^2\left(1 + \frac{r_i^2}{L^2}\right)^2\right]}$$

$$\approx \frac{\left[\frac{(\xi - 1)\left(1 - (0)^2/2\right)}{\sqrt{-(\xi - 1)^2 (0)^2 + 1}} + 1\right]^2 \left[-(\xi - 1)^2 (0)^2 + 1\right]}{\left[L^2(1 + 0)^2\right]}$$

$$\approx \frac{\xi^2}{L^2}$$

$$(3.140)$$

Knowing that the magnitude of L is approximately 380 and that the image compression factor is generally between 1 and 2 then the following is expected.

$$\left(\frac{\partial X_i}{\partial L}\right)^2 \lesssim \left(\frac{\partial X_i}{\partial \xi}\right)^2 \tag{3.141}$$

$$\left(\frac{\partial X_i}{\partial L}\right)^2 \sigma_L^2 \lesssim \left(\frac{\partial X_i}{\partial \xi}\right)^2 \sigma_\xi^2 \text{ for } \sigma_L^2 \lesssim \frac{L^2}{\xi^2}\sigma_\xi^2 \tag{3.142}$$

$$\left(\frac{\partial X_i}{\partial L}\right)^2 \sigma_L^2 \approx \left(\frac{\partial X_i}{\partial \xi}\right)^2 \sigma_\xi^2 \text{ if } \sigma_L^2 = p_i L, \ \sigma_\xi^2 = p_i \xi \tag{3.143}$$

From this, it is observed that errors in ξ will generally contribute to the final error estimate more than L, such that for a comparable impact σ_L^2 would need to be approximately 190 times that of ξ. Such a measurement error is orders of magnitude greater than any true measurement uncertainty for the flight path length and so the influence of L can generally be treated as negligible.

To account for the induced error in Y_i recall that the terms for $\frac{\partial X_i}{\partial d_i}$ and $\frac{\partial d_i}{\partial \theta_i}$ dropped out of the ratio in equation 3.139. This same cancellation will occur for the partials with respect to Y_i such that:

$$\left(\frac{\partial Y_i}{\partial L}\right)^2 / \left(\frac{\partial Y_i}{\partial \xi}\right)^2 = \left(\frac{\partial X_i}{\partial L}\right)^2 / \left(\frac{\partial X_i}{\partial \xi}\right)^2 \tag{3.144}$$

It follows then that the same relationships described in equations 3.141 and 3.133 apply for

Y_i.

$$\left(\frac{\partial Y_i}{\partial L}\right)^2 \lesssim \left(\frac{\partial Y_i}{\partial \xi}\right)^2 \tag{3.145}$$

$$\left(\frac{\partial Y_i}{\partial L}\right)^2 \sigma_L^2 \lesssim \left(\frac{\partial Y_i}{\partial \xi}\right)^2 \sigma_\xi^2 \text{ for } \sigma_L^2 \lesssim \frac{L^2}{\xi^2}\sigma_\xi^2 \tag{3.146}$$

$$\left(\frac{\partial Y_i}{\partial L}\right)^2 \sigma_L^2 \approx \left(\frac{\partial Y_i}{\partial \xi}\right)^2 \sigma_\xi^2 \text{ if } \sigma_L^2 = p_i L, \ \sigma_\xi^2 = p_i \xi \tag{3.147}$$

Now that L and ξ have been accounted for the partials with respect to X_i^{det} and Y_i^{det} are considered. Note that the detector coordinates determine r_i and are thus involved in the calculation of both d_i and ϕ_i resulting in a summation. For X_i the partials are given as:

$$\begin{aligned}
\frac{\partial X_i}{\partial X_i^{det}} &= \frac{\partial X_i}{\partial d_i}\frac{\partial d_i}{\partial \theta_i}\frac{\partial \theta_i}{\partial \theta_i^P}\frac{\partial \theta_i^P}{\partial r_i}\frac{\partial r_i}{\partial X_i^{det}} + \frac{\partial X_i}{\partial \phi_i}\frac{\partial \phi_i}{\partial X_i^{det}} \\
&= \frac{\partial X_i}{\partial d_i}\frac{\partial d_i}{\partial \theta_i}\frac{\partial \theta_i}{\partial \theta_i^P}\frac{\partial \theta_i^P}{\partial r_i}\frac{X_i^{det}}{r_i} - \frac{\partial X_i}{\partial \phi_i}\frac{Y_i^{det}}{r_i^2} \\
&= \frac{R_i X_i^{det}\left(\frac{(\xi-1)\cos\left(\theta_i^P\right)}{\sqrt{-(\xi-1)^2\sin^2\left(\theta_i^P\right)+1}}+1\right)\cos(\phi_i)\cos(\theta_i)}{Lr_i\left(\left(\theta_i^P\right)^2+1\right)} + \frac{Y_i^{det}d_i\sin(\phi_i)}{r_i^2}
\end{aligned} \tag{3.148}$$

$$\begin{aligned}
\frac{\partial X_i}{\partial Y_i^{det}} &= \frac{\partial X_i}{\partial d_i}\frac{\partial d_i}{\partial \theta_i}\frac{\partial \theta_i}{\partial \theta_i^P}\frac{\partial r_i}{\partial X_i^{det}} + \frac{\partial X_i}{\partial \phi_i}\frac{\partial \phi_i}{\partial Y_i^{det}} \\
&= \frac{\partial X_i}{\partial d_i}\frac{\partial d_i}{\partial \theta_i}\frac{\partial \theta_i}{\partial \theta_i^P}\frac{Y_i^{det}}{r_i} + \frac{\partial X_i}{\partial \phi_i}\frac{X_i^{det}}{r_i^2} \\
&= \frac{R_i Y_i^{det}\left(\frac{(\xi-1)\cos\left(\theta_i^P\right)}{\sqrt{-(\xi-1)^2\sin^2\left(\theta_i^P\right)+1}}+1\right)\cos(\phi_i)\cos(\theta_i)}{Lr_i\left(\left(\theta_i^P\right)^2+1\right)} - \frac{X_i^{det}d_i\sin(\phi_i)}{r_i^2}
\end{aligned} \tag{3.149}$$

The same simplifications using small angle approximation and limit as $r(i/L)$ tends to 0 determines that the ratio of the squared partials is just the squared ratio of the detector coordinates. Thus, near the detector center X_i^{det} and Y_i^{det} contribute equally to the final uncertainty and will result in stronger dependencies as $|X_i^{det} - Y_i^{det}|$ diverges from zero.

$$\lim_{\theta_i^P \to 0}\left(\frac{\partial X_i}{\partial X_i^{det}}\right)^2 / \left(\frac{\partial X_i}{\partial Y_i^{det}}\right)^2 = \lim_{\theta_i^P \to 0}\left(\frac{\partial X_i}{\partial X_i^{det}}\right)^2 / \lim_{\theta_i^P \to 0}\left(\frac{\partial X_i}{\partial Y_i^{det}}\right)^2 = \frac{\left(X_i^{det}\right)^2}{\left(Y_i^{det}\right)^2} \tag{3.150}$$

Applying the same procedure as applied in equations 3.148 to 3.150 results in the following partials for Y_i.

$$\frac{\partial Y_i}{\partial X_i^{det}} = \frac{\partial Y_i}{\partial d_i}\frac{\partial d_i}{\partial \theta_i}\frac{\partial \theta_i}{\partial \theta_i^P}\frac{\partial \theta_i^P}{\partial r_i}\frac{\partial r_i}{\partial X_i^{det}} + \frac{\partial Y_i}{\partial \phi_i}\frac{\partial \phi_i}{\partial X_i^{det}} \tag{3.151}$$

$$\frac{\partial Y_i}{\partial Y_i^{det}} = \frac{\partial Y_i}{\partial d_i}\frac{\partial d_i}{\partial \theta_i}\frac{\partial \theta_i}{\partial \theta_i^P}\frac{\partial \theta_i^P}{\partial r_i}\frac{\partial r_i}{\partial Y_i^{det}} + \frac{\partial Y_i}{\partial \phi_i}\frac{\partial \phi_i}{\partial Y_i^{det}} \tag{3.152}$$

$$\lim_{\theta_i^P \to 0}\left(\frac{\partial Y_i}{\partial X_i^{det}}\right)^2 \bigg/ \left(\frac{\partial Y_i}{\partial Y_i^{det}}\right)^2 = \lim_{\theta_i^P \to 0}\left(\frac{\partial Y_i}{\partial X_i^{det}}\right)^2 \bigg/ \lim_{\theta_i^P \to 0}\left(\frac{\partial Y_i}{\partial Y_i^{det}}\right)^2 = \frac{\left(X_i^{det}\right)^2}{\left(Y_i^{det}\right)^2} \tag{3.153}$$

All of the prior analyses can be summarized for both X and Y according to 3.154 and 3.155 however comparison between the sets: $\{X_i^{det}, Y_i^{det}\}$, $\{L, \xi\}$, and $\{F, k_f, V_i\}$, proves impossible without a numeric solution that cannot be trivially generalized for multiple specimens. The required computational validation is included alongside the analysis and calibration of a the hematite system detailed in section 5.

$$\left(\frac{\partial X_i}{\partial X_i^{det}}\right)^2 \approx \left(\frac{\partial X_i}{\partial Y_i^{det}}\right)^2 \quad \left(\frac{\partial X_i}{\partial L}\right)^2 < \left(\frac{\partial X_i}{\partial \xi}\right)^2 \quad \left(\frac{\partial X_i}{\partial V_i}\right)^2 < \left(\frac{\partial X_i}{\partial F}\right)^2 < \left(\frac{\partial X_i}{\partial k_f}\right)^2 \tag{3.154}$$

$$\left(\frac{\partial Y_i}{\partial X_i^{det}}\right)^2 \approx \left(\frac{\partial Y_i}{\partial Y_i^{det}}\right)^2 \quad \left(\frac{\partial Y_i}{\partial L}\right)^2 < \left(\frac{\partial Y_i}{\partial \xi}\right)^2 \quad \left(\frac{\partial Y_i}{\partial V_i}\right)^2 < \left(\frac{\partial Y_i}{\partial F}\right)^2 < \left(\frac{\partial Y_i}{\partial k_f}\right)^2 \tag{3.155}$$

Spatial uncertainty in Z

Recall that in the Bas protocol the depth calculation is dependent on assigning each ion an individual depth increment, dz, and a correction term dz' that describes the placement on the specimen apex. The Gault reconstruction's depth determination is identical with the exception of dz'. Equations 3.156 through 3.158 denotes the correction term and the partials under the wide-angle voltage-based reconstruction.

$$dz_i' = dz'(R_i, \theta_i) = -R_i \cos(\theta_i) + R_i \tag{3.156}$$

$$\frac{\partial}{\partial R_i}dz'(R_i, \theta_i) = 1 - \cos(\theta_i) \tag{3.157}$$

$$\frac{\partial}{\partial \theta_i}dz'(R_i, \theta_i) = R_i \sin(\theta_i) \tag{3.158}$$

Continuing with the dependencies introduced by R_i consider the partials with respect to V_i, F, and k_f.

$$\frac{\partial dz_i'}{\partial V_i} = \frac{\partial dz_i'}{\partial R_i}\frac{\partial R_i}{\partial V_i} \tag{3.159}$$

$$\frac{\partial dz_i'}{\partial F} = \frac{\partial dz_i'}{\partial R_i}\frac{\partial R_i}{\partial F} \tag{3.160}$$

$$\frac{\partial dz_i'}{\partial k_f} = \frac{\partial dz_i'}{\partial R_i}\frac{\partial R_i}{\partial k_f} \tag{3.161}$$

Similar to the partials for X_i and Y_i taking the ratios of the three partials results in the ratio of the parameters as had been observed in 3.129 and 3.130. Subsequently the statements described by equations 3.131 through 3.133 also hold for dz_i' such that:

$$\left(\frac{\partial dz_i'}{\partial V_i}\right)^2 < \left(\frac{\partial dz_i'}{\partial F}\right)^2 < \left(\frac{\partial dz_i'}{\partial k_f}\right)^2 \tag{3.162}$$

$$\left(\frac{\partial dz_i'}{\partial V_i}\right)^2\sigma_{V_i}^2 < \left(\frac{\partial dz_i'}{\partial F}\right)^2\sigma_F^2 < \left(\frac{\partial dz_i'}{\partial k_f}\right)^2\sigma_{k_f}^2 \text{ for } \sigma_{V_i}^2 \le \frac{V_i^2}{F^2}\sigma_F^2 \text{ and } \sigma_F^2 \le \frac{F^2}{k_F^2}\sigma_{k_f}^2 \tag{3.163}$$

$$\left(\frac{\partial dz_i'}{\partial V_i}\right)^2\sigma_{V_i}^2 = \left(\frac{\partial dz_i'}{\partial F}\right)^2\sigma_F^2 = \left(\frac{\partial dz_i'}{\partial k_f}\right)^2\sigma_{k_f}^2 \text{ if } \sigma_{V_i}^2 = p_i^2 V_i^2,\ \sigma_F^2 = p_i^2 F^2,\ \sigma_{k_f}^2 = p_i^2 k_f^2 \tag{3.164}$$

Note however that dz_i and dz_i' have common dependencies and so the above relationship will are not guarantied to apply to the final depth, Z_i.

The impact of θ_i remains which results in dz_i' being dependent upon L, ξ, X_i^{det}, and Y_i^{det}. Taking the partials with respect to L and ξ under the expectation that they will result in a similar effect on dz_i' we find that one term is shared and the flight length requires one further term.

$$\frac{\partial dz_i'}{\partial \xi} = \frac{\partial dz_i'}{\partial \theta_i}\frac{\partial \theta_i}{\partial \xi} \tag{3.165}$$

$$\frac{\partial dz_i'}{\partial L} = \frac{\partial dz_i'}{\partial \theta_i}\frac{\partial \theta_i}{\partial \theta_i^P}\frac{\partial \theta_i^P}{\partial L} \tag{3.166}$$

Using the small angle approximation for θ_i^P and taking the limit as r_i/L approaches zero as in equation 3.140 provides the following approximation of the squared ratio of $\partial dz_i'/\partial \xi$ and $\partial dz_i'/\partial L$.

$$\lim_{r_i/L\to 0}\left(\frac{\partial dz_i'}{\partial L}\right)^2 / \left(\frac{\partial dz_i'}{\partial \xi}\right)^2 = \lim_{r_i/L\to 0}\left(\frac{\partial \theta_i}{\partial \theta_i^P}\frac{\partial \theta_i^P}{\partial L}\right)^2 / \left(\frac{\partial \theta_i}{\partial \xi}\right)^2 \approx \frac{\xi^2}{L^2} \tag{3.167}$$

Recalling that L is on the order of 380 mm for the LEAP 4000 series instruments and that ξ typically ranges from 1 to 2 then ξ is the dominant source of error in comparison to L for

dz_i' given the following conditions.

$$\left(\frac{\partial dz_i'}{\partial L}\right)^2 \lesssim \left(\frac{\partial dz_i'}{\partial \xi}\right)^2 \tag{3.168}$$

$$\left(\frac{\partial dz_i'}{\partial L}\right)^2 \sigma_L^2 \lesssim \left(\frac{\partial dz_i'}{\partial \xi}\right)^2 \sigma_\xi^2 \text{ for } \sigma_L^2 \lesssim \frac{L^2}{\xi^2}\sigma_\xi^2 \tag{3.169}$$

$$\left(\frac{\partial dz_i'}{\partial L}\right)^2 \sigma_L^2 \approx \left(\frac{\partial dz_i'}{\partial \xi}\right)^2 \sigma_\xi^2 \text{ if } \sigma_L^2 = p_i L, \ \sigma_\xi^2 = p_i \xi \tag{3.170}$$

Finally accounting for the detector coordinates we arrive at equations 3.171 and 3.172.

$$\frac{\partial dz_i'}{\partial X_i^{det}} = \frac{\partial dz_i'}{\partial d_i}\frac{\partial d_i}{\partial \theta_i}\frac{\partial \theta_i}{\partial \theta_i^P}\frac{\partial \theta_i^P}{\partial r_i}\frac{\partial r_i}{\partial X_i^{det}} \tag{3.171}$$

$$\frac{\partial dz_i'}{\partial Y_i^{det}} = \frac{\partial dz_i'}{\partial d_i}\frac{\partial d_i}{\partial \theta_i}\frac{\partial \theta_i}{\partial \theta_i^P}\frac{\partial \theta_i^P}{\partial r_i}\frac{\partial r_i}{\partial Y_i^{det}} \tag{3.172}$$

The ratio is then simply expressed without the need of approximations as:

$$\left(\frac{\partial dz_i'}{\partial X_i^{det}}\right)^2 \Big/ \left(\frac{\partial dz_i'}{\partial Y_i^{det}}\right)^2 = \left(\frac{\partial r_i}{\partial X_i^{det}}\right)^2 \Big/ \left(\frac{\partial r_i}{\partial Y_i^{det}}\right)^2 = \frac{\left(X_i^{det}\right)^2}{\left(Y_i^{det}\right)^2} \tag{3.173}$$

As in the case of X_i and Y_i the detector coordinates approximately contribute the same amount of error near the detector center and near the 45°, 135°, 225°, 315° lines projecting from the origin. One term will become dominate as $|X_i^{det} - Y_i^{det}|$ diverges from zero.

Equation 3.174 summarizes the observations regarding the partials of dz_i' thus far and indicates the same relationships as derived in the small-angle case. Once again there exist no closed form solutions that enable comparison between the sets: $\{X_i^{det}, Y_i^{det}\}$, $\{L, \xi\}$, and $\{F, k_f, V_i\}$. Furthermore, the nested trig functions further obfuscate the true comparisons as in the case of $\{L, \xi\}$ due to the need of simplifying assumptions. Finally, as in the case of the small-angle reconstruction these association do not hold for Z_i which requires a numeric comparison.

$$\left(\frac{\partial dz_i'}{\partial X_i^{det}}\right)^2 \approx \left(\frac{\partial dz_i'}{\partial Y_i^{det}}\right)^2 \quad \left(\frac{\partial dz_i'}{\partial L}\right)^2 \lesssim \left(\frac{\partial dz_i'}{\partial \xi}\right)^2 \quad \left(\frac{\partial dz_i'}{\partial V_i}\right)^2 < \left(\frac{\partial dz_i'}{\partial F}\right)^2 < \left(\frac{\partial dz_i'}{\partial k_f}\right)^2 \tag{3.174}$$

3.4 Conclusions with respect to small and wide-angle reconstructions

In conclusion we find that for both small and wide-angle reconstructions the spatial uncertainty for the reconstructed X and Y coordinates are most sensitive to the image compression

factor and field factor followed by the evaporation field. Comparatively the instrument specific flight length and applied voltage are negligible and align with our expectations given that the flight length is a known quantity for each LEAP model and that the only error associated with voltage should be dependent on the voltage controller. Opposing these are the user defined parameters of which only the field is a well estimated parameter prior to calibration by using the expected value for pure materials. The image compression factor and field factor are most commonly used by the user to calibrate the reconstruction according to their prior assumptions. One common method for this is to adjust the field factor such that the interplanar spacing of the specimen matches the true value for the material and adjust the image compression factor to minimize the planar curvature.

Furthermore, a generalized evaluation is not available for the depth coordinate, Z_i, however analysis of its constituent components the cumulative depth $\sum dz_i$ and depth correction dz_i' suggest that in agreement with X and Y the user defined factors are the most important parameters to minimize the final uncertainty. This analysis also suggests the instrument specific parameters with the exception of instrument efficiency are negligible. The efficiency is not required for calculation of (X, Y) but is as important as the field factor and image compression factor for $\sum dz_i$ and presumably Z_i.

It is also observed that the voltage and ionic volume estimates have an unpredictable influence on Z_i due to inclusion of covariance terms. The covariance terms with respect to voltage can likely be neglected alongside the expected low measurement error in the applied voltage, however should not be neglected in the case of ionic volume. Error propagation with respect to the volume provides two covariance terms, the first of which accounts for when two events possess the same ionic volume which is accounted for in our work. The second covariance term accounts for when two complex ion volume estimates rely on the same simple ion estimates as in the case of FeO and NiO_3 which would share a dependence on the volume of oxygen. This term is neglected within our analysis due to a lack of information regarding the IVAS software's internally computation.

Chapter 4

Methods for error minimization

Given the cumulative nature of the depth uncertainty derived in section 3.1 it is of interest to minimize the variance as both a global measure and a local measure. Both measures are influenced by the point processing order within the reconstruction and thus a natural extension of pointwise error propagation is to alter the reconstruction order such that the measures of error are minimized. First, alternate reconstruction origins are explored as a error minimization method while preserving the cumulative depth increments of the reconstructions. Second, this process is used to establish a new distance metric designed to minimize pairwise variances while accounting for the pairwise covariance of all points within the reconstruction.

4.1   Alternate reconstruction origins

Prior to investigating the effect of altering the reconstruction order a global measure of uncertainty must first be defined to provide a method of comparing multiple reconstructions. For this purpose either the sum of squared errors, 4.1 or the mean squared error, equation 4.2, can serve as a global metric representing in aggregate the error associated with each point. This metric is also primarily focused on the depth coordinate as the X, Y positions of each ion are independent and should not be impacted by the reconstruction order.

$$SSE_Z = \sum_{i=1}^{N} \sigma_{Z_i}^2 \qquad (4.1) \qquad MSE_Z = \frac{SSE_Z}{N} \qquad (4.2)$$

The only difference between the two metrics is accounting for the number of points, N, used in the estimate of the summed squared error. Thus when comparing reconstructions of the same point cloud SSE_Z is sufficient, however when comparing the results of different point clouds MSE_Z should instead be used as the sample sizes will differ. Focusing then on equation 4.1 and substituting in the expanded variance for Z_i provides a representation of the summed square error with separate contributions from the depth correction and the

cumulative depth increment.

$$SSE_Z = \sum_{i=0}^{n} \left[Var \left(\sum_{j=0}^{i} dz_i \right) + Var(dz') + 2cov \left(\sum_{j=0}^{i} dz_j, dz' \right) \right] \tag{4.3a}$$

$$\approx \sum_{i=0}^{n} \left[Var \left(\sum_{j=0}^{i} dz_i \right) \right] \tag{4.3b}$$

Neglecting both the covariance terms and the correction terms dz' the depth increment provides the basis for minimizing error based on the reconstruction origin. Recall the derivatives of each individual depth increment can be described according to 3.22a for the constant variables.

$$\frac{\partial dz_i}{\partial T} = (dz_i) \left(\frac{F(T)}{T} \right) = C_{dz} \frac{\Omega_i}{V_i^2} \frac{F(T)}{T} \tag{3.22a}$$

$$\text{where } F(T) = \begin{cases} 2, & \text{if } T \text{ is in } \{F, k_f, L\} \\ 1, & \text{if } T = \Omega_i \\ -2, & \text{if } T \text{ is in } \{V_i, \xi\} \\ -1, & \text{if } T \text{ is in } \{S_D, \eta\} \end{cases} \tag{3.22b}$$

From the above, one can observe that the primary differences between any two points (i, j) are the assigned ionic volume, Ω, and the voltage of the evaporation event, V. As a non-rigorous exercise neglect the covariance components of the summation and assume that the variance of a depth increment is proportional to the volume-voltage component of equation 3.22a such that:

$$SSE_Z \approx \alpha \sum_{i=0}^{n} \left[\sum_{j=0}^{i} \left(\frac{\Omega_j}{V_j^2} \right)^2 \right] \tag{4.4}$$

where α indicates the proportionality. Assuming then that the system is monoisotopic the ionic volume can be removed from the summation as a further constant. As a logical extreme consider the scenarios where the reconstruction origin is set at $i = 0$, denoted as $R0$ and is set at $i = n$ with the summation terminating at 0, denoted as RN. Accounting for the first term within SSE_Z for both scenarios results in the following:

$$SSE_Z^{R0} \approx \alpha \left(V_0^{-4} + \sum_{i=1}^{n} \left[V_0^{-4} + \sum_{j=1}^{i} V_j^{-4} \right] \right) \tag{4.5a}$$

$$\approx \alpha \left(N \cdot V_0^{-4} + \sum_{i=1}^{n} \left[\sum_{j=1}^{i} V_j^{-4} \right] \right) \tag{4.5b}$$

$$SSE_Z^{RN} \approx \alpha \left(V_N^{-4} + \sum_{i=N-1}^{0} \left[V_N^{-4} + \sum_{j=N-1}^{i} V_j^{-4} \right] \right) \tag{4.6a}$$

$$\approx \alpha \left(N \cdot V_N^{-4} + \sum_{i=N-1}^{1} \left[\sum_{j=N-1}^{i} V_j^{-4} \right] \right) \tag{4.6b}$$

Given the above and that $V_N \gg V_0$ we expect that the error contribution from point N, $N \cdot V_N^{-4}$ is smaller than that of point 0, $N \cdot V_0^{-4}$. Further separation of the summations for points $N-1$ through $N-4$ and points 1 through 4 gives the following which can be extended for all remaining points.

$$SSE_Z^{R0} \approx \alpha \left(N \cdot V_0^{-4} + (N-1) \cdot V_1^{-4} + (N-2) \cdot V_2^{-4} + (N-3) \cdot V_3^{-4} \right.$$
$$\left. + (N-4) \cdot V_4^{-4} + \sum_{i=5}^{n} \left[\sum_{j=5}^{i} V_j^{-4} \right] \right) \tag{4.7}$$

$$SSE_Z^{RN} \approx \alpha \left(N \cdot V_N^{-4} + (N-1) \cdot V_{N-1}^{-4} + (N-2) \cdot V_{N-2}^{-4} + (N-3) \cdot V_{N-3}^{-4} \right.$$
$$\left. + (N-4) \cdot V_{N-4}^{-4} + \sum_{i=N-5}^{1} \left[\sum_{j=N-5}^{i} V_j^{-4} \right] \right) \tag{4.8}$$

Considering that V_{N-i} should be larger than V_i for all i in equations 4.7 and 4.8 it is expected that $SSE_Z^{R0} \gg SSE_Z^{RN}$ meaning that a reconstruction which is built up from the last detected ion should have lower total error than one which is formed starting at the first detected ion.

Computational validation

The prior hypothesis that a reconstruction starting at the Nth event results in lower total error cannot be explicitly proven, so instead the uncalibrated hematite specimen with unit variance is used for computational validation. Note however, that while many assumptions were required to arrive at the hypothesis the calculations do not use any simplifying assumptions. Furthermore, changing the reconstruction origin from 0 to N does not require any modifications to the reconstruction code but does require the input data to be reversed and that negative voltages be provided.

A visual representation of $Var(Z_i)$ is provided in figure 4.1 for both the normal reconstruction starting at $i = 0$ and the one starting at $i = N$ which will be referred to as a reversed reconstruction going forward. From this figure the impact of the cumulative error is inverted for the reversed reconstruction with maximum uncertainties achieved at the top of
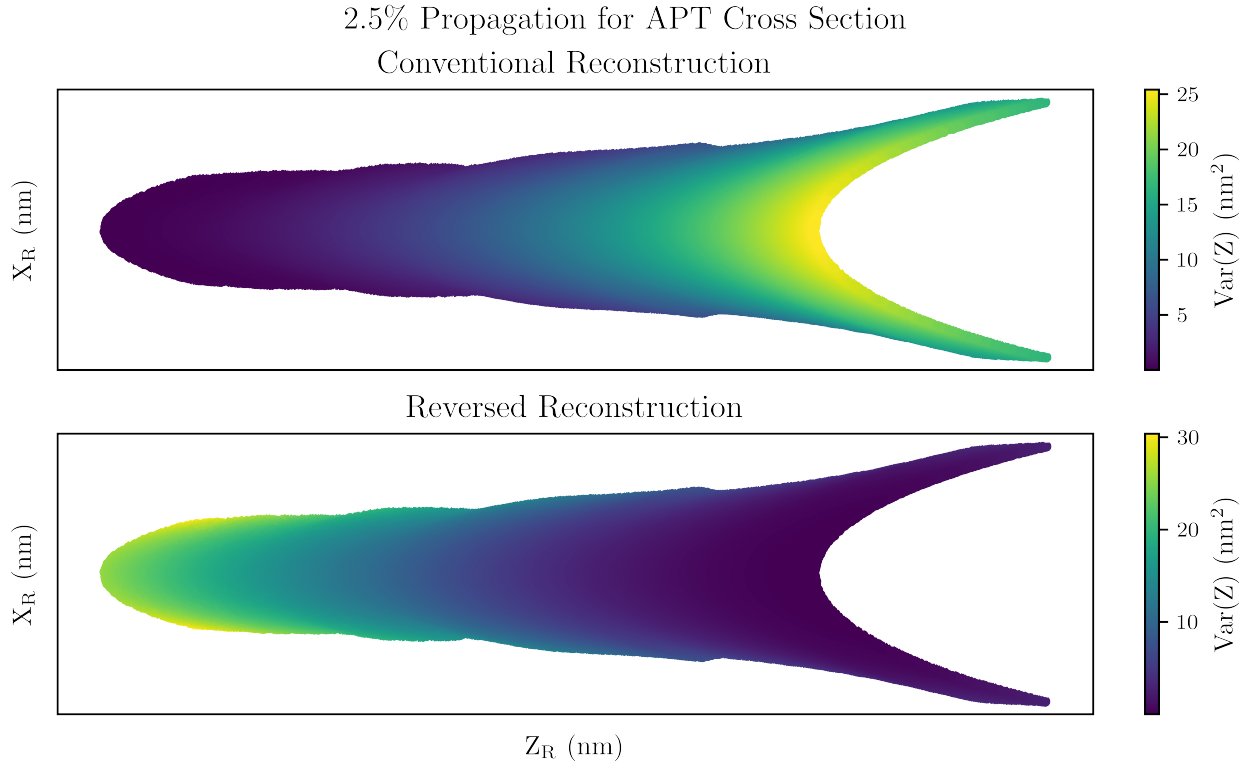
Figure 4.1: Heatmap indicating the pointwise depth uncertainties of a slice along the Z coordinate for a conventional and reversed origin small-angle reconstruction.

the conventional reconstruction and minimal uncertainty at the base of the specimen. The true comparison is made with the SSE however which is $1.45e7$ and $7.3e6$ for the normal and reversed reconstructions respectively. These values for the SSE are in agreement with our hypothesis, but do not reveal if there is an optimal origin for the reconstruction. The optimal origin on a per-specimen basis is determined by iterating through the indices of the points and performing a reconstruction with each as the origin. As in the case for the reversed reconstruction minimal modification is required for the reconstruction algorithms, in this case the data is split into two segments $i \leq j$ and $j \leq N$ where the position of the origin, j, is fixed at 0. The first segment undergoes a conventional reconstruction and the second segment the reverse reconstruction before the two are recombined into one final set of coordinates. For each index the SSE is stored and the reconstruction with the minimum SSE is selected as the best reconstruction. From figure 4.2 the ideal origin is found to be point 437154 with an SSE of $2.2e6$. The final uncertainty map is provided in figure 4.3 and indicates that points near the origin preserve minimum error and that points near the two extremes of the dataset have maximum error.

One final observation can be made for the conventional, reversed, and optimal (otherwise referred to as middle-out) reconstruction through analysis of the cumulative distribution
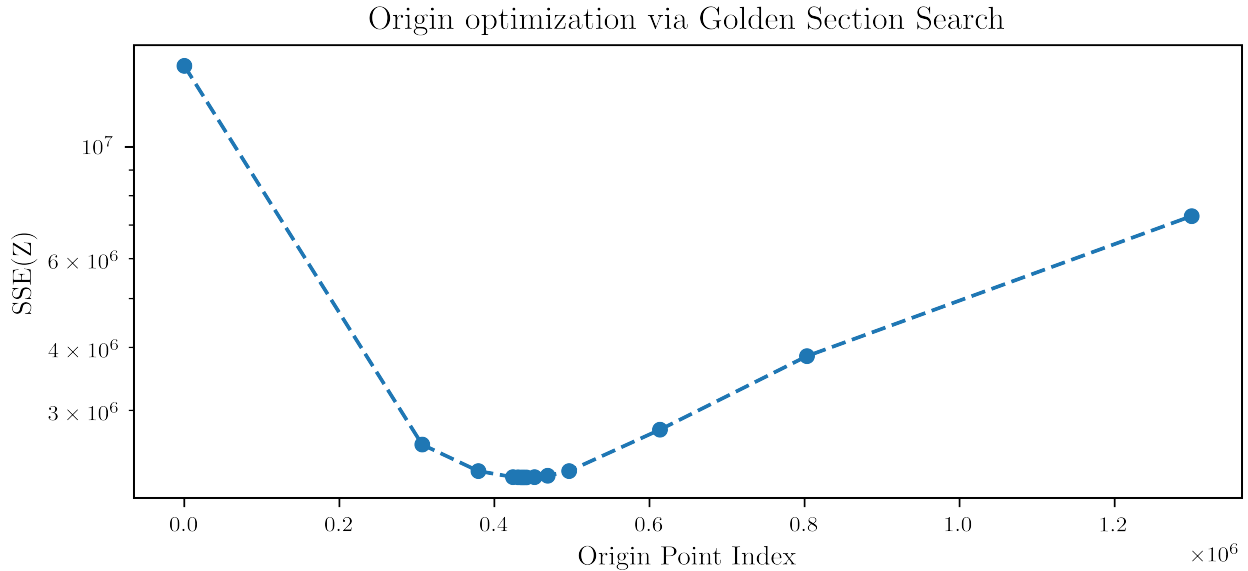
Figure 4.2: Plot measuring the sum of squared error (SSE) of a small-angle reconstruction as a function of the reconstruction origin. Parameter search was accomplished using the golden section search (GSS) method.

function for the observed Var(Z) presented in figure 4.4. Here the three reconstructions are denoted by the origin points; 0, 437154, and 1299346 respectively, and the conventional method possesses a relatively linear CDF indicating a uniform distribution of possible variance throughout the majority of the reconstruction with a final nonlinear region. The other extreme represented by the reverse reconstruction shows a highly skewed distribution with 60% of the data being contained within a linear regime until a variance of six where the curve transitions to a curved portion prior to leveling off. While the majority of the data exists at lower variances then the conventional the maximum variance is larger. The middle-out reconstruction combines the skewed distribution of the reversed focused on low variance with the relative quick plateau near 100% of the data that the conventional possessed. Furthermore, due to each of the spatial extremes being dependent only on a portion of the data the maximum variance is significantly lower than either of the other reconstructions.
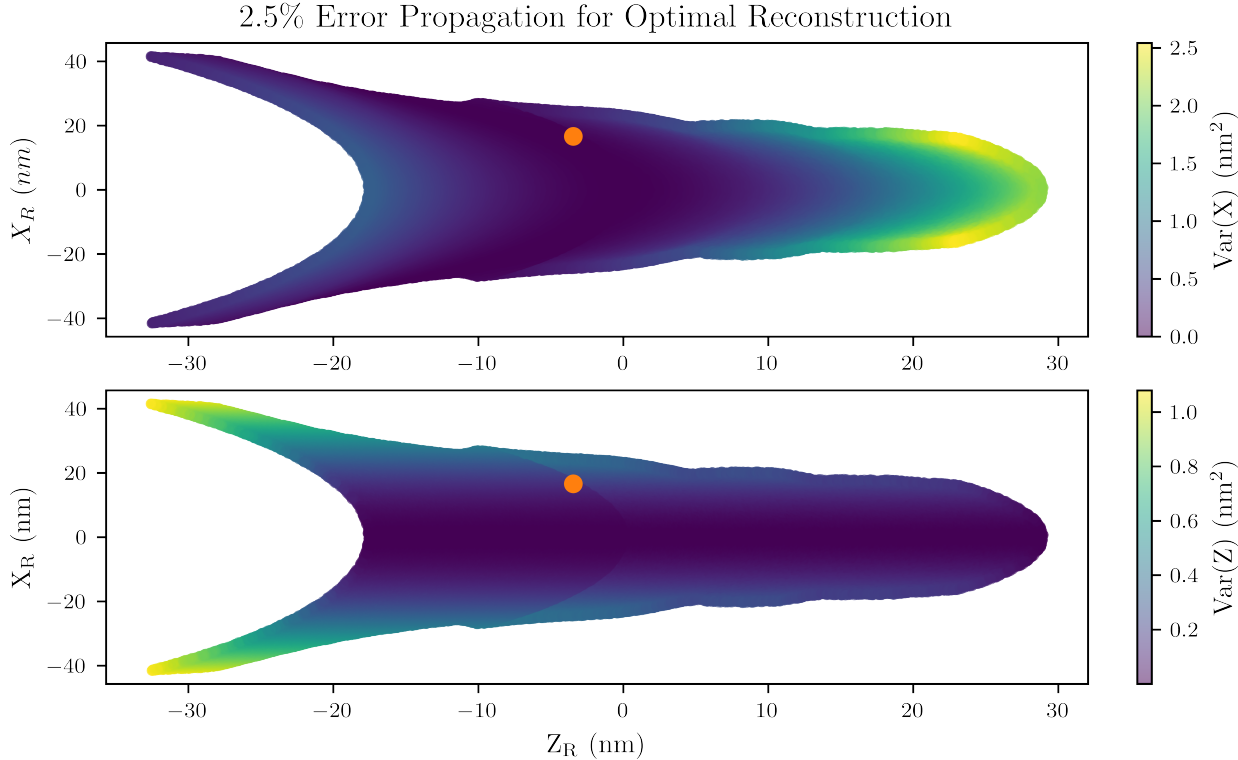
Figure 4.3: Heatmap indicating the pointwise depth uncertainties of a slice along the Z coordinate for the optimal reconstruction origin as determined by the SSE(Z). The reconstruction origin is indicated by the orange square marker.
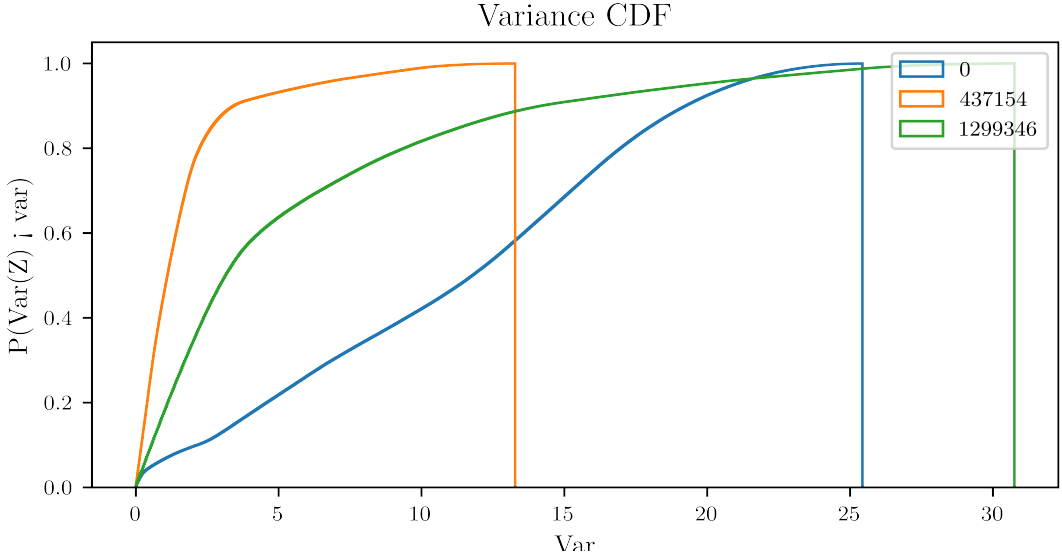
Figure 4.4: CDF's of variance for each type of reconstruction as a function of the reconstruction origin. Blue indicates a conventional reconstruction while orange and green indicate a "middle-out" and reverse reconstruction.

4.2 Ordered euclidean distance

As the reconstruction origin is shown to impact the global uncertainty via the sum of squared errors and minimizes the local uncertainty we propose a new definition of euclidean distance for analysis of atom probe data that attempts to minimize error and account for pairwise covariance. For points i, j the variance of the conventional squared euclidean distance is given according to equation 4.9 below.

$$
\begin{aligned}
Var\left(D(i,j)^2\right) = {} & 4(\Delta X)^2 \left[Var(X_i) + Var(X_j) - Cov(X_i, X_j)\right] \\
& + 4(\Delta Y)^2 \left[Var(Y_i) + Var(Y_j) - Cov(Y_i, Y_j)\right] \\
& + 4(\Delta Z)^2 \left[Var(Z_i) + Var(Z_j) - Cov(Z_i, Z_j)\right] \\
& + 8(\Delta X)(\Delta Y) \left[Cov(X_i, Y_i) + Cov(X_j, Y_j) - Cov(X_i, Y_j) - Cov(X_j, Y_i)\right] \\
& + 8(\Delta X)(\Delta Z) \left[Cov(X_i, Z_i) + Cov(X_j, Z_j) - Cov(X_i, Z_j) - Cov(X_j, Z_i)\right] \\
& + 8(\Delta Y)(\Delta Z) \left[Cov(Y_i, Z_i) + Cov(Y_j, Z_j) - Cov(Y_i, Z_j) - Cov(Y_j, Z_i)\right]
\end{aligned}
\tag{4.9}
$$

While the pointwise variances are known given the methods of reconstruction error propagation outlined in sections 3.2 and 3.3 for small and wide-angle reconstructions the pairwise covariances of the coordinates are unknown. The first approach to address the unknown covariance is the use of the Cayley-Schwarz inequality which is expected to produce an overestimate of the distance uncertainty. Alternatively, alongside the reconstruction fourteen pairwise covariance matrix could be constructed and referenced resulting in the additional memory consumption of a (N, N, 15) array. The final option is to define a new distance metric that exploits the order of events to minimize the redundant calculations in the depth coordinates. Consider the following ordered euclidean distance with the substitution of 3.7 for the depth coordinates.

$$
D(i,j)^2 = (X_i - X_j)^2 + (Y_i - Y_j)^2 + \left(dz_i' - dz_j' + \sum_{l=0}^{i} dz_l - \sum_{l=0}^{l} dz_l\right)^2 \tag{4.10a}
$$

$$
= (X_i - X_j)^2 + (Y_i - Y_j)^2 + \left(dz_i' - dz_j' + sgn(i-j)\left[\sum_{l=min(i,j)+1}^{max(i,j)} dz_l\right]\right)^2 \tag{4.10b}
$$

The primary difference in the two distances is the separation of Z_i and Z_j into cumulative depth increment and the depth correction prior to cancellation of redundant increments and introduction of a sign function, sgn. Practically equation 4.10 is performing a local reconstruction over all points in [i, j] and setting the smaller of the two indices to the origin. This local reconstruction accounts for the covariances between the increments but neglects to account for the remaining terms. Considering that $D(i,j)$ is not just dependent on points i, j but on the full set of reconstruction input variables, $\{F, k_f, L, \xi, \eta, X_{i,j}^{det}, Y_{i,j}^{det}, \Omega, V\}$ with

Ω and V indicating all possible voltages and ionic volumes, the variance can be defined with respect to the partial derivatives. Equation 4.10 does provide a format conducive to simplifying the derivatives (except for Ω and V) and one example for an arbitrary variable, T, is provided in equation 4.11.

$$
\begin{aligned}
\frac{\partial D(i,j)^2}{\partial T} = & \frac{\partial}{\partial T}(X_i - X_j)^2 + \frac{\partial}{\partial T}(Y_i - Y_j)^2 \\
& + \frac{\partial}{\partial T}\left(dz'_i - dz'_j + sgn(i-j)\left[\sum_{l=min(i,j)+1}^{max(i,j)} dz_l\right]\right)^2
\end{aligned}
\tag{4.11}
$$

The derivative is further expanded and broken down into an X, Y, and Z component in the equations below.

$$
\frac{\partial}{\partial T}(X_i - X_j)^2 = 2(X_i - X_j)\left(\frac{\partial X_i}{\partial T} - \frac{\partial X_j}{\partial T}\right)
\tag{4.12a}
$$

$$
\frac{\partial}{\partial T}(Y_i - Y_j)^2 = 2(Y_i - Y_j)\left(\frac{\partial Y_i}{\partial T} - \frac{\partial Y_j}{\partial T}\right)
\tag{4.12b}
$$

$$
\begin{aligned}
\frac{\partial}{\partial T}(Z_i - Z_j)^2 = & 2\left(dz'_i - dz'_j + sgn(i-j)\left[\sum_{l=min(i,j)+1}^{max(i,j)} dz_l\right]\right) \\
& \cdot \left(\left[\frac{\partial dZ'_i}{\partial T} - \frac{\partial dZ'_j}{\partial T}\right] + sgn(i-j)\left[\sum_{l=min(i,j)+1}^{max(i,j)} \frac{\partial dz_l}{\partial T}\right]\right)
\end{aligned}
\tag{4.12c}
$$

Utilizing equations 4.12a through 4.12c removes the need to store the covariance matrices but would require the partials to be either stored or computed as part of the metric for all of the input variables. Storage would require an array of shape (N, N + 40, 3) given N unique voltages, approximately 30 ionic species, and the constant terms in comparison to the aforementioned (N, N, 15) array required for the covariance method. If stored as the same data type the covariance matrix route would require approximately five times the memory as the the ordered euclidean distance with stored partials.

From a practical perspective the ordered euclidean distance provides an advantage with respect to the memory consumption, although this diminishes in importance if small subsets of the data are being reconstructed and analyzed. Furthermore, the current reconstruction protocols already calculate the individual partial derivatives when determining the final result such that the modification to provide additional outputs is trivial. Whereas relying on pairwise covariance matrices will requires substantial changes to the reconstruction codes. A key advantage to the pairwise method however is the ability to generalize to additional metrics by referencing the established covariance matrices.

There is one final approach to propagating error through arbitrary metrics that it would be remiss to omit from this discussion. That being the use of monte-carlo error propagation

(MCEP) instead of linear error propagation for the reconstruction process. MCEP has three main advantages; 1. minimal memory usage, 2. minimal assumptions, 3. online covariance calculation, and one disadvantage in the computational complexity and runtime. Performing and storing the coordinates for M monte-carlo simulations results in an (N, M, 3) array with $M \ll N$ and thus a lower memory usage compared to either the pairwise covariance or the stored partials. With respect to advantage 2. the only assumptions that MCEP makes it related to the distributions of the input variables as opposed to assumed both input and outputs are normally distributed. Finally, online covariance calculations can be performed on demand using the stored data along axis 1 for given points (i, j) in [0, N].

Chapter 5

Calibration methods and sensitivity validation

The primary experimental aim of this chapter is to develop a calibration method for thin film oxides which provides error bounds on the calibrated reconstruction parameters. Given the calibration uncertainty, the secondary goal is to test the hypothesis that ions far from the reconstruction origin possess higher spatial uncertainty and that the incremental increases in the depth uncertainty are due to to the cumulative nature of the depth as described in 3 for experimental atom probe specimen.

For this analysis a BCC Fe specimen with an approximately $5 - 6$ nm Fe57 enriched thin film grown in the [1 0 0] direction was provided by Pacific Northwest National Laboratory for which an initial shank-angle reconstruction presented in figure 5.1 alongside a calibrated and uncalibrated small-angle reconstruction. Conventional manufacturing of APT specimens was performed using a Ga focused ion beam (FIB) for both rough cuts and annular sharpening, and the APT data was collected using a CAMECA LEAP 4000X HR equipped with a UV 355 nm laser. The known growth orientation and flat interface of the Fe57 layer provide ideal conditions to calibrate the reconstruction according to the interplanar spacing and the specimen curvature which are predominantly governed by the ξ and k_f parameters.

The interplanar spacing calibration requires knowledge of the lattice parameter for the analyzed planes. Indexing of poles in atom probe reconstructions require multiple poles to be visible on the detector projection. However, the controlled growth orientation ensures that the plane orientation is known even in the presence of only a single crystallographic pole. For BCC Fe the lattice parameter is 0.2866 nm, however the target interplanar spacing as measured by the atom probe should instead be 0.143 as the plane defined by the body-centered atoms will also be visible within the reconstruction.

In the case of curvature the isotopically enriched thin film when perpendicular to the atom probe analysis direction can provide a global picture of the reconstruction's curvature through measurement of the film interfaces. In comparison, measures of curvature which focus on the crystallographic planes can only provide a local estimate with diminishing accuracy as the distance from the pole is increased. Furthermore, by using isotopic enrichment instead
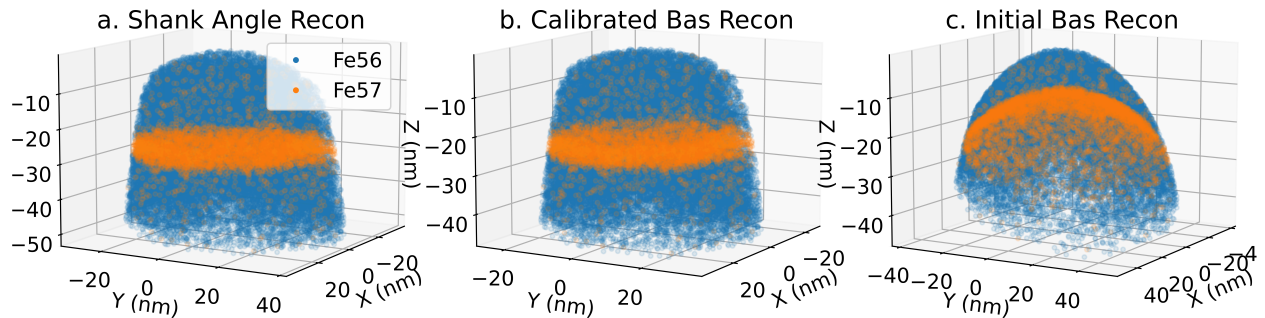
Figure 5.1: Comparison of a PNNL provided shank angle reconstruction (subfigure a.), a calibrated Bas reconstruction (subfigure b.), and an uncalibrated Bas reconstruction (subfigure c.). For recon a. and c. an image compression factor, ξ, of 1.750 and a field factor, k_f, of 3.3 are used. While for recon b. ξ and k_f are set to 1.073 and 3.098 respectively. The evaporation field is set to $33.0V/nm^3$ for all reconstructions. Subfigures a. and b. depict a flattened distribution of Fe57 ions at a depth of 25 nm whereas c. depicts a high curvature interface.

of elemental enrichment distortions in the reconstruction caused by transitioning between regions of differing required evaporation fields is minimized.

5.1   Calibration method

Interplanar spacing calibration

For interplanar spacing calibration we rely on the standard methods described in Gault et al. [40] and Larson et al. [74] involving spatial distribution maps. Spatial distribution maps (SDM) are defined according to the depth-only distance between nearby ions such that peaks correspond to atomic planes when they can be resolved. For these estimates to be accurate the planes must be orthogonal to the analysis direction or a parabolic background will be observed within the SDM. To correct for this background by aligning the analysis direction perpendicular to the crystallographic planes multiple methods exist such as DF-Fit, plane orientation extraction (POE), and the hough-transform, although for this work POE is used [55, 2, 128].

Plane orientation extraction

Plane orientation extraction (POE) was originally proposed alongside local crystallography mapping (LCM) to provide methods for systematic calibration of atom probe reconstructions in Araullo-Peters et al. [2], which should be referenced for an in depth discussion on
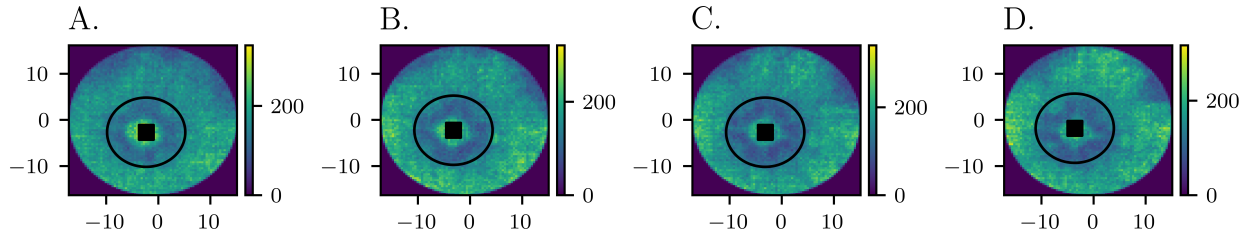
Figure 5.2: Selection of crystallographic pole according to a series detector hitmaps corresponding to different event subsets. The crystallographic pole is found to be located at $(-3.069, -2.353)$. A. is the hitmap for events 0 through 711604, B. events 711604 through 1423208, C. events 1423208 through 2134813, and D. events 2134813 through 2846417.

the method. In this work only POE is utilized as the detector hitmap data used in our reconstructions only have single poles violating LCM's reliance on multiple poles.

POE does not requires the presence of a pole, however provides the most accurate calibrations in the vicinity of pole figures. As shown in figure 5.2 poles manifest circular regions with lower detection rates, although may have a central peak. Separating the data into multiples slices the position of the pole can be tracked as a function of event number and thus depth by searching for the central peak. The pole radius can then be adjusted such that the locally depleted region is fully contained with a cylindrical ROI. Selection of the radius greatly impacts the efficacy of the POE method, with an insufficient radii resulting in insufficient counting statistics and an excessive radii resulting in an increased background level for subsequent distance histograms or spatial distribution maps.

Once the pole is extracted from the detector map, a spherical ROI at point, P, with a radius R_{POE} is selected for further analysis. The point P can either be selected according to the midpoint or mean point of the pole ROI. Subsequently a series of plane orientations $N(\phi, \Theta)$ where (ϕ, Θ) indicate the azimuthal and elevation angles, are evaluated to determine the rotation which best describes the planar arrangement within the spherical ROI. The evaluation function from [2] can be summarized as:

1. Calculate the perpendicular distance between $N(\phi, \Theta)$ and each point, p_i, such that $D(p_i - P) \leq R_{POE}$.

2. Construct a distance histogram as depicted in figure 5.3a.

3. Apply a 1D fast fourier transform, see figure 5.3b, with a median filter to separate the high crystallinity component of the FTT from the characteristic noise.

4. Determine maximum amplitude for comparison with other $N(\phi, \Theta)$.

Once the evaluation function has been applied to all possible planes the peak strength can be plotted relative to (ϕ, Θ) as seen in figure 5.3c with the maxima corresponding to the optimal planar orientation as a high amplitude within the FFT indicates a high degree of
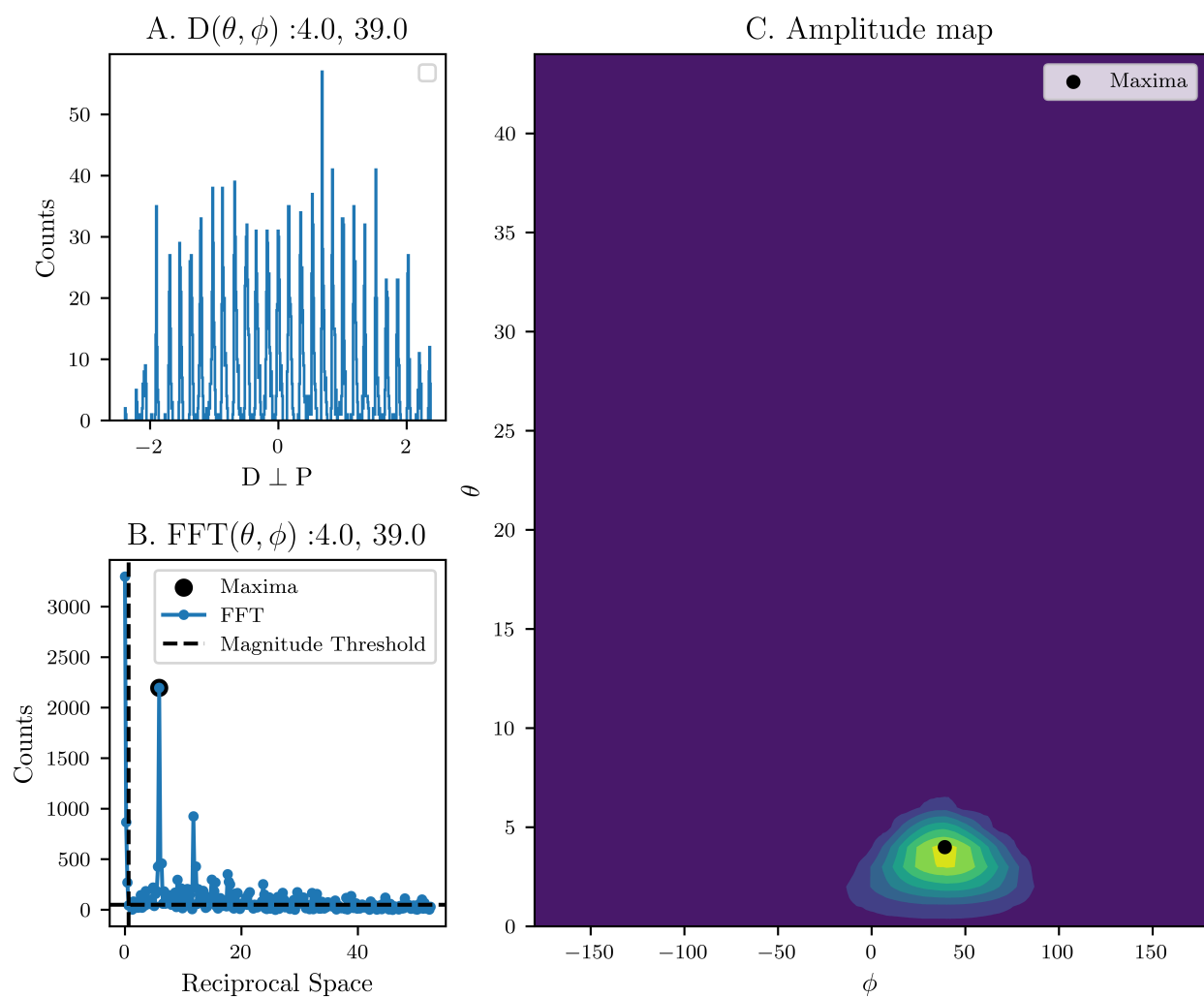
Figure 5.3: A, Distance histogram of best fit plane. B, fast fourier transform of A. C, Amplitude maps of maxima for each plane(ϕ, Θ). A high amplitude area is found for (ϕ, Θ) of (4.0, 39.0) in C. indicating the optimal rotation.
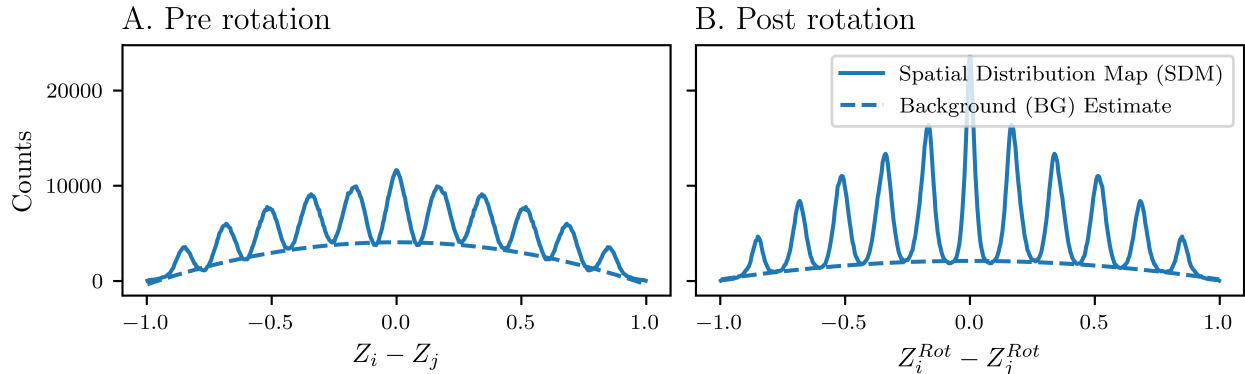
Figure 5.4: Example SDM pre (A.) and post (B.) applying the POE rotation. Post-rotation the peak intensities are maximized while the peak widths are minimized.

crystallinity. Prior application of POE indicate that varying ϕ from 0° to 360° and Θ from 0° to 45° with a step size of 1° is sufficient to find the correct rotation [2, 23, 22]. If a local calibration was desired such that POE was applied for thousands of points replacing the grid search with a gradient approach would be recommended to improve the computational efficiency.

Spatial distribution map

The most conventional way to determine the interplanar spacing within an atom probe reconstruction is the spatial distribution map although there are two alternatives. The first alternative is to use the distance histogram from the POE process, which is essentially a SDM limited to one analysis point centered on the extracted plane [2]. A second option is used in crystallography-mediated reconstruction (CMR) and relies on mean-shift clustering to identify each atomic plane within the ROI [23, 22]. Once each planes mean position is identified their orientation is corrected for and the average interplanar spacing is found. While effective mean-shift clustering is less developed as a technique when compared to spatial distribution maps and the distance histogram approach has limited count statistics. Thus, as shown in figure 5.4 a standard SDM is used to calculate the interplanar spacing once the data has been reoriented using POE.

From a SDM the interplanar spacing is defined as the average distance between the local maxima. This is conventionally performed using parameterized peak search algorithms based on the full width half max (FWHM) or difference in subsequent extrema [40, 85]. Inspired by DF-Fit a parameterless method is introduced to extract the extrema based on the residual of the best fit parabola [55]. In Haley, Bagot, and Moody [55] it was recognized that fitting a parabola to a calibrated SDM results in a parabola that matches the average value over each peaks resulting in areas of under-estimation and over-estimation which corresponding to the peaks and valleys present in the SDM.
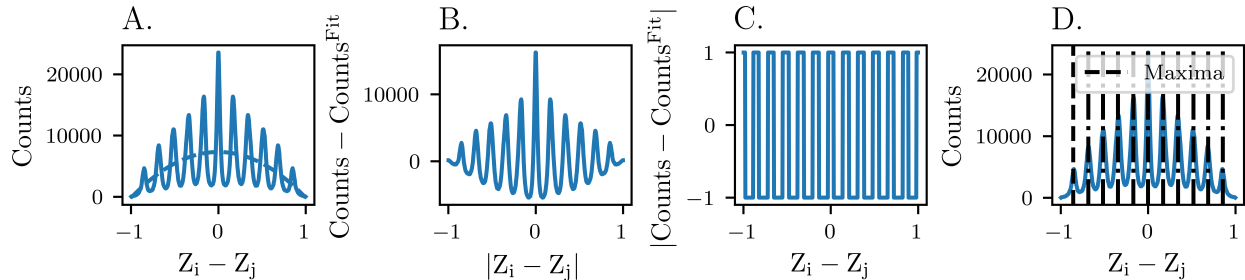
Figure 5.5: Peak Extraction process. Subfigure A. contains the initial SDM (spatial distribution map) and parabola fit while subfigure B. shows the residuals of the fit. The signed residuals are presented in C, while the extracted maxima are plotted alongside the initial SDM in D.

Making use of the residuals does not requires the magnitudes but purely the sign of each value which when plotted in figure 5.5 returns -1 for the valleys and 1 for each peak. An absolute difference in two subsequent signs of 2 indicates a boundary between two extrema. From each set of boundaries the midpoint can be taken as an approximate location of the extrema. A more accurate estimate can be found by taking the maxima/minima within these bounds and a gaussian mixture-model could be used to provide the most accurate estimate at computational cost. Finally, with the maxima known the interplanar spacing is defined as the mean separation between subsequent maxima with an error corresponding to the standard deviation of the separation.

Curvature calibration

As opposed to the methods described by Alec et al for crystal mediated reconstructions utilizing DF-Fit to estimate curvature and thus calibrate ξ we instead make use of specimen specific features [55, 23, 22]. In the case of grown thin films on a planar substrate, the curvature is known to be flat and the isotopically enriched region makes for an ideal calibration portion of the data as they specimen should have a constant evaporation field and thus the curvature of either interface is appropriate for conventional curvature calibrations. However, we propose instead to fit a parabaloid, equation 5.1c, to the point cloud composed of the enriched isotopes instead of either interface.

Doing so makes the approach more generalizable and robust when compared to using an interface and will prioritize regions of the data with higher isotopic density. This prioritization diminishes the need for explicit filtration of the isotope from the non-enriched portion of the dataset. If increased accuracy is required the data points could be weighted inversely proportional to the voronoi volume further biasing the fitting process to the high density

thin film region.

$$z = \frac{x^2}{a^2} + \frac{y^2}{b^2} \tag{5.1a}$$

$$= S \cdot \left(\frac{(x - x_0)^2}{xs^2} + \frac{(y - y_0)^2}{ys^2} \right) + C \tag{5.1b}$$

$$= \left(\frac{(x - x_0)^2}{xs} + \frac{(y - y_0)^2}{ys} \right) + C \tag{5.1c}$$

Here the base equation for a parabaloid, 5.1a, is generalized to account for a shifted maxima through (x_0, y_0, C) and a variable concavity indicated by the sign of S. Note however that these equations are only relevant for elliptic parabaloids due to each term having the same sign. The original scaling factors (a, b) can be reclaimed through (xs, ys, S) as shown below.

$$a = \frac{xs}{\sqrt{|S|}} \tag{5.2}$$

$$b = \frac{ys}{\sqrt{|S|}} \tag{5.3}$$

Once the best-fit parabaloid has been identified the gaussian and mean curvatures, presented in equations 5.4 and 5.5, are used to characterize the curvature of the film. Fixing the field factor and then minimizing the curvature over many ξ then determines the optimal compression factor conditioned on the field factor.

$$K(u, v, a, b) = \frac{4}{a^2 b^2 \left(1 + \frac{4u^2}{a^4} + \frac{4v^2}{b^4} \right)^2} \tag{5.4}$$

$$H(u, v, a, b) = \frac{a^2 + b^2 + \frac{4u^2}{a^2} + \frac{4v^2}{b^2}}{a^2 b^2 \left(1 + \frac{4u^2}{a^4} + \frac{4v^2}{b^4} \right)^{1/3}} \tag{5.5}$$

Both of the provided curvature equations indicate a pointwise curvature at point (u, v) and are maximized at the origin of the parabaloid. It should also be noted that neither formulae are scale invariant. To provide a consistent comparison among multiple ξ the depth coordinate of the reconstruction stack is scaled to $[0, 100]$ and the (X, Y) coordinates are scaled according to (X^{det}, Y^{det}) using min-max scaling routines. Furthermore the curvature is always estimated at the origin s.t. the gaussian and mean curvatures are maximized for a given reconstruction.
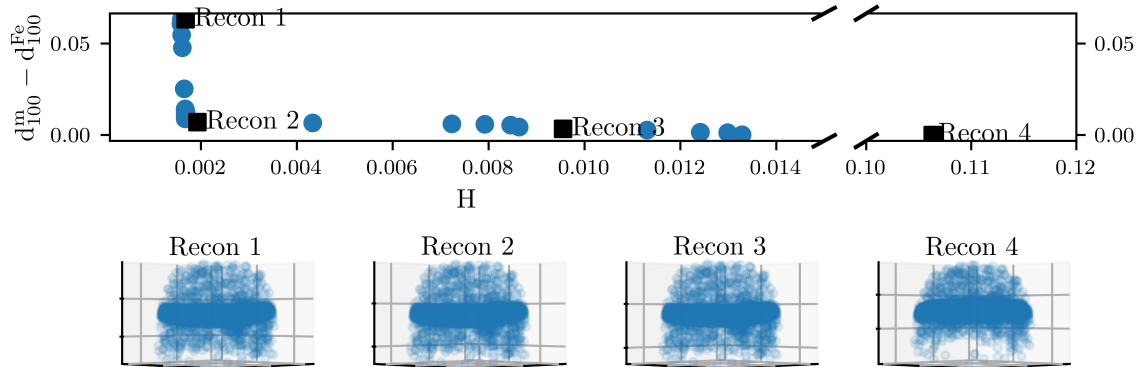
Figure 5.6: Reconstructions along the Pareto front, the set of non-dominated solutions. Recon 1 is the solution with minimal curvature, but has the largest difference in the interplanar spacing while Recon 4 minimizes the difference in interplanar spacing at the cost of curvature. Recon 2 and 3 present reconstructions with a balance of minimal curvature and correct interplanar spacing.

Multiobjective optimization

With the two objective functions defined only the optimization method is left to be defined. In the ideal case it should be enough to first optimize k_f such that the interplanar spacing is accurate followed by a subsequent minimization of curvature to select ξ. However, the interplanar spacing and curvature are functions of both parameters and so the second calibration step is not guarantied to preserve the results of the first. One possible solution is to then optimize each function in an iterative fashion until the parameters converge. Neither convergence nor the existence of a single local minima with respect to both objective is guarantied. Thus this problem falls under the purview of multi-objective optimization routines. [88, 8]

The goal of multi-objective optimization is to identify a pareto front, a set non-dominated solutions, instead of a single optimal solution. Where a "non-dominated solution is one in which no one objective function can be improved without a simultaneous detriment to at least one of the other objectives" [88]. The majority of optimization routines rely on evolutionary or swarm-based approaches to identify the pareto front [135, 20]. In this work the Pymoo python package is employed to identify the pareto front, an example of which is provided in figure 5.6 alongside possible reconstructions. Pymoo provides a selection of evolutionary algorithms, although in this work U-NSGA-III is used as it is especially efficient for problems with few objective functions as opposed to those optimized for many-objective problems [8, 108].

Multi-criteria decision making (MCDM)

As finding the pareto set is insufficient to select a singular (ξ, k_f) for the reconstruction a decision criterion must be introduced to select the ideal reconstruction from the pareto set. A detailed discussion on possible decision criterion is presented in Wang and Rangaiah [123]. Of note are the TOPSIS protocol, which is one of the most commonly used methods, and the GRA protocol. GRA has the advantage of being parameterless while TOPSIS requires user defined weights to indicate the priority of each objective function. A non-parametric version of TOPSIS can be accessed by setting the weights to 1 for each objective however so user interaction is not inherently required.

TOPSIS, technique for order of preference by similarity to ideal solution, works by first constructing a best-case, A_b, and worst-case scenario, A_w. For a minimization problem A_b is defined as the minimum value for each objective observed in the pareto-front. It follows that A_w is then the maximum values of the pareto-front. Given these two solutions the goal of TOPSIS is to minimize the distance from A_b and maximize the distance from A_w. Let C indicate a costs matrix of shape (m, n) where m indicates the number of pareto sets and n the number of objective function. TOPSIS then begins by normalizing and weighting the cost matrix as in equations 5.6 and 5.7 where w indicates the function weights.

$$C_{ij}^{norm} = \frac{C_{ij}}{\sqrt{\sum_{k=1}^{m} C_{kj}^2}} \tag{5.6}$$

$$C^{weight} = C^{norm} \cdot w \tag{5.7}$$

$$\tag{5.8}$$

Note that equation 5.6 describes vector normalization according to the original description of TOPSIS as in Hwang and Yoon [60]; for a detailed discussion on alternative normalization schemes see Vafaei, Ribeiro, and Camarinha-Matos [121]. Once weighted the reference solutions and the distances to each solution within the pareto front are defined below.

$$A_w = \{max(C_j^{weight}|j = 1, , ..., n\} \tag{5.9}$$

$$A_b = \{min(C_j^{weight}|j = 1, , ..., n\} \tag{5.10}$$

$$D_{iw} = \sqrt{\sum_{j=1}^{n}(C^{weight} - A_w)^2} \tag{5.11}$$

$$D_{ib} = \sqrt{\sum_{j=1}^{n}(C^{weight} - A_b)^2} \tag{5.12}$$

Finally a similarity metric, s_i, is defined in equation 5.13 to indicate the relative proximity of a pareto solution to the ideal and non-ideal solutions. The pareto solution which maximizes

this metric is considered to be optimal [60].

$$s_i = \frac{D_i w}{D_{iw} + D_{ib}} \tag{5.13}$$

As previously mentioned GRA, gray relational analysis, is a non-parameterized alternative to TOPSIS which compares the pareto solutions to an ideal solution and neglects to consider a non-ideal solution. GRA starts similarly to TOPSIS in that the costs matrices are first normalized but instead of vector normalization min-max scaling is performed as in equation 5.14 for a minimization routine.

$$C_{ij}^{GRA} = \frac{max_i(C_{ij}) - C_{ij}}{max_i(C_{ij}) - min_i(C_{ij})} \tag{5.14}$$

The reference point for each objective and the difference from the pareto solutions are then defined according to equations 5.15 and 5.16.

$$A_j^{GRA} = max_i(F_{ij}) \tag{5.15}$$

$$\Delta F_{ij} = |A_j^{GRA} - F_{ij}| \tag{5.16}$$

From this point the gray relational coefficient, GRC, is defined below such that the maxima indicates the optimal pareto solution.

$$GRC_i = \frac{1}{m} \sum_{j=1}^{n} \frac{min(\Delta F_{ij}) + max(\Delta F_{ij})}{\Delta F_{ij} + max(\Delta F_{ij})} \tag{5.17}$$

Our analysis indicates that both GRA and unweighted TOPSIS identify the same optimal solution of $(1.050, 3.074)$ corresponding to Recon 2 in figure 5.6. Given that two of the three objective functions provide a measure of curvature the following weights, $[0.25, 0.25, 0.5]$, were provided to TOPSIS to place a higher emphasis on the interplanar spacing resulting. This weighting ensures the total influence of curvature and interplanar spacing are equivalent and results in an estimate of $(1.073, 3.098)$ depicted in figure 5.6.

Calibration uncertainty

Neither the multiobjective optimization routines nor the pareto-optimal selection methods employed in this work do not provide the error estimates required to perform error propagation. Thus, a method to estimate the uncertainty of ξ, k_f, or preferably both must be designed. Thankfully, an error bound for the interplanar spacing can be estimated from the SDM as long as a minimum of three peaks are observed. As for the curvature estimate it would be possible to perform linear error propagation for the gaussian and mean curvature using the error bounds on the best-fit parabaloid's coefficients. However, Pymoo does not support inclusive of uncertainty estimates for the objective functions thus error must be incorporated after identification of the pareto set.

Given $[Var(K_i), Var(H_i), Var(D_i^{hkl})]$ the first approach to quantify the error of the calibration utilizes monte-carlo error propagation as described in section 2.3. Assuming K, H, and D^{hkl} follow normal distributions each pareto solution's objective functions would be perturbed according to the corresponding variance. Once the perturbed pareto set is generated the GRA and TOPSIS protocol would be used to find the pareto optimal solution and the corresponding (ξ, k_f) recorded. This process would then be repeated many times and the calibrated values expressed as the mean and standard deviation of the stored (ξ, k_f). Note, that these estimates are correlated and thus violate the assumptions of reconstruction error propagation detailed in section 3.

As an alternative linear error propagation can be performed using $Var(D_i^{hkl})$ and the following empirical relationship between D^{hkl}, k_f, and ξ [40, 23].

$$D^{hkl} \propto \left(\frac{k_f}{\xi} \right)^2 \tag{5.18a}$$

$$D^{hkl} = a \left(\frac{k_f}{\xi} \right)^2 + b \tag{5.18b}$$

Where a indicates the proportionality constant and b a constant term which are solved by fitting a linear regression model with $(k_f/\xi)^2$ and D^{hkl} as the independent and dependent variables. The model is specifically fit to a subset of the pareto front excluding the optimal solution from 5.1 corresponding to a (ξ, k_f) of $(1.073, 3.098)$. To account for the variance in D_{hkl} the subset is weighted according to the inverse of the variance as specified in Seabold and Perktold [107]. According to the weighted linear regression shown 5.7 the proportionality constant is equal to $0.016 \pm 2e\text{--}4$ and the intercept is equal to $0.126 \pm 2e\text{--}3$. The covariance of a and b is further estimated to be $-3.61e\text{--}7$ indicating that errors have an inverse relationship. Equation 5.18b is subsequently rearranged below to solve for k_f as a function of ξ, D^{hkl}, a, and b.

$$k_f = \xi \sqrt{\frac{D^{hkl} - b}{a}} \tag{5.19}$$

Given that $Var(D_i^{hkl})$ is known from the calibration process and the weighted regression provides a covariance matrix for a and b an estimate of possible k_f values which would produce the measured interplanar spacing can be determined through application of linear error propagation. The partial derivatives for equation 5.19 are defined in equations 5.20 through 5.23 and the complete variance equation is provided in equation 5.24.
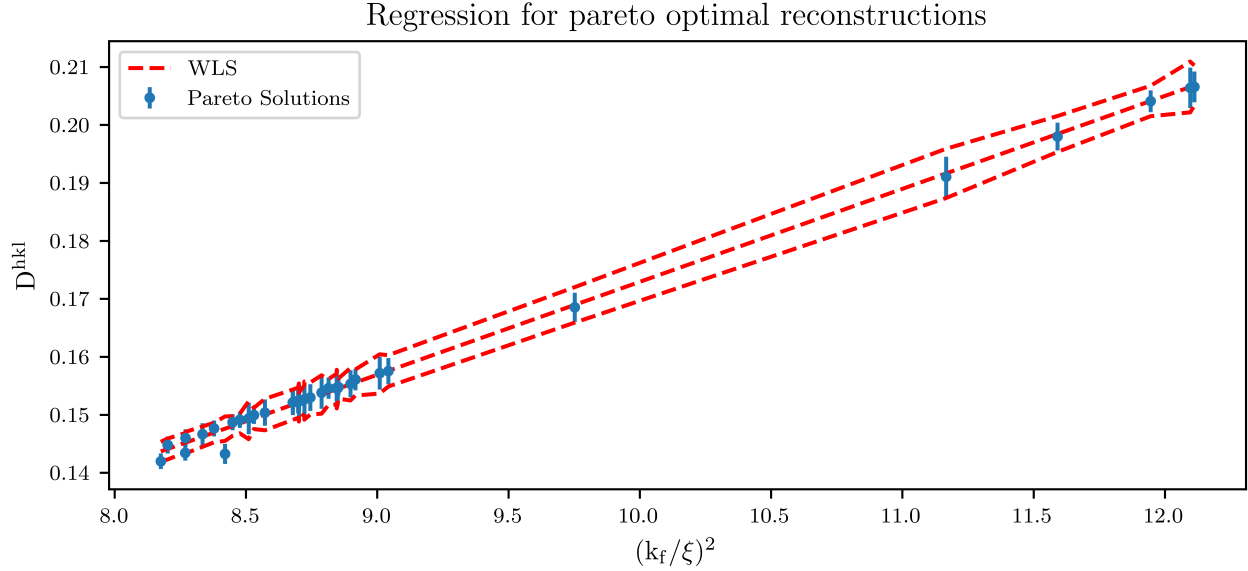
Figure 5.7: Weighted linear regression along the pareto front describing D^{hkl} as a function of ξ, the image compression factor, and k_f, the field factor. The red dashed lines indicate the regression and its confidence intervals, and the error bars are the 1σ.

$$\frac{\partial k_f}{\partial \xi} = \left(\frac{D^{hkl} - b}{a} \right)^{1/2} \tag{5.20}$$

$$\frac{\partial k_f}{\partial a} = -\frac{\xi}{2a} \left(\frac{D - b}{a} \right)^{1/2} \tag{5.22}$$

$$\frac{\partial k_f}{\partial D^{hkl}} = \frac{\xi}{2a} \left(\frac{D - b}{a} \right)^{-1/2} \tag{5.21}$$

$$\frac{\partial k_f}{\partial b} = -\frac{\xi}{2a} \left(\frac{D - b}{a} \right)^{-1/2} \tag{5.23}$$

$$
\begin{aligned}
Var(k_f) = & \left(\frac{D^{hkl} - b}{a} \right) Var(\xi) + \left(\frac{\xi^2}{4a} \cdot \frac{1}{D^{hkl} - b} \right) Var(D^{hkl}) \\
& + \left(\frac{\xi^2}{4a^3} \cdot (D^{hkl} - b) \right) Var(a) + \left(\frac{\xi^2}{4a} \cdot \frac{1}{D^{hkl} - b} \right) Var(b) \\
& + \left(\frac{\xi^2}{4a^2} \right) cov(a, b)
\end{aligned}
\tag{5.24}
$$

The same process can be repeated to find $Var(\xi)$ as a function of $Var(k_f)$ and $Var(D^{hkl})$ resulting in an estimate of (1.073 ± 0.010) which is a 0.965% error. However due to the interdependence of $Var(\xi)$ and $Var(k_f)$ an estimate of both cannot be provided simultaneously. When used in conjunction with reconstruction error propagation ξ is assumed to have zero error and $Var(k_f)$ is provided as an input. $Var(k_f)$ is chosen instead of $Var(\xi)$ as the field factor is expected to have a larger influence on the pointwise spatial uncertainty. Combining

this process with the results of the calibration procedure presented in 5.1 provides the following reconstruction parameter estimates, $(1.073\pm0, 3.098\pm0.030)$, given that $\sigma_{D^{hkl}} = 1.91e\text{--}3$. The percent error on k_f is then only 0.968% for this calibration.

5.2 Uncertainty quantification

Quantification of the reconstruction error is performed in two fashions; the first of which assesses the absolute sensitivity of the reconstruction to each parameter, by assuming a unit variance, while the second assumes a uniform percent variance in order to estimate the scaling behavior of the variance with respect to the final ion positions. Furthermore, it is necessary to consider the percent error scenario as the applied voltages can reach values of $8kV$ and there can be upwards of 50 ionic species with unique volumes. For both V and Ω then a singular variance parameter is insufficient to describe the true error where as a percent error would allow the analysis to account for the range of values by automatically scaling the variance given to the error propagation equations.

Sensitivity

Starting with sensitivity the two prevailing paradigms are local sensitivity analysis (LSA) and global sensitivity analysis (GSA) [102]. LSA strictly defines the sensitivity of a response variable as the slope with respect to it's inputs (U), letting X^{Bas} represent the response variable this corresponds to the partial derivative as in 5.25.

$$S(X_i^{Bas}, U) = \frac{\delta X_i^{Bas}}{\delta U} \text{ for U in } (F, k_f, \xi, L, \eta, X_i^{det}, Y_i^{det}, V_i, \Omega_i) \tag{5.25}$$

Because S_U, the sensitivity coefficient, corresponds to the partial derivative the reconstruction's sensitivity can be calculated by providing the reconstruction program a variance of one for the variable of interest. Under this constraint on the variance it can be shown that:

$$Var(X^{Bas}|Var(U) = 1) = \left(\frac{\delta X^{Bas}}{\delta U}\right)^2 = S^2(X_i^{Bas}, U) \tag{5.26}$$

Extending LSA to account for interactions between variables requires a computationally expensive evaluation of higher order partial derivatives for all possible permutations of U. However, the presence of interactions can be found by comparing the sum of the squared sensitivities to $Var(X_i^{Bas}|Var(u) = 1$ for u in U) which represents the variance of X_i^{Bas} evaluated with a unit variance for all possible parameters. If $\sum_{\text{u in U}} S(X_i^{Bas}, U) < Var(X_i^{Bas}|Var(u) = 1$ for u in U) then there are negatively correlated variables while a larger summation indicates positive correlations.

While LSA provides a rigorous definition of sensitivity it is inadequate to characterize the sensitivity for variables which exist over a larger domain. Global measures, such as Sobol indices, attempt to generalize results over all of the factor space but lack a unique

definition of sensitivity [102, 111]. In the case of atom probe it would be beneficial to apply GSA to the detector coordinates and voltages as they occupy a large range of values within a reconstruction. However, we are predominantly concerned with the pointwise error of individual ions and thus rely only on LSA. A global understanding of sensitivity is instead achieved by analyzing how the sensitivity varies with respect to the spatial position of the ions.

Local sensitivity analysis

In order to visualize the sensitivity as a function of position in the reconstruction a series of subsets within the reconstruction are selected. To measure the impact on the (X, Y) coordinates the first ROI is taken with respect to the Z coordinate and is selected for Z in $[-25.9, -23.6]$ such that the thin film is contained. The variances for this slice is presented in figure 5.8, A. through D. Next, a thin strip is selected within the slice to isolate a specific range of X or Y coordinates. In the case of the sensitivity of X and Y the strip is selected to minimize the possible ranges of the Y coordinate, and thus Y^{det}, for analysis of X and vice versa as the X does not depend on Y^{det} in the Bas reconstruction. The depth correction, dz', is dependent on both sets of detector coordinates however and so instead an ROI rotated 45° with respect to the origin is selected ensuring that both coordinates have an equal impact on $Var(dz')$. For visual consistency the same ROI is used for $\sum dz_j$ despite it being independent of both X^{det} and Y^{det}. The sensitivities with respect to the four most influential variables is then provided in figure 5.8, E. through H.

From this figure we see that $Var(X)$ and $Var(Y)$ are maximized when the magnitudes are maximized resulting in asymmetric variance. $Var(dz')$ and $Var(\sum dz_j)$ possess symmetric variance about the origin instead and in the case of $Var(dz')$ is maximized at the edges of the detector. Despite $Var(\sum dz_j)$ being independent of the detector coordinates we find that there is a relationship between variance and (X, Y) with a lower variance measured at the reconstruction's edge. This is likely due to the voltage as field evaporation requires higher voltages at the center of the reconstruction due to blunting of prior evaporation events.

Further conclusions are drawn from the sensitivity figures, E. through H., where it is observed that X, Y, and dz' are most sensitive to X^{det} and Y^{det} at the reconstruction's center implying that the higher variance at the specimen edge is not due to the detector coordinates as one might expect. As the distance from the center increases we observe that ξ is the most influential parameter followed by k_f. F is then found to be the least influential of these four parameters. $Var(\sum dz_j)$ is observed to be most sensitive to the ionic volume estimates, Ω, followed by the efficiency, η, image compression factor, ξ, and field factor, k_f. The normalized sensitivities are not observed to have a strong association with spatial position.

The same style of analysis is repeated with respect to depth, however the ROI selection process is altered to minimize any possible effects of (X, Y). First, a cylindrical shell is extracted with a minimum and maximum radius corresponding to 7 and 8 nm, one half of this shell is then unfolded in figure 5.9, A. through D. In the case of $Var(X^{Bas})$ the half-shell

Figure 5.8: Total variance of X, Y, dz', and $\sum dz_j$ as a function of (X, Y) coordinates indicated by figures; A, B, C, and D. Figures E through H present the sensitivity normalized by total variance for the four most influential parameters in the Bas reconstruction. Data is collected within the horizontal slice bounded by depths of -25.9 and -23.6 nm.

Figure 5.9: Total variance of X, Y, dz', and $\sum dz_j$ as a function of Z coordinate indicated by figures; A, B, C, and D. Figures E through H present the sensitivity normalized by total variance for the four most influential parameters in the Bas reconstruction. Data is collected within the cylindrical shell bounded by a radius of 7 and 8 nm.

is split along the Y axis and the opposite holds for $Var(Y^{Bas})$. The depth coordinates are split based off the same 45° rotation about the Z axis as was used in figure 5.8. The final ROI used to assess the sensitivity with respect to depth is then centered at 0 for $Var(dz')$ and $Var(\sum dz_j)$ and near 3.5 nm from the center for $Var(X^{Bas})$ and $Var(Y^{Bas})$.

From the top row of figures it is observed that $Var(X)$ and $Var(Y)$ do not strongly

Table 5.1: Sensitivity of the Bas reconstruction coordinates to the input parameters as measured by the average normalized sensitivity, $S^2_*(C,U)$, where C the assessed coordinate with respect to the variable, U, and $*$ indicates normalization by $Var(C)$. Reconstruction parameters and corresponding sensitivity are listed row-wise in order of highest to lowest sensitivity. The final row indicates the sum of the sensitivities for each coordinate, where a value of 1 indicates that there are no unaccounted for interaction terms.

Coord (C)	X^{Bas}		Y^{Bas}		dz'		$\sum dz_j$	
Priority	U	$E[S^2_*(C,U)]$	U	$E[S^2_*(C,U)]$	U	$E[S^2_*(C,U)]$	U	$E[S^2_*(C,U)]$
1	ξ	7.88e–1	ξ	7.83e–1	ξ	9.48e–1	Ω	9.98e–1
2	k_f	1.16e–1	k_f	1.23e–1	k_f	2.67e–2	η	1.11e–3
3	X^{det}	9.46e–2	Y^{det}	9.39e–2	X^{det}	1.27e–2	ξ	5.01e–4
4	F	8.34e–4	F	8.27e–4	Y^{det}	1.25e–2	k_f	6.01e–5
5	L	6.22e–6	L	6.17e–6	F	2.35e–4	F	5.29e–7
6	V	2.56e–8	V	2.56e–8	L	7.48e–6	L	3.95e–09
7	Y^{det}	0.00	X^{det}	0.00	V	7.28e–7	V	1.91e–11
8	Ω	0.00	Ω	0.00	Ω	0.00	Y^{det}	0.00
9	η	0.00	η	0.00	η	0.00	X^{det}	0.00
Sum	1.00	±1.50e–16	1.00	±1.50e–16	1.00	±1.67e–16	1.00	±1.82e–16

depend on depth and instead are maximized as X^{Bas} and Y^{Bas} increase. Opposing these are $Var(dz')$ and $Var(\sum dz_k)$ which are greatly influenced by depth but with differing directionality. $Var(dz')$ is maximized near the beginning of the reconstruction at low depths and low voltages where as $Var(\sum dz_j)$ is maximized at the end of the reconstruction as expected due to the cumulative nature of the coordinate. As for the normalized sensitivities the four most influential parameters are the same for each variance as a function of depth. X, Y, and dz', all sharing share a positive correlation between depth and the sensitivity to the detector coordinates.

Assigning a final ranking of parameter importance for each output is done by measuring the average normalized sensitivity throughout the reconstruction and is presented below in table 5.1. The results of the sensitivity analysis agree with the proposed ranking of variables according to estimates of the partial derivatives in 3.2 with the added benefit of comparing all variables where as originally the relative importance of the sets: $\{k_f, F, V\}$, $\{\xi, L\}$, and $\{X^{det}, Y^{det}\}$ could not be assessed. From these comparisons it is of note that with the exception of $\sum dz_k$ ξ is the most influential parameter and that V is of negligible importance in all cases. Furthermore, the reconstruction is more sensitive to the detector coordinates then previously thought with them generally possessing the third or fourth highest average sensitivity. It bears repeating however that this analysis does not account for the differing magnitudes of error the variables possess as it is equivalent to the scenario where each variable has the same variance, when in reality it is unlikely that all variables even have variance of similar magnitude. For instance consider that the calibrated value for k_f is 3.098 ± 0.030 and has an percent error of approximately 1%; given that F was assigned a value of 33 the error

of 0.030 would be equivalent to 0.01% of F. Furthermore, both V and Ω exist over a wide range of values and a single variance is insufficient to represent their impact. Given these limitations this analysis is extended to consider the variance conditioned upon a percent error.

Percent error analysis

Recalling that the partial derivatives of X^{Bas} or Y^{Bas} with respect to any of the input variables, denoted as U, are equal to $\frac{C}{U}$ for a shared constant, C, consider the scenario where each variable is assigned a percent error, $\sigma_U = pU$. Equation 5.27 implies then that for a given percent error X^{Bas} and Y^{Bas} are equally sensitive to all variables with an exception for the impact of X^{Det} on Y^{Bas} and vice versa.

$$Var(X^{Bas}|Var(U) = (pU)^2) = \left(\frac{\delta X^{Bas}}{\delta U}\right)^2 (pU)^2 = \left(\frac{C}{U}\right)^2 (pU)^2 = C^2 \tag{5.27}$$

This does not apply fully to either dz' or $\sum dz_j$, however there are subsets of variables with equivalent impact. It is expected that the sets (k_f, F, V), (ξ, L), and (X^{Det}, Y^{Det}) effect dz' equally given a percent error, while for $\sum dz_j$ the impact of η is expected to be $1/4$ that of ξ and Ω cannot be predicted succinctly as its the expanded derivatives depends on the frequency of each ionic species. Plotting the results in figure 5.10 validates theses expectations both as a function of (X^{Bas}, Y^{Bas}).

From this we also confirm that $Var(X^{Bas})$ and $Var(Y^{Bas})$ scale in a quadratic fashion with respect to X^{Bas} and Y^{Bas} respectively. Whereas the analysis of $Var(dz')$ along the $45°$ diagonal is best described as a fourth-order polynomial which shows steep increases in variance at the edges of the dataset and while not clearly visible a local maximum near the center surrounded by two local minima. It is also observed that for equal percent errors ξ and L have the largest impact on the variance while the remaining variables have a comparable impact, albeit the datapoints corresponding to X^{Det} and Y^{Det} have a higher degree of scatter. Finally for $\sum dz_j$ the variance is highest at the center and decreases as a function of distance from the center for all variables. Furthermore, the efficiency is found to have the smallest impact, approximately $1/4$ that of ξ and L. There does not however appear to be a large discrepancy between the impacts of $(k_f, F, V, L, \xi, \Omega)$. Differences in $Var(\sum dz_j)$ are expected to be more pronounced for larger specimen depths and so the behaviors with respect to Z^{Bas} are plotted in 5.11.

$Var(X)$, $Var(Y)$, and $Var(dz')$ appear to be equally sensitive to the input variables as in figure 5.10. However while $Var(X)$ and $Var(Y)$ possess relatively constant values irregardless of depth $Var(dz')$ is decreasing instead; standing in contrast to $Var(\sum dz_J)$ which increases exponentially with respect to depth. In the latter's case η is the least influential parameter while (k_f, F, V, L, ξ) are represented as just a single curve. The ionic volume, Ω does not possess uniform behavior from roughly 15 to 20 nm has the largest impact
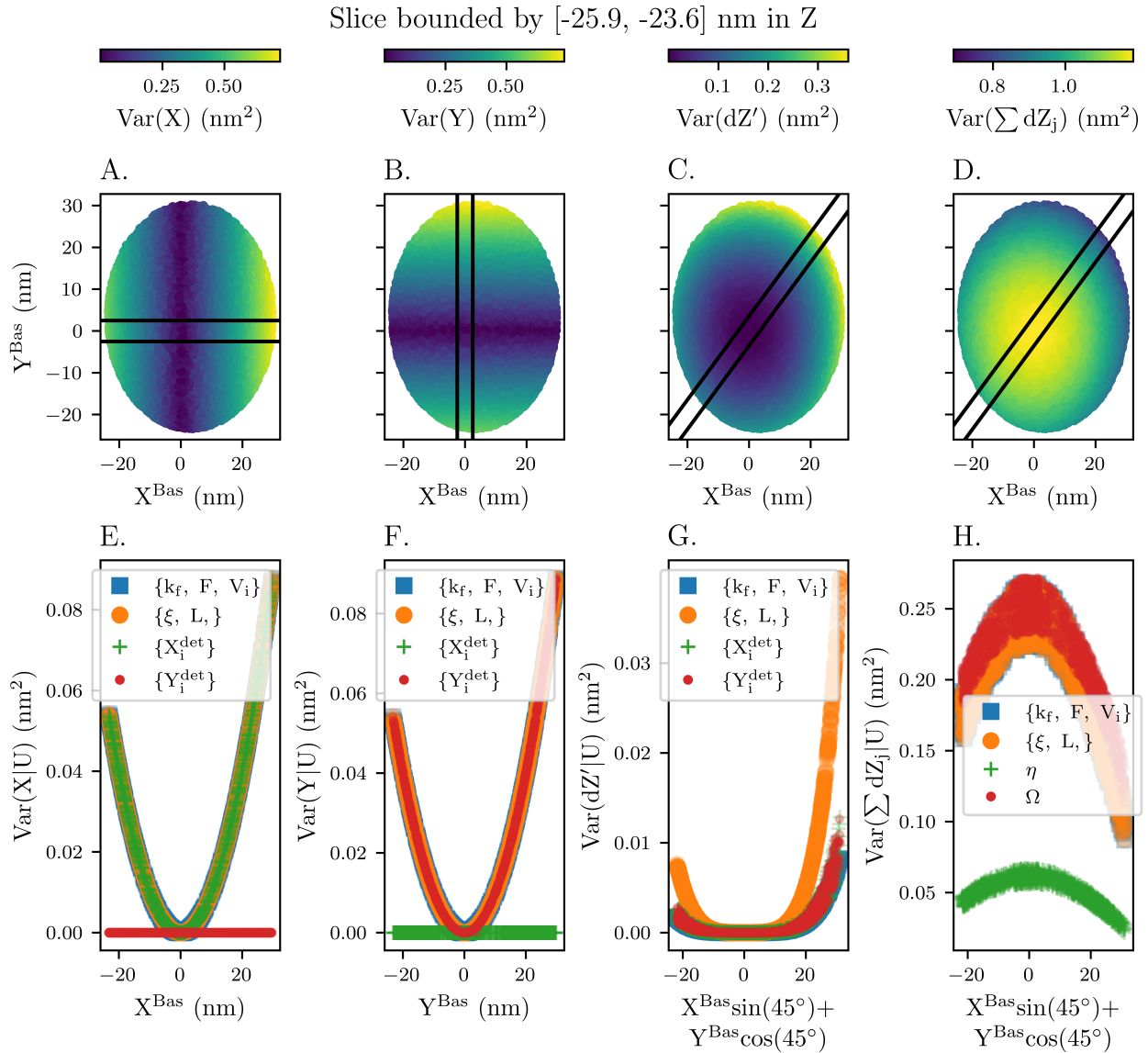
Figure 5.10: Total variance of X, Y, dz', and $\sum dz_j$ as a function of (X, Y) coordinates given by percent errors indicated by figures; A, B, C, and D. Figures E through H present the variance given a uniform percent error in each variable. Data is collected within the horizontal slice bounded by depths of -25.9 and -23.6 nm.

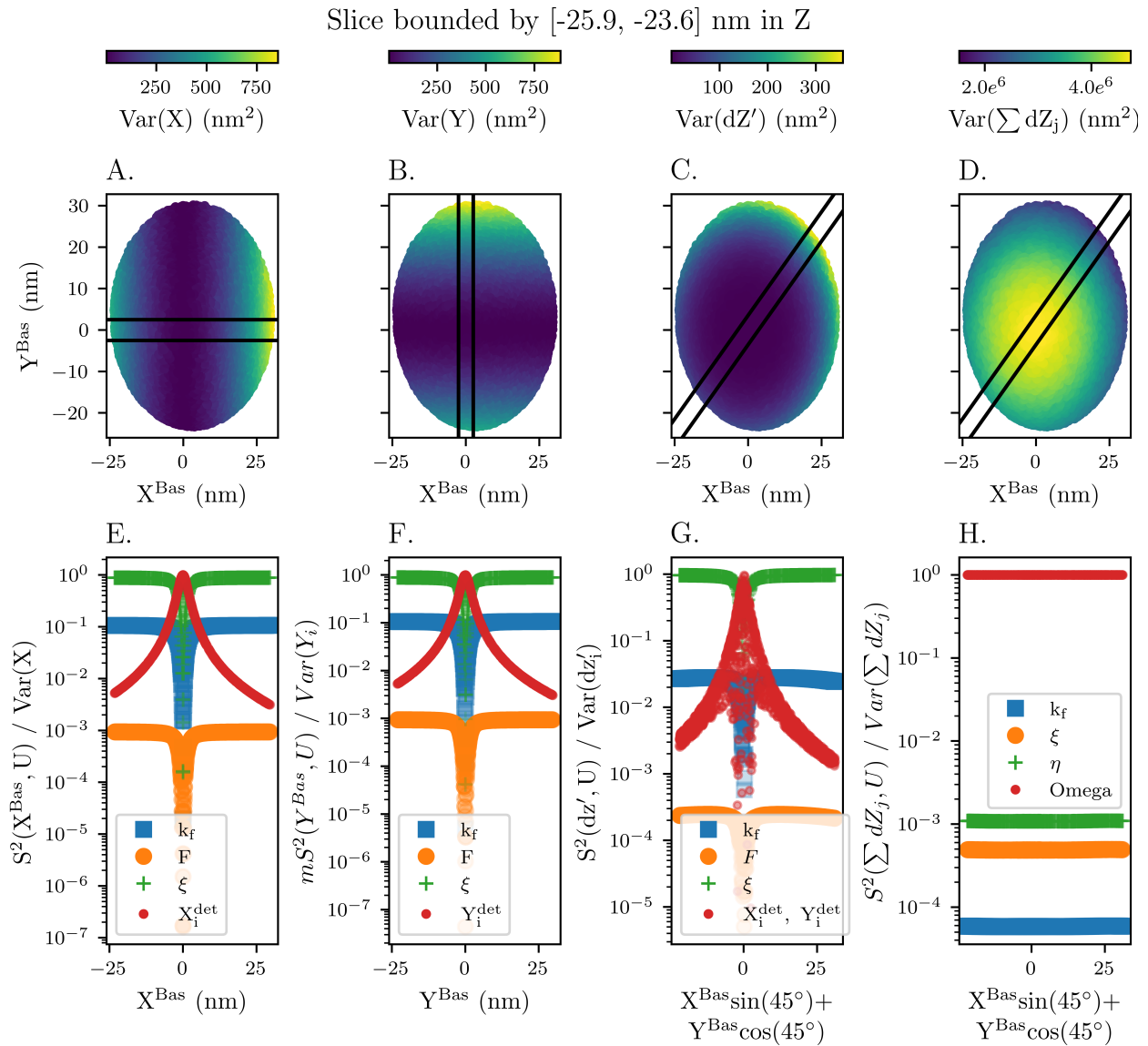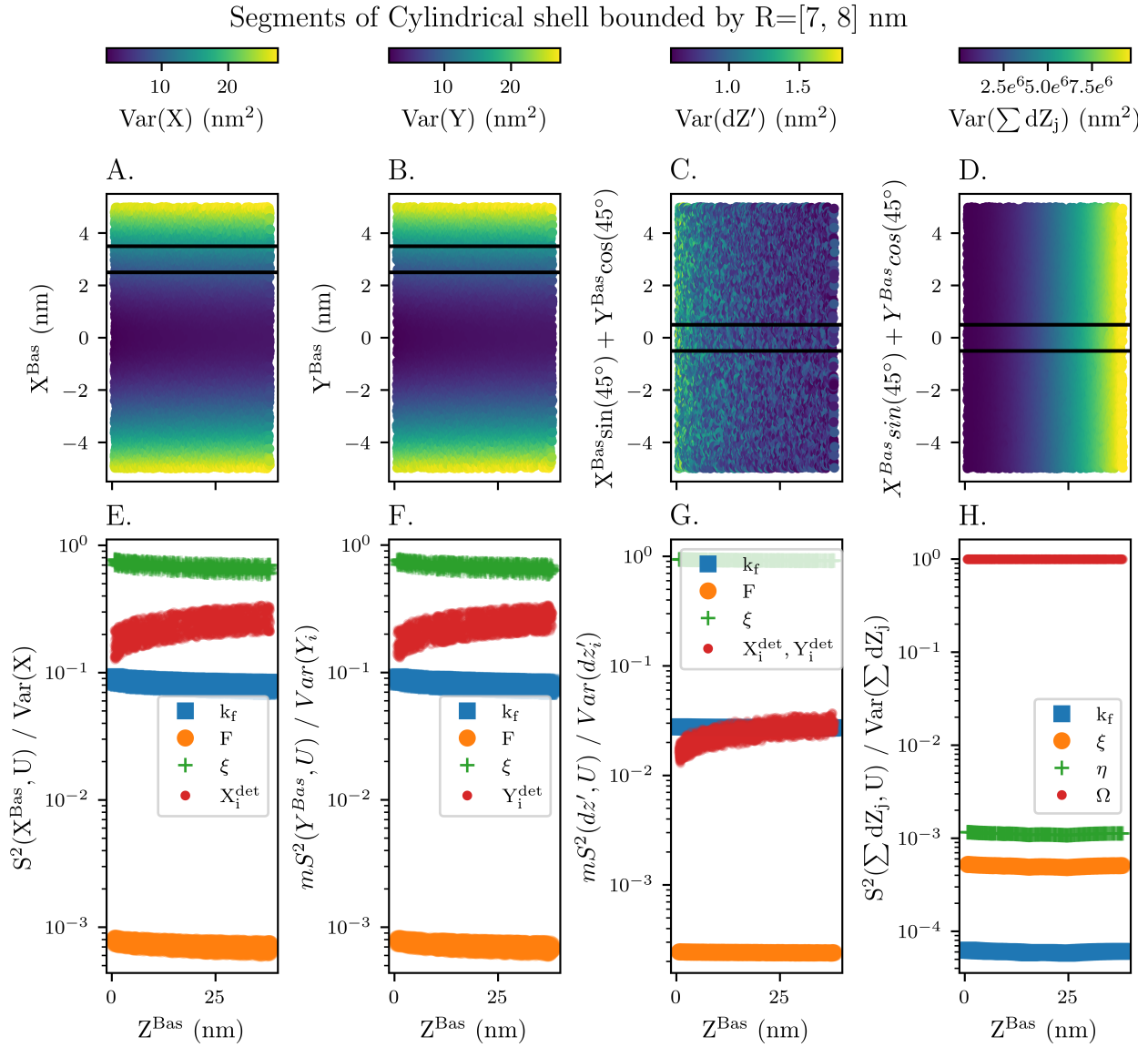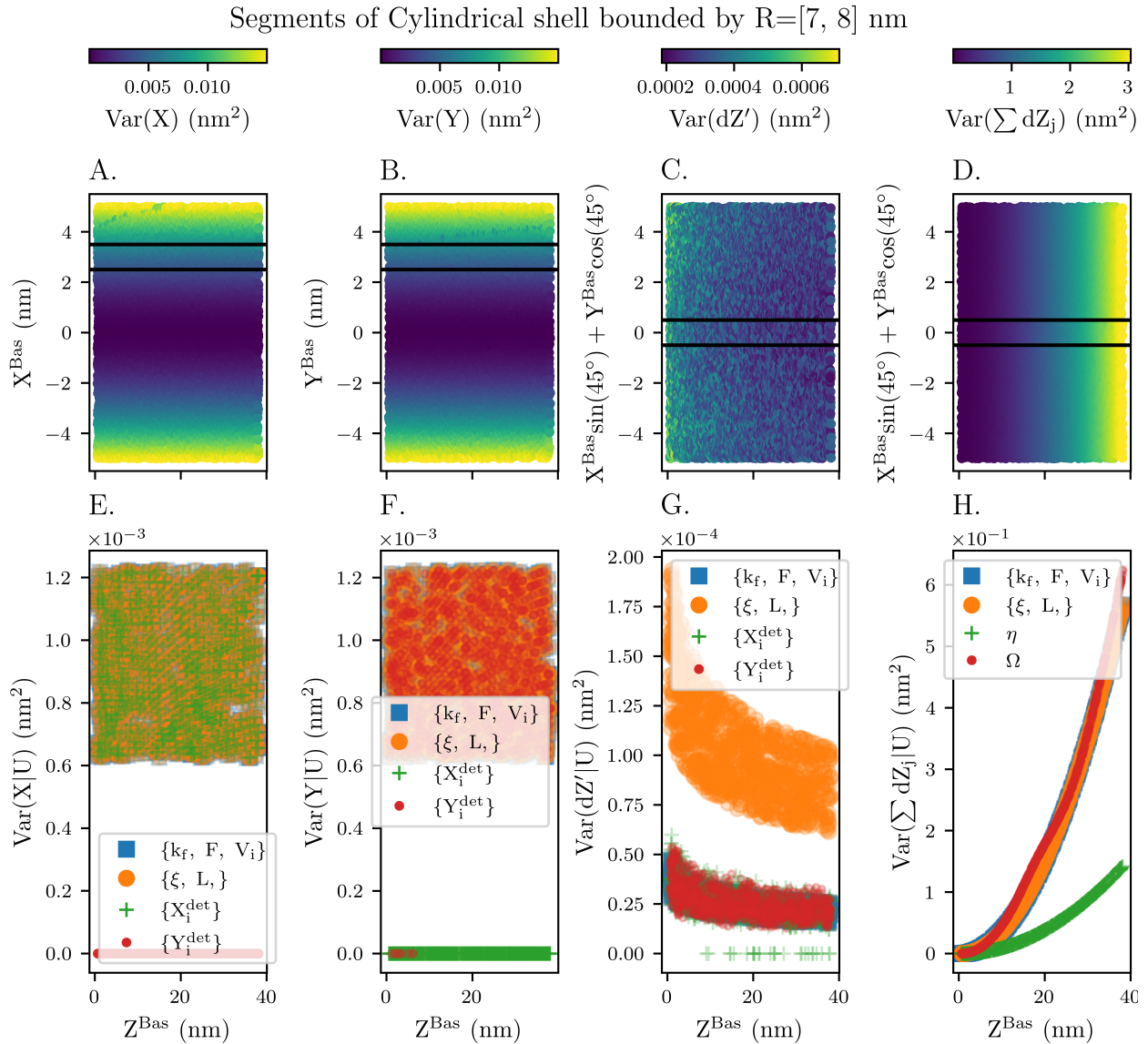Figure 5.11: Total variance given a percent error of X, Y, dz', and $\sum dz_j$ as a function of Z coordinate indicated by figures; A, B, C, and D. Figures E through H present the variance given a uniform percent error in each variable. Data is collected within the cylindrical shell bounded by a radius of 7 and 8 nm.

before appearing to overlap with (k_f, F, V, L, ξ) prior to diverging at 30 nm. The region from 20 to 30 nm corresponds roughly to the thin film and it is unclear if this behavior is due solely to changes in the composition or related to the calibration process.

5.3 Conclusions

In summary it was demonstrated that performing multiobjective optimization over a combination of conventional interplanar spacing calibration techniques and non-conventional global curvature estimates was sufficient to optimize ξ and k_f simultaneously. Furthermore, it was shown that error bounds for either ξ or k_f could be established by fitting equation 5.18b, rewritten below, along the entirety of the pareto front. The optimal values for k_f and ξ were found to be 3.098 ± 0.030 and 1.073 ± 0.010 which correspond to a roughly 1% error in either parameter. This analysis also exposed a limitation of the error propagation equations as the estimate of k_f depends on ξ and vice versa violating the assumptions of 3 that none of the input parameters are correlated.

$$D^{hkl} = a \left(\frac{k_f}{\xi} \right)^2 + b \tag{5.18b}$$

Additionally performing a sensitivity analysis with respect to both a unit variance and a uniform percent variance showed X^{Bas}, Y^{Bas}, and dz' are most sensitive to errors in ξ and k_f as was predicted during the derivations in 3. Noting that dz' only consists of the correction term which places the ion atop the hemispherical cap, it was found that cumulative depth term, $\sum dz_j$, was most sensitive to Ω, η, ξ, and k_f in descending order when considering a unit variance. When instead a percent error was applied the importance of η diminished while the variance due to Ω, ξ, and k_f converged.

When considering entirety of the depth coordinate $Var(\sum dz_j)$ was found to be greater than $Var(dz')$ for all ions implying that $Var(Z^{Bas})$ is dominated by $Var(\sum dz_j)$ neglecting any covariance terms. Additionally, $Var(\sum dz_j)$ was found to be positively correlated with specimen depth such that the position of points near the specimen base are ill-defined in comparison to those at the specimen apex. These final two observations appear to confirm our initial hypothesis, however we had predicted that the positions and properties of features, represented by many ions, would have increasing uncertainty. While it was shown that the variance of an individual ion agreed with our hypothesis we neglected to consider the covariance. Neglecting the covariance between points will result in either an overestimate or underestimate of error dependent upon the sign of the correlation and the explicit calculation. For example, accounting for covariance in differences such as those found in the euclidean distance formula will result in lower estimates of error if the points are positively correlated. A positive correlation is expected to be the case between subsequent ions as the term Z_i^{Bas} can be written as a sum of Z_{i-1}^{Bas} and a depth increment. Further, analysis that computes the covariance between ions is thus necessary to determine if the hypothesis applies to complex features and not individual ions.

Chapter 6

Measurement of epitaxially grown thin films

In this chapter the ion specific analysis from 5 is expanded to large scale structures, the isotopically enriched thin film, and properties, interplanar spacing, present within the BCC Fe specimen. The purpose of error propagation with respect to the interplanar spacing, d_{hkl}, is to identify any biases or discrepancies introduced by the scaling step in the calibration process. While determining the thickness of the thin film and its associated error is relevant to the self-diffusion studies this specimen is apart of. This sample is the as-grown non-oxidized state which serves as a baseline to compare to oxidized atom probe specimen extracted from the same foil. Thus an accurate measurement of the film thickness and understanding of the uncertainties are imperative to determine if the oxidized sample's concentration profiles have statistically meaningful differences from the non-oxidized scenario.

6.1   Monte-Carlo reconstructions

So far in this work linear error propagation has been used to calculate the pointwise error within the atom probe reconstruction and to provide closed form expressions to understand the significance of each reconstruction parameter. At this point, however linear error propagation is insufficient to analyze the uncertainty in either d_{hkl} or the film thickness. This is for two reasons; 1. both measurements are dependent on multiple ions simultaneously and would require calculations of the the all $N \cdot (N-1)$ covariance terms with N equal to $3.6e6$, 2. the iterative and discrete nature of the sub-computations prohibit practical differentiation of the full functions.

Instead a monte-carlo approach which was touched on in 4.2 as an alternative for propagating error in distance calculations and described in 2.3 is employed. Monte-carlo error propagation, MCEP, is one of the most common methods for handling so called black-box type problems, but is also commonly used alongside linear error propagation [3, 75, 33]. For the following applications of MCEP a series of reconstructions are created with fixed

values for the evaporation field, flight length, image compression factor, and efficiency of $\{F : 33.0V/nm, L : 382mm, \xi : 1.073, \eta : 0.36\}$ and the field factor, k_f is represented as a normal distribution with mean of 3.098 and standard deviation of 0.030. The remaining inputs, voltage (V), ionic volume (Ω), X^{det}, and Y^{det} are defined according to the instrument and are assumed to have zero error.

For each reconstruction k_f is sampled from the aforementioned normal distribution and the measured interplanar spacing and film thickness are saved. The mean of these results over all reconstructions is taken as the final measurement and the standard deviation is considered to represent the uncertainty. As an alternative, the deviation of the mean could be taken but this will converge to zero as the number of monte-carlo reconstructions increase and does not provide meaningful information about the spread between the reconstructions.

6.2 Interplanar spacing comparison

Given each monte-carlo reconstruction the same process used in 5.1 is employed to determine the average interplanar spacing as well as each individual difference in peak position. Unlike the calibration procedure however the point cloud is not scaled to a standard size and dimension. This was required during the calibration because the changing field and image compression factors caused large fluctuations in the point cloud dimensions such that an apriori defined ROI was insufficient for finding the required orientation or interplanar spacing. Standardization of the data was chosen instead of designing a separate calibration procedure for the ROI dimensions. One goal of this analysis is to then compare the interplanar spacing in the non-standardized case and determine if the calibration process produced biased estimates of d_{hkl}.

Monte-Carlo plane orientation extraction

The same hyperparameters were used for the monte-carlo POE process as in the calibration step. As the pole position is dependent on the detector coordinates and not k_f the same pole was extracted for all reconstructions. Here the pole center and radius were defined as $[-3.07, -2.35]$ and 2.5 mm. Given a reconstruction a spherical ROI possessing a 2.5 nm radius was then placed at the mean position of the Fe58 ions contained within the pole. In all cases the elevation angle, Θ, was incremented from $0°$ to $45°$ while the azimuthal angle, ϕ ranged from $-180°$ to $180°$. The step size for both angles was $1°$.

Analysis of $1,000$ monte-carlo simulations provides a set of three distinct (ϕ, Θ) corresponding to $(-180, 0)$, $(58, 1)$, and $(57, 1)$, which are plotted alongside a randomly chosen amplitude map in figure 6.1. The $(-180, 0)$ rotation accounted for 998 of the reconstructions. This indicates that planes within the region of interest remain highly orthogonal to the analysis direction given perturbation in the field factor, k_f. The other two rotations are likely due to minor numerical fluctuations in the intensity map supported by the presence
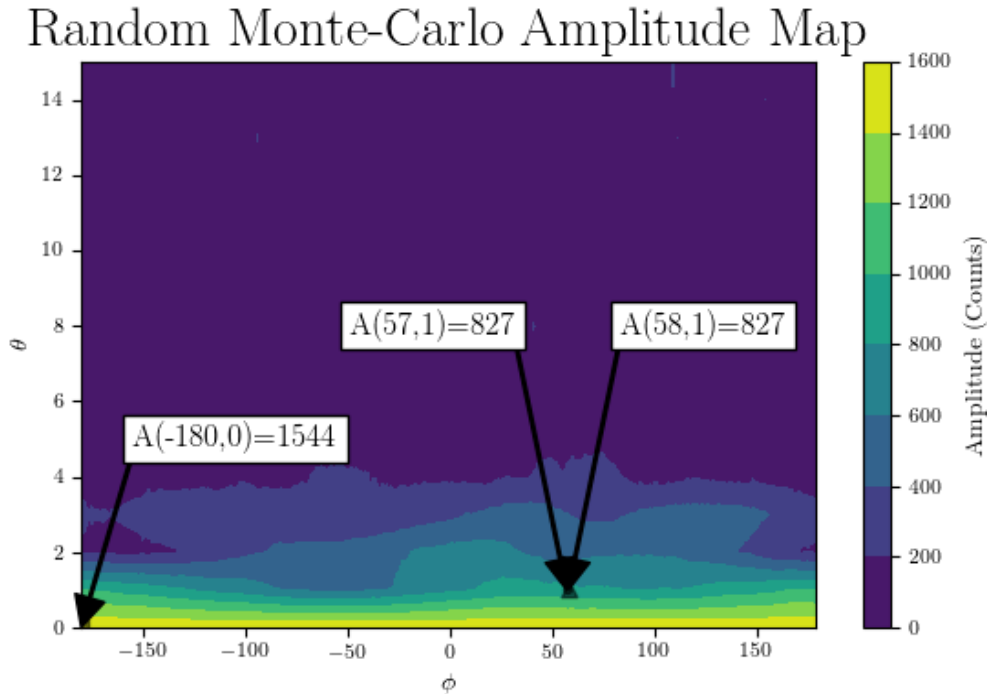
Figure 6.1: Distribution of (ϕ, θ) as determined by plane orientation extraction overlaid atop a randomly chosen amplitude map. There are three unique rotations with a rotation of $(-180°, 0°)$ for 998 reconstructions and a single reconstruction each for $(57°, 1°)$ and $(58°, 1°)$.

of a large band of high intensity values for all possible ϕ. Fixing ϕ the intensity is then inversely proportional to Θ.

Note, that the minimal rotation is expected given that aligning the detector center with the crystallographic pole is a known method to minimize the relative curvature of the planes at the pole. Furthermore, the atom probe specimen was specifically made to be perpendicular to the [1 0 0] planes. Finally, the discrete nature of the grid search is likely the reason for the unique rotation angles, whereas a continuous mapping may have exposed a sub-degree spread.

Monte-Carlo D_{hkl}

The spatial distribution maps, SDM, were generated by placing a one nm spherical ROI about each Fe58 ion in order to preferentially target the thin film. For each reconstruction the the individual peak positions within the SDM were stored alongside the adjacent plane spacing, and the interplanar spacing's mean and standard deviation.

From figure 6.2 thirteen distinct planes, indexed from 0 to 12, are resolved within the spherical ROI. Recall that the lattice parameter is 0.2866 nm for BCC Fe and that the
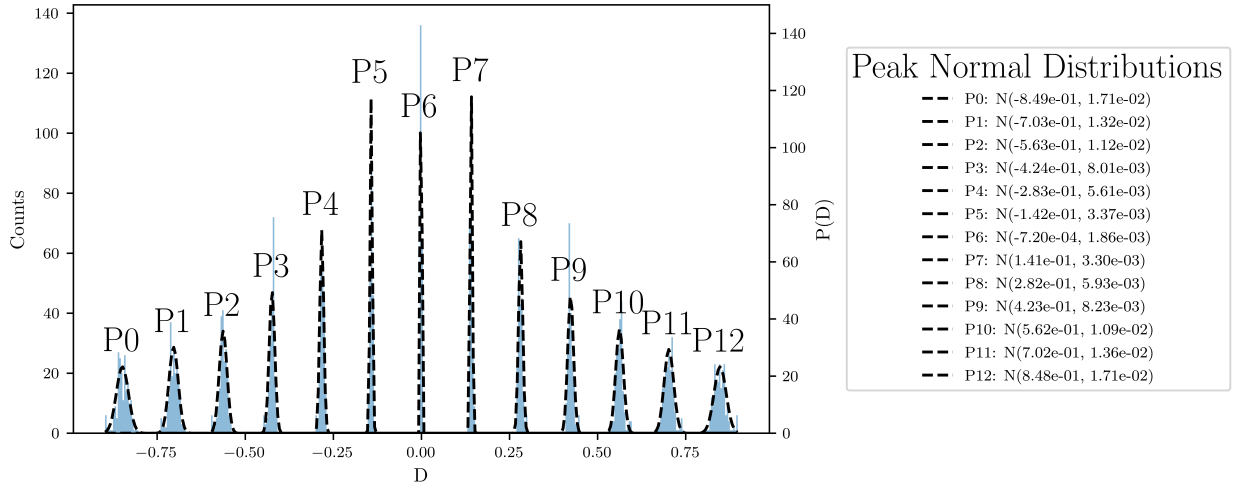
Figure 6.2: Option B. Distribution of thirteen peaks extracted from the spatial distribution maps (SDMs) of 1,000 monte-carlo reconstruction. Each peak, approximating the relative position of an atomic plane, is defined according to a normal distribution, $N(\bar{x}, \sigma)$.

expected interplanar spacing is 0.1433 nm given that the body-centered plane is resolvable. Then it should be possible to resolve fourteen planes within the ROI as it spans a total length of 2 nm. However, as the central peak corresponds to the plane each ion belongs to only thirteen peaks can be observed.

The number of resolved planes and their planes remained constant for all of the reconstructions. Assuming that each peak follows a gaussian distribution the standard deviation increased proportionally with the average distance, D, from the reference ion. Each monte-carlo reconstruction then provided eleven estimates for [1 0 0]. Taking the mean and standard deviation of all $11,000$ estimates then provides final estimate for D_{MC}^{hkl} of $0.142 \pm 4.2e\text{--}3$ nm. Repetition of this analysis while fixing k_f as 3.098 produces an estimate of $0.142 \pm 3.45e\text{--}3$ nm while the as provided reconstruction estimates the spacing to be $0.150 \pm 3.05e\text{--}3$.

The monte-carlo estimates and the fixed field factor estimates are comparable differing only in that the monte-carlo possesses a larger uncertainty as one would expect. However, the PNNL provided reconstruction is less accurate tending toward higher values, but is marginally more precise. According to the calibration procedure the expected value for D_{Cal}^{hkl} was $1.433 \pm 1.91e\text{--}3$. When compared to the prior three measurements we observe the lowest standard deviation and also that the mean value is higher than 0.142 despite the same field factor being used. This discrepancy could be due to the scaling procedure increase the number of peaks within the SDM or biasing the results, however the exact cause is indeterminate.

6.3   Film thickness

Measurement of concentration profile FWHM as a proxy for film thickness

The standard method of measuring the size of features possessing either elemental or isotopic enrichment is to generate a 1D concentration profile orthogonal to the feature surface [40, 74]. This is done under the assumption that the width, often defined as the full width at half maximum or FWHM, of the concentration profile is correlated with the physical properties of the feature of interest. For this experiment the property of interest is the film thickness as a function of lateral position within the reconstruction. Given that the film should be nearly perpendicular to the depth coordinate due to the calibration process a cylindrical ROI centered with the reconstruction is sufficient to measure the film thickness. However, as mentioned during the calibration and interplanar spacing measurements the film orientation is expected to diverge as it approaches reconstruction boundaries. To measure the thickness as a function of radius an annular ROI is used instead of a purely cylindrical one.

Once the ROI is identified the 1D concentration profile is calculated. This is commonly accomplished by generating a histogram of the depth coordinates within the ROI, requiring user input to determine the bin size. For atom probe the bin sizes are often set as a multiple of the lattice parameter or an estimate of the current reconstruction's resolution. Besides errors induced by binning the primary downside to this method is that the histogram produces a discrete estimate. As an alternative kernel density estimates (KDE) can be employed which provide a continuous distribution, but increase the number of required inputs as most methods require both a kernel and an associated bandwidth which is equivalent to the bin size. While there are optimization routines for both bandwidth and bin size the former generally relies on k-fold cross validation and is computationally expensive whereas the later is insufficient for analysis of multimodal distributions. Recent advancements in density estimates have however removed these limitations by optimizing the kernel instead of the bandwidth as demonstrated by fastkde [95, 94].

Despite these advancements this study found that computing the concentration profile using the fastkde method was not cost effective when performed for multiple ROI over many monte-carlo reconstructions. Furthermore, the kernel density estimates are inherently normalized which makes it difficult to calculate ratios of different isotopes. In lieu of this a sliding window estimate was using to leverage the computational simplicity of the histograms while producing a pseudo-continuous measurement of the concentration profile. In this method the equivalent to the bandwidth or bin size is the window size, which was set as a multiple of the lattice parameter.

In figure 6.3 an example of the Fe58 and Fe57 abundance are plotted in the leftmost graph with a span indicating the FWHM with respect to the Fe58 ions. The distributions of these two isotopes show a relative increase in the Fe58 content centered at a depth of -26 nm which corresponds with the thin film. Instead of using purely the Fe58 ions to measure the thickness according to the FWHM, a ratio measurement is presented in the rightmost
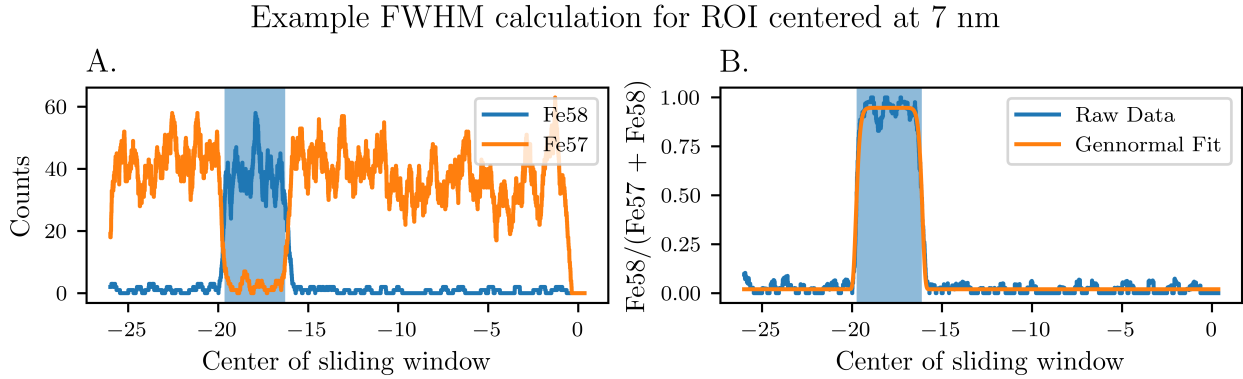
Figure 6.3: Depiction of the sliding-window method for estimating 1D concentration profiles. The estimate is applied to both Fe57 and Fe58 species with the FWHM of the Fe58 profile shown with a vertical span in subfigure A. An example of a relative concentration profile is shown on the right-hand side, subfigure B, alongside a generalized normal, gennormal, fit to the data which is able to accurately capture the tophat profile whereas a normal distribution would result in an artificially sharp apex.

figure. One advantage of this is that the noise levels at the top of the Fe58 enriched region are decreased and the borders of the peak are sharpened. Finally, a generalized normal distribution with background, eq 6.1, is also fit to the data to provide one final estimate of the FWHM. This is done to account for the baseline concentration of Fe58 within the surrounding matrix and when the background is low should agree with the FWHM of the relative measurement.

In this equation β, α, and μ are the parameters inherent to the generalized normal distribution while A and B are the amplitude and background corrections. The shape parameter, β, controls the degree to which the generalized normal approximates its children distributions which consists of normal and Laplacian distributions to name a few. When β is two the distribution approaches a normal whereas one indicates a Laplacian. As β approaches inf the distribution models a uniform distribution. Generally the peak apex flattens as β increases as is observed in figure 6.3. α is the typical scale parameter governing the spread of the distribution and μ is the mean. This function does also contain the gamma function, $\Gamma(1/\beta)$ which serves as a normalizing constant.

$$A \cdot \left(\frac{\beta}{2\alpha\Gamma(1/\beta)} exp \left[-\left(\frac{|x-\mu|}{\alpha} \right)^{\beta} \right] \right) + B \tag{6.1}$$

Measurement of Film thickness with respect to a sliding annular ROI

Following the process outlined above the film thickness is measured for a series of annular ROI with a fixed radial width of 1.433 nm which corresponds to five times the lattice parameter of BCC Fe. When the annuli are compared they are represented as the mean radius of the annulus, for example if the annulus is bound by the radii, 5 and 7 nm, is is described as the $R6$ annulus. Similar to the sliding window estimate for the concentration profile a pseudo-continuous description of the film thickness is produced by incremented the mean radius of the annulus in step sizes of 0.22567 nm. This step size was determined by the number of desired measurements and according to the minimum and maximum radius to probe.

The results of this analysis over 200 reconstructions is provided in figure 6.4 for 100 different annuli. Compared to the monte-carlo interplanar spacing estimate which took four hours to evaluate $1,000$ reconstruction, these calculations took thirteen hours providing a limit on the number of simulations that could be performed. Note that the error bars in the figure denote the 1σ bounds and that while the measurement specific errors had minor fluctuations the average error in the estimates remained fairly constant over all radii. The fitted FWHM error had the least fluctuations and the errors averaged to approximately 0.10 nm regardless of measurement method.

From the figure it can be seen that the initial measurements of the mean film thickness hover in the range of 5.2 to 5.4 nm which the FWHM of the Fe58 isotopes providing the lower bound. These estimates are relatively consistent up to a mean radius of 10 nm at which the measured thickness decreases to a local minima of 5.0 nm for the Fe58 FWHM and a a minima of 5.2 for the gennormal fit. There is a slight recovery in the FWHM values at the mean ROI radius approaches 16 nm, however this is followed by an ever decreasing estimate which drops from an estimate of 5.1 nm for the gennormal fit at a radius of 20 nm to approximately 4.6 nm over a 3 nm change in the mean radius.

Comparison of the three over the sliding roi

There are four possibles causes for this behavior: 1. the true film thickness is not uniform, 2. measurement of the profile over an annulus is insufficient to capture asymmetry induced by the reconstruction, 3. the remaining curvature in the reconstruction is resulting in a non-orthogonal estimate of film thickness, 4. the use of a global compression factor for the reconstruction is resulting in a point cloud compression which is proportional to the radius of the ions. Cause 1 is unlikely as epitaxial film growth generally produces films with a high degree of uniformity. Possibility 2 cannot be ruled out given that the bounds of X^{Bas} and Y^{Bas} are $[-24.9, 32.2]$ and $[-24.732.7]$ nm due to to placement of the detector center at the pole. We consider this an a less probable source of error compared to 3 and 4 however as the maximum annulus radius was set to 23.3 to preempt measurement of an annulus partially populated with ions.

This leaves option 3 and 4, if cause 4 is assumed to be negligible then a non-orthogonal measurement is expected to provide an increase in the FWHM as the signal should be signal should be diluted with a lower peak intensity as only a portion of the ions are appropriately
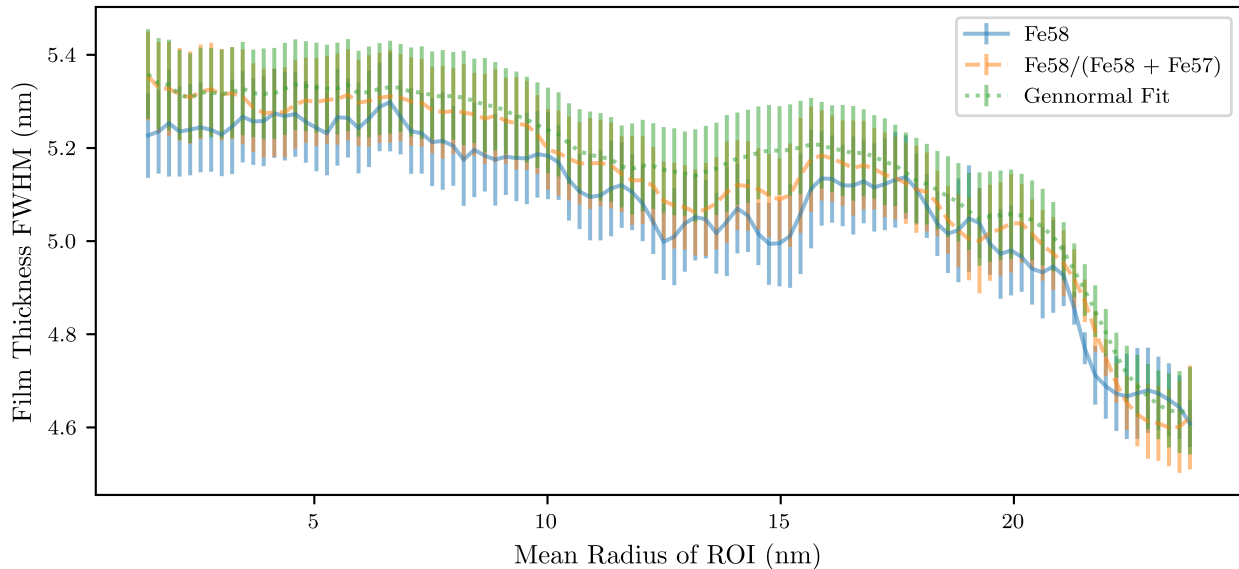
Figure 6.4: The film thickness, measured according to the FWHM of the concentration profiles as a function of mean radius of the annular ROI. The Fe58 profile is depicted in blue while the the relative abundance of Fe58 to all Fe species and its gennormal fit are shown in orange and green respectively. The error bars correspond to 1σ as measured from the monte-carlo reconstructions. As the annulus departs from the reconstruction center the measured thickness decreases gradually until an mean radius of approximately 17 nm at which point the estimate decreases rapidly reaching minimum of 4.6 nm.

aligned and a corresponding larger spread. In extreme cases the spread could manifest as a general increase in the background signal and a decrease in the FWHM, however fitting method should explicitly correct for this. The gennormal FWHM measurement exhibits the same behavior as the other two measurements which should be more susceptible and so while possible this is considered less likely than 4. These causes are not mutually exclusive and we expect some curvature as the multiobjective optimization was unable to ensure that both the curvature and difference from the true interplanar spacing was zero. It is then a possibility that compression within the reconstruction overrides the influence of non-orthogonal measurements. To further probe this behavior we turn our attention to the fit parameters for generalized normal over all annuli in figure 6.5.

Analysis of the gennormal fit parameters

The scale parameter is approximately 14 for the first ROI and decreases steadily as a function of radius to minimum of 4. This indicates that the concentration profile is akin to a tophat kernel near the center of the reconstruction as was observed in figure 6.3 and while it does not reach a true gaussian distribution, with $\beta = 2$, the apex takes on a higher curvature. The scale parameter, α, which also governs shape to a lesser degree does not change as rapidly and remains with a mean value of 2.75 for most radii. There is a local
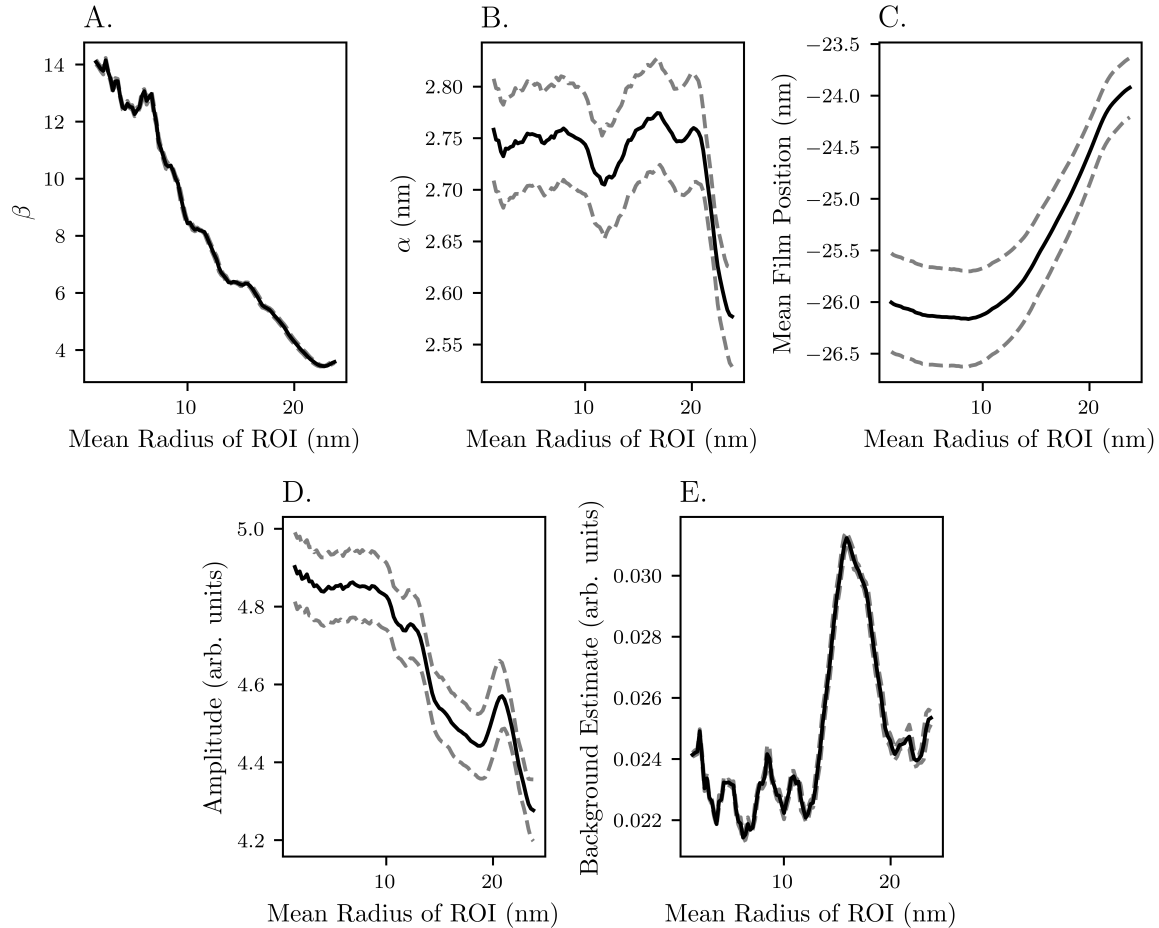
Figure 6.5: Fit parameters of the generalized normal distribution with uniform backgrounds and associated 1σ error bounds as a function of mean ROI radius. Subfigure A. shows the shape parameter, β which is shown to decrease as function of radius approaching a more gaussian distribution starting from a flattop kernel. Subfigure B. measures the scale parameter, α, which averages near a value of 2.75 nm until a radius of 20 nm at which point is decreases rapidly. Subfigure C. depicts the distributions mean which is a proxy for measuring the thin film's center. The mean position reaches a local minimum near -26 nm near a radius of 10 nm prior to increasing to an approximate maxima of -24 nm at a the maximum ROI radius of 23.3 nm. Subfigure D. plots the amplitude, A, which is inversely proportional with radius and generally decreases with the exception of a peak near 20 nm. Subfigure E. depicting the background parameter, B, sits in the 0.22 to 0.24 range until a maxima of 0.032 is reached near a mean radius of 16 with a subsequent drop at 20 nm which corresponds with the peak in amplitude.

minima near a radius of 12.5 nm and a significant global minima of 2.55 nm at the final measured radii. This drastic drop begins near a radius of 20 nm, and suggests that the ions are becoming more concentrated within a smaller region and supports cause 4, the hypothesis that over-compression at the extremes of the reconstruction are the source of the smaller FWHM values.

Moving from the shape governing parameters the impact of radius on, μ, indicates that the center of the film remains near an initial value of -26 nm up until a radius of 12.5 nm at which point the mean position of the film increases with a inflection point near an ROI radius of 16 nm and a final film position of -24 nm. This measurement suggests that their is non-negligible curvature affecting the fitting process supporting hypothesis 3. From this however, a comparable impact on the scale parameter is expected which does not exhibit significant changes over the same range of radii.

Looking to the amplitude, A, and background contributions, B, it is seen that A is on average inversely proportional although it is not a linear relationship for the rate of decrease begins to increases near a radius of 10 nm. As the background is relatively constant in this range and β is decreasing resulting in a more strongly peaked apex it is likely the changes in amplitude are due to the changes in the generalized normal's maxima and not other causes. While the background is approximately constant there is a notable spike which appears to correlate with the apparent inflection point at an ROI radius of 16 nm in the μ curve.

In summary analysis of the fitting parameters suggests a non-negligible curvature in the thin film results in a gradual decreases of the FWHM at intermediate radii as supported by observations of μ and B. While rapid changes in α observed from 20 nm onward corresponding to an equivalent change in the measured FWHM suggests that a radius dependent compression effect exists which is amplified nears the edges of the reconstruction.

Comparison to as-provided reconstruction

Given the as-provided reconstruction the same process is repeated with two changes, the first of which is that the number of sliding annuli is increased from 100 to 122 with the same radial step size. As the spatial bounds are now $[-33.8, 34.8]$ and $[-29.8, 37.3]$ for X^{PNNL} and Y^{PNNL} an increased number of ROI maintains the same prior step size. The maximum radius for the annuli are increased proportionally to 29 nm to prevent analysis of a partially filled ROI. The second change is that no monte-carlo reconstructions can be performed to estimate the uncertainty of the calculations. However, it is still possible to calculate the uncertainty in the estimates of the gennormal fit using the fit covariance matrix.

The results are summarized in figure 6.6 where similar trends can be observed to the calibrated reconstruction. The FWHM values once again decrease with respect to mean radius, however this appears to be at a higher rate, prior to undergoing a rapid drop in FWHM measurements at 25 nm instead of the at 20 nm. Also, the FWHM values tend to be higher relative to those from the calibrated reconstruction starting at value of 5.65 nm and reaching a minima of 4.9 nm. The gennormal fit parameters also exhibit comparable behavior but shifted to higher radii. The main difference in behavior is that of the mean

radius which ranges from -27.5 to -28.5 nm and has a roughly parabolic shape with a local minima and two local maxima of equivalent magnitude at the minimum and maximum radius. If the shifting mean position is indicative of film curvature as proposed this implies that despite having lesser curvature the same general trend of decreasing FWHM is observed. Furthermore, the fact that the same rapid drop in FWHM is observed for large radii supports the proposal that over-compression of the thin film is the cause for this behavior. One final observation is that on average ratio of the film thicknesses of the calibrated and PNNL reconstruction over the first 100 annuli is 0.933 while the ratio of the measured interplanar spacing is 0.9446. It appears then that the difference in film thickness estimates may be due primarily to the differences in the interplanar spacing.
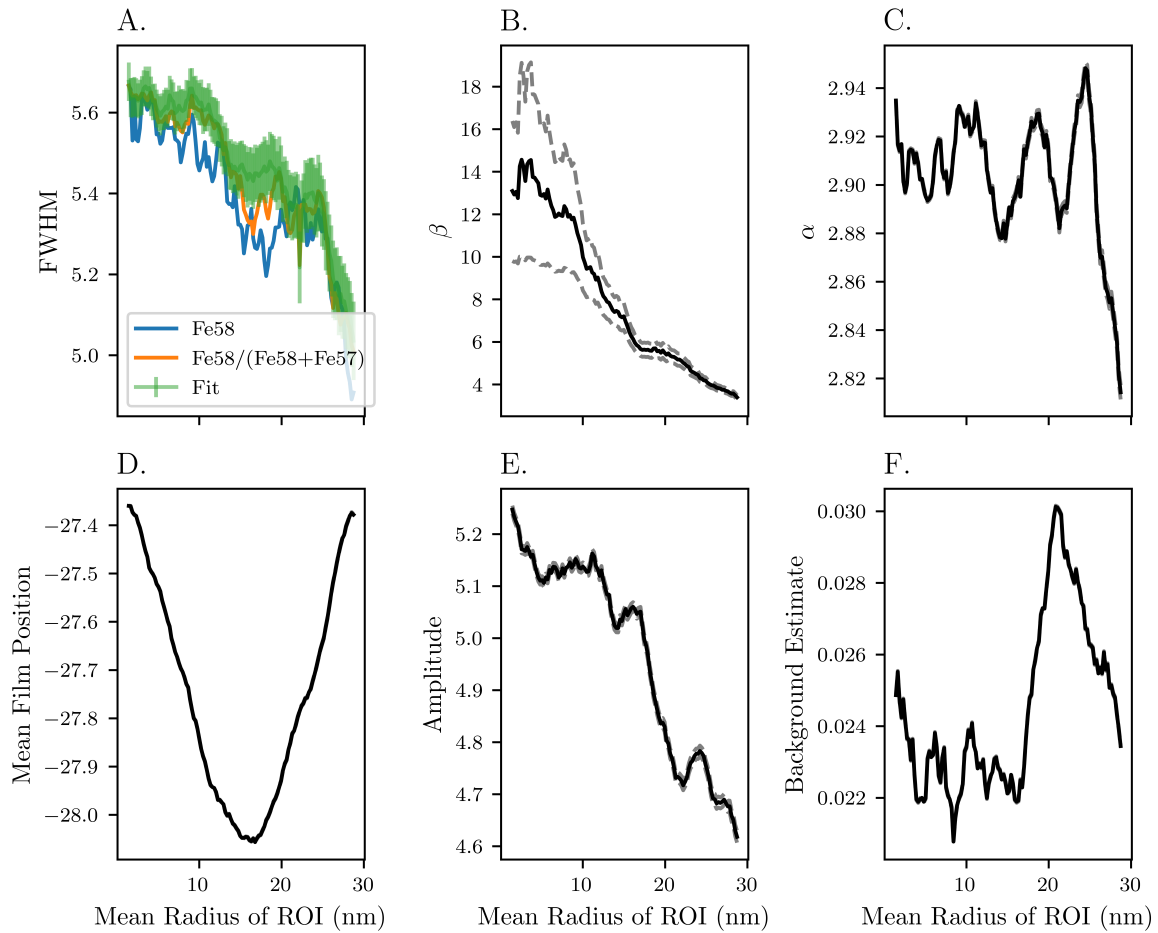
Figure 6.6: FWHM estimates and fit parameters of the generalized normal distribution for the as-provided PNNL reconstruction. 1σ error bounds are provided as a function of mean ROI radius when possible based upon the covariance matrix of the gennormal fit. Subfigure A. depicts three different FWHM measurements decreasing as a function of radius with a large change in radius occurring near a radius of 25 nm. Subfigure B. shows the shape parameter, β which is shown to decrease as function of radius approaching a more gaussian distribution starting from a flattop kernel. Subfigure C. measures the scale parameter which fluctuates between 2.88 and 2.94 nm until a radius of 25 nm at which point is decreases rapidly. Subfigure D. depicts the distributions mean which is a proxy for measuring the thin film's center. Starting at an estimate of -27.4 the mean position reaches a local minimum near -28 nm near a radius of 16 nm prior to returning near to the original estimate. Subfigure E. plots the amplitude, A, which is inversely proportional with radius and generally decreases with the exception of a minor peak near 25 nm. Subfigure F. depicting the background parameter, B, sits in the 0.22 to 0.24 range until a maxima of 0.032 is reached near a mean radius of 22.5 nm with a subsequent decrease.

6.4 Conclusions

In this chapter it has been shown that monte-carlo approaches are appropriate to provide estimates of uncertainty for complex calculations as demonstrated by calculating the interplanar spacing and film thickness for the isotopically enriched BCC Fe specimen. With respect to the interplanar spacing the original calibration method provided as estimate of $0.1433 \pm 1.91e{-}3$ nm while the monte-carlo approach found that the interplanar spacing was $0.142 \pm 4.2e{-}3$ nm. While no formal hypothesis tests were carried out to compare these two estimates both fall well within opposite's error and suggest that the scaling component of the calibration did not greatly bias the results. Furthermore, it was shown that the original as provided reconstructions had a higher estimate of $0.150 \pm 3.05e{-}3$ and that the differences in the interplanar spacing manifested when measuring the film thicknesses, were for each measured ROI the calibrated thin film was measured as 0.933 of the provided PNNL reconstruction.

Speaking of the thickness measurements for the thin film, a procedure for analyzing the 1D concentration profiles through a sliding annular ROI was proposed to calculate spatially aware estimates of the film thickness with respect to the radius from the reconstruction center. For both reconstructions it was observed that the film thickness, when measured using the FWHM, decreased as a function of the mean ROI radius up until a drop-off point which was 20 nm for the calibrated reconstruction where a significant rapid change in the FWHM was seen. Analysis of the fitting parameters for the generalized normal distributions fit to the concentration profiles suggested that while the calibrated film did possess residual curvature that alone did no explain the gradual decrease in thickness which was observed in the PNNL reconstruction which had no-observed curvature according to the fit's mean parameter. The drop-off at large radii is instead believed to be due to over-compression of the point cloud as this was associated with equivalent drops in the scale parameter of the fit, α.

According to the calibrated reconstruction and monte-carlo estimates the film thickness ranged from 5.4 nm to 5.0 nm over a 20 nm spread prior to the rapid descent to 4.6 nm. In the case of the as provided reconstruction the thickness was found to be within 5.7 nm and 5.3 nm within a 25 nm span over the mean radius and reached a global minima at 4.9 nm. The growth target for this specimen was the 5 to 6 nm range and with the exception of the high radius measurements both reconstruction support that this growth target was achieved when measured via the FWHM. It should be noted however, that alternative measurements such as the full width at tenth maximum, TWHM, would result in larger estimates.

Chapter 7

Consensus clustering

7.1 Theory

Monti Consensus Clustering

Parameter selection is a fundamental limitation of both k-centers and density based clustering algorithms. For k-based clustering algorithms Monti et al. [84] proposed consensus clustering, a resampling-based parameter selection method. The aim of of consensus clustering is to measure the inherent stability of the resulting clusters for random perturbations of the original dataset. In Monti clustering parameter selection and cluster validation is achieved through visualization of a Consensus matrix, measuring the likelihood points are clustered together, and analysis of the empirical cumulative distribution function (ECDF) for all values within the matrix.

Definition of Consensus

Considering that atom probe tomography data is a point set contained within three spatial dimensions we identify a generalized point set, S, within RN. Let S(1), S(2), ... S(H) indicated the perturbations of S where H is the number of perturbations to generate and S(h) indicates an individual perturbation. M(h) then denotes the NxN connectivity matrix for S(h) and is defined below:

$$M^h(i,j) \begin{cases} 1, & \text{if i, j are contained within the same cluster} \\ 0, & \text{else} \end{cases} \qquad (7.1)$$

Initially, the Monti protocol employed resampling of S and thus used a series indicator matrices $I^{(h)}$ to provide a normalization of $M^{(h)}$ as $M^{(p)}$ shown in equation 7.2. Here p indicates the algorithm parameters and in the case of Monti et al. is the number of expected clusters and for DBSCAN would be (O, ϵ). The indicator matrices are required as points (i, j) are not guaranteed to exist in each resample. In the absence of subsampling eq 7.2

is simplified to equation 7.3 and uses the number of perturbations, H, as the normalization constant.

$$\mathcal{M}^{(p)}(i,j) = \frac{\sum M^{(h)}(i,j)}{\sum I^{(h)}(i,j)} \tag{7.2}$$

$$\mathcal{M}^{(p)}(i,j) = \frac{\sum M^{(h)}(i,j)}{H} \tag{7.3}$$

Thus the consensus index, $\mathcal{M}^{(p)}(i,j)$, measures the number of times points i and j are assigned to the same cluster normalized with respect to the number of perturbations that contain both points. $\mathcal{M}(i,j)$ is bound within 0 to 1, where perfect consensus is achieved when $\mathcal{M}$ is populated only with 1 and 0. This indicates that clustering on each $S^{(h)}$ produces identical clustering partitions with respect to each pair of points.

From $\mathcal{M}^{(p)}$, two measures of consensus are defined corresponding to an individual cluster and an individual point, s_i. First, let us introduce the cluster consensus, m(k), which measures the average consensus between pairs assigned to a cluster. Let I_k indicates the indices of points belonging to cluster k.

$$m(k) = \frac{1}{N_k(N_k-1)/2} \sum_{\substack{i,j\in I_k \\ i<j}} M(i,j) \tag{7.4}$$

The second statistic $m_i(k)$ measures the average consensus of point i, e_i, relative to all other points in the cluster where $1\{e_i \in I_k\}$ returns 1 when the condition is true and 0 otherwise:

$$m_i(k) = \frac{1}{N_k - 1\{e_i \in I_k\}} \sum_{\substack{j\in I_k \\ i\neq j}} M(i,j) \tag{7.5}$$

Selection Criterion

Monti et al, proposed analysis of $\mathcal{M}$'s value distribution, the consensus distribution, for identification of the optimal k-parameter. As previously mentioned perfect consensus is achieved when $\mathcal{M}$ is populated solely by 1 and 0 which would result in an ECDF with a relatively flat region between the two values which is demonstrated in figure 7.1. Monti provides the following definition for the consensus ECDF from 0 to 1:

$$CDF(c) = \frac{I \sum M(i,j) \leq c}{N(N-1)/2} \tag{7.6}$$

Here N indicates the number of rows and thus columns of the consensus matrix, $\mathcal{M}$, as it is a square matrix and I.... is the indicator function. Identification of the ideal cluster number is then achieved by comparing the relative areas, A(K), underneath the ECDF as follows:

$$A(K) = \sum [x_i - x_{i-1}]CDF(x_i) \tag{7.7}$$
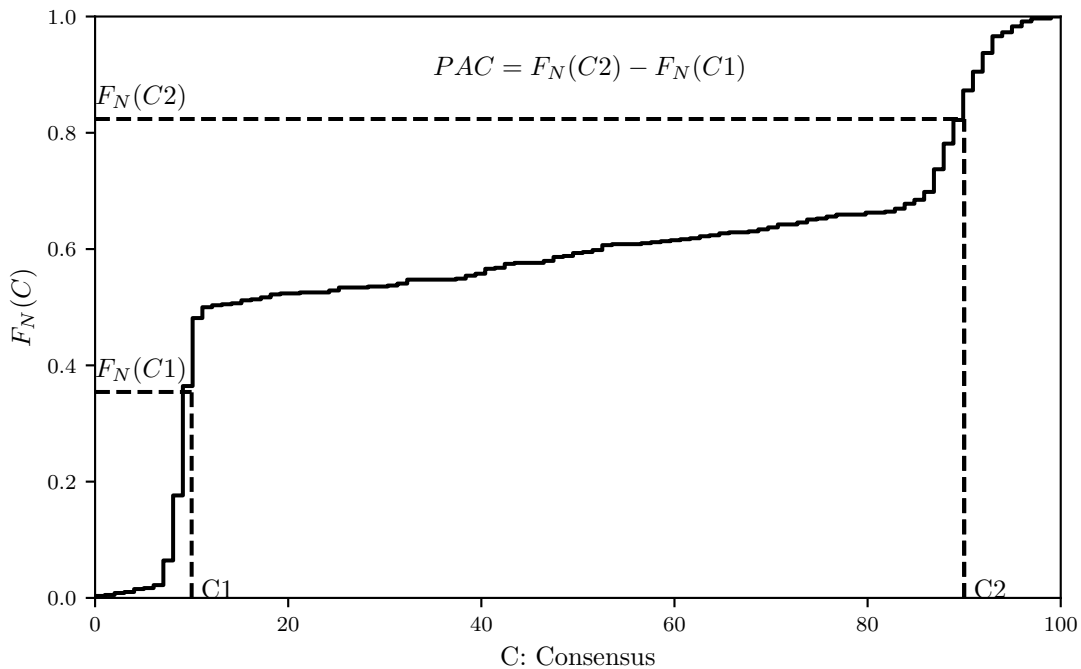
Figure 7.1: Empirical cumulative distribution function (ECDF) of the consensus matrix. C_1 and C_2 denote the consensus value hyper-parameters used in the Şenbabaoğlu, Michailidis, and Li [109] method of consensus clustering. Recommended values for these parameters are 0.1 and 0.9 times the total number of clustering attempts, and were reported to have minimal impact on the results [109, 66].

For incremental steps in K the maximum of the proportional change in area $\Delta(K)$ serves as a general rule of thumb for finding optimal K±1 due to the assumption that inherently unstable spurious clusters will provide negligible changes in A(K).

$$\Delta(K) = \begin{cases} A(K), & \text{if K} = 2 \\ \frac{A(K+1)-A(K)}{A(K)}, & \text{if K} > 2 \end{cases} \tag{7.8}$$

The preceding definition of $\Delta(K)$ is the most general form of the metric, however as noted by Monti et al, not all clustering algorithms guarantee that A(K) decreases as the number of expected clusters, K, increases and thus modifications have to be made per algorithm. For use with self-organizing maps it is specifically mentioned that A(K) should be replaced with Â(K), the maximum observed area for all evaluated K.

Method Limitations

While the Monti procedure has inherent limitations when applied to K based clustering algorithms it is not certain that the same complications will exist for density based appli-

cations due to the change in parameter from the number of clusters to a representation of local density. The necessity of changing the selection criterion is evident as it is unclear if increases in a distance threshold in many density based clustering algorithms will result in the same relative behavior captured by 7.8. Nor is it obvious how to apply the proportional change method to multi-parameter algorithms such as DBSCAN. However, optimizing over non-K parameters also circumvents the inability of $\Delta(K)$ to distinguish between one and two clusters. Another source of ambiguity which is relevant for all advancements of Monti consensus clustering is the treatment of noise or matrix data in density based approaches. If the noise is treated as a cluster the consensus matrix could be influenced by the percent of noise data through biasing of the distribution to one, on the other hand omitting the consensus of noise may instead bias the distribution to values of zero. The final limitation is computational as CC requires clustering of H permutations resulting in O(HA) complexity where H is the number of perturbations and A is the complexity of the clustering algorithm.

Proportion of Ambiguous Clustering

Development of the PAC metric

Lacking a rigorous assessment and comparison of consensus clustering to alternative metrics, Şenbabaoğlu, Michailidis, and Li [109], demonstrated the impact of intra-cluster distances and singular clusters on Monti consensus clustering in genomics data. For both square and circular unimodal distributions CC identified a bias to larger K in the absence of cluster structure, with the circular data splitting into seven clusters as opposed to the minimum threshold of two suggested by Monti et al. Furthermore, a K=4 partition for the square data was most stable and it was hypothesized that the four corners served as an anchor point.

Assessment of $\Delta(K)$ for structured data was carried through generation of up to six normal distributions with a set intra-cluster separation distance. CC continued to separate single clusters into stable subclusters and was also shown to have maxima at K = 3 regardless of the number of clusters for a wide range of separation distances. To overcome these biases the Proportion of Ambiguous Clustering (PAC) with the selection criterion defined below:

$$PAC_k(x_1, x_2) = CDF_k(x_2) - CDF_k(x_1) \tag{7.9}$$

$$\text{optimal K} = \arg \min_k PAC_k \tag{7.10}$$

The PAC score introduces two additional hyperparameters x_1 and x_2 bound on the range (0, 1) which influence the area of the CDF where the degree of flatness is measured. When compared to $\Delta(K)$ as well as five other metrics for the multimodal datasets PAC is reported as having an overall accuracy of 80% while the next highest metric achieved 60% and $\Delta(K)$ a value of 40%.

Considerations of PAC for clustering dense data

Concerns regarding the behavior of $\Delta(k)$ for non K-based methods is resolved through PAC due to its independent of prior parameter evaluations and ease of translation to multi-parameter algorithms. An additional undisclosed merit of PAC is the possibility of optimization routines to reduce the number of function calls and thus time complexity of the overall search of parameter space. It should be noted however that such routine's often rely on the PAC parameter space being continuous and differentiable which is unknown. Due to PAC's independence from prior results it also opens up direct comparison of clustering algorithms for the same dataset such that the ideal algorithm and parameter combo possesses the minimum PAC.

While PAC poses less challenges for application with density based algorithms there are two possible scenarios which will result in a PAC of zero for a wide range of parameters. The first of which occurs when the entire dataset is reported as a singular cluster when the density threshold is set below the optimal value and the second of which is when the dataset is labeled completely as noise. The latter occurs when the density threshold is sufficiently high that no features exceed this value. In these cases M will be populated entirely by 1s or 0s and thus the PAC will be zero due to the density being distributed over a single value. It is also unclear if the PAC distribution is unimodal or bimodal with respect to the input parameters. In the bimodal case a local minima between the maxima may be sufficient, but selection in the unimodal case is ambiguous.

M3C: Monte Carlo Consensus Clustering

Relative Clustering Stability Index

Monte Carlo reference-based consensus clustering (M3C)'s goal is to eliminate the systematic bias present in the original CC algorithm and provide a formal hypothesis test to differentiate between one and two clusters for K-based clustering. The premise of M3C is to generate a series of reference datasets which emulate the real data's characteristics such as covariance structure without the presence of clustering hierarchies and structure [66]. Direct comparison of the PAC scores for the original data to a wide range of simulated datasets is achieved through a new metric the relative cluster stability index (RCSI) below:

$$RCSI_K = log_{10}(\frac{1}{B} \sum Pref_{Kb}) - log_{10}(Preal_K) \tag{7.11}$$

Here B indicates the number of Monte Carlo simulations or reference datasets for a given K while Pref and Preal correspond to the PAC score for a given simulation and the original dataset. In this scheme a negative RCSI represents a scenario where the clusters in the real data are less stable than those in the references and a positive value indicates the opposite. Theoretically, the optimal parameter should then correspond to the maximum measured RCSI.

The RCSI alone does not resolve the K = 1/2 dilemma so John et al, introduced a hypothesis test to identify if the number of clusters is statistically significant. The Monte Carlo p-value, P_k, tests the hypothesis that Preal came from a single gaussian cluster against the null hypothesis that it was generated from multiple gaussian clusters according to a set significance level, α. To calculate P_k, let O_K and B represent the number of Pref less than or equal to Preal and total number of simulations respectively. P_k is then:

$$P_K = \frac{O_k + 1}{B + 1} \tag{7.12}$$

Application to density-based clustering

While calculation of PAC does not produce any significant changes in time complexity the introduction of simulations by M3C changes the complexity from O(HA) to O(BHA) where the addition of B represents the number of reference datasets. In the event of parallel computing the complexities for the PAC and RCSI metrics can be cut by a factor of C, the number of processors. B can be set to a low value to save on computational resources in exchange for higher error in the average Pref and lack of power for the Monte Carlo p-value. For context John et al, set B and H both to 100 and noted that the runtime was heavily impact by the number of samples in the datasets as the initial algorithms complexity is multiplied by the BH total computations for a single parameter.

Similar, to PAC being biased to zero in extreme cases with density based algorithms the RCSI is theorized to return highly negative and even undefined values in two edge cases. Consider that for APT the null hypothesis is instead that the data is uniformly distributed representing the matrix distribution of some element of interest and assume that the real data's average density is higher than the references. In this scenario, it is possible that for some parameter set clustering the real data identifies clusters while the reference does not. Ignoring the noise data, Pref would then be zero and the RCSI undefined. This is also the result when the real dataset is identified as singular cluster while the references are still subdivided into multiple clusters. It is further unclear how minimal clustering in either dataset will impact the RCSI and if the maxima is still corresponds to the optimal parameter.

7.2   DMC3: Density-based Monte Carlo Consensus Clustering

Accounting for noise

In adapting M3C for density-based clustering algorithms the existence of "noise" data which falls below the effective density thresholds identifying a cluster must be addressed. The two most direct options available are to either treat the "noise" label as a cluster and consider thus increment $M^{(p)}(i, j)$ when points i and j are labeled as noise during a permutation or

to reject the "noise" cluster and not increment $M^{(p)}(i,j)$. One complication with either approach is the prediction of its influence on the consensus distribution due to the variable amount of "noise" in an individual dataset. In low noise applications neither method is likely to greatly bias the end results, however in high noise scenarios, such as those in APT data, option one is expected to bias the consensus distribution to one due to the high consensus in the "noise" cluster. Alternatively, neglecting the noise may bias the distribution to zero instead. Thankfully both the prior defined PAC and RCSI possess two hyperparameters (x_1, x_2) which can be set to omit the large value density at zero or one.

Inclusion of the noise into M is then dependent on the information they contain, points near the boundary clusters are more likely to be interchangeably labeled as belonging to the cluster or noise and measuring the consensus of these points relative to the "noise" cluster and real clusters. On the other hands points sufficiently far from clusters are unlikely to contribute additional information about the real clusters, but may provide information on spurious clusters that arise from statistical noise in the background. To address the possible benefit of noise inclusion define a new noise connectivity matrix, $M_N^h(i,j)$, and two new consensus matrices corresponding to the noise consensus, $\mathcal{M}_N^{(p)}(i,j)$, and the overall labeling consensus, $\mathcal{M}_L^{(p)}(i,j)$, below:

$$M_N^h(i,j) \begin{cases} 1, & \text{if i, j are labeled as noise} \\ 0, & \text{else} \end{cases} \tag{7.13}$$

$$\mathcal{M}_N^{(p)}(i,j) = \frac{\sum M_N^{(h)}(i,j)}{\sum I^{(h)}(i,j)} \tag{7.14}$$

$$\mathcal{M}_L^{(p)}(i,j) = \frac{\left(\sum M_N^h(i,j) + M^h(i,j) \right)}{\sum I^{(h)}(i,j)} \approx \mathcal{M}_N^{(p)}(i,j) + \mathcal{M}^{(p)}(i,j) \tag{7.15}$$

Deriving new metrics ambiguity metrics based upon $\mathcal{M}_N^{(p)}(i,j)$ and $\mathcal{M}_L^{(p)}(i,j)$ follows the same procedures as the PAC (equations 7.6 and 7.9) resulting in the proportion of ambiguous noise, PAN, and proportion of ambiguous labeling, PAL. The ambiguity metrics are further used alongside reference data to calculate the relative noise stability index, RNSI, and relative label stability index, RLSI, according to equation 7.11.

Cross consensus measurements

A common occurrence for non-hierarchical algorithms is cluster fragmentation, where a singular cluster is split into multiple clusters due to a combination of local density fluctuations within the cluster and variability in density among the cluster such that a single density threshold does not accurately describe all of the features. The measure of cross consensus is introduced as a means to compute the average consensus between two clusters indicating the overlap of the two features and identifying possible cluster fragmentation. The definition of

cross consensus below is similar to the cluster consensus, 7.4, with a different normalization constant.

$$m(k_1, k_2) = \frac{1}{N_{k_1} N_{k_2}} \sum_{\substack{i \in I_{k_1} \\ j \in I_{k_2}}} M(i, j) \tag{7.16}$$

Cross consensus is bound within the range (0, 1) such that values near 0 indicate no association between clusters and values near 1 indicate a high degree of association. While a large value of cross consensus can suggest that the two clusters were fragmented from an original larger cluster cross consensus also qualitatively indicates the spatial proximity of two features because nearby clusters are more likely to exchange points during the permutation process. Generally, given a maximum permutation distance, D, clusters separated by at least 2D should return a near zero cross consensus. It should be noted that a cross consensus of one is impossible as two features with cross consensus of one would instead be grouped as a single cluster by the clustering algorithm.

Determining the point and cluster consensus for the noise data follows the same formula as equations 7.4 and 7.5 with $M_N^{(p)}(i, j)$ instead of $M^{(p)}(i, j)$. Furthermore despite the point consensus in equation 7.5 being intended to only compute a point's consensus with its assigned cluster the equation does allow comparisons between any point and any cluster due to the use of indicator variables in the normalization constant. Thus, any modifications to account for noise also should allow comparison of non-noise points to the overall noise feature.

Ambiguity as a function of ϵ

Consider a set of three gaussian clusters, $\sigma_{Cl} = 0.2$ *arb. unit*, placed within a low density matrix such that each cluster contains a dense core with a smooth density transition indicating the cluster boundary. The perturbation in each dimension is defined according to independent gaussian distributions with σ arbitrarily defined as $\sigma_{Cl}/4$. The original point cloud is provided in Figure 7.2A. alongside three example perturbations in B. through D. Application of the perturbations artificially inflate the physical size of the clusters and mix the matrix and cluster points at the boundary. Fixing the order parameter at six we can investigate how either the PAC or PAN scores correspond with the consensus of individual points. In this comparison the clusters observed in the unperturbed data act as the reference. Note, that the minimum recommended order parameter for a 2-D point cloud is four, although analysis of larger datasets or those composed of high density features generally require values in excess of the minimum. The minimum value is most appropriate for datasets with negligible noise and a large degree of cluster separation.

Behavior of PAC as a function of ϵ

Plotting PAC as a function of ϵ in figure 7.3 alongside the pointwise cluster consensus (top-row) and pointwise noise consensus (bottom-row), modifications of equation 7.5 it is seen
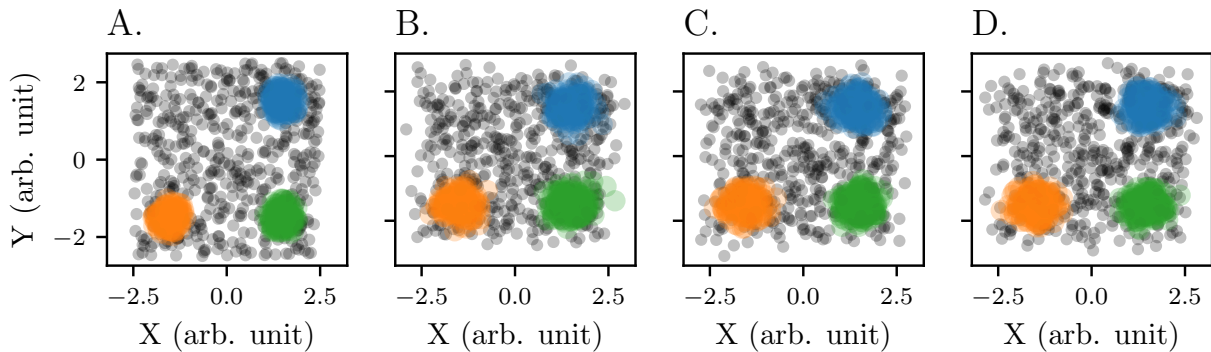
Figure 7.2: Example of generated synthetic data for a three cluster system in A. alongside three independent perturbations in B. through D.

that the PAC curve displays two local maxima and a single non-zero local minima. From here on the pointwise noise consensus is referred to as $m_i(-1)$ while $m_i(k)$ is left to refer to pointwise consensus of the observed clusters.

Near the first maxima at an ϵ of ≈ 0.13, it is found that cluster cores have a maximum cluster consensus in the 0.7 to 0.8 range where as the points near the cluster-matrix interface report values approaching 0.6. For this epsilon the majority of the matrix report near zero consensus for all $m_i(k)$ as one would expect. Conversely, the noise-consensus measurements indicate that the matrix points report a $m_i(-1)$ between 0.8 to 1.0, with lower values of approximately 0.6 at the interface. As expected the cluster-cores report a near zero $m_i(-1)$. From this first point-cloud it should be noticed that $max(m_i(-1))$ is significantly higher than $max(m_i(k))$ despite a PAC score on the order of 0.13. In this case the noise consensus scores are indicating that the clustering algorithm is confident in the binary assignment of points to either cluster or noise. When clustering the non-perturbed data four clusters of sizes 181, 172, 176, and 6 points were observed while analysis of the perturbed point clouds suggest that on average 7 ± 2 clusters were observed over the 100 perturbations resulting in a size distribution consisting of 740 clusters in total. The mean and standard deviation of the size distribution was 73 ± 77 points with a maximum of 186 points. While the average cluster size was below the expected size of 176 points the maximum only differs by 12 points. Given the above clustering results it is unlikely that the cluster cores are being fragmented from an excessive density threshold but a small amount of minor features are arising at the cluster borders under the applied perturbations.

It is then expected that at the local minima the number of clusters should decrease and that $m_i(k)$ should increase as the algorithm becomes more confident in the assignment of points to a specific cluster. Indeed, this is what is observed at an ϵ of ≈ 0.21, where $m_i(k)$ approaches 1.0 for the dense cores. The consensus of the boundary points also increase indicating that they are placed within the same clusters more consistently despite the perturbation. Simultaneously, more of the matrix points are assigned to the clusters

Figure 7.3: A 3-cluster synthetic point cloud is plotted at four different epsilon values correlating to extrema and inflection points of PAC in subfigure E. The series of top-row point clouds (A. through D.) are color coded according to the maximum cluster consensus on a pointwise basis, $Max(m_i(K))$, while the bottom-row point clouds (F. through I.) are color coded according to the noise consensus, $m_i(-1)$. For both measures of consensus values near 0 and 1 indicate high degrees of certainty in label assignment and in the case of cluster consensus low ambiguity in the PAC score.

which results in lower $m_i(-1)$. A less obvious observation is that the spatial width of the cluster-matrix interface also increases proportionally to the search radius, ϵ, and so points farther from the interface begin to be clustered. Because of this even points far from the individual clusters such as those in the upper-left quadrant defined on the ranges of $[-2, 0]$ and $[0, 2]$ for X, Y report on average a $m_i(-1)$ of 0.4 despite the absence of clusters within this quadrant. This is a result of the pointwise noise consensus being more representative of global phenomena as it compares the co-assignment of points as noise regardless of physical distance. This stands in contrast to the cluster consensus which is limited inherently to points in close spatial proximity of a specific cluster. It should be noted however that despite a lower PAC of 0.! the number of observed clusters has increased while the average sizes compared to the prior maxima. A set of 18 clusters were extracted from the nonperturbed point cloud yet 15 ± 2 clusters were identified over the 100 perturbations. In the former the three main features grew in size up to 200 points while the majority of the clusters were in the range of 10 points. The perturbed cluster sets actually showed a decrease in the average size to 50 ± 82 points. From this point it is clear that minimizing the ambiguity does not necessarily correlate with the correct size statistics.

Moving to the second local maxima at ≈ 0.32, which was proposed to correspond to random clustering within the matrix we observe that pointwise cluster consensus values continue to increase with a large proportion of points achieving perfect cluster consensus. At a distance of 1 arb. unit from the cluster interfaces the average $m_i(k)$ is ≈ 0.65. This behavior is most evident in the space between the three clusters, while random fluctuations are the most likely culprit for the cluster consensus of points in the upper-left quadrant. The pointwise cluster consensus in the upper-left quadrant are elevated compared to the prior minima, but are lower than the values found in quadrants containing clusters. The prior trends regarding $m_i(-1)$ continue and at this point the majority of the points report near-zero consensus, due to the continuous assignment of matrix points to different clusters. The clustering trends of the point cloud invert compared to the prior minima with respect to the number of clusters with only seven clusters found in the nonperturbed data and 3 ± 1.5 in the perturbed point clouds. At this ϵ the average sizes also increase to 307 indicating that the matrix is constituting a larger proportion of each observed cluster.

Finally, the right-skewed tail of the second maxima is examined which shows universal clustering of all points as a single cluster with a consensus value approaching 1.0 to a set of 2 clusters. Conversely, all points report a noise-consensus value of 0 continuing the previously identified trends. This is evidence of the aforementioned 0 ambiguity edge-case which the use of reference distributions is intended to correct for.

Behavior of PAN as a function of ϵ

Turning to the correlation of pointwise behavior with the PAN values in figure 7.4 it is observed to be similar to PAC, but the effects are less pronounced in proximity to the extrema, which occur at lower ϵ. It should be the noted that while the curve shapes and prevalence of extrema is dependent on the relative proportion of the points composing the
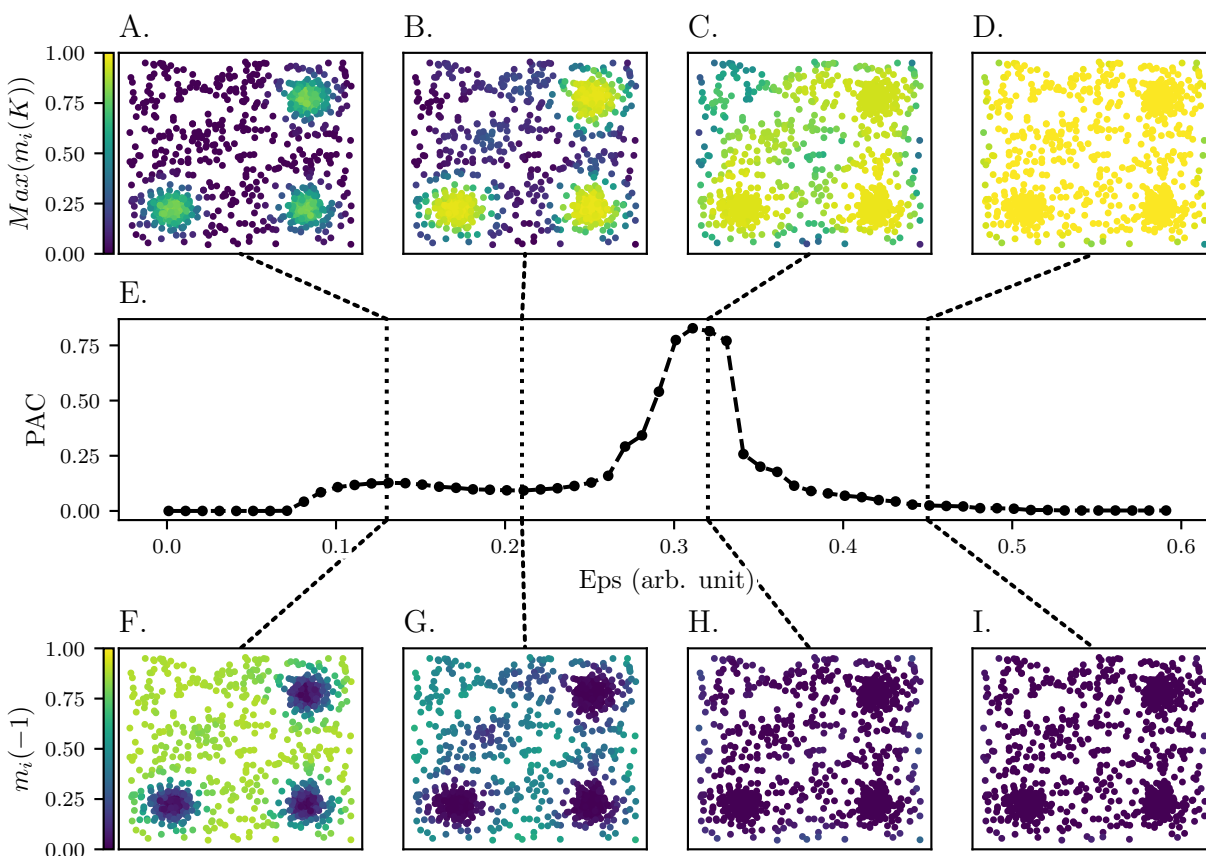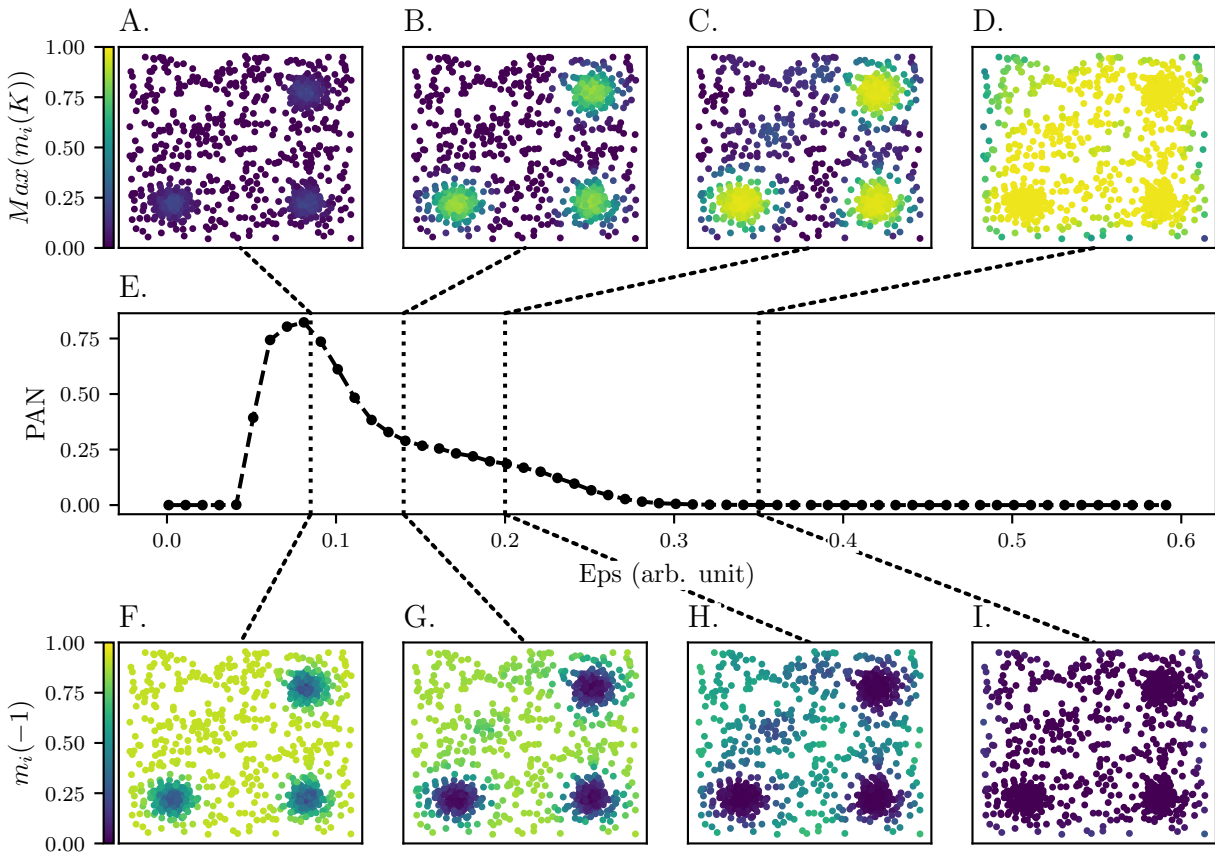
Figure 7.4: A 3-cluster synthetic point cloud is plotted at four different epsilon values corresponding to the PAN's extrema and inflection points in subfigure E. The series of top-row point clouds (A. through D.) are color coded according to the maximum cluster consensus on a pointwise basis, $Max(m_i(K))$, while the bottom-row point clouds (F. through I.) are color coded according the noise consensus values, $m_i(-1)$. For both measures of consensus values near 0 and 1 indicate high degrees of certainty in label assignment and in the case of noise consensus low ambiguity in the PAN score.

clusters and matrix, the PAN curve in this case has a primary low ϵ maxima with a gradual decrease up to a 0.14 arb. units for ϵ at which point there is a change in the rate and minor plateau before the final drop in PAN to zero. This plateau is likely due to the influence of random clustering of the matrix as was the case in the second extrema for the PAC value.

At the first extrema, 0.085, the pointwise cluster consensus figure shows a negligible consensus between the points and any identified clusters, while $m_i(-1)$ is near 1.0 for the majority of the points. The cluster cores serve as the exception which report values closer to 0.4. The juxtaposition of these two values indicate that while the cluster cores are inconsistently classified as noise alongside the matrix points, the found clusters are also inconsistent

given the point cloud perturbations. Practically, the noise consensus indicates that these points are likely to belong to a cluster compared to the rest of the dataset but the exact grouping of these points as individual clusters is indeterminate. When compared to the PAC's first maxima the ambiguity in the noise metrics do appear to be the result of cluster fragmentation as an average of 16 ± 3 clusters were observed over the perturbations with a lower maximum cluster size of 112 and a size of 20 ± 22. The observed cluster sets are best described as consisting of high-density cores with surrounding satellite clusters.

In the absence of a clear minima ϵ is increased to 0.14 to correspond approximately to the right-hand inflection point. Here it is observed that $m_i(-1)$ of the dense cores approach zero indicating that these points are highly likely to belong to clusters while maintaining values near 1.0 for the matrix atoms indicating consistent association with the noise label. Simultaneously, the cluster consensus for these matrix points remain near zero, but the cores of the clusters have increased consensus with the identified clusters s.t. the cluster centers report an average $m_i(k)$ of 0.65. It then appears that at this ϵ the resulting clusters are providing a more balanced split between consistent allocation of points to individual clusters and assignment as noise. Note that, detailed analysis of the cluster set is neglected in this dection as a near identical cluster set was described alongside discussion of the PAC's first extrema located at an ϵ of 0.13

The next ϵ investigated is 0.2 which was selected to represent an approximate location of the second extrema due to its lack of prevalence in this dataset and the proximity to the local minima of the PAC score. Due to this the extracted clusters sets are comparable and are left out f this section to instead focus on the consensus scores. At this point, the pointwise consensus behavior begins to converge with that reported as a function of PAC. Here the cluster consensus approaches 1.0 for the cluster's cores, but the noise consensus measurements of the matrix points have begun to decrease towards 0.5 indicating less confidence in the classification of these points as noise.

Continuing to the edge-case of zero ambiguity in the noise assignment, we find that much like the previous analysis of the PAC values the noise consensus is universally near zero while the cluster consensus approaches 0.6 and upwards for points known to belong to the matrix. The near-zero noise consensus and the zero PAN values implies that all points belong to a cluster and should not be labeled noise, and that the only ambiguity within the clustering results is tied to the assignment of points to specific clusters.

Overview of PAN and PAC

In summary analysis of figure 7.3 and 7.4 suggests that the PAC and PAN values represent certainty in different aspects of the clustering outputs. When the notion of ambiguity separated into two measurements PAC is indicative of the consistency of co-assigning points to a cluster whereas the PAN metric is measuring instead the likelihood that points are labeled as noise regardless of how often they are placed within the same cluster. The use of these two metrics and subsequently the corresponding relative stability metrics is dependent on the properties of the clustering output the user desires to optimize.

Considering a low to zero background noise scenario such as those in Monti et al. [84] the PAC score is suggested for use as the concern is consistent clustering and not correct identification of noise the For high background scenarios the choice is less clear, for a single pass clustering attempt it may be that the PAC score is more useful than the PAN score to prevent cluster fragmentation and overlap. On the other hand preliminary analysis suggests that a two-stage or multi-pass approach optimizing the first clustering step according to PAN would accurately remove the noise-atoms. From here the output would be treated as a new point cloud for a subsequent step where the individual clusters are extracted from a now low-noise environment using PAC. This style of two-stage analysis using clustering algorithms is uncommon compared to other noise reduction techniques but has been used before by applying the density-based clustering (DeBaCL) algorithm to the output of hierarchical Density-based spatial clustering of applications with noise (HDBSCAN) [46, 47, 48].

Behavior of RCSI and RNSI as a function of ϵ

Thus far only the ambiguity scores for the real data have been thoroughly discussed alongside the pointwise consensus scores. Discussion of the relative stability metrics must focus on the final clustering and accuracy to a known truth given that there exist no current pointwise equivalents. Therefor a reference distribution is defined for comparison with the synthetic set of clusters. Assuming a homogeneous distribution of solute species within the matrix using a uniform distribution with a fixed density would provide the best reference. In our experiments the solute density is known, however this information is unknown apriori for the majority of atom probe experiments. In the case of experimental atom probe the most common method to produce a reference dataset is to randomly sample from the remaining ions until the total number of points match the point cloud of interest [122, 26, 112, 27, 17, 114]. This approach is also referred to as random labeling or mass-randomization and is selected even if it subpar in the current application so that the analysis is better reflective of the experimental scenario.

Thus a uniform distribution consisting of $10N_{points}$ is generated within the same spatial bounds as the synthetic dataset such that when subsampling N_{points} for the 24 reference distributions it is unlikely to generate an identical subset. In the experimental case, a single large subsampling could serve as the parent distribution for the references or each reference could be generated from the complete point cloud. The former is chosen in this implementation of DMC3 to reduce the amount of memory used to store the parent point cloud. Each reference distribution is then perturbed 100 times for each ϵ. The subsequent PAC and RCSI scores are provided in 7.5 while the PAN and RNSI scores are provided in 7.6.

Comparing PACreal and PACref it is observed that PACref only has one extrema which in theory corresponds to the random clustering expected to occur in the matrix. The shift of this peak, ΔP, to lower ϵ relative to PACreal is likely the result of the reference method overestimating the background density, as N_{points} is dependent on the amount of points contained within clusters and those arising from the matrix. If this is the case then ΔP

Figure 7.5: Comparison of cluster ambiguity scores, PAC, in subfigure A. and the resulting relative cluster stability index, RCSI, in subfigure B. between a three cluster system and a uniform reference. The resulting cluster outputs for three different ϵ are provided in subfigures C. through E. The clustered data denoted as real shows two maximas corresponding to ambiguity of the clusters and matrix while the reference data shows a single maxima representative of the matrix as expected. A comparison of the RCSI and the adjusted mutual information, AMI, below shows that the AMI is maximized near the minima in disagreement with the maxima as described in prior works.

should approach 0 as N_{matrix} approaches N_{points}. It follows then that the error between the true matrix density and reference density should be minimized in high-noise datasets.

The relative cluster stability index is plotted alongside a metric of accuracy, the adjusted mutual information (AMI), in 7.5B. Compared to alternative metrics such as the adjusted rand index the AMI better reflects the accuracy of class assignments when the class sizes are unbalanced or are small in comparison to the total dataset. To calculate the AMI the labels from clustering the nonperturbed data is compared to the ground truth known from the data generation process. Additionally, the impact of the random perturbations on the dataset could be gauged by comparing the perturbed cluster labels to either the ground truth or nonperturbed labels. The comparison to the ground truth is not available in the case of an experimental dataset but comparing the perturbed and nonperturbed cluster outputs would remain possible.

Comparing the RCSI and AMI we find that unlike conventional consensus clustering maximizing the RCSI does not correlate to maximizing the AMI [66]. Instead this suggests that the best AMI, 0.894, is achieved when transitioning from highly negative RCSI, indicating a higher ambiguity in the real data, to a positive RCSI. Optimization routines would be unable to converge to such a point and so minimizing the RCSI appears to be the best approximation to ensure a sufficient, although non-optimal AMI of 0.888. Do note however, that there is a second negative region for high ϵ, due to the mismatch between the right-hand tails of the PAC curves. In the case of this dataset this region can be filtered out of the optimization by enforcing a minimum number of clusters of two. This constraint matches the inability of the prior methods to distinguish between one and two features.

Assuming an accurate density for the references selecting this minima is akin to running a mini-max optimization routine for the dual parameter system of PACref and PACreal. Alternatively, minimization of the RCSI can be described as maximizing the ambiguity due to the clusters while minimizing the ambiguity induced from the background point density, reflected by the low reference ambiguity. Figure 7.5C-E supports this description as the final cluster set in D. is composed of three well defined clusters with zero features arising from the random noise, while A. fragments the clusters and E. finds 17 features due to the random density fluctuations within the background distribution. Furthermore the resulting cluster sizes for the minima match closely with the expected mean size of 174.

Analysis of the noise metrics confirms that the zero-crossing point is near ideal with an AMI of 0.888, but unlike the RCSI minimization is not a sufficient target for optimization. The reason being that while the RCSI had an initial rapid decrease into the negatives followed by a gradual approach to the local minima the RNSI approaches the minima abruptly and slowly increases until a rapid transition to positive values is achieved. The result of this is that the minima would occur at smaller epsilon and farther from both the zero-crossing point and AMI's maximum relative to the RCSI. Maximization of RNSI is left as the only optimization target, however is limited in use because 1. there is not a sharply peaked extrema and 2. the maxima corresponds with random clustering of the matrix as seen in Figure 7.6. Similar to the RCSI there is a second negative region due to the mismatch in ambiguity curves however there are also fluctuations for large ϵ. The fluctuations are likely
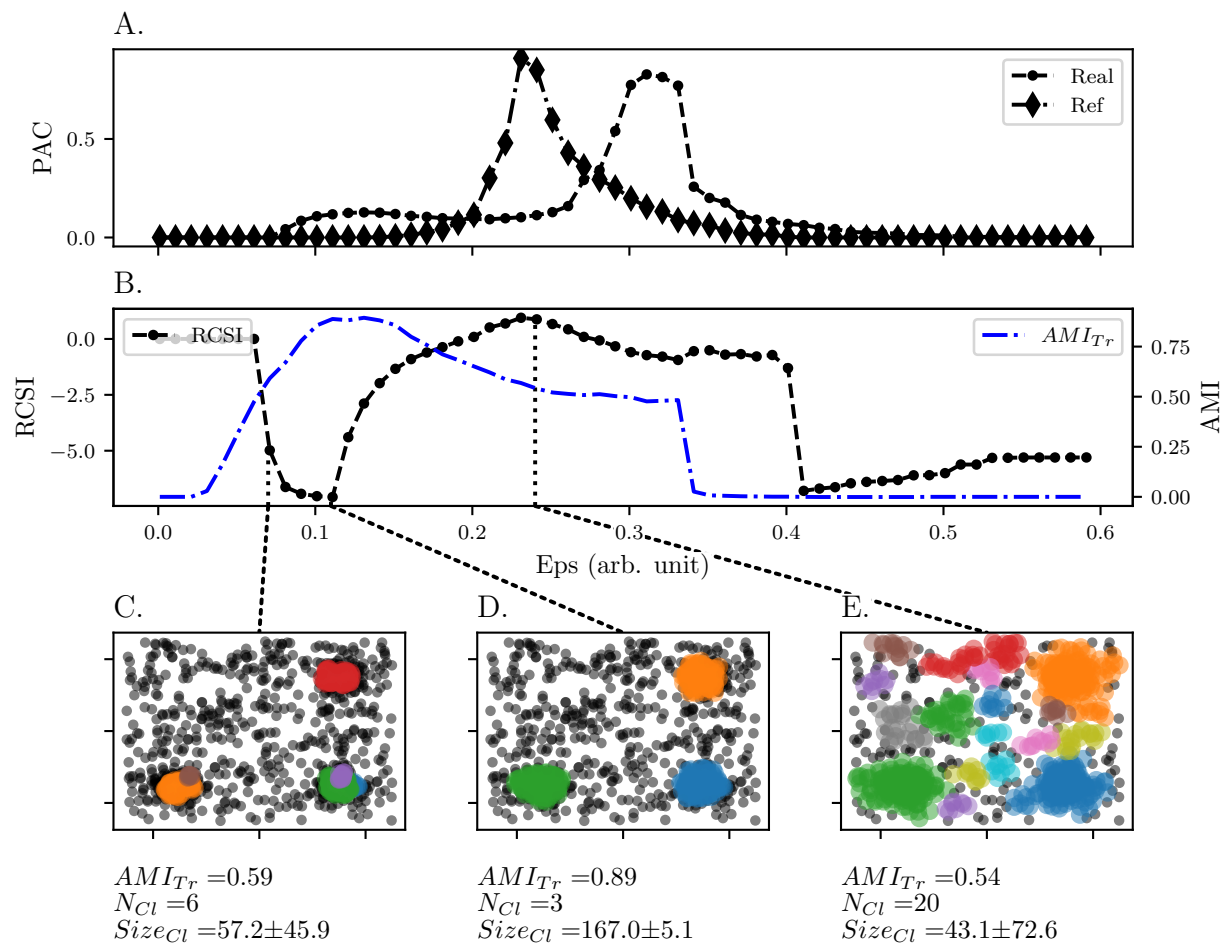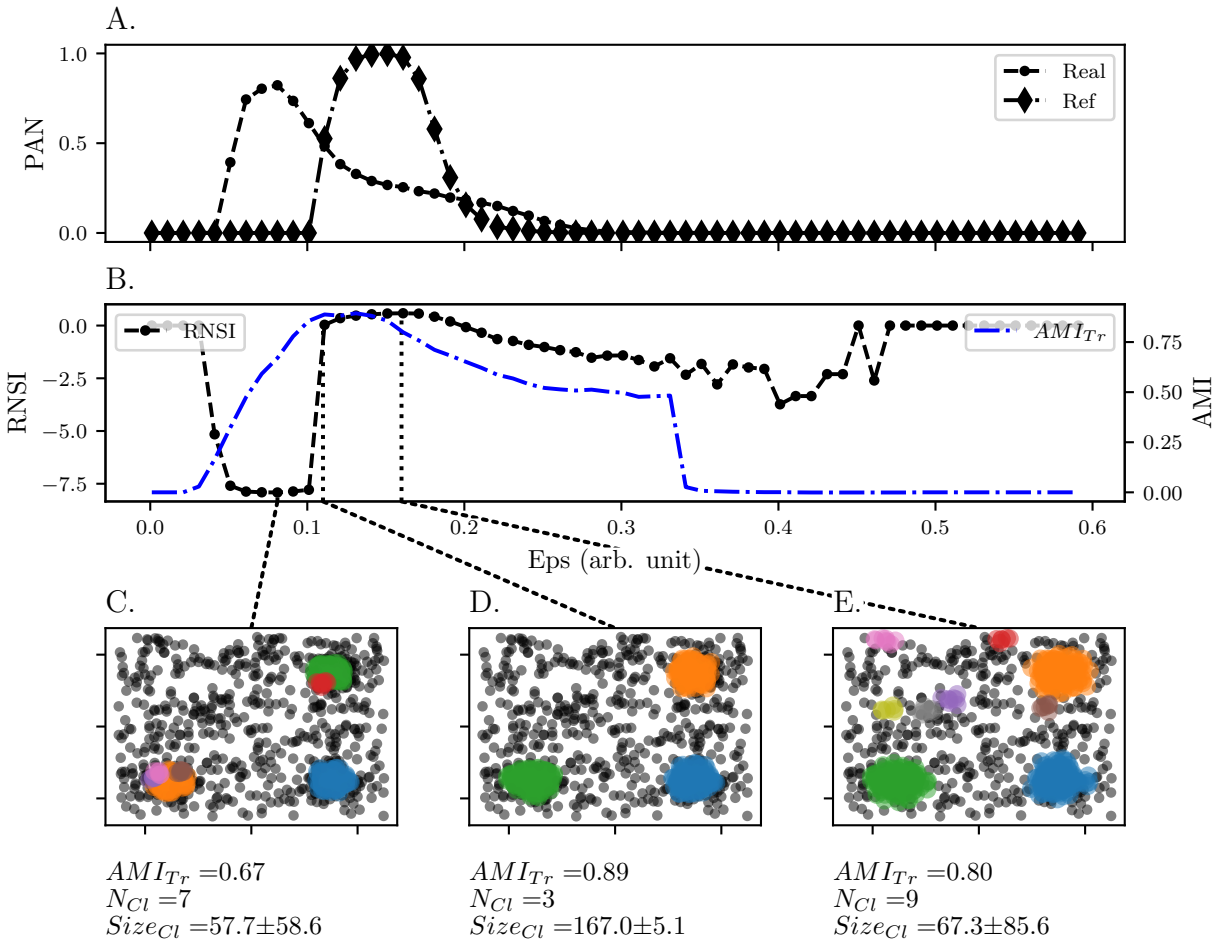
Figure 7.6: Comparison of noise ambiguity scores, PAN, in subfigure A. and the resulting relative noise stability index, RNSI, in subfigure B. between a three cluster system and a uniform reference. The resulting cluster outputs for three different ϵ are provided in subfigures C. through E. Both the clustered data and reference data possess a single maxima. Max(PANreal) corresponds to cluster ambiguity and possesses a right hand tail due to ambiguity arising from the matrix. Max(PANref) is approximately aligned with this tail supporting the conclusion it is due to the matrix. A comparison of the RNSI and the adjusted mutual information, AMI, below shows that the AMI is maximized near the zero-crossing point. Despite the identification of spurious clusters at the maxima the AMI suggests it is a superior optimization target compared to the minima.
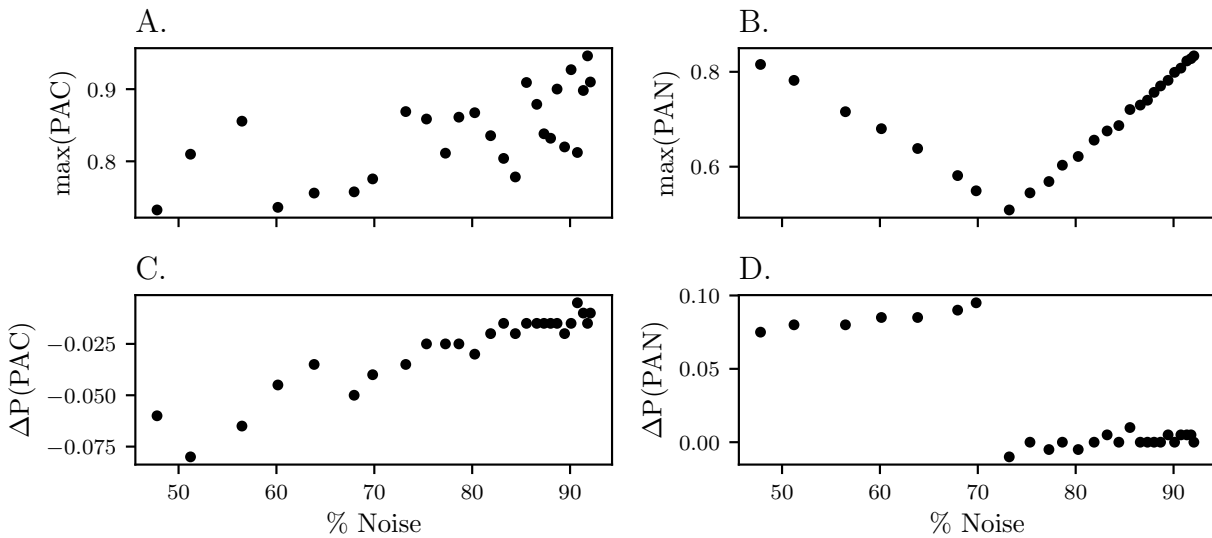
Figure 7.7: Influence of an increased proportion of matrix (noise) atoms on the ambiguity metrics measured as the maximas of PACreal and PANreal in subfigures A. and B. as well as the difference in positions of the maxima in subfigures C. and D. As the noise percentage increases max(PACreal) initially appears stagnant prior to increasing as the noise percentages surpass 80%. C. shows that the PACreal extrema approaches PACref linearly as the noise percentage increases. Contrary to this behavior is the PAN data in B. and D. Here there are two distinct regions with the noise percentages greater than 75% showing similar behavior to PAC while the opposite is observed below this threshold.

due to a sharp increase in the matrix ambiguity when the point cloud is being merged into a small number of large clusters and could be addressed by the same constraint on cluster number similar to the RCSI.

Importance of noise

While analyzing the impact of ϵ on the relative stability metrics the impact of the noise was neglected and only the impact of correct density estimates was acknowledged. However, the fact that these curves do not just depend on the density of the clusters and matrix but also on the ratio of high to low density data was alluded to. While changes in the reference density shift only shift the position of the reference extrema changes to the noise proportion of the dataset alters both peak positions and magnitudes as shown in 7.7

In 7.7A. the magnitude of the PACreal extrema is plotted as a function of the percent noise showing that from 50% to 70% noise the maxima remains at approximately 0.75 Past 70% the noise percent and maxima appear positively correlated albeit with scatter. Furthermore the difference in extrema positions between the reference and real PAC scores, $\Delta P(PAC)$ depicted in 7.7C. shows that the distance measured in units of ϵ decreases. Given
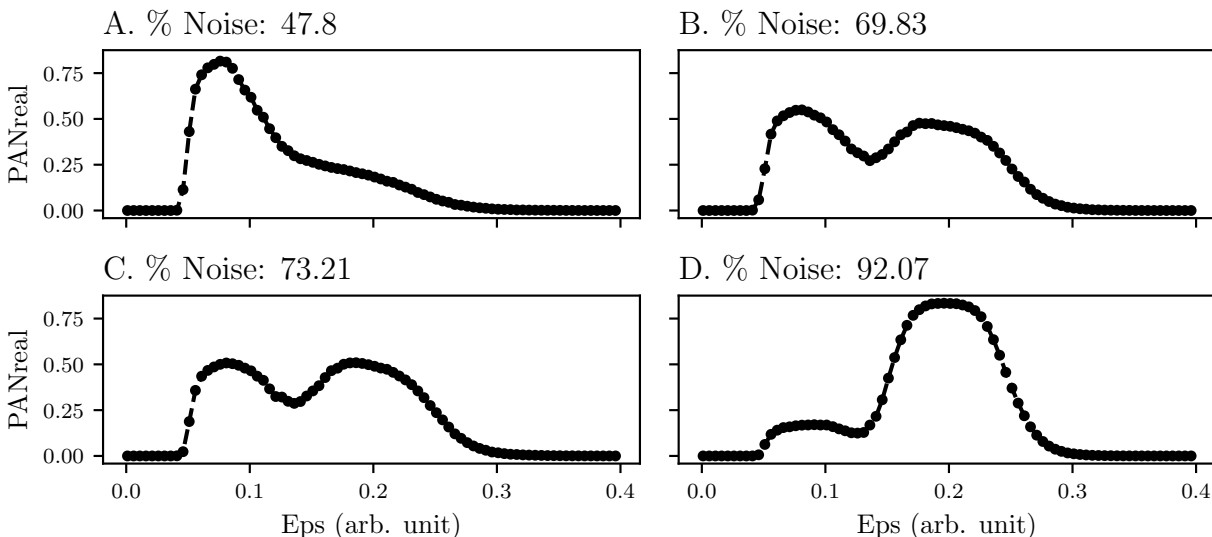
Figure 7.8: Impact of noise percentage for four PAN curves. Treating the PAN curve as a decomposition of a cluster and noise ambiguity the decrease in max(PANreal) corresponds to a less prevalent cluster PAN peak as seen when increasing the noise percentage from A. to B. Moving from B. to C. crosses a threshold such that the matrix PAN peak is the dominant extrema which continues to increase in magnitude as in D. At D. the noise component would most strongly match that of PAN_{ref} resulting in the smaller difference in peak position.

that this maxima corresponds to the ambiguity arising from spurious clustering of the matrix atoms this implies that similarity between the PACreal and PACref curves increase as the noise percentage of the dataset increases. Stated differently, in high noise situations the reference more accurately reflects the matrix distribution of atoms but does not account for the interaction between the clusters and matrix.

Focusing instead on 7.7B. and D. it is observed that the peak magnitude is composed of a linearly decreasing region and an increasing region with the split occurring near a noise level of 70%. Analysis of the peak positions in D. reinforce that 70% noise indicates a difference in behavior as for lower noise percentages the extrema for PANref is at higher ϵ than PANreal with the difference increasing as a function of the noise percent. However, at 70% there is a sharp decrease to a value of 0.02 for all remaining noise levels. In the prior discussion on the behavior of the ambiguity scores as a function of ϵ it was proposed that the curves should be considered as a mixture of two features with one indicating ambiguity primarily due to the clusters and the other the ambiguity arising from noise. Considering this perspective and that the reference attempts to simulate the matrix it seems that prior to 70% noise level the maximum PAN scores corresponds to the cluster component and post 70% is the matrix. The specific curves for a set of four noise levels is plotted below in 7.8 as confirmation of this hypothesis.

Figure 7.9: Difference in accuracy metrics relative to the maximum observed AMI when minimized (A.) and maximized (B.). The highest observed AMI per noise level is used as a standardization metric to account for the increased difficulty of clustering high noise datasets. With an exception at 50.0% noise minimization is shown to provide AMI scores that are within 0.025 of the maximum AMI up to a noise percent of 73, at which point the AMI degrades more quickly than expected in the highest noise scenarios. Maximization of the RCSI becomes less accurate as the noise percent increases and the difference relative the optimal solution is an order of magnitude larger than minimization

Above, it is clear than 7.8A. demonstrates a scenario where the initial clustering of the high-density data results in the highest ambiguity scenario based off the presence of one dominant extrema with a right-hand tail for the lower-density portion of the dataset. Opposite this, D. shows the scenario where the low-density data provides the highest ambiguity and there is a left-hand shelf for the high-density region. In between these two are B. and C. where an overlap of the high-density and low-density regions results in a raised plateau with a PAN of approximately 0.50 with two minor extrema. For 71.9% noise the left-hand extrema is the maxima while the right-hand extrema is larger for 74.2%. For the tested noise levels this behavior differs from the PAC scores where the right-hand low-density extrema was always the maxima.

The impact of the noise percent on the use of the relative stability indices as optimization metrics is explored in figures 7.9 and 7.10. In these figures the impact is measured as the difference in the adjusted mutual information, AMI, between the selected cluster set and the most accurate set for each noise level.

Analysis of the RCSI optimizations above shows that minimization outperforms maximization for all tested noise levels. The best case scenario for the maximization occurs at 50.0% noise whereas minimization of the RCSI results in smaller differences relative to the best-case clustering until 70.0% noise is reached at which point the accuracy begins to decrease. Given that 50.0% was the lowest tested noise level and this is the point when the two optimizations are most similar it is possible that in low noise situations maximization is preferred. However, given that high-noise scenarios are more representative of typical atom probe datasets minimization of the metric is recommended.
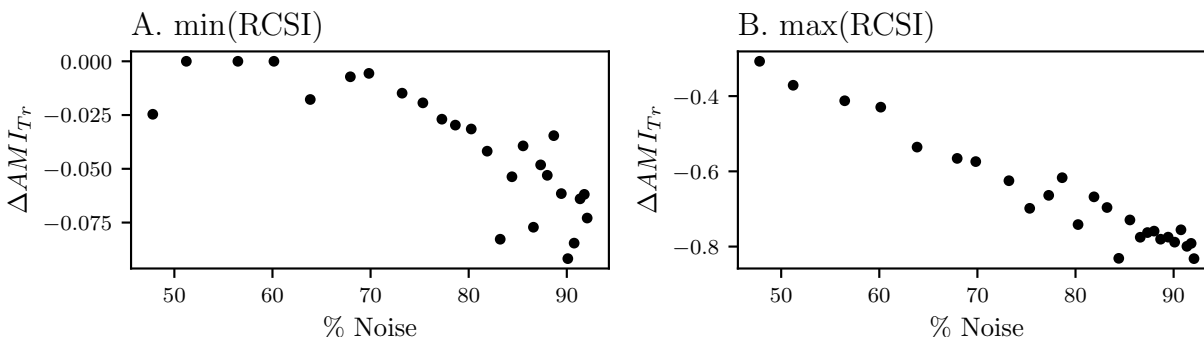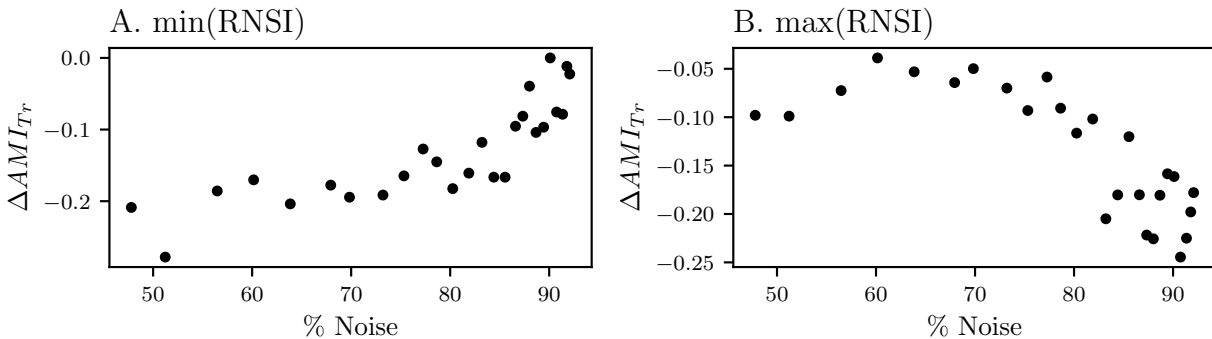
Figure 7.10: Difference in accuracy metrics relative to the maximum observed AMI when minimized (A.) and maximized (B.). The highest observed AMI per noise level is used as a standardization metric to account for the increased difficulty of clustering high noise datasets. Minimization of the RNSI is shown to have increasing accuracy as a function of the noise percentage. Whereas maximization results in increasing accuracy until 70.0% noise at which point there is an abrupt increase in accuracy until there is drop off in the relative accuracy at 90.0%

Minimization of the RNSI in A. depicts the opposite trends of RCSI maximization observed in 7.9B. and provides an increasing accuracy compared to the optimal solution as the noise percentage increases. Maximization on the other hand demonstrates poor relative AMI values above 90.0% noise but values on the same order as the minimization of the RCSI. The decreasing accuracy begins 70.0% which is expected to correspond to the change in the dominant extrema discussed in reference to figure 7.8. It appears then that either min(RCSI) or max(RNSI) are sufficient optimization metrics over the largest range of background levels, but given that the efficacy of min(RCSI) degrades more slowly compared the max(RNSI) it is identified as the optimization metric. To support this claim, the optimized cluster sets for low, medium, and high-noise proportion data are provided in 7.11 through 7.13 alongside the solution that maximizes the AMI.

In the lowest noise scenario at 47.8% the optimal solution in A. found one additional cluster alongside min(RCSI) in B. However, while the extra cluster in A. is due to random clustering of the noise component of the dataset the feature in B. is spatially linked to one of the seeded clusters. In C. the larger selected ϵ from maximizing the RNSI resulted in larger clusters and additional random clusters. Finally, as expected the smaller distance threshold found in D. when minimizing the RNSI resulted in the lowest AMI and clusters which are fragmented due to a high density threshold. In the medium noise scenario of 73.2% the optimal solution in A. found the correct number of cluster and the correct size distribution. The minimization of the RCSI found one additional cluster from the background and a second feature which appears to be a fragment of the seeded clusters. In C. the larger selected ϵ from maximizing the RNSI did not result in larger clusters as in the low-noise scenario but
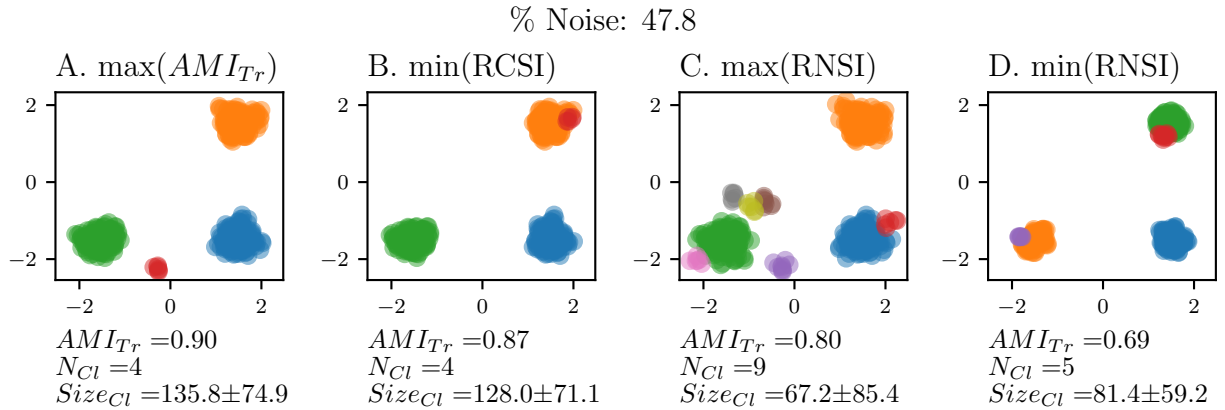
Figure 7.11: Comparison of cluster outputs when using A. max(AMI), B. min(RCSI), C. max(RNSI), and D. min(RNSI) to select ϵ given an order of 6 for a low-noise scenario. In A. a single spurious cluster was found originating from the matrix, while any excess clusters in B. and D. are due to cluster fragments. In C. an extra six clusters were found in close proximity to the real features.
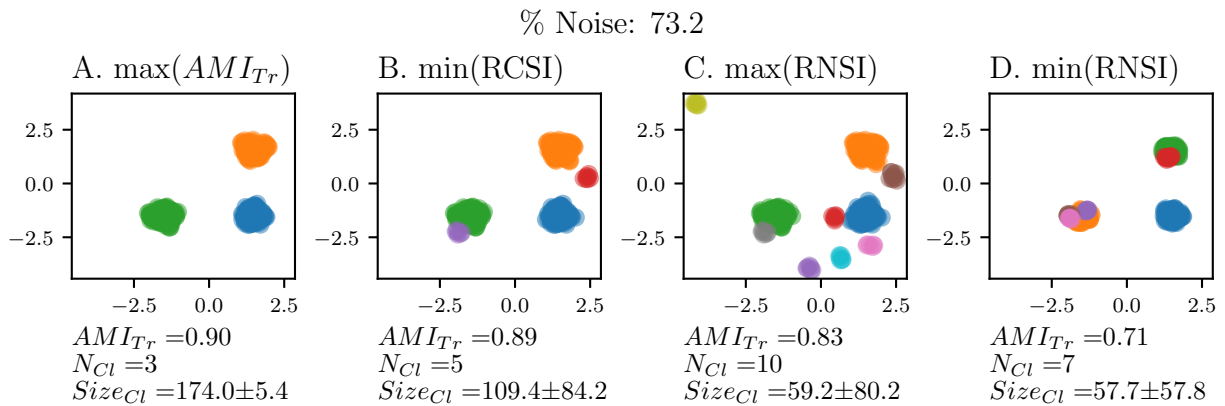
Figure 7.12: Comparison of cluster outputs when using A. max(AMI), B. min(RCSI), C. max(RNSI), and D. min(RNSI) to select ϵ given an order of 6 for a medium-noise scenario. The optimal solution in A. found the exact number of clusters with a correct mean size. B. found two additional clusters, one of which as a cluster fragment and another from the matrix. An additional seven clusters were found in C. arising from the matrix while the excess clusters in D. remain from fragmentation.

% Noise: 92.0

| A. max(AMI_{Tr}) | B. min(RCSI) | C. max(RNSI) | D. min(RNSI) |

AMI_{Tr} =0.88
N_{Cl} =8
$Size_{Cl}$ =68.9±81.0

AMI_{Tr} =0.81
N_{Cl} =17
$Size_{Cl}$ =37.1±66.3

AMI_{Tr} =0.70
N_{Cl} =33
$Size_{Cl}$ =22.6±50.4

AMI_{Tr} =0.86
N_{Cl} =5
$Size_{Cl}$ =94.6±70.5
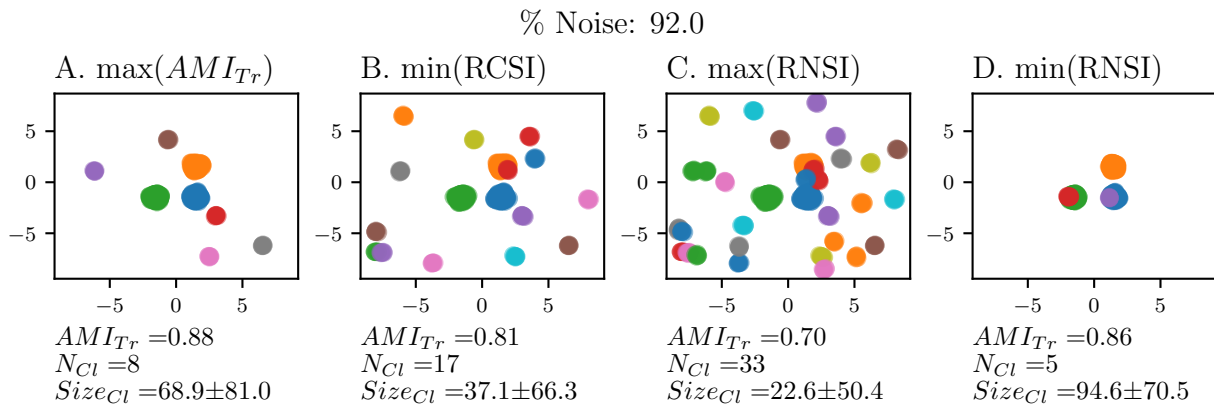
Figure 7.13: Comparison of cluster outputs when using A. max(AMI), B. min(RCSI), C. max(RNSI), and D. min(RNSI) to select ϵ given an order of 6 for a high-noise scenario. In the optimal solution, A., a set of five random clusters were observed in addition to the three known features. B. and C. show the same behavior at increased rate with 14 additional clusters in B. and 30 in C. No additional clusters are found in D. that come from the matrix but instead two clusters are split.

still resulted in seven additional clusters due to the noise. Using the RNSI minima as the metric continued to provide the lowest AMI and result in cluster fragments.

With a noise level of 92.0% the high noise scenario continued the trends observed in the prior two examples when maximizing the AMI and RNSI, as well as minimizing the RCSI where random clusters are found due to the noise in larger amounts. Now, subfigure D. using min(RNSI) as the metric still produced fragments, but no longer had the lowest AMI among the optimization metrics. Instead at an AMI of 0.86 it outperformed both of the other two metrics. Note that because the AMI compares the accuracy of labeling both noise and clustered points it will be biased towards label assignments which correctly identify the largest features, in this case the noise. Because of this while minimization of the RNSI is not ideal for finding the correct clusters it is very efficient at removing the noise component of the data leaving the densest part of the clusters. On the other hand min(RCSI) is less efficient at identifying the noise component but the three largest clusters are much closer to their true sizes.

One final way in which the ambiguity and stability metrics are impacted by noise is the metric continuity with respect to the clustering parameters. Consider the "ideal" case where the clusters exists in a vacuum with nonexistent matrix. In this scenario, the cluster ambiguity is expected to still have two maxima, one of which corresponds to high levels of cluster fragmentation and a second which corresponds to when ϵ is sufficiently large to enable trading of the cluster's border points. In between these two peaks there is an expected zero-ambiguity region where each cluster achieves perfect consensus. Given this scenario each peak of the PAC curve is expected to be continuous given a sufficient number of points within
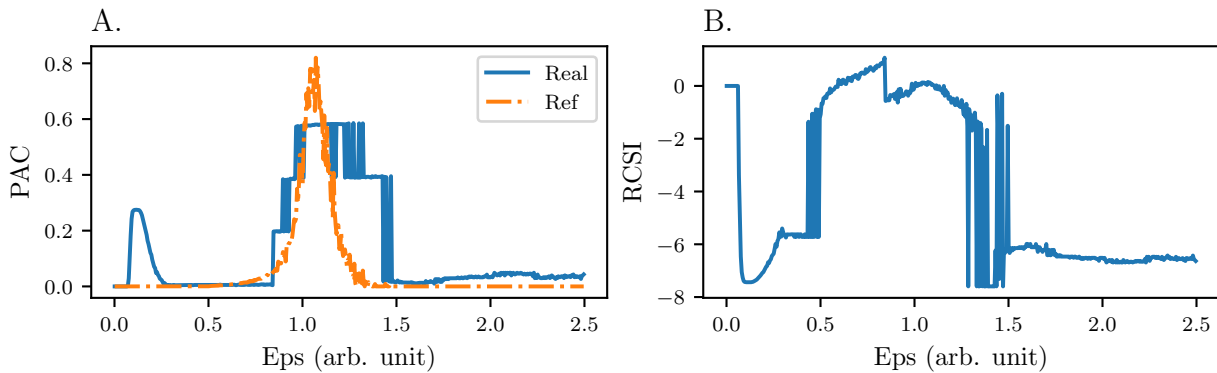
Figure 7.14: Impact of noise incorporation on the proportion of ambiguous clustering (PAC) and relative cluster stability (RCSI) metrics. In subfigure A. the absence of noise results in variable continuity. At low ϵ values continuous behavior is shown during the core formation phase, but exhibits discrete jumps in the remaining three phases. In contrast stands subfigure B, where the addition of 3% noise atoms removed almost all discontinuous jumps. Additionally, the relative size of the core formation extrema is reduced by an order of magnitude. Also show how this makes the position of the extrema match better. i.e. noise enhanced random variable

each cluster and therefore the full curve should be continuous. However, when downsampling the high noise dataset such that the noise level is 10% instead of 90&, the second peak in 7.14A. is surrounded by discrete jumps in the the PAC. The reference data does not show this behavior, but the RCSI in 7.14B. maintains these discrete changes. In the case of PAC this occurs for larger ϵ that corresponds to the few background points being assigned to clusters inconsistently for short spans of ϵ. Once the ϵ is sufficiently large for the current ambigious points it is routinely assigned to the same clusters resulting in a rapid drop in the PAC score. increase the background concentration reestablishes PAC as a continuous measure because individual perturbations do not greatly impact the localized density around each point.

Thus far it has been established that higher levels of background noise, 1. enable naive density estimates that are more representative of the true matrix distribution, 2. establishes more consistent minimization objectives, and 3. ensures that the ambiguity and relative stability metrics remain as continuous objective functions. In other words, the presence of noise is beneficial to DMC3 and enhances the robustness of the algorithms and accuracy of the reference distribution generation. In light of this counter-intuitive reliance on a non-zero noise concentration the term, noise enhanced random variable (NERV) is coined to describe the relative stability indices.
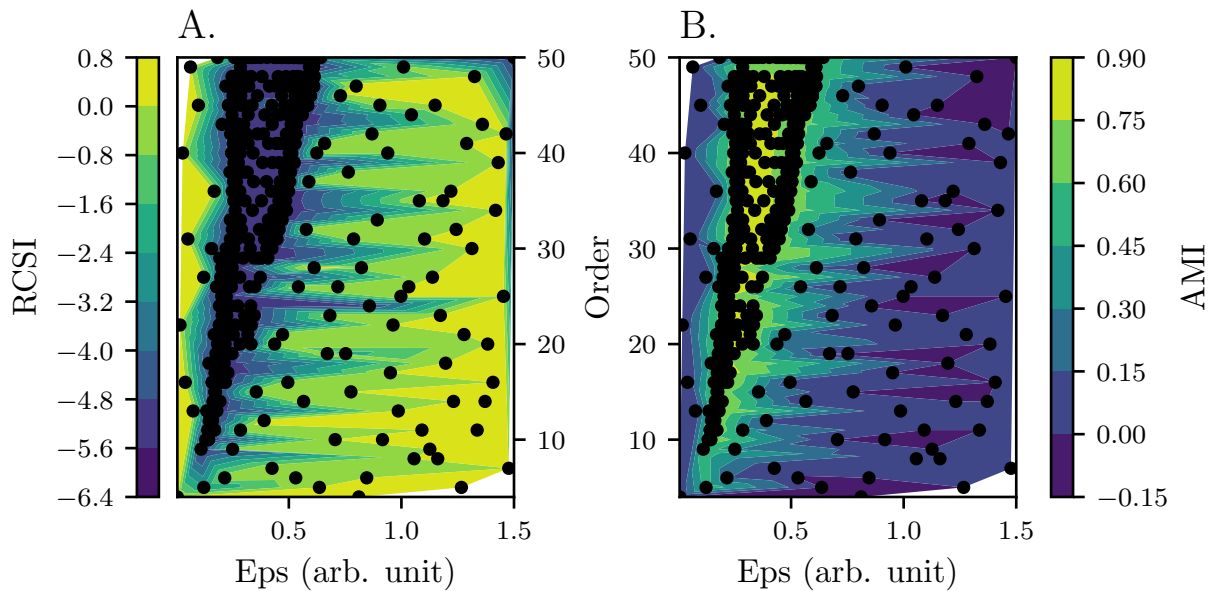
Figure 7.15: Tricontour maps for RCSI (A.) and RNSI (B.) for the 92% matrix dataset. Both RCSI and RNSI are biased towards large order, with (ϵ, O) of $(0.611, 48)$ and $(0.234, 43)$ corresponding to the global minima. The AMI scores for those two positions are 0.62 and 0.59 compared to the most optimal solution with an AMI of 0.81 at $(0.297, 29)$.

Optimal parameter selection for density-based algorithms

Thus far the discussion of parameter optimization has focused on the distance parameter given a fixed order parameter. Extension to a two-parameter optimization has proven problematic due to 1. the computational complexity, and 2. an observed bias in both the RCSI and RNSI metrics. Addressing the computational complexity is trivial in comparison to correcting for the bias and was accomplished by using a gaussian process, available in Head et al. [58], to estimate parameter space and converge on a on a global minima. The goal of using gaussian process regression is to provide an approximation of the RCSI and RNSI metrics expressed as a series of multivariate gaussians [35, 106]. Once initialized given an exploratory search of the parameter space the approximation is used to suggest the next sets of parameters to evaluate which are then used to update the approximation iteratively. While the initial generation is costly the gaussian process limits the number of function evaluations needed to converge compared to traditional optimization routines. Due to the increased efficiency compared to line-scans as was done in the prior section the metric's bias was discovered and is shown by the contour maps in figure 7.15.

It is evident that both metrics are biased towards the selection of high order parameters which does not correspond with the highest accuracy scores when measured by the adjusted mutual information. This limits the efficacy of DMC3 as a general method for two-parameter

optimization but specifically impacts the ability of DMC3 to identify small clusters when both DBSCAN input parameters are variable. Fixing the order parameter however does enable optimization of the ϵ parameter.

Cluster filtration by perturbation statistics

Filtration of cluster sets based on a minimum feature size is commonplace within both the atom probe and clustering communities. The minimum feature size is normally set by analyzing the cluster size distribution with the rational being that the size distribution is bimodal with a peak or small clusters due to random density fluctuations and a peak corresponding to the average feature size assuming they are homogeneous. However, the number of clusters present serves as a fundamental limit when estimating the size distribution and the bimodal assumption is not guarantied. One method to circumvent this limitation is to instead approximate the size distribution for a uniform point cloud and set the minimum cluster size such that it minimizes the chance of a cluster from the uniform background to be included in the final cluster set. This approach is expanded upon for DMC3 by exploiting the perturbed datasets to increase the sample size.

Using the high-noise dataset from 7.2 as an example originally only 17 clusters were observed and on average only 22.3 clusters were found in the non-perturbed references. Inclusion of the cluster sets from the perturbed data increases the sample size of real clusters from 17 to 2113 and increases the reference clusters from 22.3 per reference to 2, 229. In total there are 55, 630 samples with which to generate any cluster statistics of interest. In this case, we investigate the cluster size, in figure 7.16A, as is done in conventional approaches, but also include the cluster consensus scores in figure 7.16B.

In the above size distributions the reference data has a zero-probability chance for clusters greater than 17 points in size. Choosing this as the min sample size is an aggressive filtration step which removes 1, 809 of the clusters from the analysis of the perturbed data resulting in a mean cluster size of 160.8 instead of 28.8. Furthermore, applying this constraint to the non-perturbed data reduces the number of clusters from 17 to three and increase the mean size from 37.1 to 180.3. Given that three clusters were seeded with mean size of 175 the resulting cluster sets are much closer to the truth given this filtration. This is confirmed by the AMI which improves from 0.807 to 0.920 which is comparable to the accuracy of the low-noise scenario.

The same style of filtration can be performed with the cluster consensus scores as well. Using the same simplistic threshold the maximum consensus found in the perturbed references is 0.055. With this threshold the mean size of the perturbed clusters is 81.96, while four clusters of mean size 82.0 were found in the non-perturbed data. This filtration step is less effective than using the cluster size and only improves the AMI to 0.916. Both of the above flirtations are rudimentary and only made use of the reference distributions, while the main benefit of the perturbation statistics is for the implementation of more complex filters such as those based off of conditional probabilities. Furthermore, using multiple independent test statistics such as size and consensus in tandem enables the clusters to be grouped to
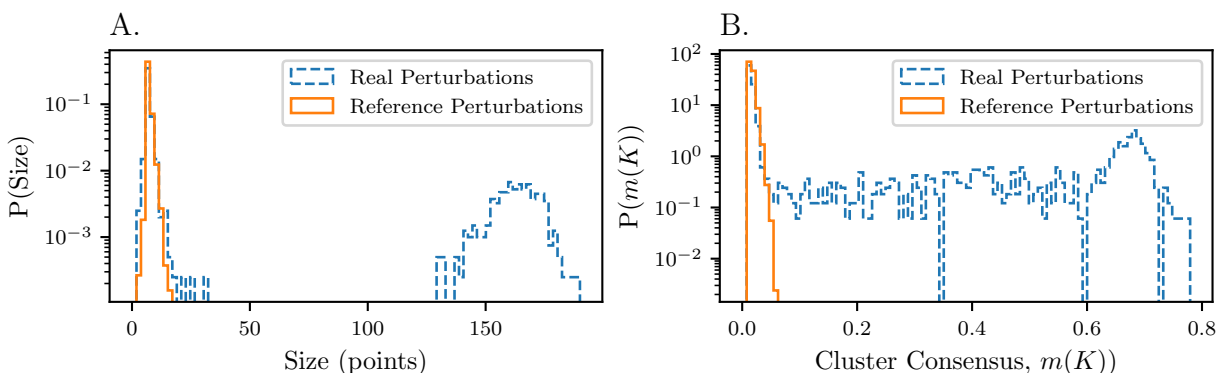
Figure 7.16: Perturbation statistics for cluster size, A., and cluster consensus B. For the perturbations of the real datasets containing clusters and the references representative of matrix distribution. The perturbations of the real dataset have a bimodal distribution in both cases as expected but additionally has a non-zero consensus between the two modes for the cluster consensus. The reference distributions have a unimodal distribution based around small clusters with low consensus representing clusters which originate from random matrix clustering.

better understand what the different clusters represent. As shown in figure 7.17A. the scatter plot of the size and consensus is composed of two subfeatures. One of which corresponds to large cluster size and high consensus which compose the cluster cores as confirmed by plotting the point clouds for all perturbations in figure 7.17B. This leaves the the second grouping for small cluster size that expands over the entire range of consensus values. By introducing the statistics for the reference distributions this feature is further split into a low and high-consensus region. The high-consensus region corresponds the boundary region of the clusters as indicated by the ring structures in figure 7.17D. while the low-consensus region is representative of the random clustering originating in the background distribution.
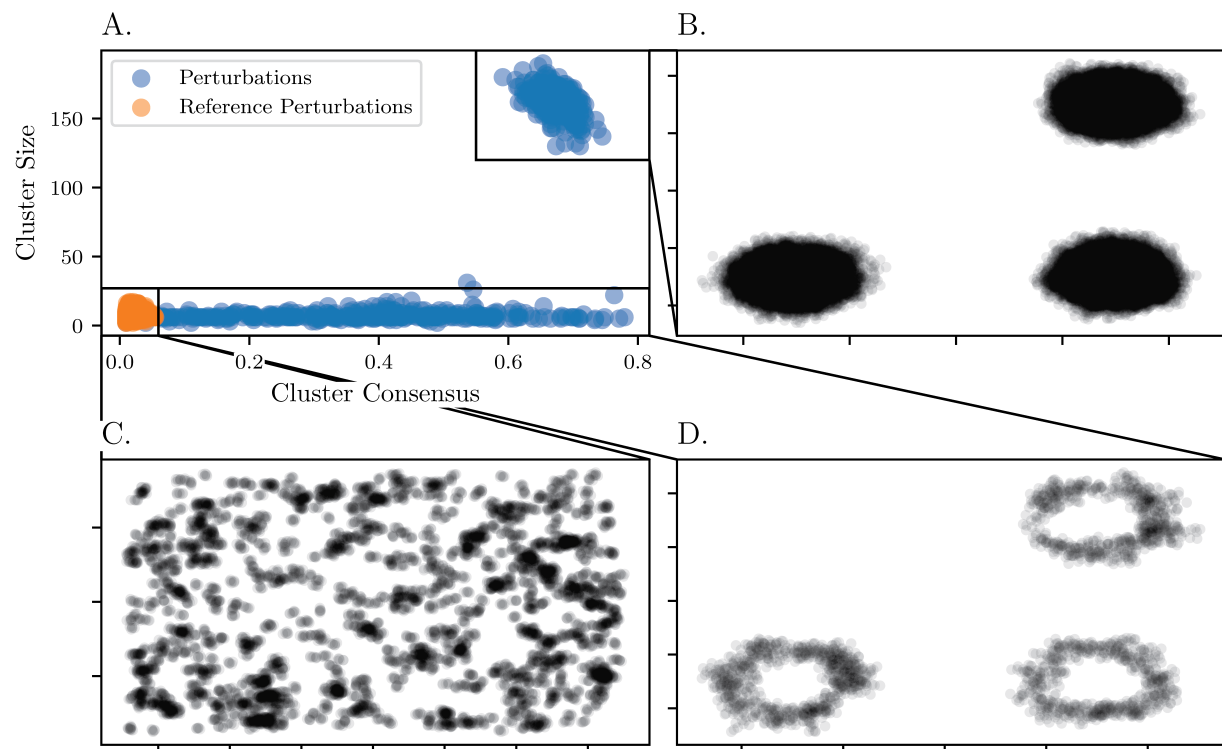
Figure 7.17: 2D scatter plot of cluster size and cluster consensus for the perturbed datasets, A., alongside the portions of the dataset corresponding to each region of the scatter plot. The cluster cores correlating with large sizes and high consensus are presented in B. while the interfaces between the clusters and the matrix are expressed in D. as a ring structure. The random clusters represented by small size and low consensus are plotted in C.

Chapter 8

Application of DMC3 to simulated Fe-Cu alloys

To demonstrate the efficacy of DMC3 with respect to conventional clustering of atom probe specimens a DMC3 is used to set the ϵ parameter for a given order and min points on a series of synthetic APT datasets. These datasets originate from a round robin study where nine different atom probe groups analyzed the same data to both develop best practices for clustering and to determine the expected clustering variability due to user bias [78, 27]. According to the data generation tools published by the Marquis group for subsequent work it is believed that each of the datasets started with an FCC iron lattice with a random solution of Cu atoms in the matrix achieved by randomly replacing Fe atoms [46, 47]. Additional Cu was added to the dataset as Cu-rich precipitates by randomly changing the Fe atoms within a fixed region of interest per cluster to the target composition. To generate smooth concentration gradients a gaussian displacement was applied to each atom with the delocalization distance set to be a multiple of the lattice parameter. Finally, downsampling was applied to replicate the detection efficiency, 37%, of the atom probe.

While the above data generation process is believed to be the same as in Marquis et al. [78] it could not be verified and so in order to provide a direct comparison with the literature the original data from the round robin study was acquired from the researchers at Pacific Northwest National Lab who partook in the study. However, as this data does not come with cluster labels a set of similar synthetic datasets were generated using the toolbox developed for Ghamarian and Marquis [46] and Ghamarian, Yu, and Marquis [47]. The datasets in the original study were referred to as D1, D2, D3, and D4 but in this work DM will be used to denote the round robin datasets and DE will specify that the data was newly produced for this work. A visual overview of the DM data is provided in figure 8.1 while the cluster properties; size (atoms), radius (nm), Cu concentration, and the matrix Cu concentration are provided in table 8.1.

While the original study was primarily concerned with the number of observed clusters and the mean size the logical extension is to consider the impact of user bias and the associated uncertainty on nuclear relevant properties such as hardness. Under the dispersed

A. DM1   B. DM2   C. DM3   D. DM4
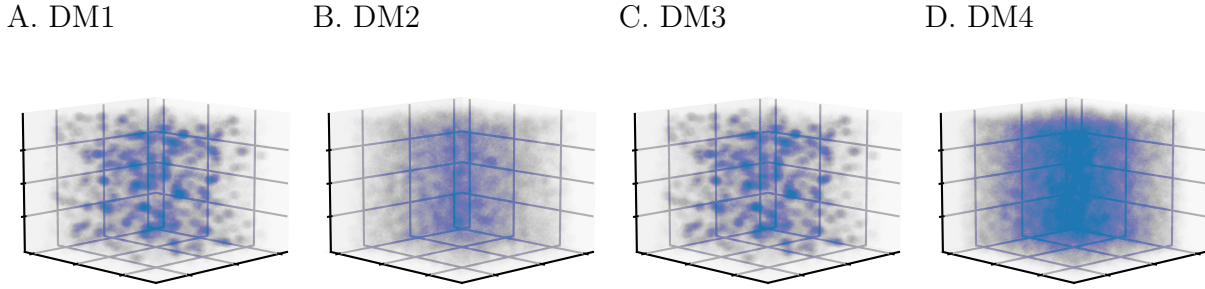
Figure 8.1: Comparison of the four datasets from Marquis et al. [78]. Dataset 1, or DM1, is a high contrast dataset with large separation distance between clusters. Dataset 2, or DM2, focuses on identification of small clusters. Dataset 3, or DM3, contains many large clusters in close proximity to one another. Dataset 4, or DM4, contains a high background concentration of Cu which makes visualizing the clusters impossible even with downsampling of the point cloud.

Table 8.1: Cluster and matrix properties for the four synthetic datasets analyzed in Marquis et al. [78]. All properties except for the size as measured in number of atoms are provided in the literature while the sizes were specified according to internal documents [105]). N_k indicates the number of clusters and composition is abbreviated to comp.

Dataset	N_k	Radius (nm)	Size (atoms)	Cluster Comp. (at. %)	Matrix Comp. (at. %)	Inter-cluster Spacing (nm)
DM1	176	1.1 ± 0.1	139	75	< 0.07	5
DM2	96	1.2 ± 0.1	30	20	< 0.07	6
DM3	275	1.2 ± 0.1	44	40	< 0.07	2.2
DM4	169	1.0 ± 0.1	30	30	10	6

barrier hardening model the expected hardening for each set of calculations is calculated according to equation 8.1b[4, 116].

$$\Delta \sigma_Y = m\alpha\mu b\sqrt{Nd} \tag{8.1a}$$

$$= m\alpha\mu b\sqrt{2Nr} \tag{8.1b}$$

Where $m = 3.06$ is the Taylor factor of the FCC system, $\mu = 86 GPa$ is the shear modulus of 304SS, $b = a_0\sqrt{3}/2$ is the burgers vector of the $< 111 >$ family of dislocations, N is the number density, and d is the precipitate diameter [97, 104, 116, 4, 126]. The strengthening

Table 8.2: Discrepancy in cluster sizes when measured by radius and atom number as well as the calculated sizes given the other property.

Dataset	Radius (nm)	Radius(Size) (nm)	Size (atoms)	Size(Radius) (atoms)
DM1	1.1 ± 0.1	1.04	139	142 ± 38
DM2	1.2 ± 0.1	1.02	30	49 ± 12
DM3	1.2 ± 0.1	0.92	44	98 ± 23
DM4	1.0 ± 0.1	0.91	30	40 ± 12

parameter α is size-dependent and given by Hu et al. [59] as equation 8.2b

$$\alpha = 1 - exp\left[-\left(\frac{d}{d_{ref}}\right)^n\right] \tag{8.2a}$$

$$= 1 - exp\left[-\left(\frac{2r}{d_{ref}}\right)^n\right] \tag{8.2b}$$

Here the reference diameter, d_{ref}, and the scaling parameter, n, are set to 4 nm and 2 as in Bai et al. [4]. To make use of the hardening and scaling equations for cluster sets either the number of atoms must be converted into a physical radius or the radius must be calculated from the point cloud. The latter is sensitive to aberrations from the reconstruction so the former is used with the equivalent radius governed by equation 8.3[4].

$$r = \left(\frac{n_{Cu}}{\eta}\frac{3V_{Cu}}{4\pi f_{Cu}}\right)^{1/3} \tag{8.3}$$

This modification of the equations described in Bai et al. [4] accounts for the atom probe detection efficiency, η, to calculate the radius as a function of Cu's atomic volume, V_{Cu} and the atomic fraction of Cu, f_{Cu}. Applying this conversion to the reported cluster sizes in atoms and the inverse to the radius we find that there is a discrepancy in the cluster sizes as reported. Generally the reported cluster radii are larger than the calculated values while the reported atom numbers are lower than expected given the radii. These observations are detailed in table 8.2. In light of this the expect3d hardening for each dataset is calculated with the reported size as measured in atoms and not the reported radii.

8.1   Dataset 1: large clusters with high concentration contrast

The original dataset, DM1, and the new equivalent set, DE1, were designed as the simplest data to accurately cluster by having both large features with high spatial separation and a high contrast with respect to the Cu composition of the clusters and matrix. DE1 was

Figure 8.2: Cluster set properties (A.) and adjusted mutual information scores (B.) for optimized DBSCAN parameter sets for DE1, a low noise high contrast FCC dataset. On average DMC3 underestimated the number of clusters and overestimated their sizes, but still maintained high AMI's exceeding 0.8 for all parameter sets. Setting order and min points both to 6 produced the best cluster set when measured by AMI.

produced using the cluster maker code provided by the Marquis group with the cluster radius set to 1.1 ± 0.1, cluster Cu concentration of 75%, matrix Cu concentration of 0.07%, inter-cluster spacing of 5 nm, and 176 clusters [46, 48]. The primary goal of this second dataset is to provide a dataset with a known solution as that information was omitted in the round robin dataset. Using the cluster labels to estimate the cluster size in atoms we find that the clusters are 143 ± 25 as opposed to 139 atoms for DM1. Unlike DM1 this results in the radius and number of atoms of the clusters being in agreement as estimating the number of atoms from radius gives 142 ± 38 and a radius given size of 1.09 ± 0.07.

Fixing the order and min point parameters according to those used by each group during the round robin DMC3 was used to optimize the epsilon parameter, ϵ. Note that the clustering parameters were not provided in Marquis et al. [78] but were acquired from internal documents [105]. The differences in the cluster number and sizes are provided in figure 8.2A, while the adjusted mutual information score per parameter set is from 8.2B.

From 8.2A. it is clear that DMC3 overestimated the cluster sizes at the cost of underestimated the number of clusters found in DM1. At worst the mean cluster size was 8 atoms larger than the expected value of 143 and only 168 clusters were extracted instead of 176. The closest in terms of absolute properties were the parameters for group 8, with a deficit of only 5 clusters and an excess in mean size of 1.5 atoms. This group however is not optimal when the known cluster labels are used for comparison, in this case the best AMI is achieved by group 7 with group 6 as the second best showing that the best match in terms of cluster properties is not inherently the most accurate dataset.

Moving on to DM1, the first comparison of cluster sizes is maintained (figure 8.3A.) but instead of using AMI as the second point of comparison the expected hardening (figure 8.3B.) using the dispersed barrier hardening model is used given estimated cluster sets. Note that

Figure 8.3: Comparison of the as reported group properties to the DMC3 optimized cluster parameters for DM1, a low noise high contrast FCC dataset. Subfigure A. compares the estimates of cluster number and size (atoms) while subfigure B. compares the calculated hardening with the expected hardening given the reported true cluster properties [78]. Hollow markers indicate the DMC3 results while solid indicate the literature reference. The span is indicative of the target hardening value's one standard deviation bounds.

group 9's results reported an excess of 60 clusters and is omitted from property comparison to improve the resolution when comparing the remaining groups. The first observation is that all groups regardless of DMC3 underestimate the cluster size which is in stark contrast to the analysis of DE1. Furthermore the DMC3 results tend to overestimate the number of clusters. Together with the earlier observation on the cluster sizes it reinforces the belief that either A. the data generation process is not the same or B. some properties were not accurately reported. Looking at figure 8.3B. the mean hardening, $\Delta\sigma_Y$, predicted by DMC3 is on the lower end of the expected hardening with one standard deviation extending to the upper bound of the expected value. Groups 1, 4, 6, 7, and 8 report a closer hardness value to the expected compared to DMC3 while 5 and 2 are lower. All of the clusters sets with the exception of group 9 do fall within the one σ bounds of the expected. Do note that the errors on cluster size are not known for the reference experiments.

8.2 Dataset 2: small clusters with low concentration contrast

The original dataset, DM2, and the new equivalent set, DE2, were designed to emulate the challenge of identifying small clusters with a lower Cu contrast. DE2 was generated with the following input parameters; cluster radius of 1.2 ± 0.1, cluster Cu concentration of 20%, matrix Cu concentration of 0.07%, inter-cluster spacing of 6 nm, and 96 clusters [46, 48]. Using the cluster labels to estimate the cluster size in atoms we find that the clusters are 49 ± 10 as opposed to 30 atoms for DM2. Unlike DM2 this results in the radius and number
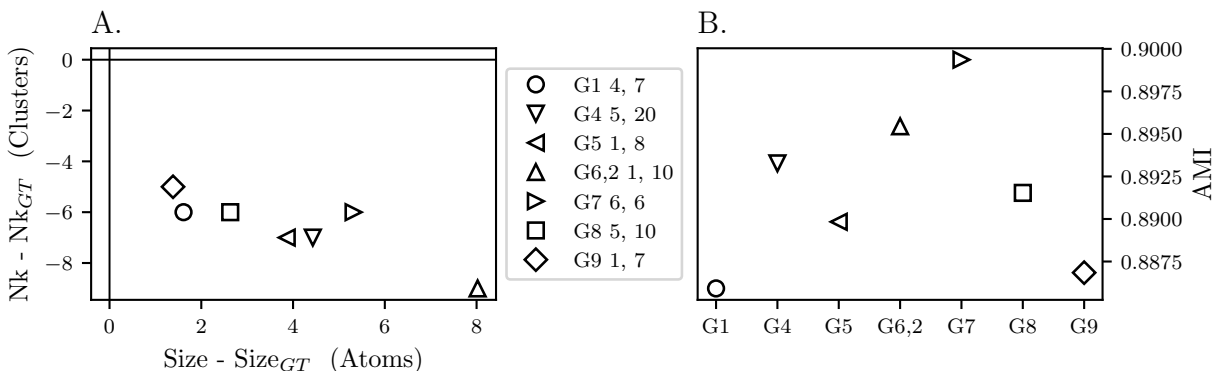
Figure 8.4: Cluster set properties (A.) and adjusted mutual information scores (B.) for optimized DBSCAN parameter sets for DE2, a small cluster low contrast FCC dataset. On average DMC3 overestimated the number of clusters and their sizes, but still maintained AMIs ranging from 0.74 to 0.8 for all parameter sets. Setting order and min points to 8 and 11 produced the best cluster set when measured by AMI.

of atoms of the clusters being in agreement as estimating the number of atoms from radius gives 49 ± 12 and a radius given size of 1.19 ± 0.08.

Once again the order and min point parameters were fixed according to those used by each group during the round robin with epsilon being selected by DMC3. Note that the clustering parameters were not provided in Marquis et al. [78] but were acquired from internal documents [105]. The differences in the cluster number and sizes are provided in figure 8.4A, while the adjusted mutual information score per parameter set is from 8.4B.

From 8.4A. it is clear that DMC3 generally overestimated the cluster sizes and numbers found in DM2. This difference compared to DM1 is likely due to the a lower density threshold which allowed random clusters to be found in the matrix and additional matrix atoms to be added to the clusters. At worst the mean cluster size was 15 atoms larger than the expected value of 49 and 103 clusters were extracted instead of 96. The closest in terms of absolute properties were the parameters for group 6, with an excess of only 1 cluster and an excess in mean size of 5 atoms. This group is nearly optimal with an AMI of 0.78 when the known cluster labels are used for comparison. The optimal AMI is achieved for group 1's parameters which finds an extra two clusters and has a mean size of 58 atoms. Half of the parameter sets estimated the cluster size within one standard deviation of the true mean size and all parameter sets were correct within two standard deviations.

Moving on to DM2, the first comparison of cluster sizes is maintained (figure 8.5A.) and the second point of comparison the expected hardening (figure 8.5B.) using the dispersed barrier hardening model. The first observation is that DMC3 consistently underestimates the number of clusters which is once again the opposite of the observations for our generated data. More often than not it also overestimates the feature sizes. The reference data does not consistently over/underestimate the number of cluster sizes but the groups with the
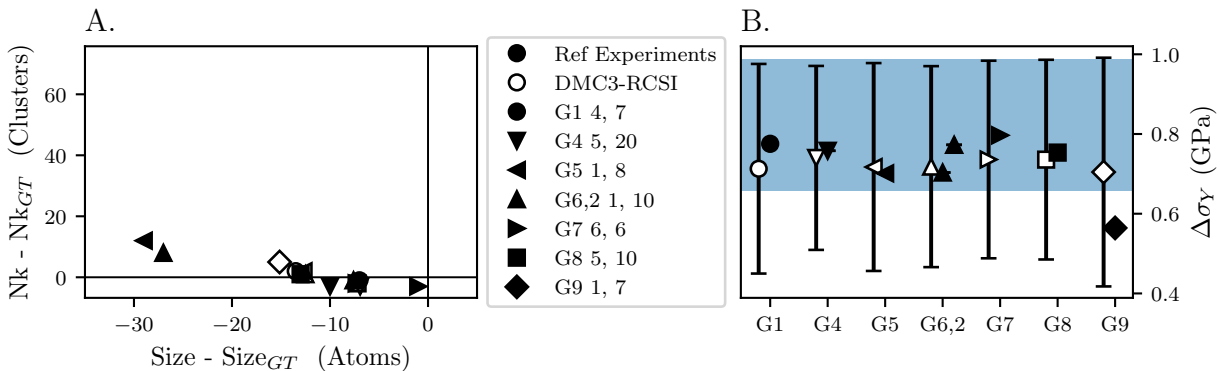
Figure 8.5: Comparison of the as reported group properties to the DMC3 optimized cluster parameters for DM2, a small cluster low contrast FCC dataset. Subfigure A. compares the estimates of cluster number and size (atoms) while subfigure B. compares the calculated hardening with the expected hardening given the reported true cluster properties [78]. Hollow markers indicate the DMC3 results while solid indicate the literature reference. The span is indicative of the target hardening value's one standard deviation bounds.

closer estimate of cluster number tend to overestimate the size, see groups 5, 4, and 7. These observations reinforces the belief that either A. the data generation process is not the same or B. some properties were not accurately reported. Looking at figure 8.5B. the mean hardening, $\Delta\sigma_Y$, predicted by DMC3 is not consistently on the high or low end of the expected hardening. With the exception of group 6 the DMC3 hardness values are closer to the expected value. All of the DMC3 clusters sets fall within the one σ bounds while only four of the results from Marquis et al. [78] fall within this range.

8.3 Dataset 3: clusters with low separation distance

The original dataset, DM3, and the new equivalent set, DE3, were designed to emulate the challenge of identifying clusters in close proximity. A common error for this type of data is merging of adjacent clusters which will result in overestimates to cluster size and an underestimate of the number of clusters. DE3 was generated with the following input parameters; cluster radius of 1.2 ± 0.1, cluster Cu concentration of 40%, matrix Cu concentration of 0.07%, inter-cluster spacing of 2.2 nm, and 275 clusters [46, 48]. Using the cluster labels to estimate the cluster size in atoms we find that the clusters are 98 ± 16 as opposed to 44 atoms for DM3. Unlike DM3 this results in the radius and number of atoms of the clusters being in agreement as estimating the number of atoms from radius gives 98 ± 24 and a radius given size of 1.19 ± 0.07.

Once again the order and min point parameters were fixed according to those used by each group during the round robin with epsilon being selected by DMC3. Note that the
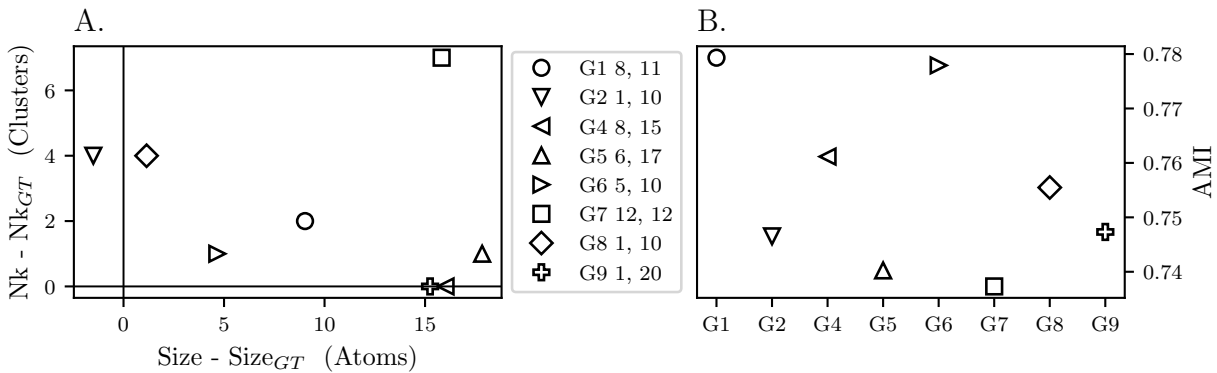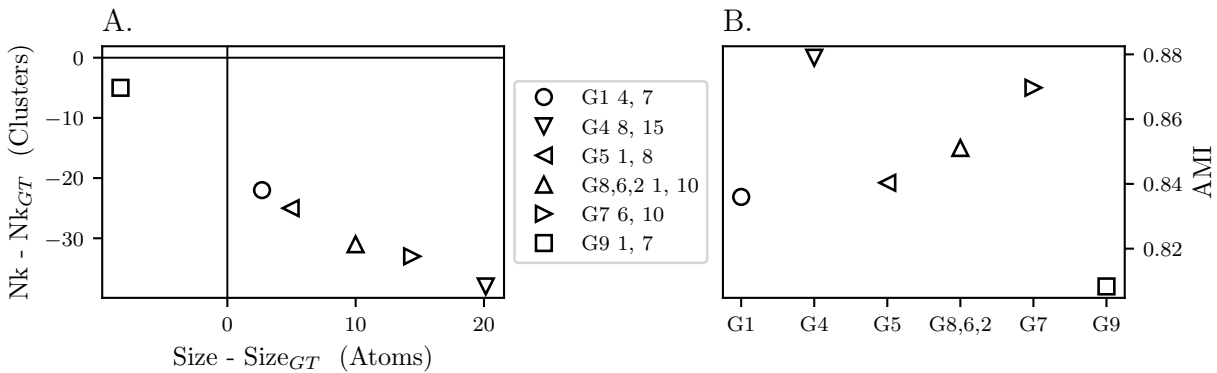
Figure 8.6: Cluster set properties (A.) and adjusted mutual information scores (B.) for optimized DBSCAN parameter sets for DE3, a low noise high contrast FCC dataset. On average DMC3 underestimated the number of clusters and overestimated their sizes, but still maintained high AMI's exceeding 0.8 for all parameter sets. Setting order and min points both to 8 and 15 produced the best cluster set when measured by AMI.

clustering parameters were not provided in Marquis et al. [78] but were acquired from internal documents [105]. The differences in the cluster number and sizes are provided in figure 8.6A, while the adjusted mutual information score per parameter set is from 8.6B.

From figure 8.6A. it is clear that DMC3 merged clusters resulting in a gross underestimation of cluster number and larger cluster sizes than exist. At worst the mean cluster size was 20 atoms larger than the expected value of 98 and 240 clusters were extracted instead of 275. The closest in terms of cluster number were the group 9 parameters with approximately 270 clusters and a size deficit of 8 atoms on average. On the other hand group 1 produced the cluster set with the smallest overestimate in size. In figure 8.6B. it is evident that despite the group 4 parameters resulting in the largest difference with respect to cluster size and number it is the most accurate clustering given an AMI of 0.88. Four of the six parameter sets resulted in a mean cluster size estimate within one standard deviation.

Moving on to DM3, the first comparison of cluster sizes is maintained (figure 8.7A.) and the second point of comparison the expected hardening (figure 8.7B.) using the dispersed barrier hardening model. The first observation is that DMC3 underestimates the number of clusters and overestimates the size in agreement with the belief that clusters are being merger. Of note however is the magnitude as the group 4 parameter set overestimated size by only 20 atoms for DE3 but is overestimating the DM3 sizes by 80. It should be noted that this difference could be explained by the noted discrepancy in reported cluster sizes as given the reported radius 98 atoms would be expected in DM3 which would drop the overestimate by approximately 50 atoms. On average most groups from the literature underestimate cluster number and overestimate the size with exceptions for group 5 and 9. Looking at figure 8.7B. the mean hardening, $\Delta\sigma_Y$, predicted by DMC3 is consistently higher than the expected value with its one standard deviation error bar approaching the
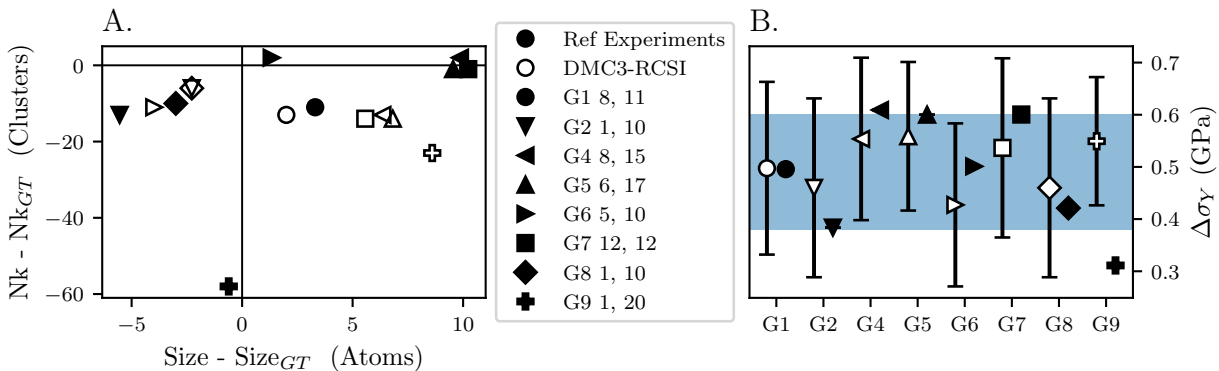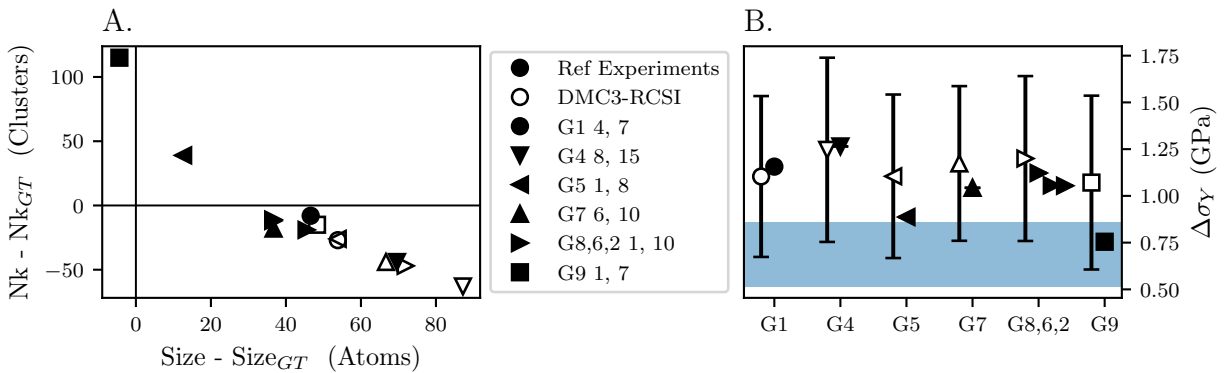
Figure 8.7: Comparison of the as reported group properties to the DMC3 optimized cluster parameters for DM3, a low inter-cluster separation distance FCC dataset. Subfigure A. compares the estimates of cluster number and size (atoms) while subfigure B. compares the calculated hardening with the expected hardening given the reported true cluster properties [78]. Hollow markers indicate the DMC3 results while solid indicate the literature reference. The span is indicative of the target hardening value's one standard deviation bounds.

mean value. There is not a clear pattern indicating if DMC3 or the literature reference data provide more accurate estimates of hardening, but groups 5 and 9 are the closest with group 9 being the only estimate to value within target range.

8.4 Dataset 4: small cluster with 10% matrix concentration.

Prior attempts to perform clustering on DM4 exposed a fundamental flaw in relying on estimates of cluster number and size alone to gauge group performance. Out of the groups that used density-based clustering algorithms in Marquis et al. [78] group 7 was the only one to identify more than 100 clusters with 170 clusters found with a mean size of 69 atoms, however this result is described as "a result of chance". When compared to the ground truth group 7 missed identifying some subset of the clusters and found an equivalent number of random clusters resulting in a "accurate" estimate of the cluster number. In light of this we diverge from the analysis method carried out for the prior three datasets and initially perform clustering on DE4 for a single set of order and min points parameters set at $(10, 1)$. The cluster results for DMC3 are then compared to the best-case clustering results using the adjusted mutual information, given that the labels are known for DE4, to assess what further post processing may be of use for DM4.

The intent was then to cluster DM4 using the parameters found by applying DMC3 to DE4, however due to a discrepancy between the listed cluster Cu content in the internal documents and the published paper DE4 was generated with a cluster concentration of 40%

instead of 30% as was reported in Marquis et al. [78]. Ignoring the prior discrepancy with respect to cluster radius and size this further reduces the ability to generalize from DE4 to DM4.

DE4 was generated with the following input parameters; cluster radius of 1.0 ± 0.1, cluster Cu concentration of 40%, matrix Cu concentration of 10%, inter-cluster spacing of 6 nm, and 169 clusters [105]. Using the cluster labels to estimate the cluster size in atoms we find that the clusters are 58 ± 11 which are roughly double the expected size for DM4. Due to the large size of DE4 with an excess of 800,000 Cu atoms a spatial subset of the data consisting of only 90,000 Cu atoms is used to optimize the epsilon parameter. Unlike subsampling which distorts the point cloud density taking a spatial subset maintains the density and noise-to-cluster ratio of the data while enabling a similar increase in speed. Even then DMC3 took approximately nine hours to analyze 100 values for ϵ.

Given a fixed order of 10 and min points set to 1 DMC3 identified an ϵ of 0.5777 by minimizing the RCSI. The resulting cluster set presented in figure 8.8a. however significantly differs from the ground truth in subfigure B and found $1,122$ clusters with sizes of 12 ± 6 atoms. The AMI score for this label assignment is the lowest of all the DE datasets at 0.158 recalling that 0 is equivalent to random labeling and 1 is perfect. However, for these fixed order and min point parameters the best AMI scores that can be achieved was found to be only 0.159 corresponding to an $]epsilon$ of 0.5771. In other words DMC3 was as accurate as possible for the single-parameter optimization and a multiobjective optimization routine is imperative for use with difficult to cluster datasets.

Following this revelation, attempts were made to reincorporate min points as a parameter by plotting the cluster size distributions in figure 8.9 alongside the cluster consensus distributions. Theses statistics were additionally calculated for 24 reference datasets describing the null hypothesis. From this two thresholds can be identified based on the likelihood of a cluster with a given size or consensus originating from the matrix or as an actual component of a cluster. In doing so 146 clusters in the upper right quadrant of figure 8.9C. are selected as the improved cluster estimate and plotted in figure 8.10. While the mean size does not reach the expected value the mean cluster size does increase from 12 to 23 atoms and the AMI score increase from 0.158 to 0.212.

A. DMC3 Clusters: 1122

B. True Clusters: 169
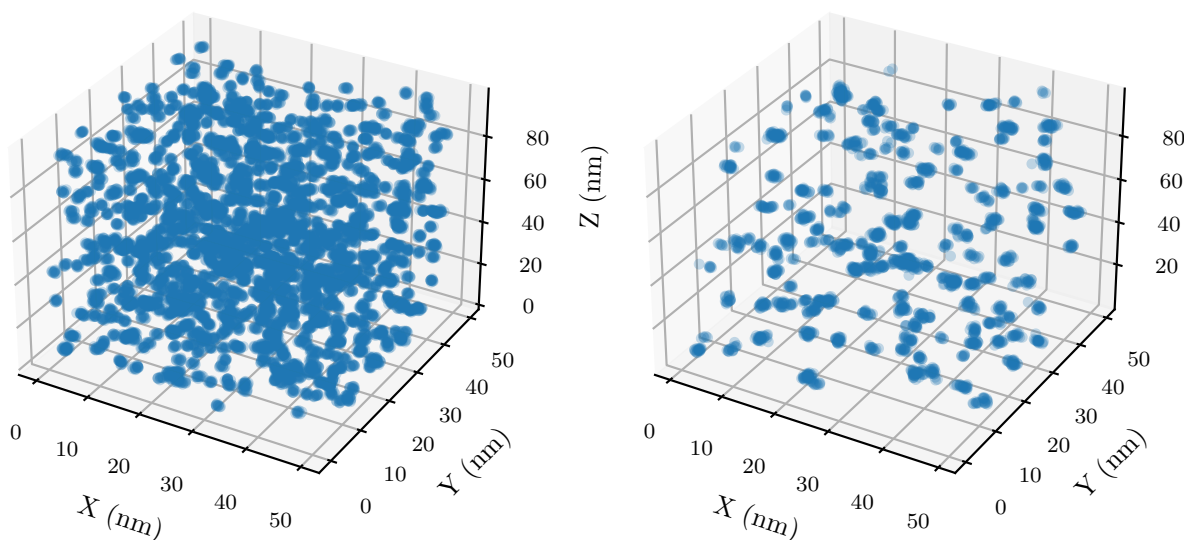
Figure 8.8: DMC3 identified clusters (A.) alongside the ground truth cluster (B.) for DE4, a high matrix concentration dataset. $1,122$ clusters were found with a mean size of 12 atoms instead of 169 clusters with mean size of 56. The accuracy as measured by AMI was 0.159.
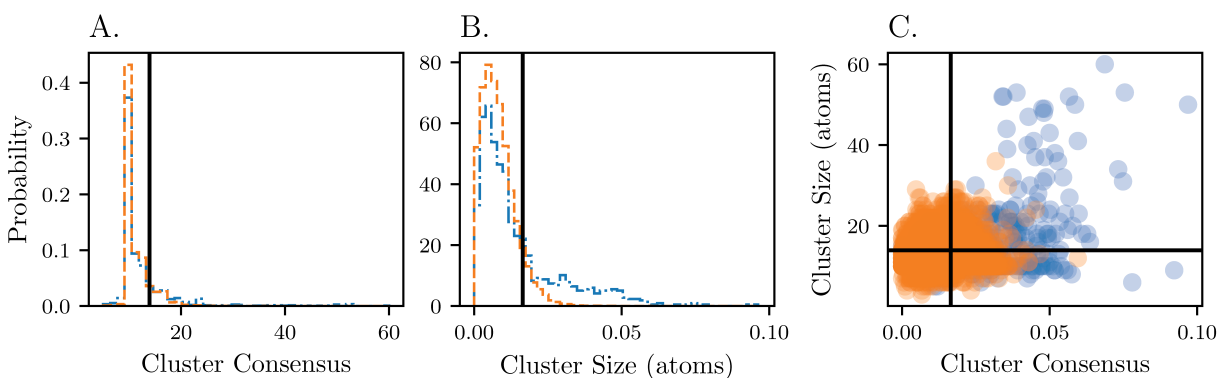
Figure 8.9: Post-processing efforts for the DMC3 cluster set based on cluster consensus (A.) and cluster size (B.). The scatter plot in C. is then separated based off the identified threshold values establishing a new cluster set occupying the upper right quadrant. Orange measurements are from clustering of 24 reference datasets and the blue result from DE4.
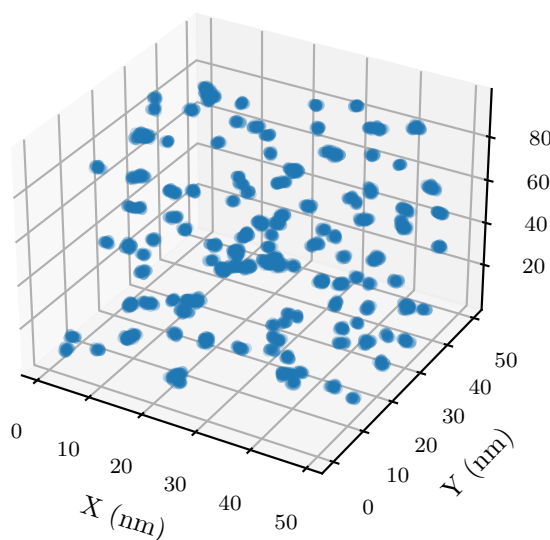
A. DMC3 Clusters: 146   B. True Clusters: 169
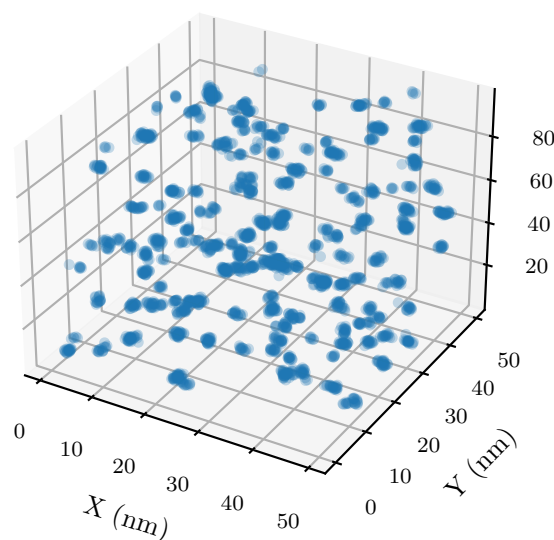
Figure 8.10: DMC3 identified clusters with post-processing based on size and consensus (A.) alongside the ground truth cluster (B.) for DE4, a high matrix concentration dataset. The original $1,122$ clusters was reduced to 146 and the mean size of 12 atoms was increased to 23 instead of the expected 169 clusters with mean size of 56. The AMI improved from 0.159 to 0.212.

Chapter 9

Conclusion

9.1 The uncertainty of Atom Probe

This work had proposed the pointwise uncertainty in atom probe was worse in the depth
dimension and even scaled cumulatively. This hypothesis appears to stand in contradiction
to studies focusing on the resolution of atom probe, however as demonstrated there is a
high degree of correlation between each coordinate estimate such that the pointwise error is
not expected significantly impact local calculations which resolution estimates from spatial
distribution maps, etc. rely on. This hypothesis was shown to hold in theory based upon
application of linear error propagation for all possible atom probe input parameters enabled
sensitivity analysis to be performed for all three atom probe coordinates. Generally, the X
and Y coordinates were found to be most sensitive to the image compression factor, ξ and
the field factor k_f while the depth coordinate had an additionally sensitivity to the ionic
volumes, Ω.

Furthermore, this study demonstrated how the calibration of an isotopically-enriched thin
film based on curvature and interatomic spacing was able to provide the initial parameter
uncertainties for propagation not just through the reconstruction but even to the calculation
of the thin film thickness. The thin film was measured by the FWHM to range from 5.0 nm
to 5.4 nm near the center of the specimen but was shown to be sensitive to over compression
of the point cloud near the reconstruction's edge resulting in a 4.6 nm width. Our results
fell on the lower end of the growth's target thickness of 5 to 6 nm.

9.2 Use of Density-based Monte-Carlo Consensus Clustering

On the clustering front the main goal of this work was to automate DBSCAN's parameter
selection by modifying a consensus clustering approach to work for density-based clustering
algorithms. It was shown that with the modified relative stability metrics it is beneficial to

minimize and not maximize the metrics as was the case when selecting the optimal cluster number. Over a wide range of noise percents and cluster conditions minimization of the RCSI selected near ideal ϵ parameters for clustering when measured by the adjusted mutual information score, however attempts to optimize both the distance parameter, ϵ, and the order, O, parameter provided evidence that the RCSI is a biased metric that attempts to choose higher order and ϵ pairs if allowed that match the same approximate density as lower order solutions.

With this knowledge, DMC3 was used to select new ϵ parameters for a set of four synthetic datasets from a prior round robin study on reproducible atom probe analysis in addition to four newly simulated datasets [78]. Of these datasets DMC3 provided competitive estimates on three of the four test scenarios, although was shown to generally favor extraction of denser cluster cores and omit the boundary zones of the features and was more inclined to merge clusters in close proximity when compared to the subject matter experts. In the reference work the main properties of interest were cluster size and number, but this was extended in this work to also include the hardening coefficient given the observed cluster sets. The expected hardening according to the DMC3 cluster results was on the low end for the first two datasets, DM1 and DM2, while the hardening was overestimated for DM3. For all of these datasets the expected hardening generally fell within one standard deviation of the DMC3 result and the hardening given the round robin data provided similar estimate to DMC3. It appears then that DMC3 was not superior to the subject matter experts but could extract comparable cluster sets and derived properties.

The fourth dataset was omitted from the prior discussion for two reasons 1. the round robin data came with no ground truth labels which necessitated the generation of our own datasets and 2. no single group came close to the true solution according to the study leads with knowledge of the true cluster set. This final dataset consisted of an ultra-high Cu background of 10% in comparison to the other three datasets with sub 0.007% Cu, furthermore the clusters said to be 30 atoms in size. Together these factors produce a difficult dataset to cluster that requires access to the cluster labels to gauge method efficacy. In light of that DMC3 was instead applied to a new synthetic dataset meant to emulate the round robin data and DMC3 found an excessive amount of clusters at $1,122$ compared to the true value of 169. In spite of this sweeping over a large range of ϵ while holding order constant found that this solution with an AMI of 0.158 differed from best solution with an AMI of 0.159. The cluster size and cluster consensus scores were then further used select a subset of the clusters believed to be real features reducing the cluster set down to 146 features and improving the AMI to 0.211. So while the cluster sets were inaccurate both in size and number it was not due to DMC3 performing poorly for a single-parameter optimization but actually a limitation imposed by the current stability metrics which cannot be used for multi-objective parameter estimation.

Bibliography

[1] "A Technology Roadmap for Generation IV Nuclear Energy Systems Executive Summary". In: (Mar. 2003). DOI: 10.2172/859105. URL: https://www.osti.gov/biblio/859105.

[2] Vicente J. Araullo-Peters et al. "A new systematic framework for crystallographic analysis of atom probe data". In: *Ultramicroscopy* 154 (2015), pp. 7–14. ISSN: 0304-3991. DOI: https://doi.org/10.1016/j.ultramic.2015.02.009. URL: https://www.sciencedirect.com/science/article/pii/S0304399115000248.

[3] A. Arduino et al. "Monte Carlo method for uncertainty propagation in magnetic resonance-based electric properties tomography". In: *2017 IEEE International Magnetics Conference (INTERMAG)*. 2017, pp. 1–2. DOI: 10.1109/INTMAG.2017.8007964.

[4] Xian-Ming Bai et al. "Modeling copper precipitation hardening and embrittlement in a dilute Fe-0.3at.%Cu alloy under neutron irradiation". In: *Journal of Nuclear Materials* 495 (2017), pp. 442–454. ISSN: 0022-3115. DOI: https://doi.org/10.1016/j.jnucmat.2017.08.042. URL: https://www.sciencedirect.com/science/article/pii/S0022311517307894.

[5] P Bas et al. "A general protocol for the reconstruction of 3D atom probe data". en. In: *Appl. Surf. Sci.* 87-88 (1995), pp. 298–304.

[6] J.F. Bates. "The effects of temperature changes on the swelling of AISI 316". In: *Journal of Nuclear Materials* 98.1 (1981), pp. 71–85. ISSN: 0022-3115. DOI: https://doi.org/10.1016/0022-3115(81)90388-3. URL: https://www.sciencedirect.com/science/article/pii/0022311581903883.

[7] Philip R. Bevington and D. Keith Robinson. *Data reduction and error analysis for the physical sciences*. 3rd ed. Boston: McGraw-Hill, 2003. ISBN: 9780072472271.

[8] J. Blank and K. Deb. "pymoo: Multi-Objective Optimization in Python". In: *IEEE Access* 8 (2020), pp. 89497–89509.

[9] Blavette, D. et al. "Direction et distance d'analyse á la sonde atomique". In: *Rev. Phys. Appl. (Paris)* 17.7 (1982), pp. 435–440. DOI: 10.1051/rphysap:01982001707043500. URL: https://doi.org/10.1051/rphysap:01982001707043500.

[10] W. Blum, P. Eisenlohr, and F. Breutinger. "Understanding creep—a review". In: *Metallurgical and Materials Transactions A* 33.2 (Feb. 2002), pp. 291–303. ISSN: 1543-1940. DOI: 10.1007/s11661-002-0090-9. URL: https://doi.org/10.1007/s11661-002-0090-9.

[11] Shannon M. Bragg-Sitton et al. "Metrics for the Technical Performance Evaluation of Light Water Reactor Accident-Tolerant Fuel". In: *Nuclear Technology* 195.2 (2016), pp. 111–123. DOI: 10.13182/NT15-149. eprint: https://doi.org/10.13182/NT15-149. URL: https://doi.org/10.13182/NT15-149.

[12] B. Burton. "The influence of solute drag on dislocation creep". In: *Philosophical Magazine A* 46.4 (1982), pp. 607–616. DOI: 10.1080/01418618208236916. eprint: https://doi.org/10.1080/01418618208236916. URL: https://doi.org/10.1080/01418618208236916.

[13] CAMECA. *Atom Probe Suite, AP Suite*. Version 6. URL: https://www.cameca.com/service/software/apsuite.

[14] CAMECA. *Integrated Visualization and Analysis Software, IVAS*. Version 6. URL: https://www.cameca.com/service/software/ivas.

[15] Jon Carmack et al. "Overview of the U.S. DOE Accident Tolerant Fuel Development Program". In: (Sept. 2013). URL: https://www.osti.gov/biblio/1130553.

[16] George R. Caskey, David E. Rawl, and David A. Mezzanotte. "Helium embrittlement of stainless steels at ambient temperature". In: *Scripta Metallurgica* 16.8 (1982), pp. 969–972. ISSN: 0036-9748. DOI: https://doi.org/10.1016/0036-9748(82)90135-1. URL: https://www.sciencedirect.com/science/article/pii/0036974882901351.

[17] A. Cerezo and L. Davin. "Aspects of the observation of clusters in the 3-dimensional atom probe". In: *Surface and Interface Analysis* 39.2-3 (2007), pp. 184–188. DOI: https://doi.org/10.1002/sia.2486. eprint: https://analyticalsciencejournals.onlinelibrary.wiley.com/doi/pdf/10.1002/sia.2486. URL: https://analyticalsciencejournals.onlinelibrary.wiley.com/doi/abs/10.1002/sia.2486.

[18] Shengli Chen and David Bernard. "On the calculation of atomic displacements using damage energy". In: *Results in Physics* 16 (2020), p. 102835. ISSN: 2211-3797. DOI: https://doi.org/10.1016/j.rinp.2019.102835. URL: https://www.sciencedirect.com/science/article/pii/S2211379719329869.

[19] Shufen Chu et al. "In situ atomic-scale observation of dislocation climb and grain boundary evolution in nanostructured metal". In: *Nature Communications* 13.1 (May 2022), p. 4151. ISSN: 2041-1723. DOI: 10.1038/s41467-022-31800-8. URL: https://doi.org/10.1038/s41467-022-31800-8.

[20] Carlos A. Coello Coello. "An Introduction to Multi-Objective Particle Swarm Optimizers". In: *Soft Computing in Industrial Applications*. Ed. by António Gaspar-Cunha et al. Berlin, Heidelberg: Springer Berlin Heidelberg, 2011, pp. 3–12. ISBN: 978-3-642-20505-7.

[21] William R Corwin et al. "Generation IV Reactors Integrated Materials Technology Program Plan: Focus on Very High Temperature Reactor Materials". In: (Aug. 2008). DOI: 10.2172/951084. URL: https://www.osti.gov/biblio/951084.

[22] Alec C. Day, Andrew J. Breen, and Simon P. Ringer. "A Crystallography-Mediated Reconstruction (CMR) Approach for Atom Probe Tomography: Solution for a Singleton Pole". In: *Ultramicroscopy* 224 (2021), p. 113262. ISSN: 0304-3991. DOI: https://doi.org/10.1016/j.ultramic.2021.113262. URL: https://www.sciencedirect.com/science/article/pii/S030439912100053X.

[23] Alec C. Day, Anna V. Ceguerra, and Simon P. Ringer. "Introducing a Crystallography-Mediated Reconstruction (CMR) Approach to Atom Probe Tomography". In: *Microscopy and Microanalysis* 25.2 (2019), pp. 288–300. DOI: 10.1017/S1431927618015593.

[24] Frédéric De Geuser and Baptiste Gault. "Metrology of small particles and solute clusters by atom probe tomography". In: *Acta Materialia* 188 (2020), pp. 406–415. ISSN: 1359-6454. DOI: https://doi.org/10.1016/j.actamat.2020.02.023. URL: https://www.sciencedirect.com/science/article/pii/S1359645420301270.

[25] Frédéric De Geuser et al. "Correlated field evaporation as seen by atom probe tomography". In: *Surface Science* 601.2 (2007), pp. 536–543. ISSN: 0039-6028. DOI: https://doi.org/10.1016/j.susc.2006.10.019. URL: https://www.sciencedirect.com/science/article/pii/S003960280601082X.

[26] S. Dhara et al. "Atom probe tomography data analysis procedure for precipitate and cluster identification in a Ti-Mo steel". In: *Data in Brief* 18 (2018), pp. 968–982. ISSN: 2352-3409. DOI: https://doi.org/10.1016/j.dib.2018.03.094. URL: https://www.sciencedirect.com/science/article/pii/S235234091830307X.

[27] Yan Dong et al. "Atom Probe Tomography Interlaboratory Study on Clustering Analysis in Experimental Data Using the Maximum Separation Distance Approach". In: *Microscopy and Microanalysis* 25.2 (2019), pp. 356–366. DOI: 10.1017/S1431927618015581.

[28] David L.J. Engberg et al. "Resolving mass spectral overlaps in atom probe tomography by isotopic substitutions – case of TiSi15N". In: *Ultramicroscopy* 184 (2018), pp. 51–60. ISSN: 0304-3991. DOI: https://doi.org/10.1016/j.ultramic.2017.08.004. URL: https://www.sciencedirect.com/science/article/pii/S030439911 6302145.

[29]   Martin Ester et al. "A Density-Based Algorithm for Discovering Clusters in Large Spatial Databases with Noise". In: *Proceedings of the Second International Conference on Knowledge Discovery and Data Mining*. KDD'96. Portland, Oregon: AAAI Press, 1996, pp. 226–231.

[30]   S. A. Fabritsiev and V. D. Yaroshevich. "Mechanism of helium embrittlement of metals and alloys". In: *Strength of Materials* 18.9 (Sept. 1986), pp. 1194–1202. ISSN: 1573-9325. DOI: `10.1007/BF01522803`. URL: `https://doi.org/10.1007/BF0152280 3`.

[31]   R.G. Faul Kner. "11 - Grain boundaries in creep-resistant steels". In: *Creep-Resistant Steels*. Ed. by Fujio Abe, Torsten-Ulf Kern, and R. Viswanathan. Woodhead Publishing Series in Metals and Surface Engineering. Woodhead Publishing, 2008, pp. 329–349. ISBN: 978-1-84569-178-3. DOI: `https://doi.org/10.1533/9781845694012.2.3 29`. URL: `https://www.sciencedirect.com/science/article/pii/B97818456917 83500115`.

[32]   Peter Felfer et al. *Atom Probe Toolbox*. URL: `https://github.com/peterfelfer/At om-Probe-Toolbox`.

[33]   Massimiliano Ferrucci, Evelina Ametova, and Wim Dewulf. "Monte Carlo reconstruction: a concept for propagating uncertainty in computed tomography". In: *Measurement Science and Technology* 32.11 (July 2021), p. 115006. DOI: `10.1088/1361-650 1/ac07db`. URL: `https://doi.org/10.1088/1361-6501/ac07db`.

[34]   Hongguang Fu, Xiuqin Zhong, and Zhenbing Zeng. "Automated and readable simplification of trigonometric expressions". In: *Mathematical and Computer Modelling* 44.11 (2006), pp. 1169–1177. ISSN: 0895-7177. DOI: `https://doi.org/10.1016/j.m cm.2006.04.002`. URL: `https://www.sciencedirect.com/science/article/pii /S0895717706001609`.

[35]   R. Garnett, Michael A. Osborne, and Stephen J. Roberts. "Gaussian Processes for Global Optimization". In: 2008.

[36]   B. Gault et al. "Advances in the reconstruction of atom probe tomography data". In: *Ultramicroscopy* 111.6 (2011). Special Issue: 52nd International Field Emission Symposium, pp. 448–457. ISSN: 0304-3991. DOI: `https://doi.org/10.1016/j.ultr amic.2010.11.016`. URL: `https://www.sciencedirect.com/science/article/pi i/S0304399110003062`.

[37]   B. Gault et al. "Impact of directional walk on atom probe microanalysis". In: *Ultramicroscopy* 113 (2012), pp. 182–191. ISSN: 0304-3991. DOI: `https://doi.org/10.10 16/j.ultramic.2011.06.005`. URL: `https://www.sciencedirect.com/science/a rticle/pii/S0304399111001756`.

[38]   Baptiste Gault et al. "Advances in the calibration of atom probe tomographic reconstruction". In: *Journal of Applied Physics* 105.3 (2009), p. 034913. DOI: `10.1063/1 .3068197`.

[39] Baptiste Gault et al. "Atom probe crystallography". In: *Materials Today* 15.9 (2012), pp. 378–386. ISSN: 1369-7021. DOI: `https://doi.org/10.1016/S1369-7021(12)70164-5`. URL: `https://www.sciencedirect.com/science/article/pii/S1369702112701645`.

[40] Baptiste Gault et al. *Atom Probe Microscopy*. en. 2012th ed. New York, NY: Springer, 2014.

[41] Baptiste Gault et al. "Dynamic reconstruction for atom probe tomography". In: *Ultramicroscopy* 111.11 (2011), pp. 1619–1624. ISSN: 0304-3991. DOI: `https://doi.org/10.1016/j.ultramic.2011.08.005`. URL: `https://www.sciencedirect.com/science/article/pii/S0304399111001999`.

[42] Baptiste Gault et al. "Estimation of the reconstruction parameters for Atom Probe Tomography". In: (Oct. 2015). DOI: `10.1017/S1431927608080690`. arXiv: `1510.02889 [physics.ins-det]`.

[43] Baptiste Gault et al. "Reflections on the Spatial Performance of Atom Probe Tomography in the Analysis of Atomic Neighborhoods." In: *Microscopy and microanalysis : the official journal of Microscopy Society of America, Microbeam Analysis Society, Microscopical Society of Canada* (2021), pp. 1–11.

[44] Baptiste Gault et al. "Spatial Resolution in Atom Probe Tomography". In: *Microscopy Microanal.* 16.1 (2010), pp. 99–110. DOI: `10.1017/S1431927609991267`. arXiv: `1510.02893 [physics.ins-det]`.

[45] B.P. Geiser et al. In: *Microscopy and Microanalysis* 15 (suppl 2) (2009), pp. 292–293. ISSN: 2.

[46] I. Ghamarian and E.A. Marquis. "Hierarchical density-based cluster analysis framework for atom probe tomography data". In: *Ultramicroscopy* 200 (2019), pp. 28–38. ISSN: 0304-3991. DOI: `https://doi.org/10.1016/j.ultramic.2019.01.011`. URL: `https://www.sciencedirect.com/science/article/pii/S0304399118303267`.

[47] Iman Ghamarian, Li-Jen Yu, and Emmanuelle Marquis. "Quantification of Solute Topology in Atom Probe Tomography Data: Application to the Microstructure of a Proton-Irradiated Alloy 625". In: *Metallurgical and Materials Transactions A* 51 (Nov. 2019). DOI: `10.1007/s11661-019-05520-6`.

[48] Iman Ghamarian, L.-J Yu, and Emmanuelle Marquis. "Morphological classification of dense objects in atom probe tomography data". In: *Ultramicroscopy* 215 (May 2020), p. 112996. DOI: `10.1016/j.ultramic.2020.112996`.

[49] *GIF R&D Outlook for Generation IV Nuclear Energy Systems: 2018 Update*. `https://www.gen-4.org/gif/upload/docs/application/pdf/2021-11/gif_rd_outlook_for_generation_iv_nuclear_energy_systems__2018_update_new_cover.pdf`. Accessed: 2023-03-14 [Online].

[50] Robert Gomer. *Field emissions and field ionization*. en. New York, NY: American Institute of Physics, 1992.

[51] Hans David Gougar. "Assessment of the Technical Maturity of Generation IV Concepts for Test or Demonstration Reactor Applications, Revision 2". In: (Oct. 2015). DOI: 10.2172/1236803. URL: https://www.osti.gov/biblio/1236803.

[52] Jeffery B. Greenblatt et al. "The Future of Low-Carbon Electricity". In: *Annual Review of Environment and Resources* 42.1 (2017), pp. 289–316. DOI: 10.1146/annurev-environ-102016-061138. eprint: https://doi.org/10.1146/annurev-environ-102016-061138. URL: https://doi.org/10.1146/annurev-environ-102016-061138.

[53] Anjum Hajat, Charlene Hsia, and Marie S. O'Neill. "Socioeconomic Disparities and Air Pollution Exposure: a Global Review". In: *Current Environmental Health Reports* 2.4 (Dec. 2015), pp. 440–450. ISSN: 2196-5412. DOI: 10.1007/s40572-015-0069-5. URL: https://doi.org/10.1007/s40572-015-0069-5.

[54] D. Haley, P. Choi, and D. Raabe. "Guided mass spectrum labelling in atom probe tomography". In: *Ultramicroscopy* 159 (2015). 1st International Conference on Atom Probe Tomography and Microscopy, pp. 338–345. ISSN: 0304-3991. DOI: https://doi.org/10.1016/j.ultramic.2015.03.005. URL: https://www.sciencedirect.com/science/article/pii/S0304399115000479.

[55] Daniel Haley, Paul A. J. Bagot, and Michael P. Moody. "DF-Fit: A Robust Algorithm for Detection of Crystallographic Information in Atom Probe Tomography Data". In: *Microscopy and Microanalysis* 25.2 (2019), pp. 331–337. DOI: 10.1017/S1431927618015507.

[56] S. Hamada et al. "Temperature dependence of swelling in type 316 stainless steel irradiated in HFIR". In: *Journal of Nuclear Materials* 155-157 (1988), pp. 838–844. ISSN: 0022-3115. DOI: https://doi.org/10.1016/0022-3115(88)90426-6. URL: https://www.sciencedirect.com/science/article/pii/0022311588904266.

[57] Constantinos Hatzoglou, Gérald Da Costa, and François Vurpillot. "Enhanced dynamic reconstruction for atom probe tomography". In: *Ultramicroscopy* 197 (2019), pp. 72–82. ISSN: 0304-3991. DOI: https://doi.org/10.1016/j.ultramic.2018.11.010. URL: https://www.sciencedirect.com/science/article/pii/S0304399118300494.

[58] Tim Head et al. *scikit-optimize/scikit-optimize*. Version v0.9.0. Oct. 2021. DOI: 10.5281/zenodo.5565057. URL: https://doi.org/10.5281/zenodo.5565057.

[59] Xunxiang Hu et al. "Modeling of irradiation hardening of iron after low-dose and low-temperature neutron irradiation". In: *Modelling and Simulation in Materials Science and Engineering* 22.6 (July 2014), p. 065002. DOI: 10.1088/0965-0393/22/6/065002. URL: https://dx.doi.org/10.1088/0965-0393/22/6/065002.

[60] Ching-Lai Hwang and Kwangsun Yoon. "Methods for Multiple Attribute Decision Making". In: *Multiple Attribute Decision Making: Methods and Applications A State-of-the-Art Survey*. Berlin, Heidelberg: Springer Berlin Heidelberg, 1981, pp. 58–191. DOI: 10.1007/978-3-642-48318-9_3. URL: https://doi.org/10.1007/978-3-642-48318-9_3.

[61] J.M. Hyde et al. "Lateral and depth scale calibration of the position sensitive atom probe". In: *Applied Surface Science* 76-77 (1994), pp. 382–391. ISSN: 0169-4332. DOI: https://doi.org/10.1016/0169-4332(94)90371-9. URL: https://www.sciencedirect.com/science/article/pii/0169433294903719.

[62] Kazuma Ito, Hideaki Sawada, and Shigenobu Ogata. "First-principles study on the grain boundary embrittlement of bcc-Fe by Mn segregation". In: *Phys. Rev. Mater.* 3 (1 Jan. 2019), p. 013609. DOI: 10.1103/PhysRevMaterials.3.013609. URL: https://link.aps.org/doi/10.1103/PhysRevMaterials.3.013609.

[63] Bo Jansson and Arne Melander. "On the critical resolved shear stress from misfitting particles". In: *Scripta Metallurgica* 12.6 (1978), pp. 497–498. ISSN: 0036-9748. DOI: https://doi.org/10.1016/0036-9748(78)90194-1. URL: https://www.sciencedirect.com/science/article/pii/0036974878901941.

[64] Miaomiao Jin, Penghui Cao, and Michael P. Short. "Predicting the onset of void swelling in irradiated metals with machine learning". In: *Journal of Nuclear Materials* 523 (2019), pp. 189–197. ISSN: 0022-3115. DOI: https://doi.org/10.1016/j.jnucmat.2019.05.054. URL: https://www.sciencedirect.com/science/article/pii/S002231151930011X.

[65] Shuoxue Jin et al. "Irradiation evolution of Cu precipitates in Fe1.0Cu alloy studied by positron annihilation spectroscopy". In: *Journal of Nuclear Materials* 499 (2018), pp. 65–70. ISSN: 0022-3115. DOI: https://doi.org/10.1016/j.jnucmat.2017.11.011. URL: https://www.sciencedirect.com/science/article/pii/S0022311517306967.

[66] Christopher John et al. "M3C: Monte Carlo reference-based consensus clustering". In: *Scientific Reports* 10 (Feb. 2020), p. 1816. DOI: 10.1038/s41598-020-58766-1.

[67] M. Johnson et al. "Irradiation-induced microstructure and microchemistry effects on mechanical properties in ferritic-martensitic alloys". In: *Materialia* 20 (2021), p. 101228. ISSN: 2589-1529. DOI: https://doi.org/10.1016/j.mtla.2021.101228. URL: https://www.sciencedirect.com/science/article/pii/S2589152921002313.

[68] John E. Kelly. "Generation IV International Forum: A decade of progress through international cooperation". In: *Progress in Nuclear Energy* 77 (2014), pp. 240–246. ISSN: 0149-1970. DOI: 10.1016/j.pnucene.2014.02.010. URL: https://www.sciencedirect.com/science/article/pii/S0149197014000419.

[69] Pushker A. Kharecha and James E. Hansen. "Prevented Mortality and Greenhouse Gas Emissions from Historical and Projected Nuclear Power". In: *Environmental Science & Technology* 47.9 (May 2013), pp. 4889–4895. ISSN: 0013-936X. DOI: 10.1021 /es3051197. URL: https://doi.org/10.1021/es3051197.

[70] Son H. Kim, Temitope A. Taiwo, and Brent W. Dixon. "The Carbon Value of Nuclear Power Plant Lifetime Extensions in the United States". In: *Nuclear Technology* 208.5 (2022), pp. 775–793. DOI: 10.1080/00295450.2021.1951554. eprint: https://doi .org/10.1080/00295450.2021.1951554. URL: https://doi.org/10.1080/002954 50.2021.1951554.

[71] G. Kinchin and R. Pease. "The Displacement of Atoms in Solids by Radiation". In: *Reports on Progress in Physics - REP PROGR PHYS* 18 (Jan. 1955), pp. 1–51. DOI: 10.1088/0034-4885/18/1/301.

[72] H.H. Ku. "Notes on the use of propagation of error formulas". en. In: *Journal of Research of the National Bureau of Standards, Section C: Engineering and Instrumentation* 70C.4 (Oct. 1966), p. 263. ISSN: 0022-4316. DOI: 10.6028/jres.070C.025. URL: https://nvlpubs.nist.gov/nistpubs/jres/70C/jresv70Cn4p263_A1b.pdf (visited on 01/18/2022).

[73] D. J. Larson, K. F. Russell, and M. K. Miller. "Effect of Specimen Aspect Ratio on the Reconstruction of Atom Probe Tomography Data". In: *Microscopy and Microanalysis* 5.S2 (1999), pp. 930–931. DOI: 10.1017/S1431927600017979.

[74] David J Larson et al. *Local electrode atom probe tomography: A user's guide.* en. New York, NY: Springer, 2016.

[75] S. H. Lee and W. Chen. "A comparative study of uncertainty propagation methods for black-box-type problems". In: *Structural and Multidisciplinary Optimization* 37.3 (May 2008), p. 239. ISSN: 1615-1488. DOI: 10.1007/s00158-008-0234-7. URL: https://doi.org/10.1007/s00158-008-0234-7.

[76] Johnnye Lewis, Joseph Hoover, and Debra MacKenzie. "Mining and Environmental Health Disparities in Native American Communities". en. In: *Curr Environ Health Rep* 4.2 (June 2017), pp. 130–141. DOI: 10.1007/s40572-017-0140-5.

[77] Hans Magnusson and Rolf Sandström. "The Role of Dislocation Climb across Particles at Creep Conditions in 9 to 12 Pct Cr Steels". In: *Metallurgical and Materials Transactions A* 38.10 (Oct. 2007), pp. 2428–2434. ISSN: 1543-1940. DOI: 10.1007/s1 1661-007-9280-9. URL: https://doi.org/10.1007/s11661-007-9280-9.

[78] Emmanuelle Marquis et al. "On the Use of Density-Based Algorithms for the Analysis of Solute Clustering in Atom Probe Tomography Data". In: Jan. 2019, pp. 2097–2113. ISBN: 978-3-030-04638-5. DOI: 10.1007/978-3-030-04639-2_141.

[79] K. Maruyama. "8 - Fundamental aspects of creep deformation and deformation mechanism map". In: *Creep-Resistant Steels*. Ed. by Fujio Abe, Torsten-Ulf Kern, and R. Viswanathan. Woodhead Publishing Series in Metals and Surface Engineering. Woodhead Publishing, 2008, pp. 265–278. ISBN: 978-1-84569-178-3. DOI: `https://doi.org/10.1533/9781845694012.2.265`. URL: `https://www.sciencedirect.com/science/article/pii/B9781845691783500085`.

[80] Frederick Meisenkothen et al. "Atom Probe Mass Spectrometry of Uranium Isotopic Reference Materials". In: *Analytical Chemistry* 92.16 (2020). PMID: 32693575, pp. 11388–11395. DOI: `10.1021/acs.analchem.0c02273`. eprint: `https://doi.org/10.1021/acs.analchem.0c02273`. URL: `https://doi.org/10.1021/acs.analchem.0c02273`.

[81] Frederick Meisenkothen et al. "Exploring the accuracy of isotopic analyses in atom probe mass spectrometry". In: *Ultramicroscopy* 216 (2020), p. 113018. ISSN: 0304-3991. DOI: `https://doi.org/10.1016/j.ultramic.2020.113018`. URL: `https://www.sciencedirect.com/science/article/pii/S030439912030005X`.

[82] E. Meslin, B. Radiguet, and M. Loyer-Prost. "Radiation-induced precipitation in a ferritic model alloy: An experimental and theoretical study". In: *Acta Materialia* 61.16 (2013), pp. 6246–6254. ISSN: 1359-6454. DOI: `https://doi.org/10.1016/j.actamat.2013.07.008`. URL: `https://www.sciencedirect.com/science/article/pii/S1359645413005107`.

[83] M. K. Miller. "Field Ion Microscopy". In: *Atom Probe Tomography: Analysis at the Atomic Level*. Boston, MA: Springer US, 2000, pp. 45–83. ISBN: 978-1-4615-4281-0. DOI: `10.1007/978-1-4615-4281-0_3`. URL: `https://doi.org/10.1007/978-1-4615-4281-0_3`.

[84] Stefano Monti et al. "Consensus Clustering: A Resampling-Based Method for Class Discovery and Visualization of Gene Expression Microarray Data". In: *Machine Learning* 52 (July 2003), pp. 91–118. DOI: `10.1023/A:1023949509487`.

[85] Michael P. Moody et al. "Qualification of the tomographic reconstruction in atom probe by advanced spatial distribution map techniques". In: *Ultramicroscopy* 109.7 (2009), pp. 815–824. ISSN: 0304-3991. DOI: `https://doi.org/10.1016/j.ultramic.2009.03.016`. URL: `https://www.sciencedirect.com/science/article/pii/S0304399109000497`.

[86] K.L. Murty et al. "3 - Creep deformation of materials in light water reactors (LWRs)". In: *Materials Ageing and Degradation in Light Water Reactors*. Ed. by K.L. Murty. Woodhead Publishing Series in Energy. Woodhead Publishing, 2013, pp. 81–148. ISBN: 978-0-85709-239-7. DOI: `https://doi.org/10.1533/9780857097453.1.81`. URL: `https://www.sciencedirect.com/science/article/pii/B9780857092397500031`.

[87] Y. Nagai et al. "Kinetics of irradiation-induced Cu precipitation in nuclear reactor pressure vessel steels". In: *Applied Physics Letters* 87.26 (2005), p. 261920. DOI: 10.1063/1.2159091. eprint: https://doi.org/10.1063/1.2159091. URL: https://doi.org/10.1063/1.2159091.

[88] Sukanta Nayak. "Chapter nine - Multiobjective optimization". In: *Fundamentals of Optimization Techniques with Algorithms*. Ed. by Sukanta Nayak. Academic Press, 2020, pp. 253–270. ISBN: 978-0-12-821126-7. DOI: https://doi.org/10.1016/B978-0-12-821126-7.00009-7. URL: https://www.sciencedirect.com/science/article/pii/B9780128211267000097.

[89] Ba Nghiep Nguyen, Charles H. Henager, and Richard J. Kurtz. "Modeling thermal and irradiation-induced swelling effects on the integrity of Ti3SiC2/SiC joints". In: *Journal of Nuclear Materials* 495 (2017), pp. 504–515. ISSN: 0022-3115. DOI: https://doi.org/10.1016/j.jnucmat.2017.09.011. URL: https://www.sciencedirect.com/science/article/pii/S0022311517303471.

[90] Bram F. Noble and Jackie E. Bronson. "Integrating Human Health into Environmental Impact Assessment: Case Studies of Canada's Northern Mining Resource Sector". In: *Arctic* 58.4 (2005), pp. 395–405. ISSN: 00040843. DOI: 10.2307/40513106. URL: http://www.jstor.org/stable/40513106 (visited on 03/14/2023).

[91] Kai Nordlund et al. "Improving atomic displacement and replacement calculations with physically realistic damage models". In: *Nature Communications* 9.1 (Mar. 2018), p. 1084. ISSN: 2041-1723. DOI: 10.1038/s41467-018-03415-5. URL: https://doi.org/10.1038/s41467-018-03415-5.

[92] Kai Nordlund et al. "Primary radiation damage: A review of current understanding and models". In: *Journal of Nuclear Materials* 512 (2018), pp. 450–479. ISSN: 0022-3115. DOI: https://doi.org/10.1016/j.jnucmat.2018.10.027. URL: https://www.sciencedirect.com/science/article/pii/S002231151831016X.

[93] "Nuclear Power in a Clean Energy System". In: (2019). License: CC BY 4.0. URL: https://www.iea.org/reports/nuclear-power-in-a-clean-energy-system.

[94] Travis A. O'Brien et al. "A fast and objective multidimensional kernel density estimation method: fastKDE". In: *Computational Statistics & Data Analysis* 101 (2016), pp. 148–160. ISSN: 0167-9473. DOI: https://doi.org/10.1016/j.csda.2016.02.014. URL: https://www.sciencedirect.com/science/article/pii/S0167947316300408.

[95] Travis A. O'Brien et al. "Reducing the computational cost of the ECF using a nuFFT: A fast and objective probability density estimation method". In: *Computational Statistics & Data Analysis* 79 (2014), pp. 222–234. ISSN: 0167-9473. DOI: https://doi.org/10.1016/j.csda.2014.06.002. URL: https://www.sciencedirect.com/science/article/pii/S016794731400173X.

[96] G. R. Odette and G. E. Lucas. "Embrittlement of nuclear reactor pressure vessels". In: *JOM* 53.7 (May 2001), pp. 18–22. ISSN: 1543-1851. DOI: 10.1007/s11837-001-0081-0. URL: https://doi.org/10.1007/s11837-001-0081-0.

[97] G. R. Odette and G. E. Lucas. "Recent progress in understanding reactor pressure vessel steel embrittlement". In: *Radiation Effects and Defects in Solids* 144.1-4 (1998), pp. 189–231. DOI: 10.1080/10420159808229676. eprint: https://doi.org/10.1080/10420159808229676. URL: https://doi.org/10.1080/10420159808229676.

[98] H. Oikawa and Y. Iijima. "7 - Diffusion behaviour of creep-resistant steels". In: *Creep-Resistant Steels*. Ed. by Fujio Abe, Torsten-Ulf Kern, and R. Viswanathan. Woodhead Publishing Series in Metals and Surface Engineering. Woodhead Publishing, 2008, pp. 241–264. ISBN: 978-1-84569-178-3. DOI: https://doi.org/10.1533/9781845694012.2.241. URL: https://www.sciencedirect.com/science/article/pii/B9781845691783500073.

[99] L.J. Ott, K.R. Robb, and D. Wang. "Preliminary assessment of accident-tolerant fuels on LWR performance during normal operation and under DB and BDB accident conditions". In: *Journal of Nuclear Materials* 448.1 (2014), pp. 520–533. ISSN: 0022-3115. DOI: https://doi.org/10.1016/j.jnucmat.2013.09.052. URL: https://www.sciencedirect.com/science/article/pii/S002231151301129X.

[100] Jammal R et al. *The Fukushima Daiichi Accident*. STI/PUB/1710. Vol. 1-3. Vienna (Austria): IAEA, 2015. ISBN: 978-92-0-107015-9. URL: http://www-pub.iaea.org/books/IAEABooks/10962/The-Fukushima-Daiichi-Accident.

[101] Randa S. Ramadan et al. "Environmental and health impact of current uranium mining activities in southwestern Sinai, Egypt". In: *Environmental Earth Sciences* 81.7 (Mar. 2022), p. 213. ISSN: 1866-6299. DOI: 10.1007/s12665-022-10341-9. URL: https://doi.org/10.1007/s12665-022-10341-9.

[102] Saman Razavi and Hoshin V. Gupta. "What do we mean by sensitivity analysis? The need for comprehensive characterization of "global" sensitivity in Earth and Environmental systems models". In: *Water Resources Research* 51.5 (2015), pp. 3070–3092. DOI: https://doi.org/10.1002/2014WR016527. eprint: https://agupubs.onlinelibrary.wiley.com/doi/pdf/10.1002/2014WR016527. URL: https://agupubs.onlinelibrary.wiley.com/doi/abs/10.1002/2014WR016527.

[103] Michael Buchdahl Roth and Paulina Jaramillo. "Going nuclear for climate mitigation: An analysis of the cost effectiveness of preserving existing U.S. nuclear power plants as a carbon avoidance strategy". In: *Energy* 131 (2017), pp. 67–77. ISSN: 0360-5442. DOI: https://doi.org/10.1016/j.energy.2017.05.011. URL: https://www.sciencedirect.com/science/article/pii/S0360544217307491.

[104] Kathryn C Russell and L.M Brown. "A dispersion strengthening model based on differing elastic moduli applied to the iron-copper system". In: *Acta Metallurgica* 20.7 (1972), pp. 969–974. ISSN: 0001-6160. DOI: `https://doi.org/10.1016/0001-6160(72)90091-0`. URL: `https://www.sciencedirect.com/science/article/pii/0001616072900910`.

[105] Dan Schreiber. Private Communication. 2021.

[106] Artur M. Schweidtmann et al. "Deterministic global optimization with Gaussian processes embedded". In: *Mathematical Programming Computation* 13.3 (Sept. 2021), pp. 553–581. ISSN: 1867-2957. DOI: `10.1007/s12532-021-00204-y`. URL: `https://doi.org/10.1007/s12532-021-00204-y`.

[107] Skipper Seabold and Josef Perktold. "statsmodels: Econometric and statistical modeling with python". In: *9th Python in Science Conference*. 2010.

[108] Haitham Seada and Kalyanmoy Deb. "A Unified Evolutionary Optimization Procedure for Single, Multiple, and Many Objectives". In: *IEEE Transactions on Evolutionary Computation* 20.3 (2016), pp. 358–369. DOI: `10.1109/TEVC.2015.2459718`.

[109] Yasin Şenbabaoğlu, George Michailidis, and Jun Li. "Critical limitations of consensus clustering in class discovery". In: *Scientific reports* 4 (Aug. 2014), p. 6207. DOI: `10.1038/srep06207`.

[110] *Ceramic Composites for Near Term Reactor Application*. Vol. Fourth International Topical Meeting on High Temperature Reactor Technology, Volume 2. High Temperature Reactor Technology. Sept. 2008, pp. 1–10. DOI: `10.1115/HTR2008-58050`. eprint: `https://asmedigitalcollection.asme.org/HTR/proceedings-pdf/HTR2008/48555/1/2716491/1\_1.pdf`. URL: `https://doi.org/10.1115/HTR2008-58050`.

[111] I.M Sobol'. "Global sensitivity indices for nonlinear mathematical models and their Monte Carlo estimates". In: *Mathematics and Computers in Simulation* 55.1 (2001). The Second IMACS Seminar on Monte Carlo Methods, pp. 271–280. ISSN: 0378-4754. DOI: `https://doi.org/10.1016/S0378-4754(00)00270-6`. URL: `https://www.sciencedirect.com/science/article/pii/S0378475400002706`.

[112] Leigh T. Stephenson et al. "New Techniques for the Analysis of Fine-Scaled Clustering Phenomena within Atom Probe Tomography (APT) Data". In: *Microscopy and Microanalysis* 13.6 (2007), pp. 448–463. DOI: `10.1017/S1431927607070900`.

[113] Evan K. Still et al. "Alpha Shape Analysis (ASA) Framework for Post- Clustering Property Determination in Atom Probe Tomographic Data". In: *Microscopy and Microanalysis* 27.2 (2021), pp. 297–317. DOI: `10.1017/S1431927620024939`.

[114] Paul D. Styman et al. "Quantitative methods for the APT analysis of thermally aged RPV steels". In: *Ultramicroscopy* 132 (2013). IFES 2012, pp. 258–264. ISSN: 0304-3991. DOI: `https://doi.org/10.1016/j.ultramic.2012.12.003`. URL: `https://www.sciencedirect.com/science/article/pii/S0304399112002902`.

[115] W.P. Sun and J.J. Jonas. "Influence of dynamic precipitation on grain boundary sliding during high temperature creep". In: *Acta Metallurgica et Materialia* 42.1 (1994), pp. 283–292. ISSN: 0956-7151. DOI: https://doi.org/10.1016/0956-7151(94)90070-1. URL: https://www.sciencedirect.com/science/article/pii/0956715194900701.

[116] L. Tan and J.T. Busby. "Formulating the strength factor α for improved predictability of radiation hardening". In: *Journal of Nuclear Materials* 465 (2015), pp. 724–730. ISSN: 0022-3115. DOI: https://doi.org/10.1016/j.jnucmat.2015.07.009. URL: https://www.sciencedirect.com/science/article/pii/S0022311515300957.

[117] John R. Taylor. *An introduction to error analysis: the study of uncertainties in physical measurements*. 2nd ed. Sausalito, Calif: University Science Books, 1997. ISBN: 9780935702422.

[118] Kurt A. Terrani. "Accident tolerant fuel cladding development: Promise, status, and challenges". In: *Journal of Nuclear Materials* 501 (2018), pp. 13–30. ISSN: 0022-3115. DOI: https://doi.org/10.1016/j.jnucmat.2017.12.043. URL: https://www.sciencedirect.com/science/article/pii/S0022311517316227.

[119] P. A. Thorsen. *The influence of the grain boundary structure on diffusional creep*. Tech. rep. RISO-R–1047(EN). Denmark, 1998, p. 126. URL: http://inis.iaea.org/search/search.aspx?orig_q=RN:29042641.

[120] Tien Tsong. "Mechanisms of surface diffusion". In: *Progress in Surface Science* 67 (May 2001), pp. 235–248. DOI: 10.1016/S0079-6816(01)00026-0.

[121] Nazanin Vafaei, Rita A. Ribeiro, and Luis M. Camarinha-Matos. "Assessing Normalization Techniques for TOPSIS Method". In: *Technological Innovation for Applied AI Systems*. Ed. by Luis M. Camarinha-Matos, Pedro Ferreira, and Guilherme Brito. Cham: Springer International Publishing, 2021, pp. 132–141. ISBN: 978-3-030-78288-7.

[122] Jing Wang et al. "The Application of the OPTICS Algorithm to Cluster Analysis in Atom Probe Tomography Data". In: *Microscopy and Microanalysis* 25.2 (2019), pp. 338–348. DOI: 10.1017/S1431927618015386.

[123] Zhiyuan Wang and Gade Pandu Rangaiah. "Application and Analysis of Methods for Selecting an Optimal Solution from the Pareto-Optimal Front obtained by Multiobjective Optimization". In: *Industrial & Engineering Chemistry Research* 56.2 (2017), pp. 560–574. DOI: 10.1021/acs.iecr.6b03453. eprint: https://doi.org/10.1021/acs.iecr.6b03453. URL: https://doi.org/10.1021/acs.iecr.6b03453.

[124] J. Weertman. "Theory of Steady-State Creep Based on Dislocation Climb". In: *Journal of Applied Physics* 26.10 (1955), pp. 1213–1217. DOI: 10.1063/1.1721875. eprint: https://doi.org/10.1063/1.1721875. URL: https://doi.org/10.1063/1.1721875.

[125] X. J. Wu and A. K. Koul. "Grain boundary sliding in the presence of grain boundary precipitates during transient creep". In: *Metallurgical and Materials Transactions A* 26.4 (Apr. 1995), pp. 905–914. ISSN: 1543-1940. DOI: 10.1007/BF02649087. URL: https://doi.org/10.1007/BF02649087.

[126] Zhiping Xiong, Ilana Timokhina, and Elena Pereloma. "Clustering, nano-scale precipitation and strengthening of steels". In: *Progress in Materials Science* 118 (2021), p. 100764. ISSN: 0079-6425. DOI: https://doi.org/10.1016/j.pmatsci.2020.1007 64. URL: https://www.sciencedirect.com/science/article/pii/S00796425203 01286.

[127] Yong Yang et al. "Irradiation Microstructure of Austenitic Steels and Cast Steels Irradiated in the BOR-60 Reactor at 320°C". In: *Proceedings of the 15th International Conference on Environmental Degradation of Materials in Nuclear Power Systems — Water Reactors*. Ed. by Jeremy T. Busby, Gabriel Ilevbare, and Peter L. Andresen. Cham: Springer International Publishing, 2016, pp. 2137–2149. ISBN: 978-3-319-48760-1.

[128] L. Yao et al. "Crystallographic structural analysis in atom probe microscopy via 3D Hough transformation". In: *Ultramicroscopy* 111.6 (2011). Special Issue: 52nd International Field Emission Symposium, pp. 458–463. ISSN: 0304-3991. DOI: https://doi.org/10.1016/j.ultramic.2010.11.018. URL: https://www.sciencedirec t.com/science/article/pii/S0304399110003086.

[129] Chunyu Yin et al. "A Multi-Scale Simulation Study of Irradiation Swelling of Silicon Carbide". In: *Materials* 15.9 (Apr. 2022), p. 3008. DOI: 10.3390/ma15093008. URL: https://doi.org/10.3390/ma15093008.

[130] Lichao Yuan and Yujie Wei. "A multi-scale algorithm for dislocation creep at elevated temperatures". In: *Theoretical & Applied Mechanics Letters* 11.1 (2021), pp. 100230-48-100230–53. ISSN: 2095-0349. DOI: 10.1016/j.taml.2021.100230. URL: /article /id/62352ea0ca140b60b527fbc5.

[131] "1 - Creep Behavior of Materials". In: *High Temperature Deformation and Fracture of Materials*. Ed. by Jun-Shan Zhang. Woodhead Publishing, 2010, pp. 3–13. ISBN: 978-0-85709-079-9. DOI: https://doi.org/10.1533/9780857090805.1.3. URL: htt ps://www.sciencedirect.com/science/article/pii/B978085709079950001X.

[132] "11 - Mechanisms of Grain Boundary Sliding". In: *High Temperature Deformation and Fracture of Materials*. Ed. by Jun-Shan Zhang. Woodhead Publishing, 2010, pp. 172–181. ISBN: 978-0-85709-079-9. DOI: https://doi.org/10.1533/9780857090805.1.1 72. URL: https://www.sciencedirect.com/science/article/pii/B97808570907 99500112.

[133]   "3 - Dislocation Motion at Elevated Temperatures". In: *High Temperature Deformation and Fracture of Materials*. Ed. by Jun-Shan Zhang. Woodhead Publishing, 2010, pp. 28–39. ISBN: 978-0-85709-079-9. DOI: `https://doi.org/10.1533/978085709080 5.1.28`. URL: `https://www.sciencedirect.com/science/article/pii/B9780857 090799500033`.

[134]   "9 - Diffusional Creep". In: *High Temperature Deformation and Fracture of Materials*. Ed. by Jun-Shan Zhang. Woodhead Publishing, 2010, pp. 139–153. ISBN: 978-0-85709-079-9. DOI: `https://doi.org/10.1533/9780857090805.1.139`. URL: `https://www .sciencedirect.com/science/article/pii/B9780857090799500094`.

[135]   Aimin Zhou et al. "Multiobjective evolutionary algorithms: A survey of the state of the art". In: *Swarm and Evolutionary Computation* 1.1 (2011), pp. 32–49. ISSN: 2210-6502. DOI: `https://doi.org/10.1016/j.swevo.2011.03.001`. URL: `https://www .sciencedirect.com/science/article/pii/S2210650211000058`.